Universidade de Lisboa
Faculdade de Medicina de Lisboa


# STRUCTURE AND MECHANISM OF KYNURENINE 3-MONOOXYGENASE, A CANDIDATE HUNTINGTON'S DISEASE DRUG TARGET

**MARTA ISABEL MAGALHÃES MOTA DO AMARAL**

**DOUTORAMENTO EM CIÊNCIAS BIOMÉDICAS**
**ESPECIALIDADE NEUROCIÊNCIAS**

**ABRIL 2013**

Universidade de Lisboa

Faculdade de Medicina de Lisboa


# STRUCTURE AND MECHANISM OF KYNURENINE 3-MONOOXYGENASE, A CANDIDATE HUNTINGTON'S DISEASE DRUG TARGET

**MARTA ISABEL MAGALHÃES MOTA DO AMARAL**

Orientador: Prof. Dr. Tiago Flemming Outeiro
Co-Orientadores: Prof. Dr. Nigel Scrutton
Dr. Flaviano Giorgini

**DOUTORAMENTO EM CIÊNCIAS BIOMÉDICAS**
**ESPECIALIDADE NEUROCIÊNCIAS**

**A impressão desta dissertação foi aprovada pelo Conselho Cientifico da Faculdade de Medicina de Lisboa em reunião de (*data em que recaiu a aprovação*)**

# *TABLE OF CONTENTS*

# *LIST OF TABLES*

# *LIST OF FIGURES*

# *LIST OF ABBREVIATIONS*

| | |
|---|---|
| **AD** | Alzheimer's disease |
| **ARH** | Aryl hydrocarbon receptor |
| **BBB** | Blood brain barrier |
| **BMGY** | Buffered Glycerol complex Medium |
| **BMMY** | Buffered Methanol Complex Medium |
| **BNA4** | Kynurenine 3-monooxygenase gene from *Saccharomyces cerevisiae* |
| **CD** | Circular dichroism |
| **CMC** | Critical micelle concentration |
| **DDM** | n-Dodecyl–β-maltoside |
| **DRI** | Differential refractive index |
| **EL-MS** | Electrospray Ionisation Mass Spectrometry |
| **FAD** | Flavin mononucleotide |
| **FDA** | Food and Drug Administration |
| **FMN** | Flavin adenine dinucleotide |
| **GST** | Glutathione S-transferase |
| **HD** | Huntington's Disease |
| **HDAC** | Histone deacetylase |
| **HTT** | Huntingtin |
| **IDO** | Indoleamine-2,3-dioxygenase |
| **IPTG** | Isopropyl β-D-thiogalactopyranoside |
| **JM6** | 2-(3,4-dimethoxybenzenesulfonylamino)- 4-(3-nitrophenyl)-5-(piperidin-1-yl)methylthiazole |
| **KAT** | Kynurenine aminotransferase |
| $k_{cat}$ | Turnover number |
| $K_d$ | Dissociation constant |
| $K_i$ | Inhibitor constant |
| $K_m$ | Michaelis constant |
| **KMO** | Kynurenine 3-monooxygenase |
| $K_{obs}$ | Observed rate constant |
| **KP** | Kynurenine pathway |
| **KYNA** | Kynurenic acid |
| **LB** | Lisogeny Broth |
| **LDAO** | Lauryldimethylamine-oxide |
| **L-KYN** | L-kynurenine |
| **mHTT** | Mutant huntingtin |
| **m-NBA** | m-nitrobenzoylalanine |
| **mRNA** | Messenger RNA |
| **mTOR** | Mammalian target of Rapamycin |
| **MALLS** | Multi Angle Laser Light Scattering |
| **MD** | Molecular dynamics |
| **MIR** | Multiple isomorphous replacement |
| **MOI** | Multiplicity of infection |
| **Mr** | Average molecular weight |
| **MR** | Molecular replacement |
| **NAL** | Nicotinoylalanine |

| | |
|---|---|
| **NMDA** | N-methyl-D-aspartate receptors |
| **NMR** | Nuclear magnetic resonance spectroscopy |
| **OG** | Octyl-glucoside |
| **PD** | Parkinson's disease |
| **PDA** | Photodiode array |
| **PHBH** | p-hydroxybenzoate hydroxilase |
| **QUIN** | Quinolinic acid |
| **$R_h$** | Hydrodynamic radius |
| **RNAi** | RNA interference |
| **ROS** | Reactive oxygen species |
| **Ro 61-8048** | 3,4-dimethoxy-*N*-[4-(3-nitrophenyl)thiazol-2-yl]benzenesulfonamide |
| **SAD** | Single Wavelength Anomalous Dispersion |
| ***Sc*KMO** | *Saccharomyces cerevisiae* kynurenine 3-monooxygenase |
| **SD** | Standard deviation |
| **SeMet** | Selenomethionine |
| **siRNA** | Small inhibitory RNA |
| **TDO2** | Tryptophan 2,3- dioxygenase |
| **TG** | Transglutaminase |
| **$T_m$** | Melting temperature |
| **tTG** | Tissue transglutaminase |
| **3-HK** | 3-hydroxykynurenine |
| **3-HANA** | 3-hydroxyanthranilic acid |
| **6xHis** | Polyhistidine tag |

# ABSTRACT

Huntington's disease (HD) is a neurodegenerative disorder caused by a polyglutamine expansion in the huntingtin protein. There are currently no effective therapeutics available to treat this disorder despite intense research in the field. Recently, however, the flavoenzyme kynurenine 3-monooxygenase (KMO) emerged as a promising candidate therapeutic target for HD. KMO is an FAD-dependent outer mitochondrial membrane protein which catalyses the conversion of L-kynurenine (L-KYN) to 3-hydroxykynurenine (3-HK). It has been shown that inhibition of KMO activity is protective in yeast, fruit fly, and mouse models of HD [1–5]. Additionally, it has been also implicated in the pathophysiology of several other neurological conditions such as Alzheimer's and Parkinson's Disease, AIDS-dementia complex, amyotrophic lateral sclerosis, depression and schizophrenia [6, 7].

Despite major interest in pharmacological targeting of KMO, only a few potent inhibitors are currently available, and none are known to appreciably penetrate the blood-brain barrier in adult animals [3, 8]. Furthermore, the molecular basis of KMO inhibition by available lead compounds has remained unknown and for that reason KMO crystal structures in complex with tight binding inhibitors would be of undeniable interest for the future design of new small molecule inhibitors that can penetrate the blood-brain barrier and could ultimately have major therapeutic value.

The aim of this thesis was to produce high levels of KMO protein for structural, functional, and mechanistic studies, with the final goal of developing novel inhibitors that possess the selectivity and affinity to open up new opportunities for therapeutic intervention and inform the development of brain-penetrant KMO inhibitors.

Several constructs, including both full length and truncated forms of human KMO (*Hs*KMO), were efficiently overexpressed and purified and kinetic analysis of pure recombinant KMO showed a $K_m$ value for L-kynurenine of 22.62± 4 μM which is very similar to that observed for the rat liver mitochondria preparations (16 μM) [9] and human liver enzyme (13.0 ± 3.3 μM) [10]. The tight-binding substrate-like inhibitor UPF 648 was found to bind recombinant KMO tightly ($K_i$ 56.7 nM). The poor stability and low expression yield of human KMO however prevented crystallisation. We thus turned our attention to *Saccharomyces cerevisiae* KMO (*Sc*KMO), which is highly related to human KMO (38 % identity and 51 % similarity). The biochemical characterisation of *Sc*KMO

was carried out by using a combination of UV/Visible absorbance spectroscopy, fluorescence spectroscopy, HPLC-based assays and stopped-flow analyses and revealed that *Sc*KMO enzyme was active as a flavin-dependent monooxygenases, generated authentic 3-HK in HPLC-based assays and was inhibited by UPF 648 ($K_i$ 74 nM) with potency similar to that with *Hs*KMO.

The structure of *Sc*KMO was determined using selenomethionine single anomalous diffraction and subsequent crystal structures were solved to 1.85 Å resolution. We were unable to obtain a complex with the kynurenine substrate but succeeded in co-crystallising the enzyme with UPF 648, a tight-binding substrate-like inhibitor. UPF 648 binds close to the FAD cofactor and perturbs the local active-site structure, preventing productive binding of the substrate kynurenine.

Functional assays and targeted mutagenesis revealed that the active-site architecture and UPF 648 binding are essentially identical in human KMO, validating the *Sc*KMO–UPF 648 structure as a template for structure-based drug design. This will inform the search for new KMO inhibitors that are able to cross the blood–brain barrier in targeted therapies against HD and other neurological diseases.

# RESUMO

A doença de Huntington é uma doença neurodegenerativa causada por uma mutação no gene que codifica a proteína huntingtina. Apesar do grande desenvolvimento cientifico no campo das neurociências não existe actualmente nenhum tratamento capaz de tratar ou retardar o progresso desta doença. A enzima quinurenina mono oxigenase (KMO) surgiu recentemente como importante alvo terapêutico para a doença de Huntington. KMO é uma flavoproteína mitocondrial que catalisa a conversão do substrato quinorinina em 3-hidroxiquinorinina. Vários estudos mostraram que a inibição da actividade da KMO é neuroprotectora em modelos animais de Huntington, incluindo modelos de levedura, de *Drosophila* e de rato [1–5]. Esta enzima está igualmente relacionada com outras doenças neurológicas como por exemplo Alzheimer, Parkinson, complexo AIDS demência, esclerose lateral amiotrófica, depressão e esquizofrenia [6, 7].

Apesar do grande interesse terapêutico da KMO, até à data foram desenvolvidos poucos inibidores especificos para esta enzima, e nenhum deles comprovou ser eficiente a atravessar a barreira hemoto-encefálica em modelos animais.

O conhecimento da estrutura molecular da KMO em complexo com substratos ou potenciais inibidores é desta forma fundamental para o desenvolvimento de novas moléculas capazes de penetrar a barreira hemoto-encefálica. O objectivo principal da presente tese é produzir quantidades significativas da proteína KMO para o desenvolvimentos de estudos estruturais, funcionais e mecanisticos com o objectivo futuro de desenvolver novos fármacos que possuam a selectividade e afinidade necessárias para intervenções terapêuticas.

A proteina humana KMO foi eficientemente expressa e purificada, e estudos cinéticos da respectiva proteina revelaram um valor de $K_m$ para quinorinina (22.62± 4 μM) bastante semelhante ao valor calculado para preparações mitocondriais de fígado de rato (16 μM) [9] e humano (13.0 ± 3.3 μM) [10]. Estudos de inibição enzimática com o inibidor forte da KMO (substrato análogo) UPF 648, revelaram também que este se liga com uma afinidade nanomolar ($K_i$ 56.7 nM). Os baixos niveis de expressão proteica em conjunto com a instabilidade da proteina impossibilitaram o processo de crsitalização e futuros estudos estruturais. Consequentemente, o projecto foi direccionado para a proteína homologa KMO de *Saccharomyces cerevisiae* (*Sc*KMO), que apresenta 38 % de identidade e 51 % de similaridade com a proteina humana.

A caracterização bioquimica da proteina *Sc*KMO foi realizada utilizando uma combinação de várias técnicas biofisicas, como espectroscopia de UV-visivel e de fluorescência, HPLC e ensaios de stopped-flow, mostrando que o mecanismo enzimático da *Sc*KMO se assemelha a maioria das flavoproteinas, e mostrando que esta enzima é inibida pela molécula UPF 648 de modo semelhante a homóloga humana ($K_i$ 74 nM).

A estrutura da *Sc*KMO foi inicialmente determinada usando o método da dispersão anómala a um unico comprimento de onda e estruturas subsequentes foram determinadas com uma resolução de 1.85 Å. Foi igualmente determinada a estrutura da ScKMO em complexo com a molécula UPF 648. Este inibidor liga-se na proximidade do cofactor FAD e perturba a estrutura do sitio activo, impossibilitando a ligação do substrato quinorinina.

Estudos de mutagenese sitio-dirigida em aminoácidos do sitio activo e respectivos ensaios enzimáticos revelaram que a arquitectura do sitio activo é identico à proteina humana, validando a estrutura *Sc*KMO–UPF 648 como base para o futuro desenvolvimento de moléculas baseadas na estrutura da proteina, e consequentemente a pesquisa de novos farmacos capazes de atravessar a barreira hemato-encefalica e com potencial terapêutico para a doença de Huntington e outras doenças neurológicas.

# *PUBLISHED ARTICLES*

Amaral, M., Levy, C., Heyes D.J., Lafite P., Outeiro, T., Giorgini, F., Scrutton, N., *Structural basis of inhibition in the neurodegeneration target kynurenine 3-monooxygenase*, Nature, doi:10.1038/nature12039

# *ACKNOWLEDGMENTS*

I would like to express my deepest gratitude to my supervisors, Professor Nigel Scrutton, Tiago Outeiro and Flaviano Giorgini for their valuable support, encouragement and precious guidance and for giving me the opportunity to work on this project. Their capacity to transmit their vast knowledge gave me motivation to work hard and to improve my skills every day.

I must give special thanks to Dr Derren Heyes and Dr. Colin Levy for all their patience and expert help in guiding me through new techniques in the laboratory, for all reading and corrections they have done in impressive detail and timescales of this work and for sharing their knowledge whenever I needed. I am particularly thankful to Michiyo Sakuma for all her help and technical support over the last four years and to the Enzymology group for their unending support and friendship.

I also would like to thank Professor David Leys and for solving my crystal structures and for crystallographic advice.

Over and above all, I am sincerely thankful to all people around me, particularly my family for their patience and support.

**This work was funded by Fundação para a Ciência e Tecnologia, Portugal**

# CHAPTER 1

# INTRODUCTION

# 1. INTRODUCTION

## 1.1. HUNTINGTON'S DISEASE

### 1.1.1. Historical background

*"Of its hereditary nature. When either or both the parents have shown manifestations of the disease ..., one or more of the offspring almost invariably suffer from the disease ... But if by any chance these children go through life without it, the thread is broken and the grandchildren and great-grandchildren of the original shakers may rest assured that they are free from the disease"*[11]

Originally called simply 'chorea', 'hereditary chorea' or 'chronic progressive chorea', Huntington's disease (HD) has been recognised as a disorder since the Middle Age. However it was just in 1872 that George Huntington gave an accurate definition of the disease in his first paper [11]. He described a disease affecting several generations of a family presenting similar symptoms including chorea, presence of dance-like movements, the major motor abnormality occurring in HD, cognitive and psychiatric impairment and gradual deterioration finally leading to death. Huntington also reported the autosomal-dominant hereditary nature of the disease.

The disorder has been extensively studied throughout the 20$^{th}$ century as an example of autosomal dominant inheritance. In 1983, a study conducted by the US–Venezuela Huntington's Disease Collaborative Research Project in a small town along the Lake Maracaibo in Venezuela, where there was the largest known concentration of HD in one family [12], linked the HD gene to a polymorphic DNA marker. It was only ten years later that the mutation in the gene responsible for HD was finally identified [13]. Briefly, the polymorphic DNA marker consists of an abnormal expansion of the CAG triplet in the coding region of the HD *IT15* (Interesting Transcript 15) gene on the short arm of

chromosome 4 (4p16.3), which encodes for a polyglutamine tract at the N-terminal of the huntingtin protein (HTT) [14]. Since then, several new models and approaches were developed in order to unveil the molecular pathology of HD and testing possible intervention strategies. The first mouse model of HD was created 1996 [15] and one year later the aggregation of mutant huntingtin in intranuclear inclusions was discovered in the brain of HD mice and related to the pathogenic mechanism in HD [16]. Similar findings were also made in the brains of HD patients [17]. Since then, intense research focused on the elucidation of the molecular mechanisms of the disease in order to discover potential drug targets. Several animal and cell models have been developed, potential genetic modifiers have been discovered and many aspects of neuronal dysfunction have been explored. Post-translational modifications of huntingtin protein have also been subject to several studies. The details of the genetic aspects of HD and the formation of inclusion bodies will be described throughout this Chapter as well as some of the most promising therapeutic approaches.

### 1.1.2. Epidemiology

The worldwide prevalence of HD is ~5-10 cases per 100,000 individuals, but varies to a great extent and can reach up to 700 cases per 100,000 individuals in some isolated regions of Venezuela [18, 19]. The age of onset is typically between 35 and 50, 15% of the cases can occur before 20 (juvenile HD), and as a progressive disorder the life expectancy is typically 15-20 years from onset of symptoms until death [19, 20].

### 1.1.3. The disease: Clinical presentation

HD is characterised by three distinct clinical features: movement disorder, cognitive dysfunction and psychiatric disorder [19, 21]. Chorea, the most common remarkable manifestation of HD, is a hyperkinetic movement recognisable by the involuntary, abnormal and irregular movements that can affect many parts of the body, particularly the limbs, trunk and face [22, 21]. As the disease gradually worsens, chorea often stabilises giving way to bradikynesia and rigidity [23], which is very common in other neurodegenerative pathologies such as Parkinson's disease. Gait disturbances often

affect individuals in the last stages of HD, when they lose mobility and falls are more frequent. The very last stage of the disease is characterised by the inability to swallow and ultimately the incapability of oral nutrition [21, 23].

In terms of cognitive dysfunction in HD, dementia is present in the majority of cases, starting from what it is called subcortical dementia where individuals are not able to learn new motor skills and visuospatial memory is also affected, and progresses to a certain level where all aspects of cognition are affected [22, 21, 23].

Finally, the psychiatric disturbances of HD are variable but the most common are irritability, apathy, anxiety, depression and impulsivity [24]. Suicide is also prevalent among HD patients [25, 26].

### 1.1.4. Genetic aspects and neuropathology of HD

As previously mentioned, HD is an autosomal-dominant neurodegenerative disorder caused by an abnormal expansion of the CAG triplet near the end of the 5' region of the HD gene which codes for the protein HTT [13, 27]. HTT is expressed throughout the body with the highest levels found in the testis and brain. Within the brain, it is more predominant in the neocortex, cerebellar cortex, striatum and hippocampus [28]. In cells the HTT protein is present mainly in the cytoplasm [29]. Although its exact function is not fully understood, HTT interacts with several proteins involved in intracellular transport and signalling, axonal trafficking of vesicles and gene expression and it also plays important roles in morphogenesis and apoptosis [30, 31].

In non-pathological conditions, the trinucleotide repeat present in the coding region of the HD gene varies in length from 6 to a maximum of 36 repeats and this DNA sequence is translated into a polyglutamine tract [20]. When the polyglutamine length reaches this threshold the HTT protein has different characteristics (named mHTT), with a gain of toxic function, which leads to the progressive loss of medium spiny neurons in the striatum and it is also related to cerebral cortex dysfunction [32, 33]. Interestingly, the age of onset of HD is inversely related to CAG size expansion [34, 35]. However, it is important to emphasise that just ~60 % of the variance of the age at onset is explained by the length of the CAG expansion, the remaining is related to modified genes and environment [20, 34].

The pathology of HD is restricted to the brain with atrophy and cell loss mostly marked in the striatum, more specifically in the caudate and putamen, and in the later stages cortex is also affected [19, 36, 37]. The neurons mostly affected in HD are medium-sized spiny neurons that primarily innervate the substantia nigra and globus pallidus although the mechanism of mHTT toxicity is not clearly understood [37]. The fact that the striatum is the most affected brain region in HD is in agreement with the fact that chorea is one of the main symptoms in early stages of HD, since this part of the brain plays an important role in the motor circuit and behavioral control [20].

HD is also characterised by the presence of neuritic, cytoplasmic and nuclear inclusions [38], although their role in neurodegeneration is controversial [39]. Initially thought as pathological [30], recent studies carried out in mouse and cell models of HD have shown that inclusion bodies seem to appear only after symptoms begin and cells with these aggregates seem to survive longer than those without them [20, 39, 40]. Studies in human brain tissues with different grades of HD have shown that inclusion bodies were more prevalent in cortex than in the striatum, even if striatum is the most affected region in HD [41, 42]. Furthermore, they also found that aggregates tend to increase in size in more advanced stages, which seems to suggest that they are relatively benign and persist in neurons that survive longer [41, 42]. Several other studies also confirm the hypotheses that aggregate formation might be one of the mechanisms activated by misfolded Htt to protect against toxic forms of mHtt and reduce cell death [30, 43, 44].

### 1.1.5. Diagnosis of HD

Diagnosis of the onset of HD is usually straightforward based on the appearance of physical symptoms specific to the disease. As previously described, the motor symptoms are the clinical features firstly diagnosed, specifically abrupt, excessive and random timing of involuntary movement [19, 20]. There is also a genetic test for HD that consists of a simple blood examination to confirm the number of trinucleotide repeats in the HTT gene, although a positive result is not considered a differential diagnosis because it could be obtained before the onset of symptoms. This genetic test is important to rule out the disease but it is also extremely important because it can dramatically influence

personal and family planning decisions. Since HD is an autosomal dominantly transmitted disorder, there is a 50 % chance of children from an affected individual inheriting the disease [19, 45].

Prenatal testing can also be performed using non-invasive techniques to determine the carrier status of a fetus.

The progression of the disease can be measured based on the unified Huntington's disease rating scale (UHDRS) that characterises the relevant clinical features of HD [46]. Medical functional imaging, such as fMRI and PET, can also help in the early detection of HD since they can show changes in the brain activity before symptom onset as well as to monitor the disease progression [47, 48].

### 1.1.6. Treatment of HD

Unfortunately, at present there is no effective treatment to slow or stop disease progression. The only therapies available so far act on the symptoms of HD with the intention of improving the patient's quality of life. These therapies are mainly focused treating movement disorders such as chorea and dystonia, as well as gait, speech, swallowing and fine motor tasks [49].

The only drug currently approved by the US Food and Drug Administration (FDA) in 2008 for the treatment of chorea in HD is tetrabenazine [50]. This drug has been used in Europe for several years to treat chorea and other movement disorders by reducing the quantity of dopamine released from vesicles in the brain by reversibly inhibiting the monoamine transporter type 2 (VMAT2) and therefore depleting central monoamines [49, 51]. Tetrabenazine also reduces dopamine by blocking dopamine receptors from passing on its message. However, there are some adverse side effects associated with this drug, such as sedation and somnolence, agitation, depression, akathisia, anxiety and hyperkinesia [19, 50, 51]. There are also some pharmacological approaches to treat or ameliorate other HD symptoms, including olanzepine for weight loss, selective serotonin reuptake inhibitors and mirtazapine for depression, antipsychotic drugs for psychiatric and behavioral aspects of this pathology, although they are not specific for Huntington's disease [49]. In terms of treatments for cognitive dysfunction there is no medication approved distinctively for HD. An acetylcholinesterase inhibitor

called Rivastigmine has shown some tendency for cognitive improvement in HD [52] and some other agents used in Alzheimer's disease such as NMDA receptor antagonist memantine are also being studied since they were successful in early therapeutic intervention in HD mouse models [53]. A recent study carried out by the Huntington Study Group has shown that a new antihistamine, Dimebon, may improve cognition in individuals with HD [54].

There are numerous ongoing clinical trials for the treatment of HD. Among them is the largest therapeutic clinical trial to date for Huntington disease, the 2-Care study, with 608 participants and this trial will study the effects of co-enzyme Q10 (CoQ10) on the progression of functional decline There are also several new therapeutic targets and potential disease-modifying therapies in HD currently being studied and some of them will be elucidated in the next section.

## 1.2. NOVEL STRATEGIES FOR THERAPEUTIC INTERVENTION IN HD

In this section a general overview of some of the most promising approaches to the development of treatments for HD will be given in order to clarify the enormous spectrum of alternatives that are currently being explored for the development of novel therapies able to treat or reduce HD pathology phenotypes. Figure 1.1 highlights some of the potential disease-modifying strategies for HD.

Special emphasis will be given to the Kynurenine Pathway, since this is the central theme of this thesis.

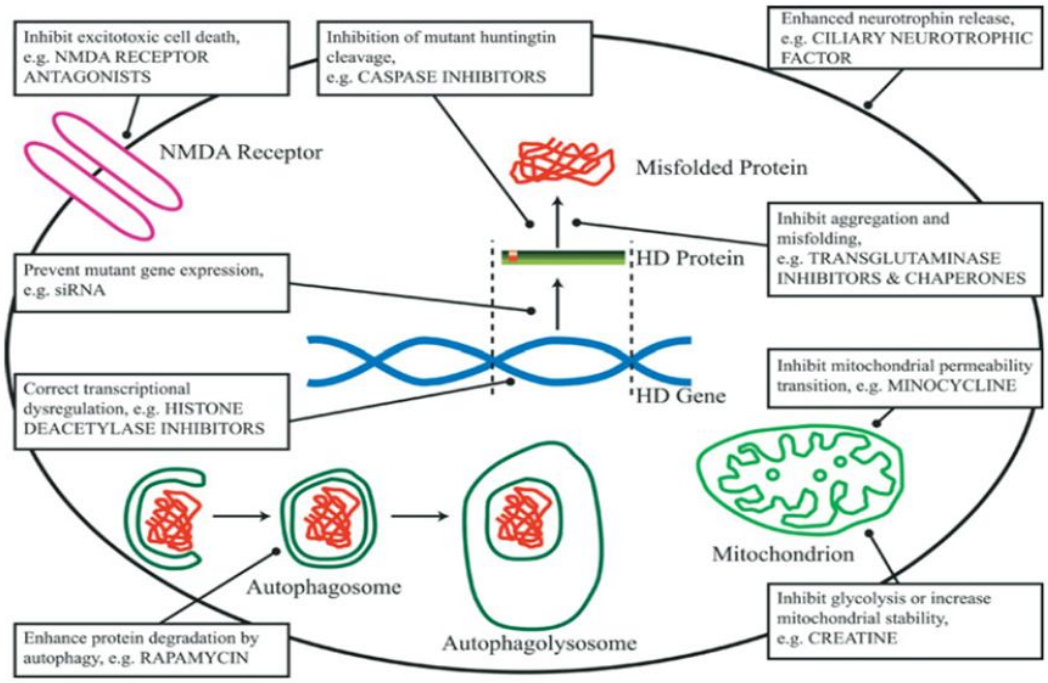


**Figure 1.1. Possible strategies for therapeutic intervention in HD therapies.** Therapies including gene silencing, transglutaminase inhibition, autophagy enhancers, HDAC inhibitors, excitotoxicity, mitochondrial dysfunction and NMDA are being currently explored. From [55].

### 1.2.1. Gene silencing approaches

Gene silencing therapy has been a very hot topic since the initial characterisation of RNA interference (RNAi) in the nematode *Caenorhabditis elegans* in 1998 and it has been extensively studied as a potential therapy for many pathologies including viral, ocular and neurodegenerative diseases as well as cancer [56]. Gene silencing is a technique that includes the use of RNAi (small double-stranded RNA molecules of ~21 nucleotides in length) and antisense oligonucleotide to *switch off* a specific gene by cleavage, degradation, or translational suppression of its correspondent mRNA and therefore suppressing the expression of the target protein [57]. The great potential of this technology is the fact that, in theory any small inhibitory RNAs (siRNAs) can be designed in order to knock down the expression of any target gene, leading to the treatment of a broad range of diseases, for example the ones caused by single mutations as occurs in HD. Several studies conducted in mouse models of HD provide evidence of

the efficiency of RNAi in decreasing the levels of Htt [57, 58]. They have shown an attenuation of striatal and cortical neuropathology and behavioral deficit as well as an increasing in the lifespan [57, 58].

One of the issues associated with gene silencing therapy in neurological diseases is the fact that most of the siRNAs do not cross the blood brain barrier (BBB) [59, 60]. Novel methods are currently being developed to deliver treatments directly to the fluid surrounding the brain, such as viral based systems, liposomes, nanoparticles and cell-penetrating peptides, among others [61, 62].

Another drawback to overcome when using this strategy as a potential treatment for HD is the fact that the majority of therapeutic molecules suppress not only the mHtt but also the wild type, and it is known that the majority of HD patients are heterozygous at the HD locus, carrying one mutant and one wild-type allele [57]. It has been shown that wild type Htt plays important roles in embryonic development, normal adult function and is protective against apoptotic neuronal death and the complete suppression of wild type Htt in mouse models resulted in neurodegeneration and death [63, 64]. Ongoing research is currently investigating the use of allele-specific gene silencing in which just mHtt is suppressed preserving the expression of normal Htt [57, 64, 65].

### 1.2.2. Transglutaminase Inhibition

As previously mentioned in Section 1.1.4, the aggregation of mHTT in inclusion bodies may have a protection function within the brain, although it is hypothesised that intermediate forms of mHTT aggregates are toxic and lead to cell death [43, 66, 67].

Transglutaminases (TG) are enzymes that catalyse the formation of ε-(γ-glutamyl) lysine isopeptide bonds between substrate proteins with consequential formation of cross-linked insoluble protein complexes and are also related to polyamination reactions at glutamine residues into specific substrate proteins[68–70]. Tissue transglutaminases (tTG) are the most ubiquitous TG and it has been shown that they are present within the neurons and are increased in affected areas in HD brain [69, 71, 72]. Several studies also suggest that tTG may contribute to the aggregation of polyglutamine proteins, including mHtt, as the addition of a polyglutamine tract may result in a protein becoming a TG substrate, which can therefore be crosslinked to form insoluble aggregates [71, 73, 74].

Cystamine and its reduced form cysteine are TG competitive inhibitors that have been tested in several HD models, including *Drosophila* and mouse models, showing that they can slow down neurodegeneration, ameliorate the striatal volume loss and striatal neuronal atrophy and improve survival [72, 75, 76]. A trial in HD patients was carried out in 2006 and showed that cystamine bitartrate (CYSTAGON®) was tolerated quite well although its efficacy was not confirmed [77]. One of the possible reasons could be the fact that the doses administered in animal models were much higher compared to the ones used in this preliminary trial and also the fact that these drugs are not entirely permeable to the BBB [77, 78]. *Raptor Pharmaceuticals* has started phase II clinical trials in 2008 testing a delayed release (DR) preparation of cysteamine bitartrate for HD and the results are expected in 2014 [79].

One of the strategies that it is currently being studied as a promising therapeutic for HD is reducing the amount of the pathogenic protein by increasing the clearance of mHTT. There are two main pathways for degradation of abnormal proteins: the ubiquitin-proteasome system and autophagy. The up-regulation of one of these pathways could be an attractive way to decrease the levels of the toxic protein, although in the case of the ubiquitin-proteasome pathway, this system can effectively digest normal polyQ containing proteins but not if they are found in aggregates [80]. Furthermore, this system fails to cleave between glutamine residues within polyglutamine tracts leaving the sequence intact and therefore it could possibly lead to increasing concentrations of isolated toxic peptides [81–84].

Autophagy has become a more valid approach because it can degrade protein complexes, such as mutant forms of Htt, and organelles, such as mitochondria. Some studies performed in *Drosophila* and mouse models have shown that autophagy induction can effectively reduce the levels of mHtt and its toxicity [85]. The up-regulation of autophagy can be done by blocking specific kinases called mammalian target of Rapamycin (mTOR) that play important roles in different cellular processes in addition to its inhibiting effects in autophagy [86]. When mTOR is repressed, either by natural mechanisms such as reduced levels of amino acids or growth factors, or by drugs, such as Rapamycin, its inhibitory effect is reduced, leading to increased autophagy [86].

Although Rapamycin has been shown to be effective in the promotion of autophagy in mammalian brains there are some concerns regarding its long term use in humans [87]. As mentioned earlier, mTOR is not just important in autophagy but there are many other cellular processes, including regulation of ribosome biogenesis and

protein translation in which these proteins are involved and as a result it can lead to some complications, for example immunosuppressive effects and impairment in wound healing [80]. For these reasons, there are currently studies being undertaken to identify novel compounds that could promote autophagy independently of mTOR. Lithium and several other mood stabiliser drugs, such as sodium valproate and carbamazepine were identified as autophagic up regulators by decreasing the levels of inositol or IP3 and decreasing the aggregation and toxicity of mHtt in cell and animal models of HD [88]. Furthermore, lithium has been used for several years to treat some affective disorders and is known to cross the blood brain barrier [89].

More recently, some other studies performed in the *Drosophila* HD model had shown that a combination therapy, using both Rapamycin to modulate the mTOR-dependent pathway and lithium to inhibit the mTOR-independent pathways, could maximise the benefits when compared to both treatments alone in addition to the fact that it would be able to reduce the dose levels of both drugs and therefore decreasing the side effects [90].

### 1.2.3. Histone deacetylase (HDAC) Inhibitors

Transcriptional deregulation has been suggested to have a key role in the pathology of HD although the mechanism that leads to the interference of gene expression is not fully understood. Several studies carried out in HD mouse models had shown downregulation of specific genes at the level of messenger RNA (mRNA) expression [15, 91]. Interestingly, these genes are involved mainly in neurotransmitter signalling, calcium metabolism and transcription and are more prominent in the striatum, which is the most affected brain region in HD [92].

In general, gene expression is regulated by transcription factors, some of them responsible for the acetylation of histones (HAT) and leading to the activation of transcription, and others for the deacetylation (HDAC) resulting in the repression of gene expression. The proposed mechanism to elucidate the transcriptional dysregulation in HD has been linked to the fact that mHtt decreases histone acetyltransferase activity by binding different transcription factors, such as CREB-binding protein (CBP), which acetylates histones and opens up DNA for transcription, and therefore decreasing the

level transcription [92]. HDAC inhibitors, such as hydroxamic acids vorinostat (SAHA), sodium butyrate and phenylbutyrate, have been studied in HD models and have proven to be effective in reducing cellular death in HD [93–95]. These compounds have been used as drug targets in cancer research. However, some of them are toxic and have serious side effects and as a result the current research is focused on the development of novel HDAC inhibitors that are more effective and with less side effects.

A novel HDAC inhibitor called HDACi 4b was reported to be effective in preventing motor deficits and striatal atrophy in HD transgenic mice as well as significantly decreasing the compound toxicity, suggesting that this inhibitor may provide clinical benefits in HD patients and slowing down the progression of the disease [96].

### 1.2.4. NMDA antagonists

The pathogenesis of some neurodegenerative disorders including HD have been linked with excessive or prolonged stimulation of amino acid receptors, particularly the subtype of glutamate receptors NMDA, in a process called excitotoxicity [97, 98]. These receptors have been directly related to excitotoxicity due to their $Ca^{2+}$ hypersensitivity, slow deactivation, and desensitisation. This will lead to high intracellular levels of this mineral, damaging the cells either by activating a number of enzymes that will destruct structures such as components of the cytoskeleton, membranes, and DNA, or by increasing the formation of reactive oxygen [99]. It has been shown that NMDA receptors are the glutamate receptors that produce more striatal lesions and affect more specifically the medium sized spiny neurons, the neurons mostly affected in the early stages of HD [97].

Several studies have provided evidence of a direct relation between mHtt and NDMA receptor-dependent excitotoxic cell death [100], but the first direct demonstration of such a link was carried out in cell lines with full length Htt with 138Q repeats cotransfected with NMDAR. The results showed an increase in the NMDAR levels and apoptotic cell death when compared to 15Q mHtt [101, 102]. Since then, several other studies performed in mouse models also revealed an increased level of NMDA mediated cell death in medium spiny neurons [103]. Interestingly, they also found that the NMDA susceptibility and overstimulation is present when mice are just 3 to 4 weeks old, even

before the onset of symptoms, which supports the hypothesis that the persistent overstimulation of NMDA receptors over a lifetime plays a key role in neurodegeneration. They will activate numerous proteases due to increased levels of calcium and oxidative stress and therefore, will make the neurons more susceptible to stress and they will eventually degenerate [104].

NMDA receptors are complexes of two NR1 subunits with two other subunits that could be NR2A, NR2B, NR2C, NR2D or NR3 [105]. The medium spiny neurons express high levels of NR2B containing NMDAR compared to other regions of the brain. This could be indicative of their susceptibility in HD since it was shown that mHtt increases the current and excitotixicity mediated by specifically this type of NMDA receptors that could lead to neuronal dysfuntion [101]. Accordingly, NMDAR antagonists have been investigated as a potential treatment of HD. Several NMDAR blocker compounds including Amantadine [106], Riluzole [107], Lamotragine [108] and Remacemide [109] have been tested already in human trials, although none of them gave promising results as expected from the previous studies in mouse models.

More recently, another NMDA antagonist called Memantine, which has been already FDA-approved for Alzheimer's disease, has been proposed as a possible therapy for HD. One study performed in 27 HD patients for two years had shown promising results with a delay of the progression of the disorder in terms of motor and cognitive symptoms [110]. Further studies are currently being carried out as a clinical phase III trial with 72 participants to measure the short-term memory, cognition and behaviour before and after treatment with Memantine [111].

Although a relationship between NMDAR overstimulation and neuronal death has already been reported, it is still unclear whether the formation of inclusion bodies is somehow modulated by synaptic activity. A recent study shows accurately that there is in fact a strong correlation between extrasynaptic NMDAR activity and IB formation [112]. They have shown that by reducing the extrasynaptic NMDAR activity using Memantine in mouse models, the levels of soluble toxic mHtt were decreased in addition to a preservation of mHtt inclusion bodies, suggesting one more time that IB are likely to be a protective mechanism to block mHtt toxicity.

### 1.2.5. Mitochondrial dysfunction and Reactive Oxygen Species

The excitotoxicity process described in the previous section carried out by glutamate receptors NMDA has been closely related to other processes such as oxidative stress and mitochondria dysfunction through several complex mechanisms, one of them being the mitochondrial calcium homeostasis [113]. As previously mentioned, one of the elements responsible for NMDAR excitotoxicity is the high levels of $Ca^{2+}$ and if such levels surpass a certain threshold it will also lead to mitochondrial damage and consequently cell death [113]. These processes are linked in a certain way that a dysfunction in mitochondria will cause a decrease in ATP levels and therefore, a depolarization of the cell membrane, which will facilitate the NMDA receptors activation by glutamate. These events will create a cycle in which the calcium influx will be constantly increased causing mitochondria disturbances and generation of reactive oxygen species (ROS) [97].

Mitochondrial dysfunction is recognised as a key process in neurodegenerative diseases due to its role in cell survival and death as well as its interaction with many proteins involved in other neurodegenerative disorders [114]. With respect to HD, it has been reported that mHtt binds to the mitochondria, changing their normal function and therefore dysregulating $Ca^{2+}$ levels [115]. So what is the relationship between wild type Htt and mitochondria and how does mHtt cause dysfunction in this organelle?

As previously described, wild type Htt is essentially a cytosolic protein but is also localised predominantly in the soma, dendrites and synaptic terminal of neurons [97]. It has been also reported to be associated with cellular organelles such as mitochondria, more specifically with the outer membrane of mitochondria [116, 117]. Although its role is not fully understood it is hypothesised that wild type Htt is involved in energy metabolism and organelle trafficking. When mHtt interacts with the mitochondria it decreases and depolarises the membrane potentials causing a dysregulation of mitochondrial $Ca^{2+}$ handling [97, 114, 115]. A recent study also pointed out that it is not the full length mHtt that interacts with the mitochondria but the N-terminal mHtt fragments[118].

Several biochemical studies in HD tissues support the contribution of mitochondrial dysfunction in HD. It has been shown by nuclear magnetic resonance spectroscopy (NMR) that patients with HD present higher levels of lactate in the cortex

and basal ganglia when compared to controls, which is consistent with impairment of energy metabolism or mitochondrial dysfunction [114]. Furthermore, there is also evidence in post mortem HD brain tissue and HD mouse models that reveal lower levels of mitochondrial oxygen consumption and glucose metabolism, as well as several defects in the complexes II and III of the mitochondria electron- transport chain mitochondrial [119]. Interestingly, studies performed in mHtt (with a polyQ of 82 glutamates) knock-in mouse embryos has shown that the overexpression of complex-II subunits restores the activity of mitochondria preventing cell death [114, 118, 120].

Although the role of mitochondrial dysfunction in the pathogenesis of HD is still not completely clear, some biochemical measures such as lactate levels or the ratio lactate/pyruvate can be important as biomarkers to follow the progression of the disease.[114].

### 1.2.6. The Kynurenine Pathway

The kynurenine pathway (KP) is the main route of tryptophan degradation in higher eukaryotics and perturbations in the levels of KP metabolites are likely to contribute to the pathogenesis of several neurodegenerative diseases, including HD as well as other pathologies such as malaria, cancer, depression and schizophrenia [6]. As this pathway is the central subject of this project, an overview of the KP will be given along with the neuroactive properties of KP metabolites and their role in neurodegeneration. The relationship between the kynurenine pathway with some of the main features involved in the neurodegenerative process, including oxidative stress, mitochondrial dysfunction, excitotoxicity and neuroinflamation will also be discussed.

The kynurenine pathway (KP) degrades >95% of tryptophan in mammals by a series of enzymatic reactions that ultimately leads to the formation of the cofactor $NAD^+$. The metabolites formed during this cascade include a subset that is neuroactive or has the capacity to generate free radicals.

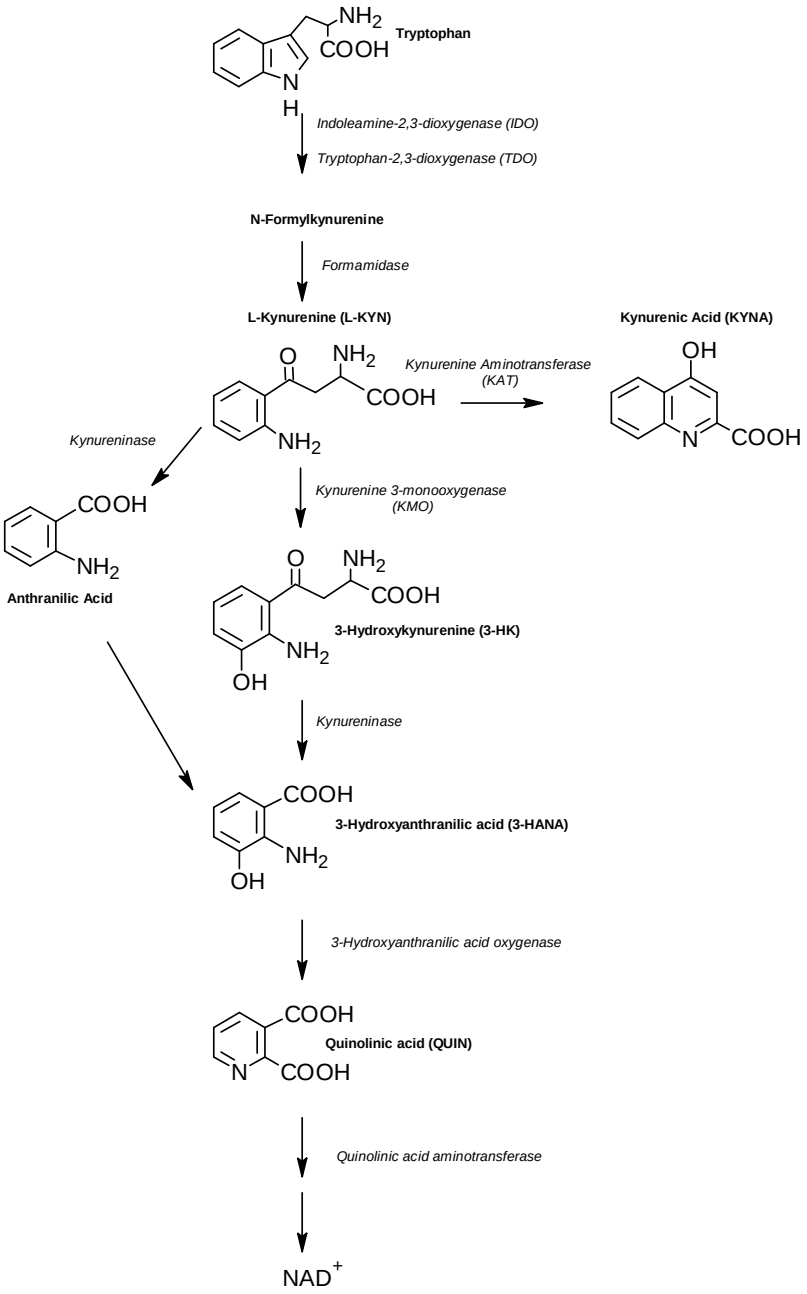


**Figure 1.2. Schematic representation of the kynurenine pathway of tryptophan degradation in eukaryotic cells.** See the text for a detailed description of the KP**.**

The initial step in the KP is the oxidative cleavage of the indole-ring present in L-tryptophan, yielding *N*-formylkynurenine, which in the brain is catalysed by either indoleamine-2,3-dioxygenase (IDO) or tryptophan 2,3- dioxygenase (TDO2), followed by the synthesis of the first stable intermediate L-kynurenine (L-KYN) [121] (Figure 1.2). Subsequently, L-KYN is metabolised via three different routes. In the first, L-KYN is

deaminated to form the neuroactive metabolite kynurenic acid (KYNA) by the kynurenine aminotransferase (KAT) family of enzymes, four of which can catalyse this reaction in mammalian brains [122]. In the second route, the same substrate is degraded to anthranilic acid by kynureninase. And in the third route, L-KYN is hydroxylated by kynurenine 3-monooxygenase (KMO) into the free radical generator, 3-hydroxykynurenine (3-HK). 3-HK is metabolised further into a second free radical generator, 3-hydroxyanthranilic acid (3-HANA) - by kynureninase and then oxidised into 2-amino-3-carboxymuconic 6-semialdehyde by 3-hydroxyanthranilate 3,4-dioxygenase. This intermediate then undergoes non-enzymatic cyclisation yielding the excitotoxic metabolite quinolinic acid (QUIN), which is subsequently transaminated to generate nicotinic acid, and ultimately the final KP product $NAD^+$ [7].

The physiological role of the KP was initially thought to be limited to the formation of the coenzyme $NAD^+$, which is involved in several biological processes, such as redox reactions essential for mitochondrial function and energy metabolism [123]. Subsequent studies have established that the metabolites produced by this biosynthetic pathway – known as kynurenines – play a variety of roles in the peripheral immune system and the central nervous system. Kynurenines are involved in peripheral immunomodulation which inhibits growth of intracellular pathogens, the maintenance of maternal immune tolerance which prevents embryo rejection, and immune surveillance [124]. KP metabolites also modulate T cells by suppressing their proliferation and inducing apoptosis, thereby mediating immune tolerance [125]. Of particular importance in the latter process is IDO, which has been found to promote immune tolerance to foreign antigens in cases of over-activation of the immune system, preventing tissue damage [126, 127]. However, this immune suppression can also result in the inability of the immune system to prevent tumour growth and survival. Indeed, IDO has been shown to be overexpressed in tumours [128, 129]. Recent studies have also found a correlation between IDO activity and aryl hydrocarbon receptor (AHR) activation by the endogenous ligand L-KYN, which appears to be important in promoting generation of regulator T cells and therefore suppressing self-reactive cells and immune responses [130, 131]. IDO inhibitors have been shown to significantly promote tumoral immune rejection and increase the efficiency of chemotherapeutic agents [132, 133]. Complementary recent work also suggests that TDO activity in tumour cells constitutively generates L-KYN, which in turn serves as a ligand for the AHR, thereby suppressing antitumor immune responses and promoting tumor cell survival [134].

In addition, KP metabolites play important roles in the central nervous system in both normal physiology and disease states. These metabolites were first linked with neurological conditions in 1978 when the stimulant and convulsive effects of kynurenines in the murine brain were described, with a particularly strong effect of QUIN observed in motor excitement [135]. Subsequently, it was found that QUIN selectively activates N-methyl-D-aspartate (NMDA) receptors, which can lead to excitotoxicity and axon-sparing lesions in cortical neurons [136, 98]. QUIN has been shown to stimulate lipid peroxidation, production of reactive oxygen species and mitochondrial dysfunction [137, 138]. Studies performed in organotypic cultures of rat corticostriatal system indicate that concentrations of QUIN even just slightly higher than physiological concentrations can cause neurodegeneration after a few weeks of exposure [139]. Spinal neurons are especially sensitive to QUIN variations, which cause cell death in nanomolar concentrations [140].

At high micromolar concentrations, KYNA is a non-selective NMDA receptor antagonist and can also block excitatory neurotransmission of other ionotropic aminoacid receptors, such as kainate and AMPA receptors [7, 141]. KYNA is also a ligand for GPR35, an orphan G protein-coupled receptor [142]. In addition, KYNA is a non-competitive antagonist of α7-nicotinic acetylcholine receptors (α7nAChRs), which are likely to be the primary target of endogenous KYNA in the brain, and therefore inhibition of KYNA synthesis leads to increased levels of acetylcholine and the neurotransmitters glutamate and dopamine [7]. Consequently, KYNA has been linked to a myriad of behaviours that involve cholinergic, glutamatergic, and dopamingeric neurotransmission [7]. Furthermore, KYNA has antioxidant capacity due to its ability to scavenge hydroxyl, superoxide anion and other free radicals [121]. As an important modulator of glutamate levels, endogenous KYNA levels have been found to provide critical neuroprotection against excitotoxic lesions induced by QUIN [143]. The therapeutic potential of KYNA as a neuroprotective agent has been considered, although its applicability is limited due to the poor ability to cross the blood-brain barrier (BBB) [144]. Thus, KYNA analogues are being developed and tested for neuroprotection [145, 146]. The level of KYNA is reduced in several neurodegenerative diseases such as HD and Alzheimer's disease (AD) [147], which likely plays an important role in modulating neurotoxicity.

Two additional KP metabolites have been implicated in neurodegeneration: 3-HK and 3-HANA. These tryptophan metabolites are neurotoxic because they induce the

formation of free radicals and elevate the oxidative stress level causing neuronal death [148, 149]. 3-HK and 3-HANA also stimulate the formation of chemokines by inducing target receptors in astrocytes, thereby potentiating brain inflammation [150, 151]. The concentration of these KP metabolites are in the range of nanomolar levels in mammalian brains but they have been found to be significantly increased in pathological conditions, such as HD [152], Parkinson's disease (PD) [153] and human immunodeficiency virus (HIV)-1-associated dementia [154]. Neuronal cell culture studies also provide strong evidence that 3-HK and 3-HANA potentiate cell death with apoptotic features, with cortical and striatal neurons being the most vulnerable to KP metabolite toxicity [148]. Furthermore, 3-HK potentiates QUIN-induced excitotoxicity, such that intrastriatal co-injection of both metabolites results in substantial neuronal loss, whereas the same doses applied individually do not cause neurodegeneration [155].

In the brain, the enzymes of the KP are primarily localised in microglia and astrocytes and not in neurons. Surprisingly, astrocytes do not seem to have kynurenine 3-monooxygenase and consequently induce the activity of KYNA. However, microglia contain very low levels of KAT and therefore induce the formation of metabolites in the QUIN branch of the KP [156]. After these metabolites are produced both in astrocytes and microglia they will be released in the extracellular milieu and affect pre and post synaptic neurons [157].

Figure 1.3 summarises the effects of the KP metabolites in some of the aspects of neurodegeneration, not only in HD but also in many other neurological diseases.

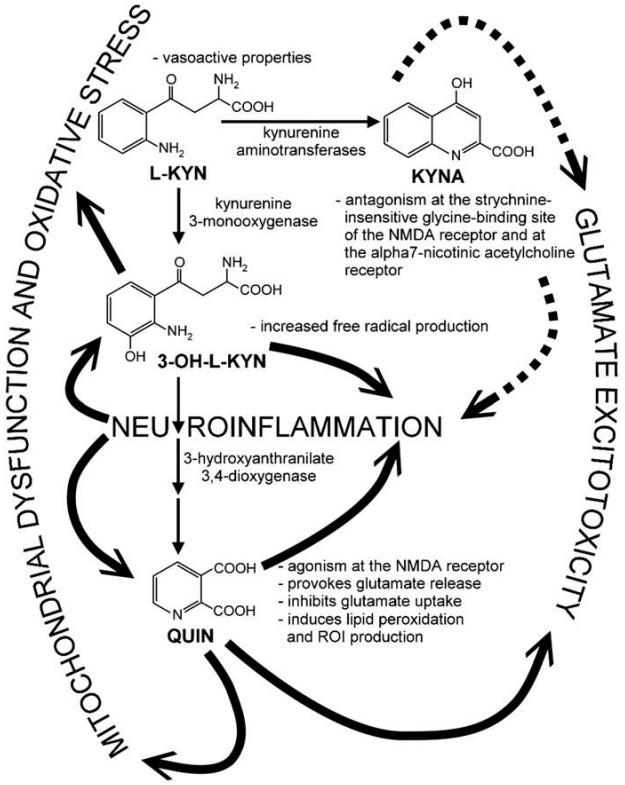


**Figure 1.3. The effects of neuroactive kynurenine pathway metabolites on the main features of the neurodegenerative process. (**3-OH-L-KYN: 3-hydroxy-L-kynurenine, KYNA: kynurenic acid, L-KYN: L-kynurenine, NMDA: N-methyl-D-aspartate, QUIN: quinolinic acid, ROI: reactive oxygen intermediates; thick solid lines: activation, thick dotted lines: inhibition [113].

Alterations in levels of KP metabolites have been implicated in the pathophysiology of several neurological conditions such as HD, Alzheimer's (AD) and Parkinson's disease, AIDS-dementia complex, amyotrophic lateral sclerosis, depression and schizophrenia [3, 37]. The most compelling evidence supporting a role for KP metabolites in neurodegenerative disease comes from studies in HD. Levels of 3-HK and QUIN are increased in the neostriatum and cortex of early stage HD patients, as well as in the brains of transgenic HD mice [158, 159]. Importantly, the elevated levels of 3-HK and QUIN in HD mouse models correlate with the onset of HD pathology [160]. Exacerbating these effects, KAT activity and KYNA levels are significantly reduced in the striatum of HD patients [161]. Both the absolute levels of the neuroactive KP metabolites and the relative levels of the neurotoxic metabolites to KYNA have been used

to support the hypothesis that the increased flux through the central branch of the KP may play an important role in HD pathology.

Although it is not clear how expression of mHtt leads to modulation of the KP, it has been demonstrated that mHtt fragments bind to mitochondria, affecting the interaction between trafficking proteins and these organelles and thereby the transport and distribution of mitochondria in neuronal processes [118]. Mitochondrial impairment in HD has been correlated with the pathological changes in the KP, particularly decreased activity of KAT enzymes, leading ultimately to an exacerbation of QUIN toxicity [162]. The localisation of KMO to the outer mitochondrial membrane further suggests that dysfunction of mitochondria may directly modulate activity of this KP enzyme, and thereby affect KP metabolism. The expression of mHtt deregulates transcription, thereby triggering KP activation in microglia both *in vitro* and *in vivo*, suggesting a mechanism for mHtt-induced perturbations in the KP, and providing additional evidence that this cell type contributes to neurodegeneration in HD [163, 164]. Moreover, the treatment of HD model mice with either HDAC inhibitors (which modulate gene expression) or KMO inhibitors reduces 3-HK levels by comparable amounts, suggesting a direct link between regulation of gene expression and KP flux. Furthermore, a direct connection between mHtt toxicity and perturbations in the KP is highlighted by observations in *Drosophila* that exogenous 3-HK is only neurotoxic in HD flies, and not control flies. This indicates that while the KP is a requisite component of mHtt toxicity, perturbation of 3-HK levels alone is not sufficient to reproduce HD phenotypes - and that additional mHtt-dependent cellular dysfunction plays a role [4]. Work carried out in HD transgenic mice has shown that increased 3-HK levels in the brain might be caused by enzymatic dysfunction, in particular upregulation of KMO activity and downregulation of kynureninase activity, shifting the KP towards formation of neurotoxic metabolites [165]. Taken together, these and other studies strongly indicate that mHtt potentiates cellular modifications that induce flux through the neurotoxic branch of the KP.

#### *1.2.6.1. Targeting the Kynurenine Pathway in HD*

As stated above, several studies support the hypothesis that the KP plays a key role in neurodegeneration in HD. A study supporting the therapeutic potential of the KP was conducted using *Saccharomyces cerevisiae* as model for HD [166]. In a genome-

wide loss-of-function suppressor screen 28 genes were found to reduce the toxicity of mHtt. One of the most potent suppressors was Bna4, the yeast orthologue of kynurenine 3-monooxygenase. Additional experiments reported in this study showed that the elimination of KAT enhances the toxicity of mHtt and elimination of other genes throughout the KP directly link the levels of 3-HK and QUIN with mHtt toxicity. Furthermore, upon suppression of KMO, there were only very low levels of 3-HK and QUIN and the formation of ROS were very similar to the controls, suggesting a direct link between KP and formation of free radicals, as previously reported.

Studies performed in transgenic *Drosophila melanogaster* also explored the KP as a potential therapeutic target in HD, especially the enzymes KMO and TDO [167]. Similar results to those described above have been reported regarding inhibition of KMO. They have shown that genetic and chemical inhibition of this enzyme led to a reduction in 3-HK levels and an increase in KYNA, yielding a consequent decrease in neurodegeneration. They also found for the first time that the inhibition of TDO also shows a neuroprotective effect in the same way as KMO in modulating the KP towards KYNA. The protective effect of KMO inhibition was reduced when flies were fed directly with 3-HK. Furthermore, feeding of KYNA to HD model flies ameliorated neurodegeneration, providing further evidence that these metabolites directly modulate neurodegeneration. Furthermore, a direct correlation between mHtt and KP was also reinforced by the fact that increased concentrations of 3-HK were only neurotoxic in Htt93Q mutants when compared to Htt20Q, even when this last mutant was sufficient to induce 3-HK formation, suggesting again that the length of polyQ in Htt generates cellular defects that will further modulate the KP [167].

Perhaps most compellingly, studies carried out in HD transgenic mice suggested that the increased levels of 3-HK present in the brain might be caused by enzymatic dysfunction, mainly up-regulation of KMO and down-regulation of kynureninase, shifting the KP towards formation of neurotoxic metabolites and ROS and consequently, neurodegeneration [165]. Treatment of R6/2 mice with HDAC and KMO inhibitors reduces the level of 3-HK by comparable amounts, suggesting a direct link between HDAC complexes and KP activation. They suggest that the dysregulation of HDAC transcription induced by mHtt is carried out before the activation of the QUIN branch of KP and could therefore modulate this pathway [165].

In combination, these results provide strong evidence that the modulation of the KP can prevent neurodegeneration and therefore the inhibition of key enzymes in this

pathway can be a valuable therapeutic approach, not only for HD but also to other neurodegenerative, inflammatory and psychiatric disorders. KMO enzyme has been of particular interest since it has a central role in modulating the KP and its inhibition could significantly decrease the neurotoxic metabolites in the QUIN branch and possibly shift the pathway towards the production of neuroprotective KYNA. To date several KMO inhibitors have been developed and characterised. The next section will be dedicated to an overview of the KMO chemical inhibitors currently available.

### *1.2.6.2. KMO inhibitors*

A selection of published KMO inhibitors is shown in Table 1.1:

**Table 1.1. Selection of KMO inhibitors**

| Compound | Structure | $IC_{50}$ | Enzyme source | Reference |
|---|---|---|---|---|
| **Nicotinylalanine (NAL)** | 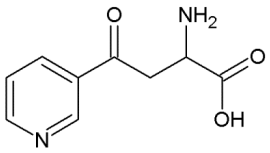 | 900±180 μM | Liver, Brain | [168, 169] |
| ***m*-nitrobenzoylalanine (mNBA)** | 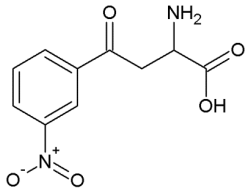 | 3.0±0.2 μM<br>0.77±0.11 μM | Brain<br>Kidney | [170] |
| **3,4-dichlorobenzoylalanine (FCE28833, PNU156561)** | 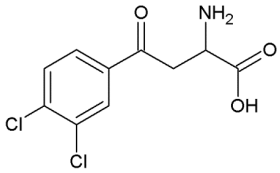 | 0.2 μM<br>0.23±0.03 μM<br>0.33±0.03 μM | Brain<br>Liver<br>Kidney | [171] |
| **UPF 648** | 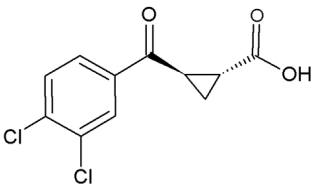 | 0.040 μM | Brain | [172] |
| **Ro 61-8048** | 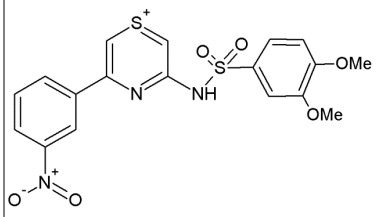 | 0.037±0.003 μM | Kidney | [173] |

The first KMO inhibitor to be described was nicotinoylalanine (NAL) and this compound is a simple analogue of the substrate L-kynurenine [168, 169]. The efficiency of NAL was tested in rat brains and it was shown to inhibit the production of QUIN and increase the concentration of KYNA, as well as being an effective anticonvulsant [168, 169]. However, due to its low potency and selectivity ($IC_{50}$ = 900 μM ) this substrate analogue was further optimised into a new compound called m-nitrobenzoylalanine (m-NBA) with an $IC_{50}$ = 0.9 μM [170]. Rats injected with m-NBA presented higher concentrations of KYN (13 times) and KYNA (5 times) in the brain compared to controls and as for NAL, it is also competent in decreasing convulsions activity and spontaneous locomotor activity [170]. In 1996 a series of KYN analogues were also published, with 3,4-Dichlorobenzoylalanine (FCE 28833, PNU 156561) being the most potent KMO inhibitor with an $IC_{50}$ = 0.2 μM [171]. This compound differs from m-NBA in the benzoylalanine, with a 3,4-dichloro substitution instead of the nitro group. The same pharmaceutical company, *Pharmacia*, started to explore the benzoylalanine side chain and concluded that the carboxylic acid has a key role in the activity of these compounds, while the elimination of the amino group does not significantly influence its activity [172]. Furthermore, it was also shown that the S-isomer is preferred. From this study, KMO inhibitors started to be developed in terms of side chains substitutions. It was found that the incorporation of a cyclopropyl ring in the side chain led to a novel and more potent inhibitor at nanomolar concentrations [172]. This new compound (UPF 648) was first evaluated in a gerbil model and was found to be more selective towards KMO than KAT, and increases the levels of kynurenine and KYNA in the plasma and brain. Since then, it has been used in several *in vivo* and *in vitro* studies to test and validate the hypothesis of KMO inhibition as a therapeutic strategy in HD.

On study showed that intrastriatal injections of QUIN in mice with a targeted deletion of KAT produced larger brain lesions when compared to controls, thus demonstrating QUIN neurotoxicity. However, the mice showed significant amelioration when treated with UPF 648, which suggests that this inhibitor can effectively reduce the 3-HK and QUIN levels and therefore, compensate the lack of the neuroprotective metabolite KYNA [143]. Furthermore, inhibition of KMO via introduction of UPF 648 into the brain not only decreases 3-HK and QUIN levels, but also increases levels of KYNA and neuroprotection in rodents [174, 175].

A screen for novel KMO inhibitors led to the identification of the compound 3,4-dimethoxy-*N*-[4-(3-nitrophenyl)thiazol-2-yl]benzenesulfonamide (Ro-61-8048), which has a high affinity for KMO ($IC_{50}$ = 37 nM) [173]. This compound was tested both *in vivo* and *in vitro* and found to inhibit rat and gerbil KMO after oral administration, as well as increase the levels of KYNA in extracellular hippocampal fluid [173]. Ro 61-8048 has also been extensively used as a tool to study the effects of KP manipulation in several diseases. For example, treatment with this inhibitor significantly decreased cell death while increasing the concentration of KYNA in a model of post-ischemic neuronal death using hippocampal slice cultures subjected to oxygen and glucose deprivation [176]. This compound has also been tested in a primate model of PD, where the prolonged administration of Ro 61-8048 was found to increase the serum levels of L-KYN and KYNA, while reducing levodopa-induced dyskinesia [177].

Regarding HD, Ro 61-8048 was tested in a HD yeast model expressing Htt103Q and significantly reduced 3-HK levels and improved yeast growth [166]. This compound was also tested in *Drosophila* and mice models of HD with the same neuroprotective benefits by shifting the KP towards production of KYNA [163, 167].

Surprisingly Ro 61-8048 does not seem to cross the blood brain barrier in rodents and therefore, the protective effects of this compound is hypothesised to be caused by an increase in the blood levels of kynurenine and the subsequent transport of this metabolite across the BBB and the preferential conversion into KYNA in the brain [178]. Furthermore, this study also reported the metabolic instability of this drug and as a result they developed a slow-release prodrug, 2-(3,4-dimethoxybenzenesulfonylamino)- 4-(3-nitrophenyl)-5-(piperidin-1-yl)methylthiazole, called JM6 [178]. This prodrug was tested not only in HD but also in AD mice models and found to ameliorate several disease-relevant phenotypes including synaptic loss and shortened lifespan [178].

As mentioned for Ro 61-8048, JM6 does not cross the BBB and therefore, the protective effects of this compound were also caused by the inhibition of KMO in blood cells. It was also claimed that this type of inhibition, compared to direct inhibition in the brain, could be useful when combined with other therapies in which compounds cross the BBB, thus avoiding toxic effects due to simultaneous use of several drugs. Although this study has taken an enormous step forward in understanding the role of the KP metabolites in the periphery and their effects in the brain, further studies will be needed to accurately determine the extent of efficacy of this methodology. While these approaches for KMO inhibition in the periphery have shown great therapeutic promise for neurodegenerative

diseases, the development of KMO inhibitors able to cross the BBB is a vital strategy to pursue as the delivery of KMO inhibitors directly to the brain may reduce levels of neurotoxic metabolites, in addition to increasing levels of neuroprotective KYNA [174, 179].

The high-resolution crystallographic structure of KMO – both with native KMO and ligand-bound enzyme - would aid in the rational design of novel KMO inhibitory compounds, which may ultimately expedite clinical application of these compounds. Since there was no structural knowledge of this enzyme, the investigation of the binding modes of possible KMO inhibitors has been carried out using structure and ligand-based computer-aided design tools based on structurally and functionally related enzymes [180, 181]. Nonetheless, obtaining the crystal structure of KMO will be necessary to truly inform rational design of novel inhibitors.

## 1.3. KYNURENINE 3-MONOOXYGENASE (KMO), A FLAVOPROTEIN MONOOXYGENASE

This section will be dedicated to the molecular characterisation of Kynurenine 3-monooxygenase. A detailed description of this enzyme will be given in terms of enzyme classification and catalytic mechanism, and a series of motifs and domains from similar enzymes will be revealed in order to predict important structural features of KMO. Studies carried out on the expression and purification of KMO from different organisms will also be presented as possible strategies to pursue and optimise in the current project.

### 1.3.1. Introduction to Flavoproteins

Flavoproteins, as the name suggests, are a group of enzymes with flavin adenine dinucleotide (FAD) or flavin mononucleotide (FMN) as a covalently or noncovalently bound prosthetic group and were first described in 1933 by Otto Warburg [182] (Figure 1.4A). A yellow protein from yeast cells was isolated and catalysed the oxidation of NADPH using oxygen as a second substrate. Nowadays hundreds of flavoproteins, with a variety of functions ranging from important roles in signal transduction, development of

mammalian foetuses to photosynthesis and DNA repair are known [183] . They also play a crucial role in redox reactions in biological systems due to their involvement in single and double electron transfer processes and provide flexibility in terms of substrates and reactions catalysed [183].

In general, flavoenzymes catalyse reactions that can be separated into reductive and oxidative half-reactions. In the reductive half-reaction the substrate reduces the flavin and in the oxidative half-reaction the flavin is re-oxidised by an electron acceptor (Figure 1.4B). These reactions will be further explored and characterised in section 1.4.2.1..

Flavoproteins can be classified based on their function into many subclasses, for example electron transferases, photolyases, synthases, dehydrogenases, disulfide reductases, oxidases, and monooxygenases [184]. Kynurenine 3-monooxygenase is a member of flavoprotein monooxygenases and therefore the next sections will be dedicated exclusively to this class of enzymes. Further information regarding the other classes of flavoproteins are detailed in references [184–186].

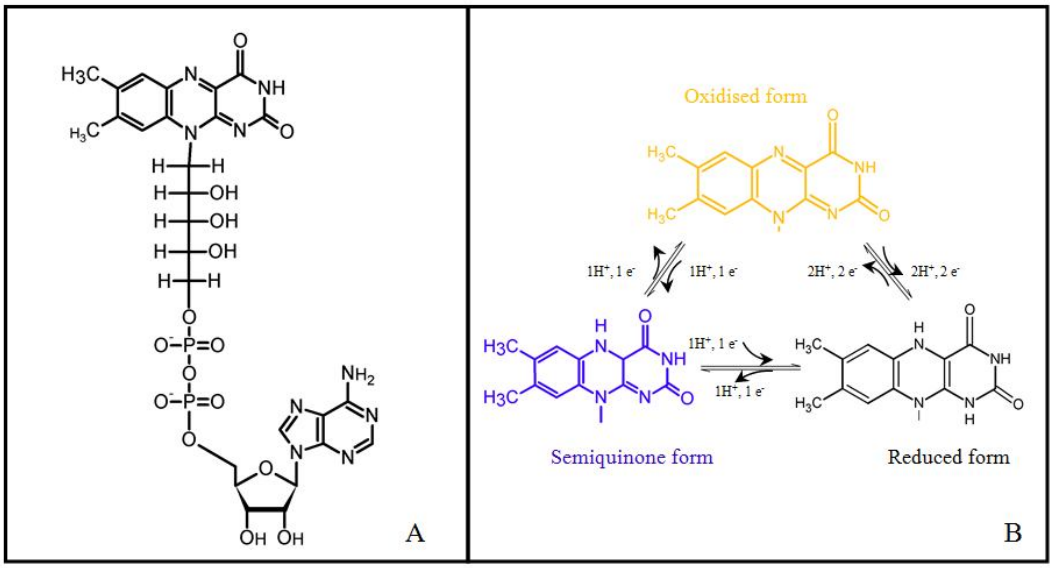


**Figure 1.4. Schematic representation of Flavin Adenine Dinucleotide** A: Flavin Adenine Dinucleotide molecule. B: Schematic representation of the three different redox states of flavin coenzymes, each state presenting different colours and the reduced form is colourless.

### 1.3.2. Flavoprotein monooxygenases

Flavoprotein monooxygenases are a vast collection of enzymes that catalyse the insertion of one atom of molecular oxygen into a substrate, using NAD(P)H to reduce the flavoenzyme cofactor from FAD to $FADH_2$. This species will then react with molecular oxygen to form flavin C4a peroxide, which is the reactive and unstable oxygen species responsible for incorporation of one molecule of oxygen into the substrate while the other is reduced into water [187] (Figure 1.5). Fraaije *et al.* (2006) divided flavoprotein monooxygenases into six major classes from A to F (Table 1-2) [187]. The focus of this work was on Class A flavoprotein monooxygenases.

**Table 1.2. Classes of external flavin monooxygenases (adapted from** [187]**)**

| Sub-class | General characteristics | Reactions | Cofactor | Coenzyme | Structural features |
|---|---|---|---|---|---|
| **A** | • Encoded by single gene<br>• $NADP^+$ is released after flavin reduction | Hydroxylation Epoxidation | FAD | NAD(P)H | One dinucleotide binding domain (Rossman fold) binding FAD |
| **B** | • Encoded by single gene<br>• keep the coenzyme NADPH/NADP+ bound duringcatalysis | Baeyer–Villiger; N-oxidation | FAD | NADPH | Two dinucleotide binding domains (Rossmann fold) binding FAD and NADPH |
| **C** | • Encoded by multiple genes encoding one or two monooxygenase components and a reductase component | *Light emission*; S-oxidation *Light emission*; S-oxidation | - | FMN NAD(P)H | TIM-barrel fold |
| **D** | • Encoded by two genes encoding a monooxygenases and a reductase | Hydroxylation | - | FAD NAD(P)H | No structure available |
| **E** | • Encoded by two genes encoding a monooxygenases and a reductase | Epoxidation | - | FAD NAD(P)H | No structure is available |
| **F** | • Encoded by two genes encoding a monooxygenases and a reductase; | Halogenation | - | FAD NAD(P)H | Two domain structure: one FAD binding domain (Rossmann fold) and a helical domain |

#### *1.3.2.1. Class A flavoprotein monooxygenases*

Class A monooxygenases are encoded by a single gene, contain a tightly bound FAD cofactor and depend on NAD(P)H as a coenzyme. An electrophilic attack to the aromatic ring is carried out by the reactive species, C(4a) hydroperoxyflavin [187]. The majority of substrates are aromatic compounds with hydroxyl or amino groups. An interesting feature about this class of flavin monooxygenases is that the reduction of the

enzyme-bound FAD- by NADPH is strongly stimulated by formation of the enzyme-substrate complex - and therefore, NADPH is only used when substrate is present in the reaction [188].

One of the enzymes used as a model system for this class of flavin monooxygenases is p-hydroxybenzoate hydroxilase (PHBH, EC 1.14.13.2), with its structure published in 1979 [189]. Since then, this enzyme has been studied in great detail due to the ability to distinguish almost all of the intermediates in the catalytic cycle by spectroscopic techniques, based on different absorbance and fluorescence properties of each species. As a result, similar experimental strategies have been used to study the catalytic mechanism of numerous flavoprotein monooxygenases and it has become a model for enzymes involved in the oxygenation of aromatic compounds.

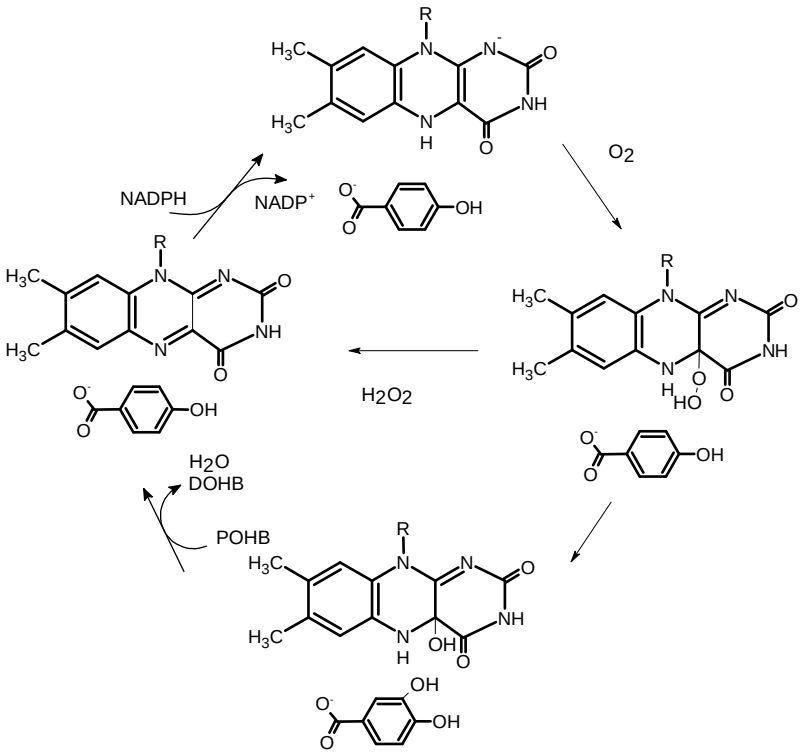


**Figure 1.5. Reaction mechanism of p-hydroxybenzoate hydroxylase.** The first step involves the substrate binding and reduction of flavin by NADPH. Next, the reduced FAD reacts with oxygen to form the first intermediate flavin C(4a)-hydroperoxide. As this species is extremely reactive it instantly hydroxylates the substrate, forming the product 3,4-diOHB, water and the second intermediate flavin C(4a)-hydroxide. In the final step this gets hydrated, leading to oxidised enzyme and the cycle is completed (Adapted from [183]).

Since the first structure of this enzyme was published, many other studies have been reported, showing enzyme complexes with substrates substrate analogues, products and NADPH (Figure 1.6). This has been extremely important, together with multiple sequence alignments studies, to identify motifs or putative sequences involved in catalysis and ligand binding of flavoproteins hydroxylases.

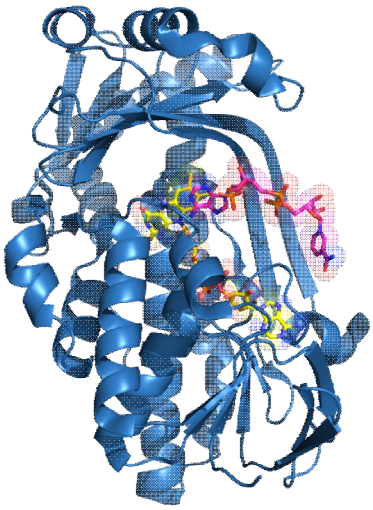

**Figure 1.6. Crystal structure of p-hydroxybenzoate and proposed interdomain binding of NADPH.** Unlike the majority of flavin monooxygenases this enzyme does not present a recognisable domain to bind NADPH. Interestingly NADPH binds in an extended conformation at the surface of the protein in a channel that crosses the binding site of FAD (Adapted from [190]).

The first clear motif found in PHBH was the dinucleotide-binding motif, containing the sequence xhxhGxGxxGxxxhxxh(x)8hxhE(D) where x is any residue and h is a hydrophobic residue. This sequence is highly conserved among proteins that use NADP(H) and FAD as coenzymes and consists of βαβ units, generally 6 β-strands and 4 α- helices [191, 192], which are generally found at the N-terminal part of the protein sequence (Figure 1.7). The central part of this consensus sequence, GxGxxG, is called the Rossmann fold [193]. There is also a second short motif in the middle of the sequence of flavoprotein hydroxylases, **GD**, which contacts with the riboflavin moiety of FAD [194]. Particularly in PHBH, this motif is localised in the re-side of the isoallaxazine ring of FAD, close to the substrate binding site[195]. Another short amino acid sequence motif for this group of enzymes, **DG**, was discovered in 1997 by Eppink *et al*. [196], and according to their crystallographic and site-directed mutagenesis studies of PHBH was

suggested to be involved in FAD binding and could also serve as the NADPH recognition site.

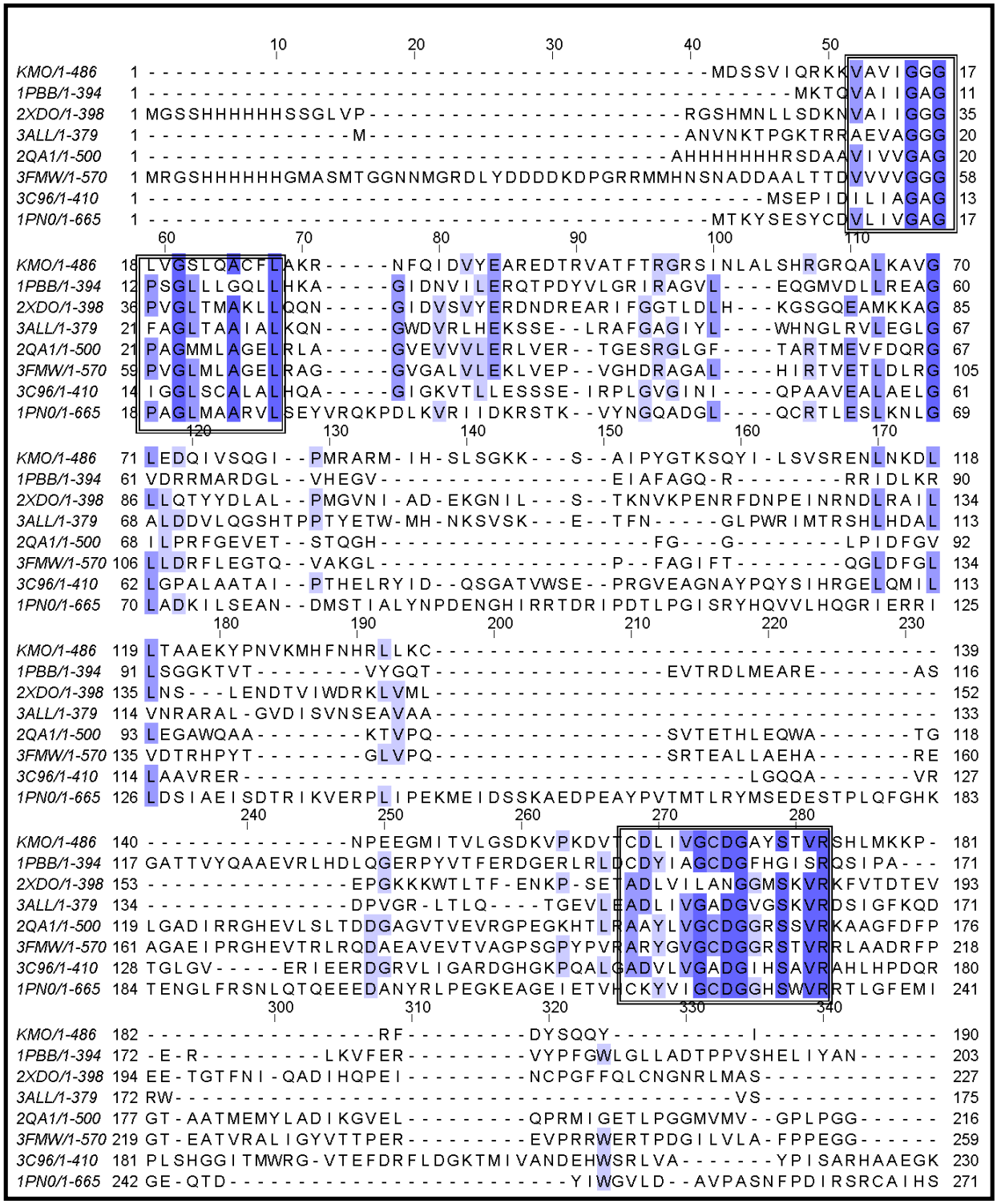

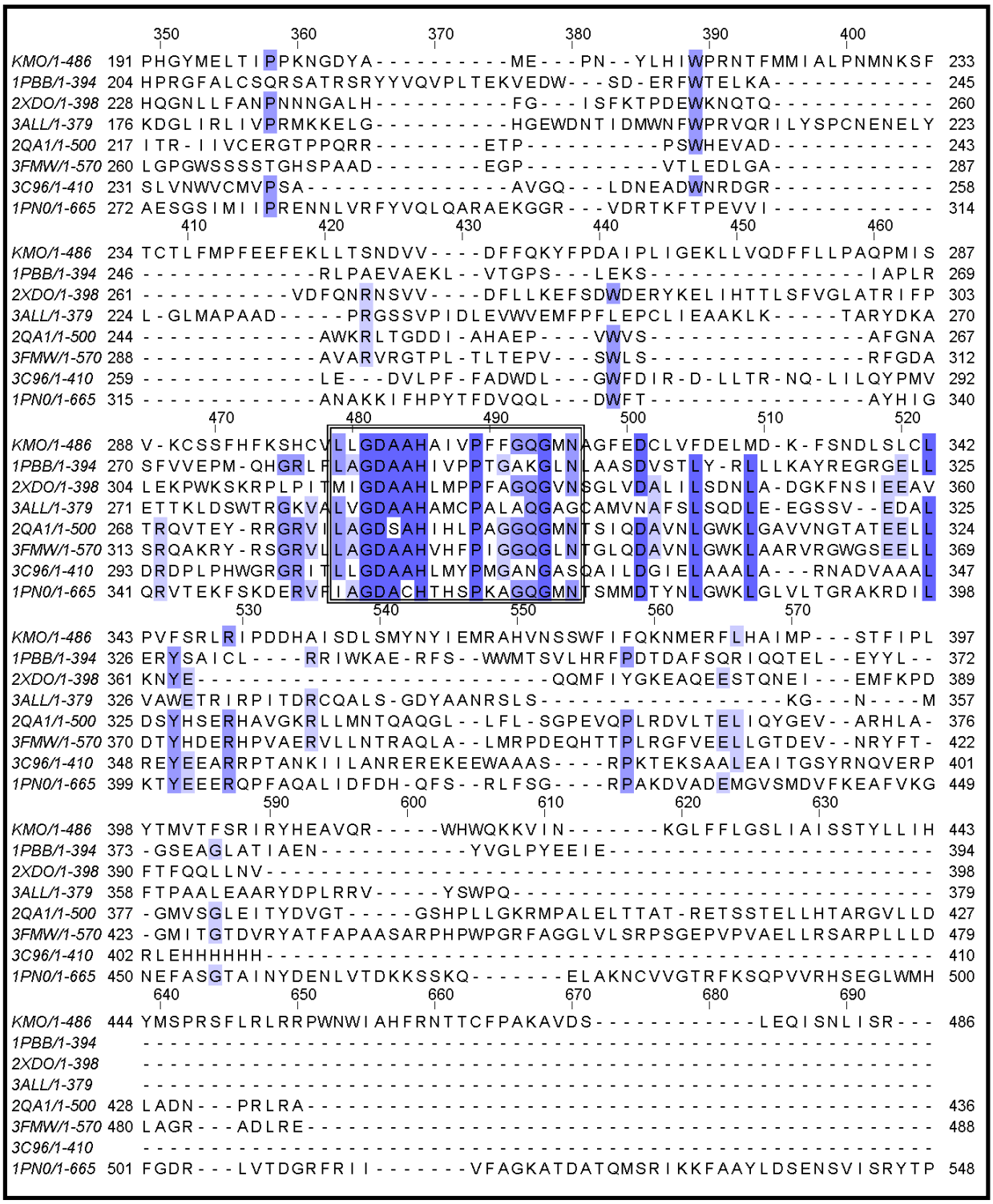


**Figure 1.7. Multiple sequence alignment of *Homo sapiens* KMO with 7 structural related proteins.** The amino acid sequences were aligned by the CLUSTAL method. 1KMO (Kynurenine 3-monooxygenase, Accession number NP_003670), 1PBB (P-Hydroxybenzoate Hydroxylase, Accession number 1PBB), 2XDO (Tetracycline Degrading Monooxygenase Tetx2, Accession number 2XDO), 3ALL (2-Methyl-3-Hydroxypyridine-5-Carboxylic Acid Oxygenase, Accession number 3ALL), 2QA1(PGAE- Aromatic Hydroxylase Involved In Angucycline Biosynthesis, Accession number 2QA1), 3FMW (Mtmoiv, A Baeyer-Villiger Monooxygenase From The Mithramycin Biosynthetic Pathway, Accession number 3FMW ), 3C96 (Flavin-Containing Monooxygenase Phzs From Pseudomonas Aeruginosa, Accession number

3C96) and 1PN0 (Phenol Hydroxylase From Trichosporon Cutaneum, Accession number 1PN0). The boxed fragments represent the common motifs found in flavoprotein monooxygenases.

### 1.3.3. Kynurenine 3-monooxygenase (KMO)

KMO is categorised as a class A flavoprotein monooxygenase and, as described in the previous section, it is an NADPH-dependent enzyme that hydroxylates an aromatic substrate and contains a tightly bound FAD cofactor. It catalyses the hydroxylation at the C3 position of L-kynurenine into 3-hydroxykynurenine with the consumption of one molecule of NADPH and $O_2$ per turnover [9, 197].

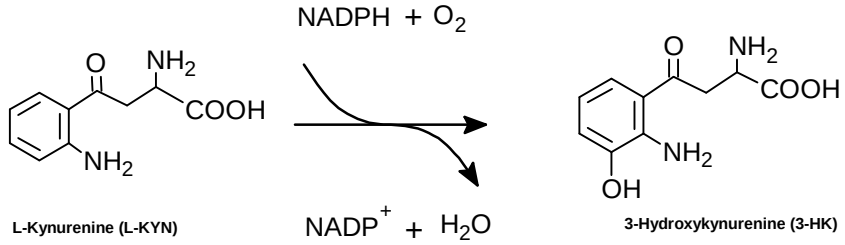


**Figure 1.8. Reaction catalysed by kynurenine 3-monooxygenase.** L-kynurenine is hydroxylated at position 3 into 3-hydroxy-kynurenine in the presence of molecular oxygen and NADPH.

Based on a number of spectroscopic and crystallographic studies on other members of this class of flavoprotein monooxygenases, it is hypothesised that the mechanism of action of KMO is similar to the reaction mechanism of p-hydroxybenzoate hydroxylase. In the reductive half-reaction, L-kynurenine binds to the oxidised KMO and FAD is reduced by NADPH to $FADH_2$. In the oxidative half-reaction, the reduced L-KYN-KMO complex reacts with dioxygen, forming the intermediate C(4a)-hydroperoxide that quickly hydroxylates the substrate L-KYN into 3-HK and releases one molecule of water [198].

KMO (EC 1.14.1.2) was first described in 1956 and is principally localised in the outer membrane of mitochondria [199, 200]. It is highly expressed in liver, kidney, endothelial cells and monocytes and lower concentrations were also found in the brain, specifically in microglia and macrophages [163, 201–204]. Interestingly, no expression was found in astrocytes where other metabolites from the KP are produced in large

amounts, such as KYN and KYNA, or in neurons [205], supporting the hypothesis that the over-activation of microglia by mHtt induces the expression of the neurotoxic metabolites 3-HK and QUIN, therefore contributing to neurodegeneration.

A number of studies have been published describing the activity of KMO from different organisms, in terms of substrate, coenzyme and cofactor specificity, as well as the proposed catalytic mechanism [206–214]. Almost all studies involving class A flavoproteins monooxygenases rely on the unique optical properties of the FAD cofactor. Since this cofactor is tightly bound in the active site, the spectral changes during catalysis can be monitored using rapid reaction kinetic instruments, giving valuable information regarding specific steps in the reaction mechanism. The binding of substrates or inhibitors can also be studied by spectroscopic methods, yielding dissociation constants and conformational changes in the active site [215].

The first attempts to purify KMO were carried out by Nisimoto *et al.* (1975). The enzyme was isolated from rat liver mitochondria and purified using a combination of anion exchange chromatography and gel filtration techniques, with phospholipids in the purified preparation [210, 211]. It was suggested that native KMO from this organism is associated with the hydrophobic region of the mitochondrial outer membrane and therefore, the use of detergents throughout purification was a requirement to stabilise the protein. Although purified protein was obtained, the yield and the specific activity was rather low [210, 211]. Other studies were also performed on KMO from other organisms such as *Saccharomyces cerevisiae* [212], *Saccharomyces carlsbergensis* [213] and *Schistocera gregaria* [214], *Pseudomonas fluorescens* [207] and *Homo sapiens* [208], describing methods for expression and purification of this enzyme, as well as enzymatic assays where some kinetic parameters were established (see Table 1.3).

Special attention will be given to two particular studies: the first study, conducted by Breton *et al*. (2000), is one of the few studies on human KMO and therefore the only data available for direct comparison with the work presented in this thesis [208]. The second report, by Crozier-Reabe *et al*. (2008), was performed in KMO from *Pseudomonas fluorescens* and presents a complete and detailed study on the reaction mechanism of this enzyme was and has been very informative for the development of kinetic assays in the present work [198].

**Table 1.3: Kinetic parameters of KMO from different organisms**

| Source organism | $K_M$ L-KYN (μM) | $K_M$ NADPH (μM) | pH-optimum | Localisation | References |
|---|---|---|---|---|---|
| *Pseudomonas fluorescens* | 11.8 | 8.5 | 8.5 | - | [198, 207] |
| *Saccharomyces cerevisiae* | 40 | 16 | 8.0 | promitochondrion | [212] |
| *Rattus norvegicus* | 25 | 23 | 7.5-8 | Mitochondrial outer membrane | [9] |
| *Sus scrofa* | 16 | - | 8.0 | Mitochondrial outer membrane | [216] |
| *Homo sapiens* | 13 | - | 7.5 | Mitochondrial outer membrane | [10, 208] |

It has proven to be very difficult to study human KMO as this enzyme is membrane associated and it has been extremely difficult to obtain sufficient quantities of protein for further characterisation [10]. The first study to produce sufficient quantities of this enzyme was performed by Breton *et al.* (2000) using recombinant human KMO [208]. The protein was expressed in COS-1 cells as a glutathione S-transferase (GST) fusion protein and purified using gluthathione-sepharose resin. The biochemical characterisation of the enzyme showed an optimal pH of 7.5, similar to that described for pig and rat liver KMO enzymes (Table 1.3), as well as similar kinetic parameters when compared to native KMO from other organisms. This provides evidence that the recombinant enzyme shows the same behaviour as KMO from tissue origin and can therefore be used as a main strategy to obtain adequate levels of protein for further biochemical and mechanistic characterisation. In the same study, different potential substrates were also tested and it was shown that this enzyme is highly specific to L-kynurenine and shows a preference for NADPH as a coenzyme and FAD as a cofactor with both presenting a 1:1 stoichiometry. It was also hypothesised that binding of the enzyme with one substrate does not influence its affinity to the other [208]. Although the data reported in this study described an important strategy to express and purify recombinant human KMO, the yield obtained was still not sufficient for structural studies.

An informative on the reaction mechanism of KMO was performed by Crozier-Reabe *et al.* (2008.) The authors explored separately the reductive and oxidative half-

reactions of KMO from *Pseudomonas fluorescens* [198]. As described in section 1.4.2.1 (class A monooxygenases), the oxidative half-reaction of class A flavoprotein monooxygenases starts with the reduction of oxygen by the reduced flavin to form the first intermediate C(4a)-hydroperoxide. Once formed, it will then react with the aromatic substrate in an electrophilic substitution reaction, and the distal oxygen is inserted typically in the ortho position of the activated ring, forming the hydroxylated product, water and the second intermediate flavin C(4a)-hydroxide, which will be hydrated to form the oxidised enzyme.

Crozier-Reabe *et al.* (2008) have shown that the oxidative half-reaction of *Pseudomonas fluorescens* KMO is similar to the majority of class A flavoprotein monooxygenases with some events differing after hydroxylation of the aromatic substrate. According to their results, the second intermediate C4(a)-hydroxyflavin was not observed and it was suggested that the dehydration of hydroxyflavin does not depend on the release of the product and takes place instantly after the hydroxylation of the aromatic substrate. One interesting result from this study is that *Pseudomonas fluorescens* KMO does not appear to be able to distinguish efficiently between the physiological and substrate-like molecules. They have tested two different KMO inhibitors, BA or *m*-NBA, and both had shown absorbance data similar to that observed with the native substrate L-Kyn when mixed with dioxygen, with the formation of hydroperoxyflavin followed by a decay of this species and an accumulation of hydrogen peroxide and the oxidized enzyme without hydroxylation of the aromatic ring. These results support the idea that the oxidative half-reaction of this enzyme is not fully dependent on the interaction between the activated ring of the substrate with the enzyme and can instead undergo the subsequent steps of catalysis in the presence of the wrong ligand, regardless of the fact that the ligand is not bound and the product is not formed [198]. The consequences of this mechanism might be of particular importance in terms of the therapeutic use of these inhibitors, since the accumulation of higher levels of hydrogen peroxide is not recommended as a therapeutic strategy and therefore other approaches may have to be pursued in order to design novel KMO inhibitors.

In terms of the reductive half-reaction, results from the same study showed that the mechanism of the enzyme is the same as the majority of class A flavoprotein monooxygenases, with the reduction by NADPH stimulated when the aromatic substrate is bound. There was also evidence supporting the hypothesis of the dynamic motion of the flavin isoalloxazine during catalysis. This hypothesis, called “waving flavin”, has

been extensively studied, particularly for PHBH [190, 217, 218] and phenol hydroxylase (PHHY) [219] enzymes, and involves movement of the isoalloxazine ring from the active site towards an "out" conformation, in order to make contact with the nicotinamide ring at the protein surface. Crozier-Reabe *et al.* (2008) reported evidence for two different flavin states in the product release step [198].

Finally, an additional aspect common to class A flavoprotein monooxygenases is the sensitivity to anions in both the reductive and oxidative half reactions [220, 221]. As expected, *Pseudomonas fluorescens* KMO is also inhibited by anions and it was hypothesised that ions might bind in the vicinity of the active site and therefore influence the flavin reactivity [208].

#### *1.3.3.1. Structural features of Kynurenine 3-monooxygenase*

Despite intense research in the development of novel KMO inhibitors, there is no information regarding the crystal structure of KMO from any organism. The investigation of the binding modes of possible inhibitors in order to understand the mechanism of action of this enzyme has been carried out using structure and ligand-based computer-aided design tools based on structurally and functionally related enzymes [180, 181]. From the multiple sequence alignment of KMO with other structurally-related proteins (Figure 1.7), in combination with functional studies carried out with other flavin monooxygenases, particularly the enzyme PHBH, there is evidence that KMO and PHBH are functionally related. Despite the fact that they only share 18 % identity, they are both NAD(P)H-dependent flavoproteins that catalyse the hydroxylation of aromatic compounds. The fact that the PHBH crystallographic structure is known in complex with the substrate and the product could be useful in predicting the interaction of KMO with its physiological substrate and ultimately, in the design of new inhibitors. Attempts were made by Pellicciari *et al.* (1996) to build a *pseudo* model of the active site of KMO based on PHBH [180]. It was assumed that these two enzymes have similar mechanisms and therefore, KMO might share the same non-covalent interactions with the substrate with a similar active site. The aromatic ring of the substrate L-kynurenine was forced to match the aromatic ring of the p-hydroxy benzoic acid. Due to the limited knowledge of the primary sequence of KMO at this time, the results of this study are not entirely reliable for the development of novel KMO inhibitors.

As pointed out in the previous section, there are published reports describing strategies for expression and purification of KMO from higher organisms, including humans. However, it has proven to be extremely difficult to obtain sufficient quantities of this enzyme for structural studies and therefore it might explain the lack of structural knowledge of this enzyme. A more realistic approach would be to try to optimise the expression levels in COS-1 cells or to overexpress recombinant KMO in lower organisms such as *Escherichia coli, Pichia pastoris* or *Saccharomyces cerevisiae.*

The amino acid sequence of *Homo sapiens* KMO shows 74.4%, 40.6%, 34.1% and 31.7% identity with those of *Ratus norvegicus, Drosophila melanogaster, Saccharomyces cereviseae* and *Pseudomonas fluorescens,* respectively (Figure 1.9). The residues coloured in blue are conserved among the five species and, as previously shown in Figure 1.7, some of these motifs are characteristic of flavin monooxygenases that require NADP(H) and FAD as coenzymes. Additionally, other conserved regions can support the hypothesis that KMO from different organisms are functional and structurally related and therefore, can be used as good homology models for the study of human KMO.

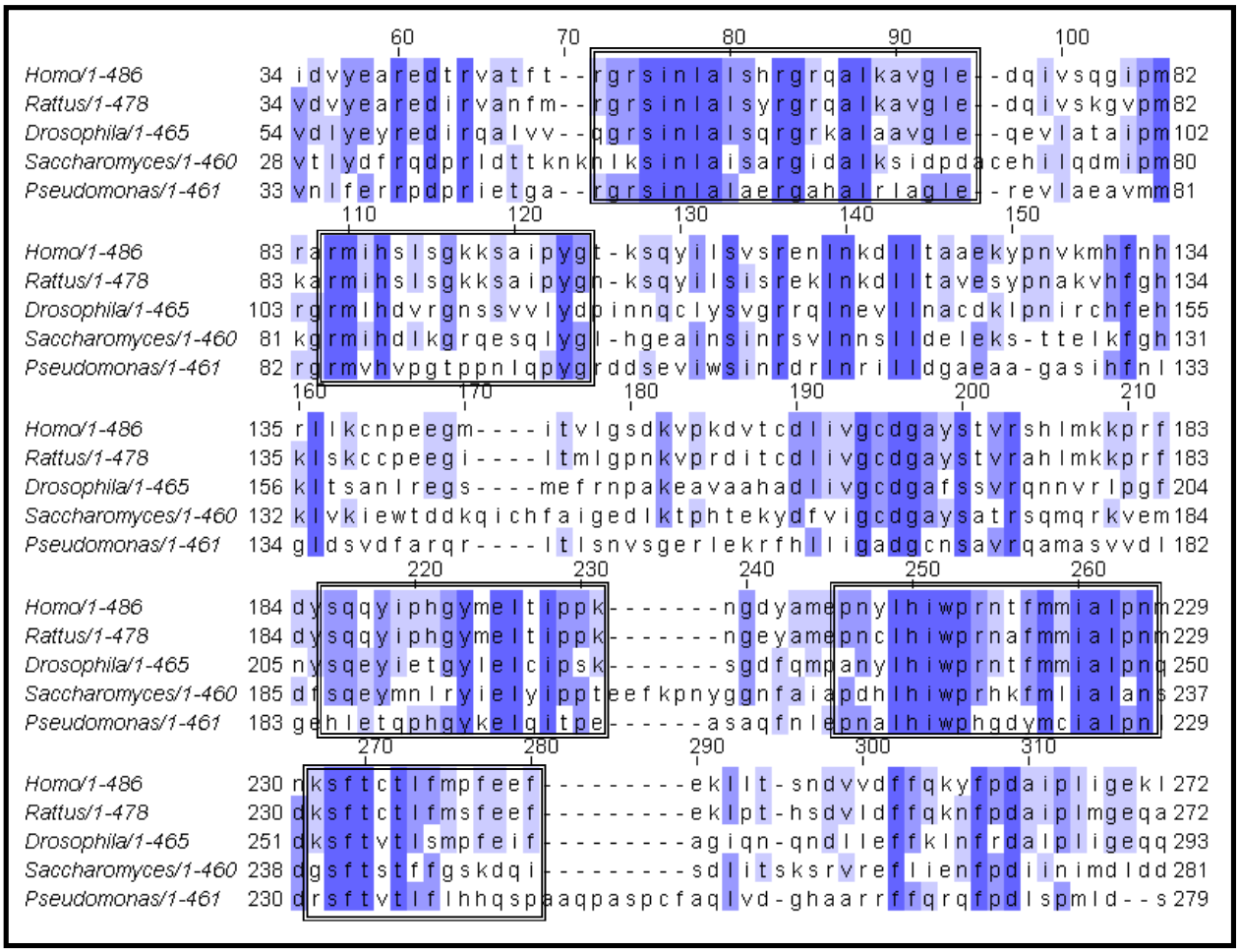

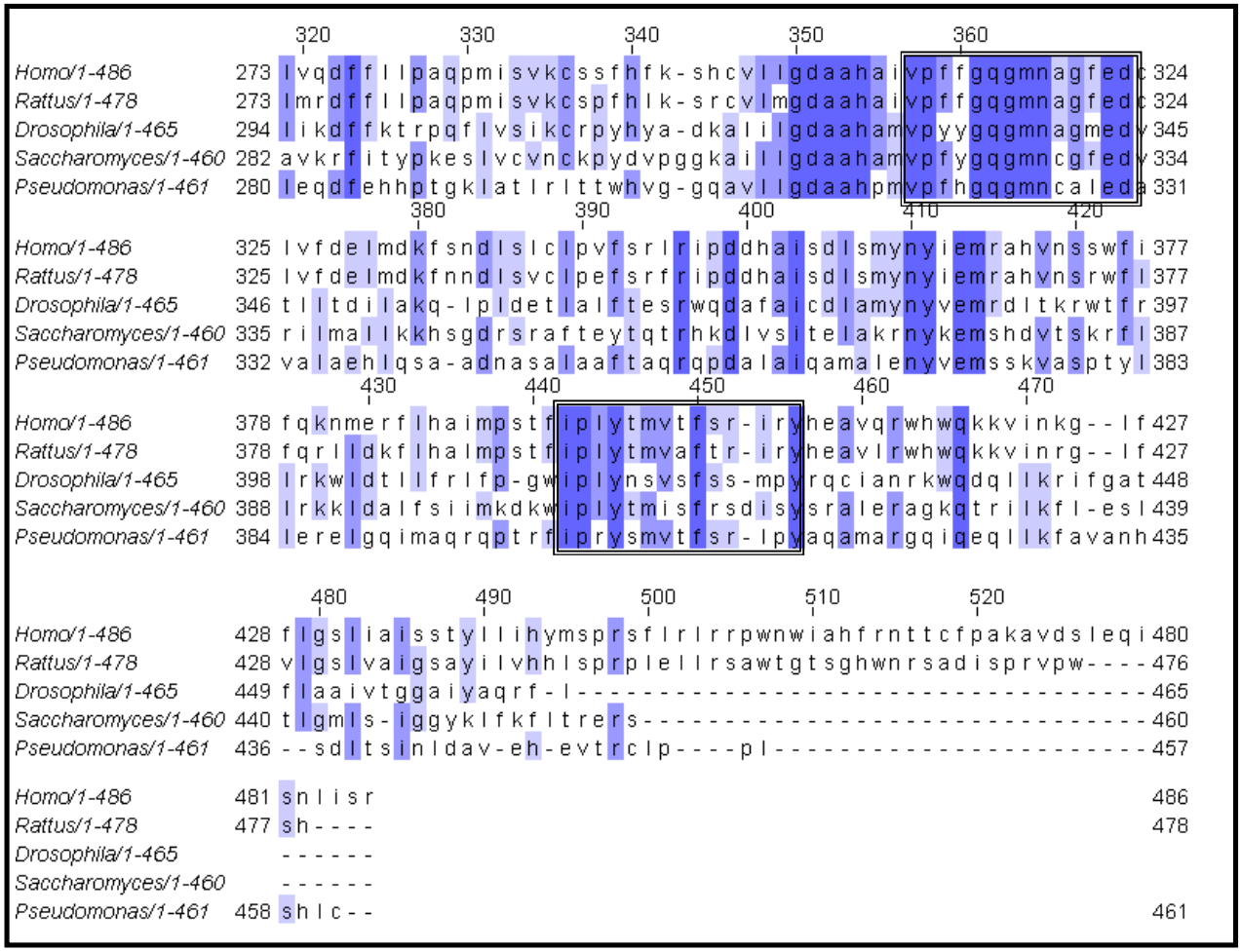


**Figure 1.9. Multiple alignment of the amino acid sequence of KMO from different organisms.** *Homo sapiens* KMO (Accession nº NP_003670), *Rattus norvegicus* KMO (Accession nº NP_067604), *Drosophila melanogaster* KMO (Accession nº A1Z746), *Saccharomyces cerevisiae* KMO (Accession nº P38169), *Pseudomonas fluorescens* (Accession nº Q84HF5). The residues are coloured according to the percentage of the residues in each column that agree with the consensus sequence. The boxed fragments are motifs conserved among KMOs from different organisms excluding the motifs characteristics of flavoprotien monooxygenases.

## 1.4. RESEARCH AIMS

There is a good deal of evidence supporting the hypothesis that the KP plays a critical causative role in the pathophysiology of several neurodegenerative disorders. It is clear that the modulation of neuroactive kynurenine metabolites, such that levels of KYNA are increased relative to 3-HK and QUIN, is desirable for neuroprotection. In particular, KMO, which lies at a critical branchpoint in the pathway, is of great interest as its inhibition ameliorates neurodegeneration by shifting the flux towards the neuroprotective branch of the KP. Despite great interest in the therapeutic potential of KMO inhibitors, to date none have been tested in clinical trials. The most promising KMO inhibitory compounds, such as Ro 61-8048, do not readily cross the blood-brain barrier (BBB), with at most ~1% of the drug reaching the brain, the major site of pathology in HD. In order to pursue KMO as a drug target for HD, it is critical to identify high-affinity inhibitors of KMO that readily penetrate the BBB. In order to rationally design novel KMO inhibitory compounds it is vital to obtain structural information for this protein, both native and bound to existing drugs. In addition, functional and mechanistic studies with wild-type and site-directed mutant versions of KMO will provide critical information for future drug design. However, performing these analyses will require large quantities of purified recombinant human KMO.

The aim of this thesis was to produce high levels of KMO protein for structural, functional, and mechanistic studies, with the final goal of developing novel inhibitors capable of crossing the blood-brain barrier. Our aim was to develop the underpinning work by solving the crystal structure of KMO to allow the development of new inhibitors, using a knowledge-based approach that embraces X-ray crystallography and biophysical analysis of inhibitor binding for future synthesis, and analysis of the efficacy of new inhibitors in HD cell models and in HD model mice.

## 1.5. OVERVIEW

Chapter 1 and 2 serve as the introduction and general materials and methods leading on to the research work presented in Chapters 3, 4 and 5. Finally a general discussion will be presented in Chapter 6 followed by conclusion and future work.

Initial studies were focused on the generation of several expressing clones of human KMO (*Hs*KMO) as both full length and truncated forms by conventional site-directed mutagenesis. We explored several constructs with redefined domain boundaries, by deleting domains that could possible lead to incorrect folding and protein insolubility in order to screen for suitable protein truncates that allow crystallisation. We have used *Pichia pastoris* for over-expression of recombinant *Hs*KMO. The yeast *Pichia pastoris* has the advantage of eukaryotic expression systems with regards to protein folding, post-translational modifications, and protein processing besides the benefit of being easy to manipulate. We have purified recombinant forms of *Hs*KMO using a combination of traditional chromatographic methods and affinity chromatography using nickel-based resins. Purified enzymes were subject to detailed characterisation by biophysical and kinetic methods. Aside from spectrophotometric characterisation and analysis of recombinant *Hs*KMO, the binding of KMO enzymes and variants to physiological substrate and potential KMO drugs were also performed by spectrophotometric titrations in order to determine dissociation constants ($K_d$) for further comparison with published results. Crystallisation trials were undertaken to obtain human KMO structures.

Due to the difficulty in expressing full length *Hs*KMO in *Pichia pastoris*, we also tried to over-express and purify this enzyme in insect cells using the baculovirus system. Since this protein is membrane associated, the expression of the full length is challenging in lower organisms such as *Pichia pastoris* because these proteins tend to be toxic for the host as well as the fact that the translation and chaperone systems of these organisms are not well adapted to the biosynthesis of human protein. In addition, eukaryotic proteins may undergo post-translational modifications that only higher eukaryotic cell lines provide the necessary machinery.

Full length *Hs*KMO was extracted from the host cell membrane by the addition of detergents to allow solubilisation. A series of detergents were tested in order to choose the one able to provide active, homogeneous and stable protein. Purification was also performed using a combination of traditional chromatographic methods and purified enzyme was subject to detailed characterisation by biophysical and kinetic methods.

Successful purification of active, detergent solubilised forms of the enzyme allowed the screening of crystallisation conditions for those particular KMO-detergent forms. The results of expression and characterisation of full length and truncated forms of *Hs*KMO form the basis of Chapter 3. The poor stability and low expression yield of human KMO however prevented crystallisation, the details will be described in the same Chapter. We thus turned our attention to *Saccharomyces cerevisiae* KMO (*Sc*KMO), which is highly related to human KMO (38 % identity and 51 % similarity).

We overexpressed and purified *Sc*KMO for crystallisation trials to provide a structural model for human KMO. The same techniques applied for *Hs*KMO were also employed for the complete characterisation of *Sc*KMO and the results will be presented in Chapter 4. Kinetic and inhibitor studies using both human and yeast enzymes were performed in parallel in order to validate our model and to prove that *Sc*KMO is a good homology model for the study of *Hs*KMO.

Established crystallisation conditions enabled us to ultimately determine the structure of *Sc*KMO by Single Wavelength Anomalous Dispersion (SAD) technique utilising the anomalous signal from SeMet. Further work was then pursued to determine structures in presence of KMO substrate and drugs (Chapter 5).

We validated our model by targeting active site residues and performed inhibitor binding and kinetic assays. This analysis will provide important functional verification of the importance of residues to inhibitor binding inferred from the structural studies. These results will be shown in Chapter 5.

A number of strategies to further elucidate the mechanism of KMO catalysis and future structural work will be suggested in Chapter 6 followed by final conclusions.

# CHAPTER 2

# GENERAL MATERIALS AND METHODS

# 2. GENERAL MATERIALS AND METHODS

## 2.1. MATERIALS

All chemicals and reagents were purchased from Sigma-Aldrich and Fisher Scientific unless otherwise stated and were of the highest grade available.

Restriction endonucleases and other DNA modifying enzymes were purchased from New England Biolabs.

*E. coli and Pichia pastoris* growth media were obtained from Formedium, High-Five ($Hi_5$) cells were cultured in Express five SFM media from Invitrogen.

As the expression of kynurenine 3-monooxygenase was carried out in three different hosts, each one with specific strains, plasmids, reagents, buffers and antibiotics, the description of the materials used in each procedure will be reported in each of the methodology sections.

## 2.2. METHODS

### 2.2.1. Protein Engineering and Primer Design

#### *2.2.1.1. Human full-length and truncated kynurenine 3-monooxygenase for expression in Pichia pastoris*

Full-length human kynurenine-3-monooxygense (KMO UniProtKB accession number O15229) was 'codon optimised' by *Qiagen* for overexpression in eukaryotic cells. Deletion mutants (ΔKMO383 and ΔKMO423) were constructed by the manipulation of the full-length gene and named so that the last residue before the truncation is indicated. The KMO gene was used as a template in the PCR reaction; the forward and reverse primers are shown in Table 2.1**.** Primers contained the restriction cloning sites EcoRI and XbaI at the 5' and 3' ends, respectively. As these constructs will be expressed in *Pichia pastoris*, the insert might contain the initiation codon as a part of a

yeast consensus sequence (G/A)NNATGG [222] for proper initiation of translation in the this host and therefore the fragment **GTC** was inserted before the start codon.

The constructs were amplified, digested with EcoRI and XbaI and inserted into pPICZ-B vector (Invitrogen) for expression of recombinant KMO protein with a C-terminal polyhistidine (6xHis) tag in *Pichia pastoris*. Amplification conditions were 98°C for 30 s, 30 cycles of 98°C for 10 s and 72°C for 45 s followed by a final polymerization step of 72°C for 10 min. The vector was pre-treated with calf intestinal alkaline phosphatase (New England BioLabs) and digested with the same restriction enzymes. The purified PCR product and pre-treated vector were self-ligated with QuickLigation Kit (New England BioLabs) and used for transformation into XL10-Gold Ultracompetent *Escherichia coli* cells (Agilent) in Low Salt Lisogeny Broth (LB) medium containing 25 μg/mL zeocin. Successful transformants were isolated and submitted for DNA sequencing by MWG Eurofins using the following forward (5'AOX) and reverse (3'AOX) primers: 5'- GAC TGG TTC CAA TTG ACA AG 3', 3'- GCA AAT GGC ATT CTG ACA TCC. The maintenance of plasmid DNA stocks and the genes of interest for protein engineering methods were done using either *E. coli* strains XL-1 Blue (Strategene) or Novablue (Novagen) super competent cells using the QIAprep® Spin Miniprep Kit (Qiagen) and stored at -20°C until further use.

**Table 2.1. KMO constructs cloned into pICZ-B vector for overexpression *Pichia Pastoris***

| KMO constructs[1] | Sense primer | Anti-sense primer |
|---|---|---|
| **KMO-His$_6$** | 5'-G GCC **GAT TTC** GTC ATG GAC AGC AGC GTG ATC CA-3' | 5'-GGC CGC TCT AGA CCG GCT GAT CAG GTT GCT-3' |
| **ΔKMO383-His$_6$** | The same as above | 5'-GGC CGC TCT AGA GTT GAT CAC TTT TTT CTG C-3' |
| **ΔKMO423-His$_6$** | The same as above | 5'-GGC CGC TCT AGA CCG TTC CAT GTT TTT CTG-3' |

[1]KMO constructs were cloned into pPICZ-B vector for expression of recombinant KMO protein with N-terminal polyhistidine (6xHis) tag in *Pichia pastoris*. The letters in bold indicate the engineered EcoRI and XbaI restriction cloning sites in the forward and reverse primers, respectively. The underlined letters indicate the yeast consensus sequence. KMO deletion mutants were named so that the last residue before the truncation is indicated.

#### *2.2.1.2. Human full length Kynurenine monooxygenases for expression in Insect cells*

The gene encoding full-length human kynurenine-3-monooxygense was synthesised by Genscript (Piscataway, NJ, USA) and was 'codon optimised' for overexpression in mammalian cells. The gene was sub-cloned into the pAcGHLT-A GST baculovirus transfer vector (BD Biosciences) as an NdeI - EcoRI fragment for overexpression in insect cells using the following forward and reverse primers: 5'-GGC ATA TGC ATG GAC AGC AGC GTG ATC CAG CGG AAG-3'; 5'-CCC GAA TTC CTA CCG GCT GAT CAG GTT GCT G-3'.

Nucleotide C was inserted between the restriction sites and the gene specific region to ensure the expressed protein was in frame. Amplification conditions were 98°C for 30 s, 30 cycles of 98°C for 10 s and 72°C for 45 s followed by a final polymerization step of 72°C for 10 min. PCRs were carried out in a Techne PHC-2 thermal cycler using Phusion High Fidelity DNA polymerase (Fynnzymes). The purified PCR product and pre-treated vector were self-ligated with QuickLigation Kit (New England BioLabs) and used for transformation in XL10-Gold Ultracompetent *Escherichia coli* cells (Agilent). Successful transformants were isolated and submitted for DNA sequencing by MWG Eurofins. The maintenance of plasmid DNA stocks were carried out as described in the previous section.

#### *2.2.1.3. Saccharomyces cerevisiae Kynurenine 3-monooxygenase for expression in E. coli*

Synthetic kynurenine 3-monooxygenase gene (BNA4 UniProtKB accession number P38169**)** from *Saccharomyces cerevisiae* was 'codon optimised' for overexpression in *E. coli by* Genscript. The gene was excised from the vector using NdeI and Xba I restriction enzymes and sub-cloned into pET15b (Merck) and pET24b (Merck) vectors pre-digested with the same restriction enzymes, for expression of recombinant KMO with N- and C-terminal $His_6$-tags, respectively. The gene fragment and pre-treated vectors were self-ligated with QuickLigation Kit (New England BioLabs) and used for transformation into XL10-Gold ultracompetent *Escherichia coli* cells (Agilent).

Successful transformants were isolated and submitted for DNA sequencing by MWG Eurofins.

*Sc*KMO deletion mutants (named so that the last residue before the truncation is indicated) and single amino acid changes (named ΔKMO394, ΔKMO394-R83A and ΔKMO394-R83M) were generated using the Stratagene Quickchange site-directed mutagenesis kit. Forward and reverse primers are shown in **Table 2.2.** Amplification conditions were 95°C for 30 s, 16 cycles of 95°C for 30 s and 55°C for 1 min and 68°C for 7 min. PCR products were incubated for 1 hour to digest the methylated template DNA and transformed into XL1-Blue supercompetent cells (Stratagene). Successful transformants were isolated and submitted for DNA sequencing by MWG Eurofins to verify the presence of the desired mutations. The maintenance of plasmid DNA stocks were carried out as described in Section 2.2.1.2.

**Table 2.2. *Sc*KMO deletion and single amino acid changes mutants were cloned into pet15b vector for overexpression *E.coli.***

| BNA4 constructs | Sense primer | Anti-sense primer |
|---|---|---|
| **ΔKMO394** | 5'- C AAA AAA CTG GAC GCT **TAG** CTG TTC AGT ATC ATC -3' | 5'-GAT GAT ACT GAA CAG **CTA** AGC GTC CAG TTT TTT G- 3' |
| **ΔKMO394-R83A** | 5'-G ATC CCG ATG AAA GGC GCT ATG ATC CAC GAT CTG-3' | 5'-CAG ATC GTG GAT CAT AGC GCC TTT CAT CGG GAT C-3' |
| **ΔKMO394-R83M** | 5'-C ATG ATC CCG ATG AAC ATG ATG ATC CAC GAT CTG AAA G-3' | 5'-C TTT CAG ATC GTG GAT CAT CAT GCC TTT CAT CGG GAT CAT G-3' |

The letters in bold in the forward and reverse primers indicate an engineered stop codon for the deletion mutant ΔKMO394. Mutated nucleotides to change amino acid are underlined in the forward and reverse primers

### 2.2.2. Agarose Gel Electrophoresis

Agarose gels (1 %) were used to visualise and separate DNA, specifically PCR products, digested fragments and vectors. 1 % (w/v) agarose was resuspended in 1 x TAE buffer and heated until the agarose was dissolved, followed by addition of 1.2 μg/mL ethidium bromide. The mixture was finally poured into a gel cast and allowed to solidify. DNA samples were mixed with 6 x loading dye (Fermentas) in volumes depending on the concentration of DNA. Samples were loaded into the wells along with 1 kb DNA ladder

(Fermentas) and the gels were run with a Sub-Cell GT system (BioRad) at 80 V for 40 min or until the loading dyes were clearly separated. The gels were visualised using a GENE FLASH Syngene Bio Imaging system and the gel was photographed using a Computar H6Z0812 lens attached to a Sony UP-895MD printer.

## 2.2.3. Protein Expression

### *2.2.3.1. Expression in Pichia Pastoris*

Large-scale preparation of DNA from XL10-Gold ultracompetent *Escherichia coli* cells were performed using the QIAprep Spin Maxiprep Kit (Qiagen) to obtain 10 μg of the relevant constructs and linearised overnight with the restriction enzyme PmeI (New England BioLabs). *Pichia pastoris* strain SMD1168H (Invitrogen) was transformed with the linearised construct by electroporation, according to the Invitrogen protocol (Catalog no. V190–20), and grown on YPDS agar plates (1 % yeast extract, 2 % peptone, 1 M sorbitol, 2 % Agar and 2 % glucose) containing 100 μg/ml zeocin for 3-4 days at 30ºC or until colonies were formed. Positive integrants were selected in a zeocin dose-dependence and used for preliminary expression trials. Glycerol stocks from each transformant containing the plasmid of interest were maintained for long-term storage.

Expression trials were carried out to find optimal protein expression conditions. Ideal conditions were chosen based on immunodetection of soluble protein using the KMO polyclonal rabbit antibody (Proteintech). Cells were grown in Buffered Glycerol complex Medium - BMGY (1 % yeast extract, 2 % peptone, 1 M potassium phosphate pH 6.0, 10 % Glycerol 0.002 % Biotin and 13.4 % ammonium sulphate without amino acids) for 18-20 hours at 30ºC to generate a high number of cells before harvesting. The cells were resuspended in Buffered Methanol Complex Medium - BMMY (the same components as BMGY with the exception that the glycerol was replaced by 0.5 % Methanol) for protein production and grown under the same conditions for a further 24 hours in 2 L baffled flasks. Cells were harvest by centrifugation and the cell pellet stored at -20ºC.

#### *2.2.3.2. Expression in Insect cells*

Baculovirus transfer vector pAcGHLTA:KMO was co-transfected into High-Five ($Hi_5$) cells cultured in Express five SFM media (Invitrogen) along with linearised baculovirus DNA (Oxford expression technologies - cathepsin deleted strain) and the recombinant virus generated was amplified to a high titre stock in $Hi_5$ cells. Test expressions were carried out by varying the virus concentration (MOI – multiplicity of infection) and times of incubations. After incubation, the plates were processed to generate samples for SDS-PAGE, small-scale glutathione sepharose purification and Western blotting.

10L Cellbag- disposable bioreactors (GE Healthcare) were used to scale up for insect cell infection. The Cellbag was filled with 0.5 L of Express five SFM media followed by inoculum in order to give a starting cell count of approximately 0.5-0.6 x $10^6$ cells/mL. The Wave bioreactor system (GE Healthcare) was set at 28ºC, rocking speed of 16 rpm and an angle of 7º. After 2-3 days, or when the cell density reached 4 x $10^6$ cells/mL, 2.5 L of fresh media was added and the process was repeated again for 2-3 more days to reach the same cell density. 2.5 L of media was added to bring the total to 5 L, together with the concentrated virus. The speed was increased to 28 rpm and the angle to 9º and the culture was kept for 3-4 days after adding the virus to the cells. The cells were then harvested at 3.000 rpm for 10 min, the pellets were snap frozen and kept at -80ºC. The stock virus was maintained for 1 month at 4ºC and re-amplified after that period.

#### *2.2.3.3. Expression in Escherichia coli*

The relevant *Sc*KMO constructs were expressed in *E. coli* BL21(DE3) (Merck) under control of the T7 RNA polymerase promoter in pET15b and pET24b vectors. Transformed cells were grown in Lisogeny Broth (LB) media (Fermentas) with appropriate antibiotics overnight at 37ºC and used for the inoculum of 10 L of LB medium, which was divided into 750 mL cultures in 2 L conical flasks. Cultures were grown at 37ºC to an optical density at 600 nm of ~0.3 and the temperature was reduced to 27ºC. Cells were induced by the addition of 0.1 mM isopropyl β-D-thiogalactopyranoside (IPTG) and grown (16-20 h) at 27ºC before being harvested by centrifugation and stored

at -20ºC. Expression host strain BL21(DE3) and plasmid maintenance strains XL-1 Blue and Novablue were maintained on LB Agar plates at 4ºC for short term stocks.

## 2.2.4. Protein Purification

### *2.2.4.1. Human full-length and truncated kynurenine 3-monooxygenase expressed in P. pastoris*

Cell pellet from was thawed at room temperature and resuspended in buffer A (20 mM potassium phosphate buffer pH 7.5, 10 % glycerol, 300 mM NaCl and 50 μM FAD) containing protease inhibitors. Cells were lysed by sonication on ice (20 s bursts at 40 % amplitude on a Bandelin Sonopolus instrument, with 40 seconds time between pulses for 20 minutes). Cell debris was removed by centrifugation at 18.000rpm for 30 min.

Soluble lysate was loaded onto a 5 mL HisTrap FF Ni Sepharose 6 Fast Flow column (GE Healthcare) pre-equilibrated with buffer A. Protein was eluted with a 50-250 mM imidazole linear gradient. Yellow fractions containing partially purified KMO were pooled and diluted 10 times in buffer B (20mM phosphate buffer pH 7.5, 10 % glycerol, 7 mM 2−mercaptoethanol) to reduce the salt and imidazole concentrations.

Protein was subsequently loaded onto a 10 mL Blue Sepharose 6 fast flow column (GE Healthcare) equilibrated with buffer B. The protein was eluted using a linear gradient to 2.5 M NaCl prepared in buffer B. Fractions containing *Hs*KMO were pooled and diluted 10-fold in buffer B to reduce the NaCl concentration. Protein was concentrated and chromatographed using a Superdex 200 10/300 GL (GE Healthcare) equilibrated with buffer C (50mM BisTris pH 6.5, 150 mM NaCl, 4 mM DTT). Pure fractions were collected and stored at -80ºC. The purity of the final fractions were analysed by SDS-PAGE and samples for crystallogenesis were concentrated to 12 mg/mL.

#### *2.2.4.2. Human full length kynurenine 3-monooxygenase expressed in insect cells*

Cell pellet was thawed at room temperature and resuspended in buffer A (20 mM potassium phosphate buffer pH 7.5, 10 % glycerol, 150 mM NaCl, 7 mM 2-mercaptoethanol, 50 μM FAD, supplemented with protease inhibitors PMSF (Sigma-Aldrich). Different detergents were tested to solubilise KMO. Cells were lysed by sonication on ice (10 seconds bursts at 20 % amplitude on a Bandelin Sonopolus instrument, with 1 minute time between pulses for 5 minutes) and cell debris was removed by centrifugation at 15.000 rpm for 30 min.

The effect of a number of various detergents, which have previously been successful in producing crystals of membrane proteins (**Table 2.3**), were investigated in the extraction and purification of *Hs*KMO. The amount of detergent used during extraction and purification procedures was chosen based on the critical micelle concentration (CMC) for each detergent. In general, a detergent must be used at concentrations above its CMC in order to act as an effective solubiliser [223]. Dot-blot analysis with human anti-KMO antibody of *Hs*KMO soluble lysate was performed using the detergents stated in Table 2.3. This technique differs from the Western blot because the protein samples are not separated electrophoretically. The samples were applied directly on a membrane (as a dot) and were detected with anti-KMO antibody.

**Table 2.3. Selection of detergents used to solubilise human kynurenine 3-monooxygenase.**

| **Detergent name** | **CMC (mM)** [224, 223] |
|---|---|
| **Triton X-100** | 0.17-0.3 |
| **CHAPS** | 8 |
| **Fos-choline 12** | 1.5 |
| **n-Dodecyl–β-maltoside(DDM)** | 0.17 |
| **LDAO** | 1.7-2.2 |
| **n-octyl-β-D-glucoside** | 25 |

Soluble lysate was incubated in a batch for 3 hours with 3 mL pre-equilibrated glutathione uniflow resin (Clontech). The resin was then packed and washed with buffer B. 0.5 mL fractions were eluted with buffer C (buffer B + 33 mM glutathione) and fractions containing GST-KMO were pooled, concentrated and loaded onto a Superdex 200 (10/30) size exclusion chromatography column (GE Healthcare) equilibrated with buffer D (20 mM Hepes pH 7.5, 5 % glycerol, 150 mM NaCl, 7 mM 2-mercaptoethanol, 50 μM FAD and 0.012 % DDM). The GST part of the fusion protein was cleaved from *Hs*KMO by overnight incubation and gentle shaking with thrombin (1 unit/100 μg of protein) before size exclusion chromatography. Pure GST-*Hs*KMO or cleaved *Hs*KMO were pooled and stored at -80ºC. The purity of final fractions were analysed by SDS-PAGE.

#### *2.2.4.3. Saccharomyces cereviseae kynurenine 3-monooxygenase expressed in E.coli*

The protocol described in Section 2.2.4.1 was followed to purify *Sc*KMO. Protein was concentrated and passed down a Superdex 200 10/300 GL (GE Healthcare) equilibrated with buffer C (25 mM Amonium Acetate pH 7.0, 150 mM NaCl, 7 mM 2-mercaptoethanol). Pure fractions were collected and stored at -80ºC. Samples for crystallogenesis were concentrated to 14 mg/mL. The His-tag was cleaved from *Sc*KMO by overnight incubation with thrombin (1 unit/1 mg of protein) with gentle shaking before loading onto the 10 mL Blue Sepharose 6 fast flow column.

### 2.2.5. SDS-PAGE and Gel staining

For protein purification analysis, the RunBlue (Expedeon) electrophoresis system (Invitrogen) with 12 % RunBlue pre-cast gels was used at 180 V for 45 min. Broad range prestained protein marker between 7-175 kDa (P7708V, New England BioLabs) was used in each run. Otherwise, SDS-polyacrylamide gels were made with 5 % and 12.5 % polyacrylamide for resolving and stacking gels respectively. Gels were run in a Mini-

Protean III gel system (BioRad) at 180 V for 1 hour. Gels were stained with Comassie stain InstantBlue (Expedeon).

### 2.2.6. Protein identification – MALDI and Western Blotting

Purified proteins were identified by trypsin-digest and MALDI-TOF peptide identification using the software Mascot (Matrix Science). The results were first matched against a set of sequences limited to the sample species using the Uniprot database and also against the generic database SwissProt to identify any contaminants within the sample. This technique was carried out in the Protein Mass Spectrometry Core Facility (University of Manchester) by Dr. Emma Jayne Keevil.

Expressed and purified proteins were also identified by Western Blotting, using either His-tag monoclonal (Invitrogen) or rabbit KMO polyclonal (Proteintech) primary antibodies. PVDF membranes were used and proteins from the SDS-PAGE gel were transferred to the membrane in a XCell IITM Blot Module (Invitrogen) at 30 V for 1 hour and then processed according to the WesternBreeze chemiluminescent imunodetection kit (Invitrogen) protocol. After blotting, membranes were washed 2 times with water for 5 min, incubated with the blocking solution (Invitrogen) for 30 min followed by 1 hour incubation with the primary antibody solution. At that point, the membranes were washed with antibody washing solution and incubated with the appropriate secondary antibody (anti-mouse or anti-rabbit depending on the primary antibody used) for 30 min followed by a final wash with washing solution. Finally, the membranes were washed with water and incubated with chemiluminiscent substrate solution for 5 min. The PVDF membrane was exposed to an X-ray film (X-OMAT AR, KODAC) for 30 seconds to 2 minutes in a dark room and scanned using the X-ray film processor (Minimedical -90, ImageWorks).

### 2.2.7. UV/visible spectroscopy

UV/Visible absorption spectra were recorded on a Cary UV-50 Bio UV/Visible scanning spectrophotometer (Agilent Technologies) using 1 cm path length quartz cells. Assuming a single binding site of FAD per KMO active site, the protein concentration

was estimated based on the extension coefficient for free FAD at the wavelength maximum for the isoalloxazine ring of the flavin at 450 nm (11,300 $M^{-1}$ $cm^{-1}$).

The dependence of the observed rate constant for reduction of KMO on the concentration of NADPH were conducted spectroscopically by mixing anaerobically 20 μM KMO with 500 μM of L-KYN and different concentrations of NADPH (10μM – 20mM) and monitoring the absorbance changes of the FAD at 450 nm to get an apparent rate constant depending on the concentration of NADPH.

### 2.2.8. Kinetic Analysis

Steady-state kinetic parameters for KMO were obtained by initial rate measurements of enzyme activity. KMO catalyses the NADPH-dependent hydroxylation of L-kynurenine to 3-hydroxykynurenine and the enzymatic reaction can be monitored by following the decrease in absorbance of NADPH at 340 nm. Activity assays were carried using a 1 cm path length quartz microcuvette (Starna Scientific) at 37ºC for *Hs*KMO and 30ºC for *Sc*KMO. 0.2 - 1 μM of pure enzyme was added to 200 μl reaction buffer (20 mM potassium phosphate pH 8.0-8.5, 7 mM 2-mercaptoethanol) containing different concentrations of NADPH and L-kynurenine (Sigma-Aldrich) and the time-dependent absorbance change at 340 nm was recorded using a UV-vis Cary 50 spectrophotometer (Agilent Technologies). Assays at each reaction condition were performed in triplicate. Apparent Michaelis constants, $K_m$, for L-kynurenine and NADPH were determined by varying the concentration of the first substrate at a constant concentration of the second substrate and *vice versa*. Reaction data were fitted to the standard Michaelis-Menten equation using Origin Software (OriginLab, Northampton, MA).

$$\upsilon = \frac{k_{cat}\,[S]}{K_m + [S]} \qquad (1)$$

where $\upsilon$ is the reaction rate, $k_{cat}$ the maximum turnover rate and $K_m$ the Michaelis-Menten constant.

Assays of the pH dependence were conducted as previously described with 200 μM of L-KYN, 200 μM NADPH and 20 mM MES, 20 mM HEPES and 20 mM CAPS

buffer at varied pH. The buffer was titrated with $H_2SO_4$ and NaOH to a range of pH values (5.0-10.0). Temperature dependence and its effect on the stability of the enzyme was also studied by following the decrease in absorbance of NADPH at 340 nm using buffer at different temperatures (10-50 °C) Data for the temperature dependence was fitted to a Gaussian curve (Equation 2) and the pH profile was fitted to the two macroscopic p$K_a$ value equation (Equation 3).

$$k_{obs} = \frac{1}{\sigma\sqrt{2\pi}} e^{\frac{-(T-\mu)^2}{2\sigma^2}} \quad (2)$$

where μ is the mean of the distribution and σ is the standard deviation.

$$k_{obs} = A_{max}\left(1 - \frac{1}{1+10^{(pKa-pH)}}\right) * \left(\frac{1}{1+10^{(pKb-pH)}}\right) \quad (3)$$

where $A_{max}$ is the maximum enzyme activity, $pK_a$ and $pK_b$ the negative log of the acid and base dissociation constants.

### 2.2.9. Product Analysis by HPLC

Kinetic analysis was alternatively monitored by following the formation of the product 3 hydroxykynurenine by $C_{18}$ reversed-phase HPLC. 0.2 - 1 μM of pure enzyme was incubated in 200 μl reaction buffer (20 mM potassium phosphate pH 8.0-8.5, 7 mM 2-mercaptoethanol) containing different concentrations of NADPH and L-kynurenine KMO inhibition by the potential KMO drug UPF 648 (supplied by Dr. Flaviano Giorgini, University of Leicester) was also measured by product analysis quantification. Enzyme (100nM) was incubated at 30-37ºC in 1 mL reaction buffer (20 mM potassium phosphate buffer pH 8.5, 7 mM 2-mercaptoethanol) containing 2 mM NADPH, 500 μM L-KYN and different concentrations (0-2μM) of the inhibitor UPF 468. The reaction was stopped with 8 % trifluoracetic acid at different time points during the assay. Precipitated protein was removed by centrifugation and the supernatant was analysed by $C_{18}$ reversed-phase HPLC equilibrated with 50 mM ammonium acetate, pH 3.0, containing 1 % methanol and 0.1 % heptanesulfonic acid; elution from the column was with 50 mM ammonium acetate, pH

4.5, containing 5 % methanol and 0.5 % heptanesulfonic acid, and monitored at 229 nm. 3-hydroxykynurenine was quantified by comparison with a 3-hydroxykynurenine calibration curve. Each experiment was performed in triplicate. The data was fitted to the Morrison equation (Equation 4):

$$\frac{v_0}{v_i} = 1 - \frac{([E]+[I]+K_i) - \sqrt{([E]+[I]+K_i)^2 - 4[E][I]}}{2[E]} \quad (4)$$

where $\upsilon_0$ is the enzyme activity without inhibitor, $\upsilon_i$ is the enzyme activity ligand concentration I, [E] is the enzyme concentration, [I] is the inhibitor concentration and $K_i$ is the inhibition constant.

### 2.2.10. Fluorescence spectroscopy

Fluorescence emission measurements were performed using a Cary Eclipse Fluorimeter (Agilent Technologies) in order to determine dissociation constants ($K_d$) for KMO / inhibitors by ligand perturbation of the flavin fluorescence. The exciting light was provided from a xenon light source and excitation and emission slit widths were 5 nm. Fluorescence emission spectra were recorded from 470 to 700 nm using an excitation wavelength of 450 nm. The perturbation in FAD fluorescence was monitored at 520 nm upon titration of L-kyn and UPF 648 into 5 μM KMO (20 mM KPi pH 8, 50 mM NaCl and 7 mM 2-mercaptoethanol) at 25ºC. $K_d$ values were calculated by fitting plots of the relative difference in emission between KMO-ligand complex and free KMO at 520 nm *versus* the ligand concentration to equation 5 This equation is a variation of the Morrison equation (Equation 2) and is used for tight binding ligands or when $K_d$ values are similar in magnitude to the concentration of enzyme used, in which case substantial amounts of both enzyme (E) and ligand (S) are consumed in the ES complex as the titration progresses. All data fitting was done using Origin software (*OriginLab, Northampton, MA*).

$$\frac{E_{obs}}{E_{max}} = 1 - \frac{([E]+X+K_d)-\sqrt{([E]+X+K_d)^2-4[E]X}}{2[E]} \quad (5)$$

where $E_{obs}$ represents the fluorescence emission difference at each ligand titration $X$, $E_{max}$ the maximal emission change at saturating ligand concentrations, [$E$] the enzyme concentration, $K_d$ the dissociation constant for the ligand bound to the protein.

### 2.2.11. Stopped-Flow Spectroscopy

The kinetics of the reductive and oxidative half reactions of KMO was monitored separately using an Applied Photophysics SX18 MVR stopped-flow spectrophotometer in an anaerobic glove box (Belle Technology) to maintain oxygen levels below 2 ppm. Multiple wavelength data were collected using a photodiode array (PDA) detector and single wavelength data were recorded using a photomultiplier tube detector.

The reductive half-reaction was initiated by anerobically mixing the oxidised enzyme with NADPH at 15ºC. One syringe of the stopped-flow apparatus was filled with 20 μM anaerobic enzyme in 20 mM potassium phosphate buffer pH 8.0, 50 mM NaCl and 7 mM 2-mercaptoethanol and the other syringe with different concentrations of anerobic NADPH (10 μM - 20 mM). All experiments were carried out with anaerobic buffer saturated by extensive bubbling with $N_2$ gas. After mixing both solutions in the stopped-flow apparatus, the absorbance decrease at 450 nm was used to measure the reduction of the flavin cofactor. All measurements were repeated at least 3 times, and transients were analysed by fitting to a standard single or double-exponential functions using Spectra kinetics software (Applied Photophysics), to generate apparent rate constants ($k_{obs}$). The same experiments were conducted with saturated concentration of L-KYN and KMO inhibitor UPF 648 in order to compare reduction rate constants with the free enzyme.

The concentration dependence of $k_{obs}$ was analysed by fitting to equation 6 to obtain values for the apparent dissociation constant ($K_d$) for the enzyme-substrate complex:

$$k_{obs} = \frac{k_{max}[S]}{K_d+[S]} \quad (6)$$

where $k_{obs}$ is the observed rate constant at each NADPH concentration and $k_{max}$ is the maximum rate constant as [NADPH] approaches infinity.

The oxidative half-reaction of KMO was studied by mixing the reduced enzyme-substrate complex or free enzyme with molecular oxygen in the stopped-flow spectrophotometer. 20 μM anaerobic enzyme in 20 mM potassium phosphate buffer pH 8.0, 50 mM NaCl and 7 mM 2-mercaptoethanol was reduced by titration with a solution of anaerobic sodium dithionite. One syringe was then filled with the reduced enzyme in complex with saturating concentrations of L-kynurenine and the other syringe with air-saturated buffer and the oxidative half-reaction was monitored at 450 nm. The dependence of the oxidation rate on $O_2$ concentration was determined by mixing the reduced KMO sample with 20 mM potassium phosphate buffer pH 8.0, 50 mM NaCl and 7 mM 2-mercaptoethanol containing varying concentrations of $O_2$ (0-1.3 mM from a 1.3 mM $O_2$-saturated stock solution) in the stopped-flow instrument. The oxygen-saturated buffer was prepared by bubbling dioxygen gas through the buffer solution for 10 minutes.All measurements were repeated at least 3 times, and transients were analysed by fitting to a standard single or double-exponential functions to generate apparent rate constants ($k_{obs}$).

### 2.2.12. Thermofluor Assay

A variety of buffers and additives were investigated using the Thermofluor Assay technique in order to maximise protein stability and assist in the protein crystallisation. Experiments were performed using a Bio-Rad CFX96 real-time system C100 thermal cycler (BioRad Laboratories). Measurements were performed using excitation and emission wavelengths of 490 and 575 nm, respectively. Unfolding curves were generated using a temperature gradient from 15 to 95°C, by performing a fluorescence measurement every 0.2°C. Fluorescence was measured and plotted against temperature in order to determine the melting temperature ($T_m$), which is calculated in the Thermofluor software *T*m based on the minimum inverted first derivative curve.

Solutions of 7.5 μl of 300 $_X$ Sypro Orange (Molecular Probes), 12.5 μl of 2 $_X$ test compound buffer (Jena Bioscience) – see Table 2.4A for components of JBS solubility

kit) and 2.5 µl of 10 mg/ml protein were mixed directly into the wells of a 96-well thin-wall PCR plate (Bio-Rad Laboratories). Control samples were run alongside. The optimal buffer conditions were selected based on the $T_m$ calculated and used for further screening using the additive kit from JBS solubility kit, shown in Table 2.4B.

**Table 2.4. JBS Solubility Kit. A - Buffer kit (100 mM), B: Additive kit.**

**A**

| *Nº* | *Buffer* | *pH* |
|---|---|---|
| **1** | Glycine | 3.0 |
| **2** | Citric Acid | 3.2 |
| **3** | PIPPS | 3.7 |
| **4** | Citric Acid | 4.0 |
| **5** | Sodium Acetate | 4.5 |
| **6** | Sodium/ Potassium Phosphate | 5.0 |
| **7** | Sodium Citrate | 5.5 |
| **8** | Sodium/Potassium Phosphate | 6.0 |
| **9** | Bis-Tris | 6.0 |
| **10** | MES | 6.2 |
| **11** | ADA | 6.5 |
| **12** | Bis-Tris Propane | 6.5 |
| **13** | Ammonium Acetate | 7.0 |
| **14** | MOPS | 7.0 |
| **15** | Sodium/Potassium Phosphate | 7.0 |
| **16** | HEPES | 7.5 |
| **17** | Tris | 7.5 |
| **18** | EPPS | 8.0 |
| **19** | Imidazole | 8.0 |
| **20** | Bicine | 8.5 |
| **21** | Tris | 8.5 |
| **22** | CHES | 9.0 |
| **23** | CHES | 9.5 |
| **24** | CAPS | 10 |

**B**

| Nº | Additive | Concentration of stock solution |
|---|---|---|
| **1** | Sodium Chloride | 80 mM |
| **2** | Sodium Chloride | 200 mM |
| **3** | Sodium Chloride | 400 mM |
| **4** | Glycerol | 20% |
| **5** | Glycerol | 40% |
| **6** | CHAPS | 8mM |
| **7** | Octyl Glucopyranoside | 0.4% |
| **8** | Octyl Glucopyranoside | 4% |
| **9** | Dodecyl Gluocoside | 0.4% |
| **10** | Dodecyl Gluocoside | 4% |
| **11** | BME | 40 mM |
| **12** | DTT | 4 mM |
| **13** | DTT | 20 mM |
| **14** | TCEP | 120 mM |

## 2.2.13. MultiAngle Laser Light Scattering (MALLS)

Pure samples of KMO (250 μL of 2 mg/mL) in 20 mM potassium phosphate buffer pH 7.5 300 mM NaCl, 7 mM 2-mercaptoethanol were applied to a Superdex 200 gel filtration column (GE Healthcare) at a flow rate of 0.71 mL/min. Eluted samples were passed through a DAWN-EOS MALLS spectrometer (Wyatt Technology corp.) detector with an Optilab rEX refractometer (Wyatt Technologies) and a quasi-elastic light scattering (QELS) detector (Wyatt) to measure the refractive index and the hydrodynamic radius ($R_h$) values, respectively. Data were collected at a 1 second interval rate using a K5 cell type and a laser wavelength of 690 nm. The average molecular weight ($M_r$) of the sample was calculated using the software ASTRA v5.21 (Wyatt Technology Corporation) based on the light scattering intensity and eluant refractive index. MALLS experiments were performed by Mrs. Marjorie Howard at the Biomolecular Interactions Facility in University of Manchester.

## 2.2.14. Structure Determination

### *2.2.14.1. Crystallisation*

Initial crystallisation trials were conducted using the commercial screens JCSGI and II (Qiagen), Clear Strategy I and II, PACT Premier and Morpheus (Molecular Dimensions) using 96-well crystallography trays. Pure proteins for crystallogenesis were passed through a Superdex 200 10/300 GL (GE Healthcare) gel filtration column to exchange the protein to the optimal buffer according to the conditions obtained in the Thermofluor Assays. The protein was concentrated and made up to 10-15 mg/mL. 200nL KMO protein or protein-ligand samples were added 1:1 to mother liquor from screens using a Phenix Crystal protein dispenser (Art robbins Instrument) to form sitting drops. Prior to setting the trays the protein was pre-incubated with ligands for ~30 minutes. Ligand concentrations equal to the protein concentration plus an amount equal to 10 x the dissociation constant were used to assure saturation. Protein conditions that were conducive for crystal growth were selected for further optimisation and potentially

successful buffer conditions were reproduced in 96-well manual trays with minimal variations so that optimal conditions for crystal growth could be achieved.

The trays were covered with crystal clear tape (Manco® Inc.) and stored in a vibration-protecting refrigerator at 277 K over a period of ~72 h. Crystals and co-crystals were harvested with PEG 200 as a cryoprotectant and immediately flash frozen in liquid nitrogen and transported to the Diamond Synchrotron (Harwell, UK) for X-ray diffraction analysis.

#### *2.2.14.2. Diffraction data processing, Structure determination and refinement*

Diffraction data were collected from single cryofrozen crystals at Diamond, Harwell, UK and processed by Dr. Colin Levy and Professor David Leys (University of Manchester). The data were scaled and integrated using XDS[225]. The Single-wavelength Anomalous Dispersion (SAD) technique utilizing the anomalous signal from SeMet was employed for initial phase determination.

Expression of selenomethione labelled protein was achieved by inhibiting the methionine biosynthesis shortly before induction of KMO expression by adding high concentrations of isoleucine, leucine, phenylalanine, lysine and threonine to the cell culture. Transformed *E. coli* cells containing the *Saccharomyces cerevisiae* KMO expression plasmid were grown in LB media at 37ºC to late exponential phase, harvested and then re-suspended in M9 minimal media and grown until mid-log phase. At that point lysine, phenylalanine, threonine (100 mg/L each), and selenomethionine, isoleucine, leucine, and valine (50 mg/L each) were added to the culture and induced 15 min after addition of amino acids with 0.1 mM IPTG. The culture was grown for 12-16 hours. Purification of selenomethionine incorporated *Saccharomyces cerevisiae* KMO was as described for conventional *Saccharomyces cerevisiae* KMO using degassed buffers.

Initial phases were obtained from a single SAD data set collected at the selenium edge. Selenium sites were located using Phenix AutoSol[226] yielding an electron density map that could be auto traced using Phenix AutoBuild[227]. The resulting model was completed through iterative rounds of rebuilding in Coot[228] and refinement in Phenix [229]. All subsequent structures were solved by molecular replacement in Phaser [230]

using this initial SeMet derived structure as the template. Structure validation with Molprobity [231] was integrated as part of the iterative rebuild and refinement procedure.

#### *2.2.14.3. KMO-Kynureine modelling*

NAMD software [232] was used to carry out all molecular dynamics (MD) simulations of the Kynurenine-KMO complex, performed by Dr. Pierre Lafite (University of Orleans). Topology and parameters files for substrate and FAD were obtained using Antechamber program [233] using AM1-BCC charges [234]. The complex model was then immersed in a periodic water box (TIP3) and neutralized by adding $Na^+$ ions. Several cycles of minimisations (steepest descent, 10 000 steps) and MD simulations (50 K, 20 ps) were performed to equilibrate the model (backbone protein atoms were kept fixed). Then MD simulations were performed (310 K, 1 ns) at a time step of 2 ps, with the protein backbone restrained on the X-ray structure conformation. Individual snapshots were extracted and minimised to assess the KMO-kynurenine interactions.

# CHAPTER 3

# BIOCHEMICAL AND BIOPHYSICAL CHARACTERISATION OF HUMAN KYNURENINE 3-MONOOXYGENASE

# 3. BIOCHEMICAL AND BIOPHYSICAL CHARACTERISATION OF HUMAN KYNURENINE 3-MONOOXYGENASE

## 3.1. INTRODUCTION

KMO is a NADPH dependent flavoprotein monooxygenase that hydroxylates the aromatic substrate L-KYN and contains a tightly bound FAD cofactor. This hydroxylation at the third position of L-KYN produces 3-HK with the consumption of one molecule of NADPH and $O_2$ per turnover [9, 197]. A number of studies have been published on the characterisation of the activity of KMO from different organisms, in terms of substrate, coenzyme and cofactor specificity, as well as strategies for expression and purification of KMO from higher organisms, including recombinant human KMO (*Hs*KMO) [208, 207, 235]. However, as this enzyme is localised to the outer membrane of mitochondria [199, 200] it has proven to be extremely difficult to obtain sufficient quantities of KMO for structural studies and therefore, there is currently no structural information available for this enzyme. Additionally, the molecular basis of KMO inhibition by available lead compounds has remained hitherto unknown. The main goal of this chapter was to gain biochemical and structural information of human KMO for the development of novel and improved KMO inhibitors that may ultimately expedite clinical application of these compounds.

The handling of membrane-associated proteins is significantly more challenging compared to soluble proteins, specifically in terms of protein expression, purification and crystallisation. Two different approaches were used in an attempt to obtain the crystal structure of *Hs*KMO and are described in the current chapter. The first approach involved the production of truncated forms of *Hs*KMO by deleting the transmembrane regions in order to prevent membrane association, insolubility or potential incorrect folding as a result of aggregation of the C-terminal region. The second approach involved the use of different overexpression systems, such as *Pichia pastoris* and insect cells/baculovirus system, both of which were previously used successfully to express other membrane proteins. Consequently, the chapter is divided into two main sections: the first is focused

on the biochemical and biophysical characterisation of truncated forms of *Hs*KMO that has been expressed in *P. pastoris* and the second part describes the characterisation of full-length *Hs*KMO expressed in insect cell using the baculovirus system.

With the aim of gaining a better understanding of the biochemistry of *Hs*KMO, the enzyme has been characterised using a variety of spectroscopic techniques. The activity and kinetic parameters are compared with published data, specifically on the native protein. Activity assays were conducted with full-length *Hs*KMO and C-terminal deletion mutants to address the influence of this region on the activity of the enzyme. Kinetic and inhibition assays with potential KMO drugs have also been carried out to compare kinetic and inhibitor constants between recombinant KMO and KMO purified from mitochondrial preparations.

## 3.2. CHARACTERISATION OF *HS*KMO USING *PICHIA PASTORIS* AS A HOST SYSTEM

### 3.2.1. Generation of multiple expression constructs for *Hs*KMO

Analysis of the *Hs*KMO primary sequence, together with predicted secondary structures software tools and reported data [200] suggests the presence of two transmembrane helices at the C-terminus of KMO between residues 384-403 and 425-447 (Figure 3.1). From the multiple sequence alignment of *Hs*KMO with *p*-hydroxybenzoate hydroxylase (PHBH) and other flavoproteins for which there are crystal structures available (Figure 1.7), we could also identify motifs that might be involved in enzyme catalysis and ligand binding. The NADP(H) and FAD binding motifs, characteristic of flavin monooxygenases, are located throughout the protein up to residue 318, whereas the transmembrane helices in the C-terminal region are suggested to serve as a membrane anchor [10]. Together, this information supported the hypothesis that the C-terminal region would be not expected to be crucial for the activity of the *Hs*KMO enzyme. Consequently, in order to improve protein instability and insolubility, and to increase the likelihood of obtaining a crystal structure of *Hs*KMO, C-terminal deletion mutants were engineered.

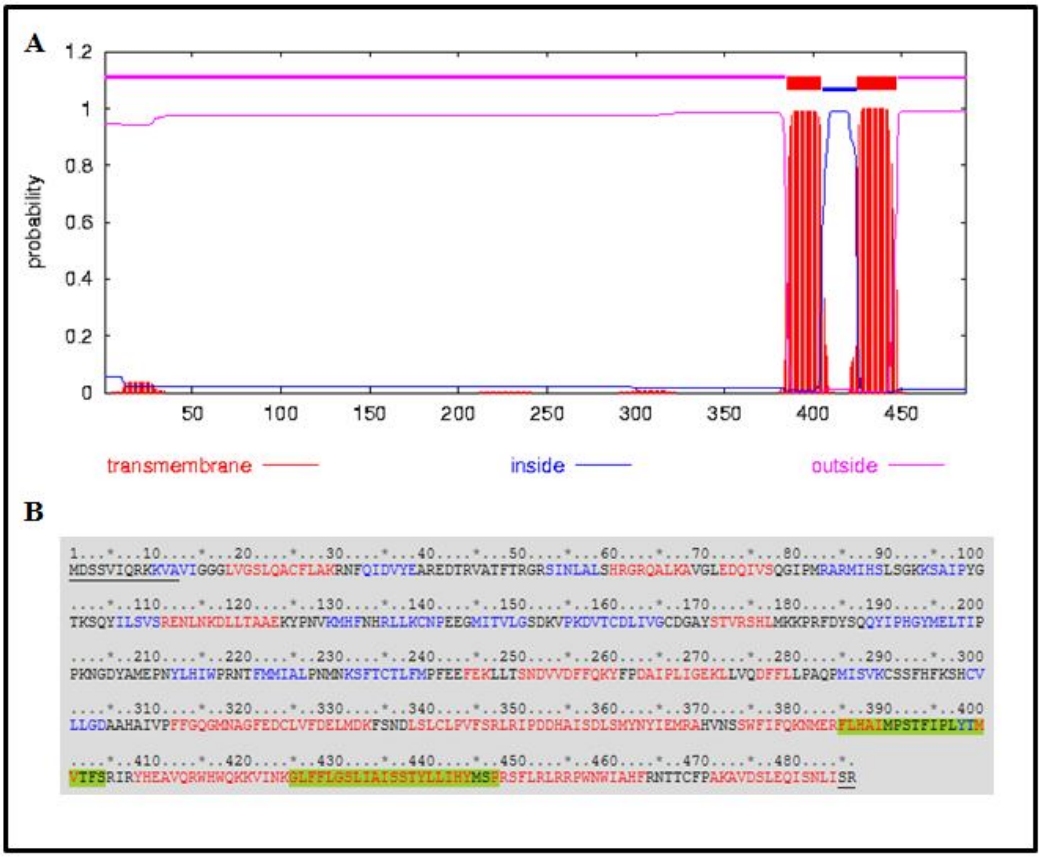


**Figure 3.1. Prediction of membrane helices in *Hs*KMO** – Panel A: The plot shows the location of the predicted transmembrane helices (between residues 384-403 and 425-447) and the most probable orientation of transmembrane helices in the sequence (by *THMM* [236]). Panel B: Prediction of secondary structures based on *Hs*KMO primary sequence. The letters coloured in black represent predicted loops, α-helices are in red and β-sheets are in blue. The letters underlined represent predicted disordered regions and residues highlighted in green are the predicted transmembrane regions (by *XtalPred* [237]).

The first truncated *Hs*KMO variant was created by deleting one putative transmembrane region, after Asp-423 (ΔKMO423) and the second truncated form was designed in order to delete both transmembrane regions (ΔKMO383) after Glu-383 (Figure 3.1). Full-length and deletion mutants were cloned into the pPICZ-B vector (*Invitrogen*) for expression of recombinant *Hs*KMO proteins in *Pichia pastoris.* The C-terminal plasmid-encoded polyhistidine (6 x His) tag, essential for downstream detection and purification, was retained in all constructs by typical cloning techniques using appropriate restriction enzymes, as the simple and direct insertion of a stop codon by site directed mutagenesis on the specific truncated sites could not be applied (see Section 2.2.1. for more details). Full-length and deletion *Hs*KMO mutants were confirmed post

minipreparation by DNA sequencing using the forward 5' AOX1 and reverse 3' AOX1 primers (Section 2.2.1.1). Transformations into *Pichia pastoris* strain SMD1168H (protease deficient strain) were conducted by electroporation and two integrants from each different construct were isolated on media containing 2 mg/mL Zeocin and selected for expression trials.

### 3.2.2. Expression and Purification of *Hs*KMO variants

Expression trials were carried out with both full-length and deletion mutants to select optimal growth conditions. Western blot analysis of whole cell extracts and soluble lysate of the *Hs*KMO variants demonstrated that neither the full-length nor the ΔKMO423 (with one predicted transmembrane region) were expressed in the *Pichia pastoris* strain SMD1168H (Figure 3.2). Several detergents such as Triton X-100, n-dodecyl β-D- maltopyranoside (DDM) and lauryldimethylamine-oxide (LDAO) were also used in the extraction of these variants, but without success. Additional *P. patoris* strains were also tested, such as X-33 and KM71H, but none were able to express these forms of *Hs*KMO. In contrast, the expression of ΔKMO383 (without any predicted transmembrane regions) resulted in soluble protein. These results appear to confirm the presence of transmembrane helices in the *Hs*KMO enzyme between residues 383 and 460.

In order to analyse the expression levels and the optimal time post-induction before harvesting cells, different time courses were tested. Cultures were supplemented with absolute methanol every 24 hours to a final concentration of 0.5 % (v/v) and induction maintained for a total period of 72 hours. It was found that ΔKMO383 production decreased with prolonged induction times and a maximal expression level was achieved after an induction period of 24 hours (Figure 3.2). As temperature may also affect recombinant protein production at high cell densities, the effect of this parameter was also assessed, ranging from 20ºC to 30ºC. Although the usual optimum temperature for protein production in *P. pastoris* is at 30°C, it was found that for ΔKMO383 the optimal expression levels occurred at 25ºC, possibly due to an improvement in the protein folding and solubility. The experiments shown henceforth will just refer to this form of the *Hs*KMO protein.

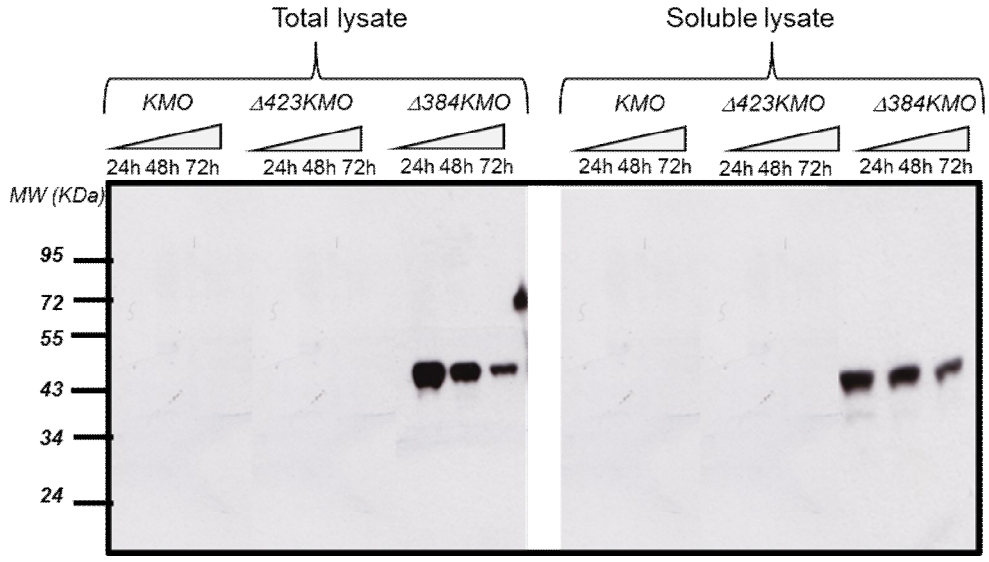


**Figure 3.2. Expression trials of *Hs*KMO proteins.** Western blot analysis of whole cells and soluble lysate of the three *Hs*KMO variants with anti-KMO antibody at different induction periods. The cultures were grown at 25ºC and supplemented with methanol to 0.5% (v/v) every 24 hours for a total incubation period of 72 hours.

As purification strategies have not previously been established or optimised for recombinant *Hs*KMO expressed in *P. pastoris*, numerous purification methodologies have been tested throughout this project, including anion (Mono Q and DE-52 columns), cation exchange (Mono S), affinity (nickel and Blue Sepharose) and size exclusion (gel filtration columns) chromatography techniques. The optimal protocol to obtain pure ΔKMO383 is described in Section 2.2.4.1. Briefly, ΔKMO383 was purified using a three step purification protocol that involves nickel affinity, Blue Sepharose and size exclusion chromatography. Ni-affinity chromatography is the logical choice as a first purification step as the expression vector contained a hexa-His tag at the C- terminus. The Blue Sepharose contains a synthetic polycyclic dye called Cibacron Blue F3G-A, which is structurally similar to cofactors, such as $NAD^+$ and therefore, certain enzymes that require adenylyl-containing cofactors tend to bind strongly to this resin. The protein is highly pure after these two steps and hence, the last step was mainly used to exchange the protein into an optimal buffer for crystallogenesis (optimal buffers are described in Section 3.2.5). Figure 3.3 shows an SDS-PAGE gel of the purity of ΔKMO383 after each purification step. The apparent molecular mass of ΔKMO383 is ~47 kDa, consistent with

the predicted mass from the amino acid sequence of 45 kDa, including the C-terminal hexa-histidine tag region.

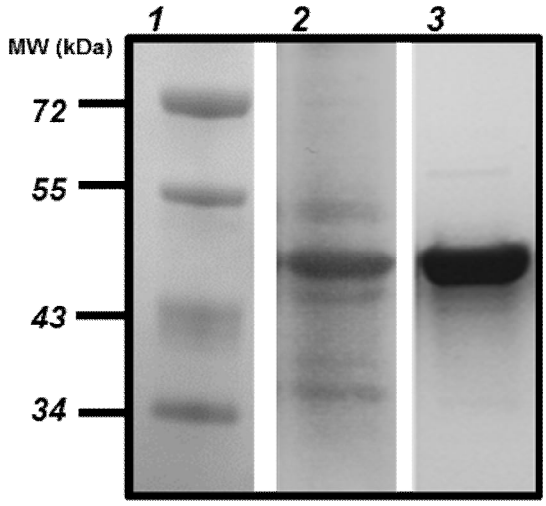


**Figure 3.3. SDS-PAGE analysis of ΔKMO383 purity after each purification step.** Lane 1: Protein Marker, Lane 2: post Nickel, Lane 3: post Blue Sepharose.

ΔKMO383 loses part of the FAD cofactor during purification suggesting that it might not be covalently-bound, as previously reported for other flavin monooxygenases [238]. Additionally, previous studies on the PHBH enzyme suggest it adopts different configurations during the catalytic reaction, and in one of these configurations the flavin is significantly more solvent exposed and therefore susceptible to escape from the active site [190]. Further details on this hypothesis will be discussed in Chapter 5. Free FAD (approximately 10 μM) was included in the purification buffers in order to retain the flavin in the enzyme throughout protein purification.

Despite the optimisation conditions, in terms of strains, time after induction and temperature, the expression yields were rather low (2-3 mg/L of culture). For future studies it might be useful to consider heterologous secretion of the recombinant protein in *P. pastoris* instead of intracellular expression. The vectors pPICZα (A,B and C) contain the α-factor secretion signal for directing secreted expression of the recombinant protein, and this may be more efficient in terms of protein extraction and purification as there are fewer protein contaminants and less protease activity. Another possible explanation for the low expression yields is that the KMO gene used in the current experiments was codon optimised for expression in higher eukaryotic cells, which have a different codon

usage when compared to *P. pastoris*, specifically in the G + C content level, which is lower (42.73%) compared to mammalian codons (52.27%) [239]. The Kasuza database provides more information regarding codon usage frequencies in different organisms [239]. The use of fermenters instead of shaker-flasks might increase the expression yields as they optimise nutrient feeding and oxygen supplementation [240, 241].

### 3.2.3. Spectral Features of ΔKMO383

The spectrum of ΔKMO383 is typical of a flavoprotein with absorbance maxima at 375 and 450 nm (Figure 3.4). Although the spectrum is very similar to that of free flavin in aqueous solution there is a resolved shoulder at ~460 nm, which indicates a perturbation in flavin cofactor (FAD) absorbance properties through binding in the protein environment. Direct reduction of the non-covalently bound FAD cofactor with sodium dithionite from the fully oxidised ΔKMO383, is demonstrated in Figure 3.5, as shown by the decrease in the visible absorption peaks.

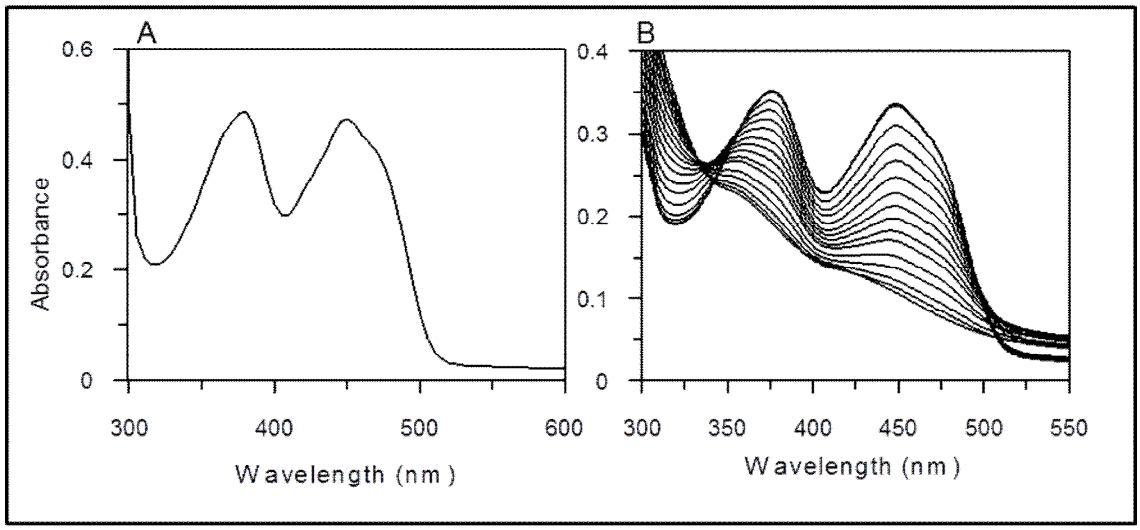


**Figure 3.4. UV-visible absorbance spectrum of purified recombinant human ΔKMO383 and anaerobic reductive titration of ΔKMO383 with sodium dithionite.** *Panel A:* The UV/visible absorption spectra were recorded at room temperature using a solution of 45 μM ΔKMO383 in buffer containing 20 mM phosphate buffer pH 7.5, 10 % glycerol, 7 mM β-mercaptoethanol. *Panel B:* The UV/visible absorption spectra were recorded at room temperature using a solution of 30 μM ΔKMO383. Titration of sodium dithionite was performed until the enzyme was fully reduced.

### 3.2.4. Kinetic and Ligand Binding studies

The initial catalytic assays were performed by measuring the oxidation of NADPH at 340 nm by varying the concentration of the enzyme with excess of L-KYN. In these assays the rate of NADPH oxidation would be expected to increase with increasing concentrations of the purified *Hs*KMO enzyme. However, it is clear that ΔKMO383 did not show significant activity at any of the enzyme concentrations used (Figure 3.5). There was also no enzyme activity when various concentrations of the substrate L-kynurenine and NADPH were used. The lack of catalytic activity suggests that the segment from position 383 to 486 is necessary for the enzymatic activity. However, due to the lack of expression of the full-length and single transmembrane deletion mutant, we were unable to identify the exact region of the C-terminus responsible for the loss of the *Hs*KMO activity. Hypotheses relating to the absence of activity will be discussed in Section 3.2.8.

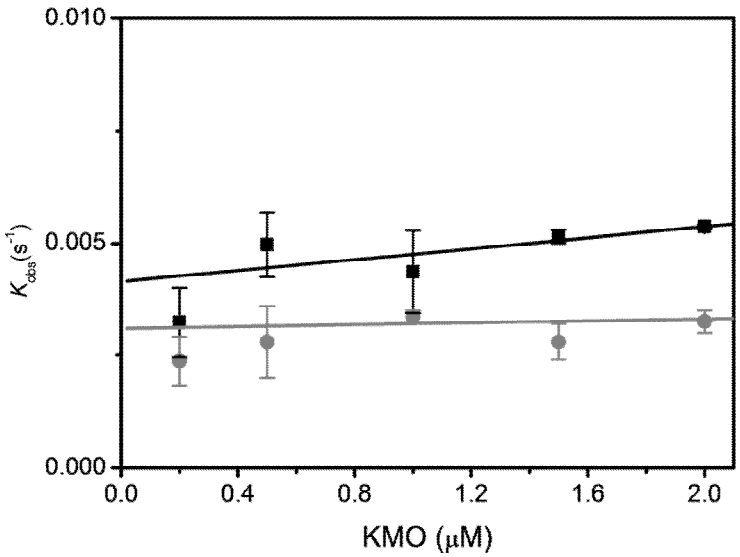


**Figure 3.5. NADPH oxidation rate vs ΔKMO383 concentration.** The KMO-catalysed reaction was monitored by measuring the oxidation of NADPH at 340 nm. 0.2-2 μM of pure enzyme was added to 200 μl reaction buffer (20 mM potassium phosphate, 7 mM β-mercaptoethanol) containing 0.15 mM NADPH and 0.15 mM L-Kyn (in black). A negative control was carried out without the substrate L-Kyn (in grey).

Additional spectroscopic studies to investigate the interactions of substrates and inhibitors were used to check whether the integrity of the ligand binding site was compromised as a result of the truncation of the transmembrane helices in the C-terminus.

As a typical class A flavoprotein monooxygenase, KMO contains one molecule of FAD per active site and therefore, the optical properties of this cofactor allow spectroscopic studies of the binding of substrates or inhibitors to yield dissociations constants for these interactions. In the visible region, FAD has absorbance maxima at 375 nm and 450 nm and a fluorescence maximum at approximately 525 nm. Certain ligands are able to quench or enhance the FAD fluorescence emission upon binding to the protein as they perturb the FAD binding pocket in the active site. Consequently, the perturbation in FAD fluorescence emission was monitored at 525 nm when titrating ΔKMO383 with L-KYN and the Ro 61-8048 KMO inhibitor (Figure 3.6).

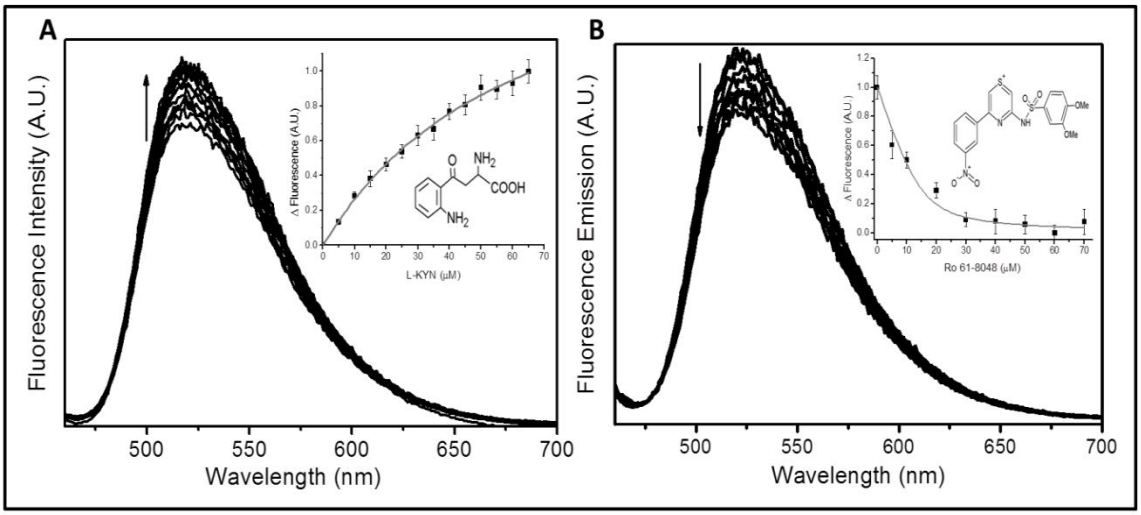


**Figure 3.6. Measurement of binding constant for L-Kyn and Ro 61-8048 by ligand perturbation of flavin fluorescence emission.** Titration of ligands to 5 μM ΔKMO was administered under atmospheric conditions at 25 ºC. The perturbation in fluorescence emission was followed at 525 nm using an excitation wavelength of 450 nm (A) Titration of L-KYN (0-70 μM from *bottom* to *top*) to ΔKMO led to an increase in the FAD fluorescence *Inset*: Fluorescence changes at 525 nm as a function of L-KYN concentration. The data were fitted to the Morrison equation to yield an observed $K_d$= 50.93 ± 5.3 μM. (B) Titration of Ro 61-8048 (0-70 μM from *top* to *bottom*) to ΔKMO383 led to a decrease in the FAD fluorescence. *Inset*: Fluorescence changes at 525 nm as a function of Ro 61-8048 concentration. The data were fitted to the Morrison equation to yield an observed $K_d$= 3.54± 0.4 μM. The structure of both ligands are shown in the respective plots.

**Table 3.1. Dissociation constants ($K_d$) for binding of L-KYN substrate and Ro 61-8048 inhibitor to ΔKMO383**

| Ligand | Dissociation constant ($K_d$) |
|---|---|
| **L-KYN** | 50.9 ± 5.3 μM |
| **Ro 61-8048** | 3.5 ± 0.4 μM |

Both ligands bind to the ΔKMO383 enzyme but give different effects on the FAD fluorescence, which is likely to reflect differences in the mode of binding. An enhancement in fluorescence was observed upon binding the physiological substrate L-KYN, which suggests that conformational changes in the protein upon ligand binding expose the flavin isoalloxazine ring to the solvent, thereby increasing its fluorescence (Figure 3.6A). The observed $K_d$ of 50.9 ± 5.3 μM is comparable with $K_m$ values for mammalian forms of KMO, which range from 13 μM in *Homo sapiens* [207] to 25 μM in *Rattus novergicus* [9] (see Table 1.3 for dissociation constants from KMO in different organisms). In contrast to the enhancement in FAD fluorescence observed with the L-KYN substrate, the Ro 61-8048 KMO inhibitor caused a quenching of FAD fluorescence (Figure 3.6B), suggesting that KMO undergoes different conformational changes/binding modes upon binding to this inhibitor. The observed $K_d$ is 3.5 ± 0.4 μM, which is significantly higher than the $IC_{50}$ value of 37 nM previously reported for this inhibitor in KMO from rat kidney mitochondria preparations [173]. Ro 61-8048 is claimed to be a competitive inhibitor and therefore, it should compete with L-KYN for the same binding pocket [242]. However, both ligands are structurally very distinct and the KMO inhibitor has a much more complex structure (Figure 3.6). Further enzymatic studies will be required in the future to validate Ro 61-8048 as a competitor KMO inhibitor.

### 3.2.5. Thermofluor assay

In order to obtain well-diffracting quality crystals for structure determination it is necessary to identify conditions that provide homogeneous, stable and soluble protein. The crystallisation of proteins can be strongly influenced by a number of factors, such as pH, ionic strength, additives, precipitants, protein concentration and temperature.

Recently, the Thermofluor assay has been used in structural biology as an important tool to identify buffer conditions that minimise protein aggregation and improve protein stability [243, 244]. Briefly, Thermofluor is a fluorescence-based thermal stability assay in which the fluorescence of certain dyes, such as SYPRO Orange, increase when exposed to hydrophobic regions of the protein compared to aqueous solution. This assay has been useful in helping to distinguish between folded and unfolded states of proteins. The transition to the unfolded state of a protein is accompanied by a corresponding increase in the dye fluorescence and can be monitored as a function of temperature using a standard real time PCR instrument by performing a high- throughput screening of buffer conditions in 96-well plates. The resulting curve usually shows a sharp transition between folded and unfolded states and the melting temperature ($T_m$) is precisely the midpoint of temperature of this unfolded transition. The $T_m$ is consequently a parameter of protein stability and any buffer and additive conditions that increase this temperature may enhance the probability of protein crystallisation. The optimal buffer conditions that were found using this technique are used during the last purification step as the buffer to exchange the protein into prior to protein crystallisation. These conditions may allow the protein to be concentrated up to a high level suitable for crystallography by minimising the likelihood of precipitation.

ΔKMO383 was subjected to the JBS Solubility Kit buffer screen (Section 2.2.12. Material and Methods) consisting of 24 buffer solutions at different pH values, ranging from 4.5 to 9.0, with concentrations of 50 mM. Among the 24 buffers tested, there were some buffers that appeared to be more favourable for ΔKMO383 stabilisation compared to the standard potassium phosphate buffer pH 7.5 buffer previously used (sample control), particularly Bis-Tris propane pH 6.5 ($T_m$= 50.6 ºC), ammonium acetate pH 7.0 ($T_m$= 49.8 ºC) and sodium phosphate pH 7.0 ($T_m$= 50.3ºC). Table 3.2 shows all the averaged $T_m$ values. The optimal buffers mentioned above were subsequently used for further assays that involved the addition of additives to improve the protein stability.

Table 3.3 gives the $T_m$ values of the additive screen assay using one of the optimal buffers, Bis-Tris Propane pH 6.5, identified in the previous assays. None of the additives tested using the JBS additive screen were found to yield significant improvements in the stabilisation of the protein. The addition of 200 mM NaCl and 4 mM DTT improved the thermal stability of the protein by 1.3ºC and 0.4 ºC respectively, when compared to ΔKMO383 in Bis-Tris Propane pH 6.5 without any additive (sample control).

Subsequently, all ΔKMO393 crystallisation samples were made up in this buffer supplemented with 150 mM NaCl and 4 mM DTT.

**Table 3.2. Melting temperatures of buffer screen of ΔKMO383**

| Buffer | pH | *T*m (°C) |
|---|---|---|
| **Citric Acid** | 4.0 | 37.3 |
| **Sodium/potassium phosphate** | 5.0 | 36.8 |
| **Sodium citrate** | 5.5 | 42.6 |
| **Sodium/potassium phosphate** | 6.0 | 46.1 |
| **Bis-Tris** | 6.0 | 45.4 |
| **ADA** | 6.5 | 49.1 |
| **Bis-Tris propane** | 6.5 | 50.6 |
| **Ammonium Acetate** | 7.0 | 49.8 |
| **MOPS** | 7.0 | 48.3 |
| **Sodium/potassium phosphate** | 7.0 | 50.3 |
| **Tris** | 7.5 | 47.2 |
| **Imidazole** | 8.0 | 47.5 |
| **Bicine** | 8.5 | 46.4 |
| **CAPS** | 10.0 | 40.2 |
| **Control (Potassium phosphate)** | 7.5 | 44.8 |

Buffers shown are from the JBS Solubility Kit part A. Buffers which did not produce a $T_m$ are not shown. Final concentrations for all buffers were 50 mM diluted from 100 mM stocks. Sample control is in 20 mM phosphate buffer pH 7.5.

**Table 3.3. Melting temperatures of additive screen of ΔKMO383**

| Addtive | *Concentration* | *T*m (°C) |
|---|---|---|
| **NaCl** | **200 mM** | 50.1 |
| **NaCl** | **400 mM** | 48.8 |
| **Glycerol** | **20%** | 45.5 |
| **Glycerol** | **40%** | 47.3 |
| **CHAPS** | **8mM** | 43.2 |
| **TCEP** | **120mM** | 46.2 |
| **BME** | **40mM** | 46.9 |
| **DTT** | **4mM** | 48.4 |
| **DTT** | **20mM** | 53.9 |
| **Sample control[1]** | - | 48.6 |

Additives shown are from the JBS Solubility Kit part B. Additives which did not produce a $T_m$ are not shown.

1 Sample control is in 50 mM bis-tris propane pH 6.5.

### 3.2.6. Multi Angle Laser Light Scattering (MALLS)

ΔKMO383 was analysed using MALLS coupled to a QELS detector and an extra gel filtration column. Essentially, this technique is able to report accurately on the average molecular weight of proteins, their radius of gyration and molecular conformation based on the hydrodynamic radius. Additionally, it also provides information regarding the stability and homogeneity of the sample in terms of aggregation or oligomeric states that are highly correlated with crystalisability. If the standard deviation (S.D.) of the $R_H$ is between 15-20 % it is classified as narrow monomodal dispersity and it is an optimal starting point for setting up crystallisation trials. As a general rule, proteins with monomodal distributions have a high probability (70-80%) of producing crystals as the presence of aggregation dramatically reduces the chances of obtaining crystals. S.D. less than 30 % is still considered reasonably monodispersed [245]. The S.D. of the $R_H$ for ΔKMO383 is 25 % across the three axes, indicating that the enzyme is a globular monomeric protein in solution, consistent with the plot from the Molecular mass ($M_r$) values, in which the molecular weight values remains constant over the duration of the elution peak. The average Mr is 44.8 kDa, which is very close to the predicted value of 45 kDa based on the primary sequence analysis. The protein gave a single light scattering peak that eluted after approximately 15 mL (Figure 3.7 - Black spectra), concurrent with a single refractive index peak (Figure 3.7 - Grey spectra).

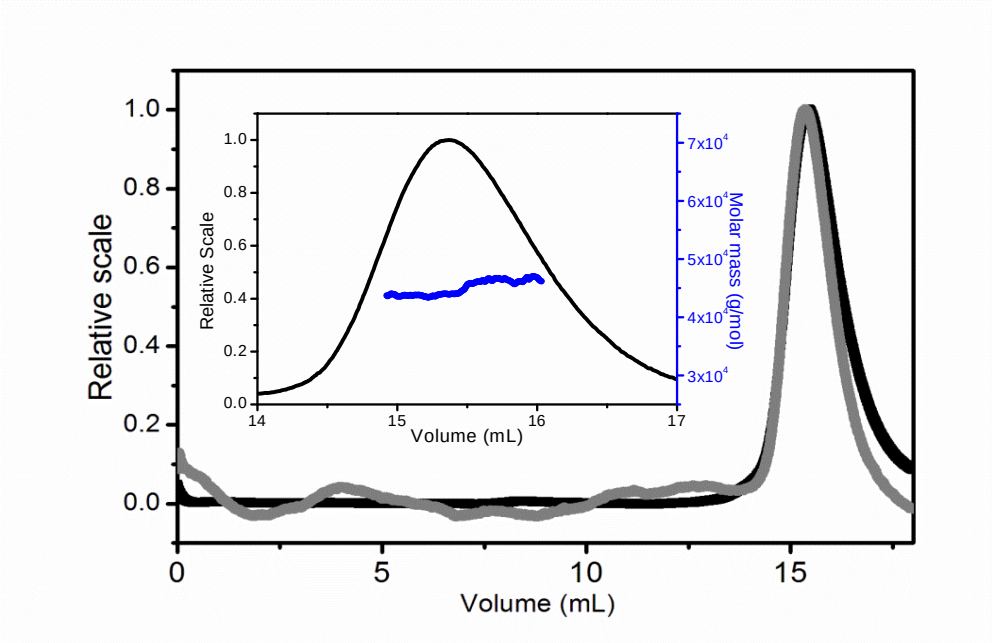


**Figure 3.7. Multi-Angle Laser Light Scattering spectra of ΔKMO383.** The black line represents light scattering data, the grey line represents the refractive index of the protein. *Inset* - The MALLS spectra shows a single peak with an average molecular weight of 44.8 kDa. B: The average molecular weight of ΔKMO383 (blue dots) spanning across the only peak. Polydispersity index is 1.0 which reflects protein stability.

The lack of information in the literature regarding the oligomerisation state of KMO from *Homo sapiens* did not allow a direct comparison with our results. The only study reporting information about the molecular weight and aggregation state was carried out in *Rattus norvegicus* KMO [210]. It was suggested, based on the elution pattern of native enzyme on size exclusion chromatography and results from SDS-PAGE, that the molecular weight of the enzyme from this species is 200 kDa and exists as a dimer in solution. It is important to emphasise that the experiments performed in this previous study were done in the presence of 1 % Triton X-100 for solubilisation of the enzyme from the outer membrane of mitochondria and therefore, the presence of detergent micelles may have contributed significantly to the overall molecular weight predicted, based on the elution peak from the gel filtration column. The fact that our *Hs*KMO variant lacks the C-terminal region did not allow a direct comparison with the results reported for *Rattus norvegicus* KMO since the transmembrane region can possibly interfere with the oligomeric state of the protein. The MALLS data collected for ΔKMO383 suggests that the protein has been isolated in a form that is suitable for crystallographic studies, although it is not in the narrow monomodal dispersity range.

### 3.2.7. Crystallisation of ΔKMO383

Extensive crystallisation trials of ΔKMO383 were performed across a range of conditions in 96-well plates using the sitting drop method. A range of protein concentrations from 5-20 mg/mL were tested with the commercially available crystallisation screens from Molecular Dimensions available in the laboratory (Details are described in Section 2.2.14.1). Co-crystallisation experiments were also performed in order to improve the chances of obtaining crystals, with L-KYN and Ro 61-8048, with a concentration of ligand that was 10-fold greater than the protein concentration to ensure ligand saturation. The crystallisation trials revealed that truncated *Hs*KMO aggregated over short timescales under the majority of crystallisation conditions. Despite efforts to optimise buffer and additive conditions to stabilise the protein, no crystals were obtained with the crystallisation kits available in the lab, including Silver bullet kits from Hampton research that are usually used when traditional screens are not successful. The protein precipitated over a short period of time in more than 60 % of the conditions.

### 3.2.8. Discussion and new approaches

Recent studies have provided strong indications that the C-terminal region of *Hs*KMO is important for its catalytic activity, although the exact role is not currently known [246]. Hirai *et al.* (2010) have reported the functional expression of full-length pig KMO in COS-7 cells together with several deletion mutants in the C-terminus. Accordingly, it was discovered that a segment of 20 amino acid residues close to the C-terminus is necessary for enzymatic activity (Figure 3.8). From the sequence alignment of pig and human KMO, this segment is part of the putative transmembrane hydrophobic domain starting from residue 421 to 441 in *Hs*KMO. It was also shown that the intracellular localisation of the deletion mutants shifted from the mitochondria to the cytosol. Taken together, it was hypothesised that the C-terminal region of KMO plays a dual role in mitochondrial anchoring and in enzymatic activity [246]. Interestingly, another study conducted on soluble full-length KMO from *P. fluorescens* obtained high levels of fully active enzyme, which was not associated with the outer membrane of the

mitochondria, suggesting that this KMO protein does not need to be attached to the membrane to catalyse the enzymatic reaction [206].


**Figure 3.8. Sequence alignment of pig liver KMO with *Hs*KMO**. The amino acid sequences were aligned by the CLUSTAL method. A putative transmembrane hydrophobic domain in KMO from pig liver and *H. sapiens* is boxed. A previous study suggests the C-terminal domain of KMO is involved in enzyme activity [246].

Although the results from the current project demonstrate that the C-terminal truncation variant is not able to catalyse the hydroxylation of the substrate L-KYN, it is still able to bind the substrate. Therefore, it is tempting to speculate that the truncation in the C-terminus might affect the co-enzyme NADPH binding site rather than the substrate binding site as no NADPH oxidation could be observed during catalytic assays. This hypothesis will be discussed further in Chapter 5 after elucidation of the crystal structure of *Sc*KMO.

As it proved impossible to crystallise ΔKMO383 subsequent efforts focused on the biochemical characterisation of full-length *Hs*KMO. Previous attempts to express full-length *Hs*KMO in *P. pastoris* were not successful and therefore, an alternative expression system was pursued, involving the insect cells/baculovirus system.

## 3.3. CHARACTERISATION OF FULL-LENGTH *Hs*KMO USING INSECT CELLS/BACULOVIRUS AS A HOST SYSTEM

### 3.3.1. Expression and Purification of *Hs*KMO

As explained previously, full-length *Hs*KMO is a membrane-associated enzyme with two transmembrane helices localised in the C-terminus. In order to circumvent the lack of full-length *Hs*KMO expression using *Pichia pastoris,* alternative expression systems that have previously been successful in expressing membrane proteins from other organisms were pursued. As the posttranslational modifications found in the majority of eukaryotic proteins can only occur in other higher eukaryotic cells it seemed logical that a higher eukaryotic host would be most suitable to produce fully functional *Hs*KMO. Insect cells are easier to manipulate and scale up than mammalian systems and they also offer a lipid environment that is more suitable for the function of membrane proteins compared to yeast, Therefore, this system was selected as an alternative to the *Pichia pastoris* host system. Several host strains and baculovirus transfer vectors were initially tested, as well as other parameters, such as multiplicity of infection (MOI) and times of incubation. Expression trials were performed systematically to find the best conditions for expression of full-length *Hs*KMO. A summary of the various conditions tested are shown in Table 3-2.

**Table 3.4. Vectors and cell lines tested for expression of *Hs*KMO in insect cells using the baculovirus system**

| Vectors | Cell line | Solubility | Expression levels |
|---|---|---|---|
| **pQE-TriSystem** | Sf9 | Soluble | Very low |
| | Hi5 | Soluble | Very low |
| **pBac2** | Sf9 | Soluble | Low |
| | Hi5 | Soluble | Low |
| **pACGHLT** | Sf9 | Soluble | Low |
| | Hi5 | Soluble | Low/Medium |

All of the vector systems tested expressed detergent solubilised *Hs*KMO (1 % Triton X-100), although they differed in terms of protein expression levels. The first vector system to be tested was the pQE-TrisSystem, as the synthetic KMO gene from *Invitrogen* was originally in this expression vector. The expression levels obtained using this system both with Sf9 and Hi5 cells were very low, just noticeable by Western Blot. To address expression protein level issues the KMO gene was efficiently sub-cloned into pBAC2 baculovirus transfer vector as a *Nde* I - *EcoR* I fragment. This vector is widely used for expression of high levels of recombinant proteins in insect cells but no significant improvements in KMO expression were detected. The KMO gene was also sub-cloned into the pAcGHLT-A GST baculovirus transfer vector and in this case, the protein expression levels were higher compared to the previous vectors, particularly when using the Hi5 insect cells strain. This baculovirus transfer vector includes an N-terminal Glutathione S-transferase tag that serves as an affinity tag and plays an important role as a solubilisation agent. Therefore, this may explain the higher expression levels of full-length KMO using this vector system. Test expressions were carried out with different MOI and times of incubation and optimal conditions were selected based on the quantity of soluble KMO expressed (Figure 3.10).

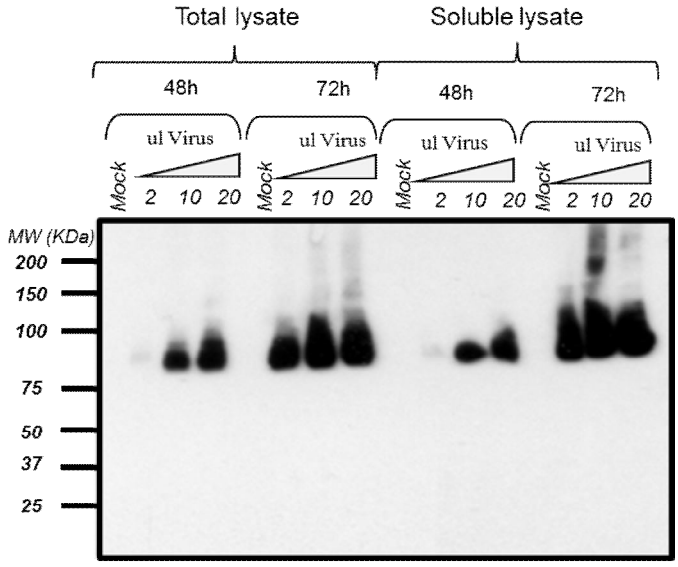


**Figure 3.9. Expression trials of full-length *Hs*KMO in Hi5 cells using the pACGHLT baculovirus vector**. Western Blot of total and soluble lysate of human KMO with anti-KMO antibody at varying MOIs and times of incubation. The cultures were grown at 28ºC for a total incubation period of 72 hours.

Figure 3.9 shows that the amount of total and soluble lysate is very similar and therefore the amount of KMO protein present in the soluble fraction can be seen as the total amount of KMO expressed within the cells. Optimal conditions were 72 hours of incubation and 20 μL of stock virus. The same conditions were also verified when scaling up of the growth cultures was carried out using the Cellbag-10 L disposable bioreactors.

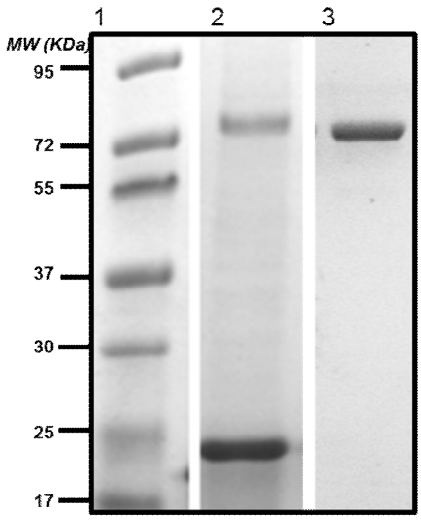


**Figure 3.10. SDS-PAGE analysis of full-length *Hs*KMO purity after each purification step**. Lane 1: Protein Markers, Lane 2: post Glutathione, Lane 3: post Gel filtration.

*Hs*KMO was purified using a two-step purification strategy that includes glutathione-Sepharose affinity followed by size exclusion chromatography (described in Section 2.2.4.2). After the first purification step just two bands were eluted, one band that runs at ~25 kDa was identified by MALDI-TOF peptide identification as the endogenous insect GST, and the higher molecular weight band, with an apparent molecular mass of ~ 80 kDa is the *Hs*KMO (Figure 3.10). The apparent molecular weight is consistent with the predicted mass from the amino acid sequence of 55 kDa including the N-terminal GST tag region (26 kDa). The endogenous GST was easily removed by gel filtration (Figure 3.11). The overall expression levels of KMO in insect cells was between 0.5-0.75 mg/L of culture, which is rather low compared to the majority of proteins expressed using the baculovirus system. However, the protein could be effectively purified without significant losses throughout the purification procedure.

The first attempts to purify KMO were conducted with the standard detergent Triton X-100, although this detergent is chemically heterogeneous and not suitable for structural studies. Consequently, a selection of detergents was chosen for an initial screening based on the previous success of these detergents in producing crystals of

membrane proteins (Table 2.3). There are many criteria that can determine the choice of detergent, ranging from micelle molecular weight, critical micelle concentration (CMC) or length of the alkyl chain [224]. From the selection of detergents tested, n-dodecyl β-D-maltopyranoside (DDM) and octyl-glucoside (OG) were the detergents that were most efficient in solubilising KMO (Figure 3.11). These two detergents were carefully chosen for small scale partial purification to verify the homogeneity of the target protein and with both conditions KMO protein was eluted in a single sharp peak by gel filtration, indicating that the protein is in a stable and well-folded form. The amount of detergent in the selected conditions was further optimised, using concentrations of detergent above its CMC in order to act as an effective solubiliser. Since DDM and OG were equally efficient in solubilising KMO, further experiments were carried out only with DDM, as this detergent is less harsh compared to OG.

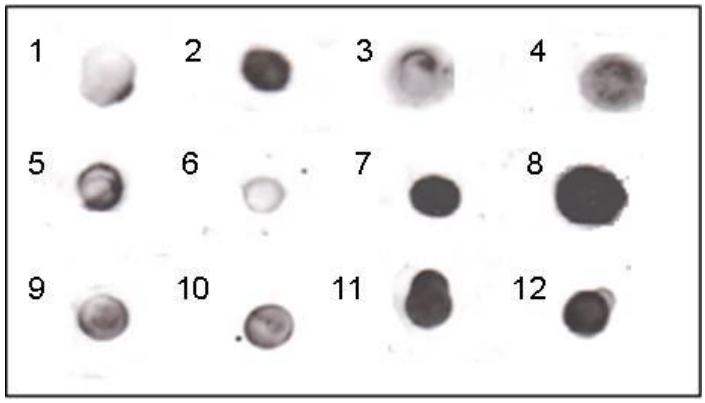


**Figure 3.11. Dot-blot analysis with human anti-KMO antibody of *Hs*KMO soluble lysate using different detergents**. The Dot blot technique is similar to the Western Blotting except that the protein samples are not separated electrophoretically but just spotted directly onto the membranes. 1- without detergent, 2- 0.1% Triton X-100, 3- 1% CHAPS, 4 - 2% CHAPS, 5 - 0.5% FC12, 6 – 1% FC12, 7 – 0.5% DDM, 8 – 1% DDM, 9 – 0.5% LDAO, 10 – 1% LDAO, 11 – 1% OG and 12 – 2% OG.

During size exclusion chromatography, the protein was eluted after 7.5 minutes, which, according to the molecular weight standards of a typical chromatogram from Superdex 200 10/300, corresponds to an apparent molecular weight that is significantly higher than expected with a Mr ≥ 300kDa (Figure 3.12). It is important to note that in some cases, particularly when studying a protein-lipid complex, a protein mass estimated by SEC may differ greatly from the actual value, possibly due to the complex shape and

possible matrix binding interactions. As previously mentioned in Section 3.2.6, there is a lack of information regarding the molecular weight and aggregation state of KMO. Studies on human KMO have predicted the molecular weight of denatured protein based on results from SDS-PAGE gels and therefore, the results are not informative in terms of the oligomeric state of the native protein [208]. Studies carried out in *Rattus norvegicus* KMO [210] suggest that the molecular weight of the enzyme is 200 kDa and it exists as a dimer in solution, although their hypothesis is based on the elution pattern of native enzyme solubilised in Triton X-100 which can in fact overestimate the true molecular weight of the enzyme. Therefore it is tempting to speculate that due to the similarity of both enzymes, *Hs*KMO may also exist as a dimer in solution.

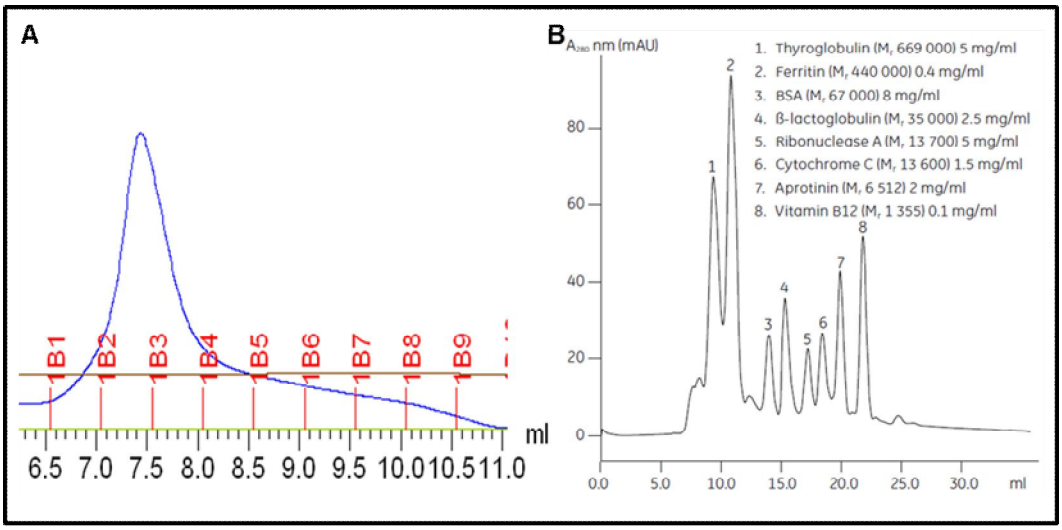


**Figure 3.12. Size exclusion chromatogram and prediction of *Hs*KMO molecular weight.** (A) Purification chromatogram of *Hs*KMO after passing down a Superdex 200 10/300 GL column using 0.012 % DDM in the buffer solution and (B) Typical chromatogram from a function test of Superdex 200 10/300 GL.

Although MALLS is widely used for the accurate determination of the molecular weight and oligomeric state of proteins it is often very difficult to use this technique to characterise membrane proteins because they are in a lipid-containing solvent. As the membrane protein-lipid complexes have different conformations and therefore, different adsorption characteristics to the column packing compared to globular proteins, the elution property of membrane and globular proteins are significantly different. Previous studies reporting the use of MALLS in combination with UV absorption and differential

refractive index (DRI) detection show that it is possible to determine the molecular masses of membrane associated proteins [247, 248]. Attempts were made to predict the molar mass of full-length *Hs*KMO based on these studies, but without success.

Although DDM is one of the gentler detergents and widely used in crystallography, the relatively large micelles (60 kDa) [223] often surround the protein and prevents crystal formation. Membrane proteins will generally bind substantial amounts of detergent and consequently, the amount of detergent in the final sample is usually higher than the concentration in the buffer. Ideally, only KMO fractions with the highest protein concentration would have been selected after size exclusion chromatography to avoid a further concentration step. However, due to the lower expression yields, more fractions were collected and therefore, they needed to be concentrated for further structural studies. To overcome the issue of excessive amounts of detergent in the final sample, an ultrafiltration membrane with a cut off higher than the micelle size was used. Since the DDM micelle size is approximately 60 kDa [223] a membrane with a cut off of 100 kDa was used to concentrate KMO and avoid excessive concentration of the detergent.

### 3.3.2. Crystallisation Trials of *Hs*KMO

Preliminary crystallisation screens with pure GST-KMO and cleaved protein using the Phoenix crystallisation robot platform were performed but no crystals were obtained with the crystallisation kits available in the lab (more details in Section 2.2.14.1). Unfortunately, extensive crystallisation conditions could not be pursued due to the very low yield of protein expression. One of the most likely reasons for the lack of protein crystals is the presence of DDM. It is widely known that the use of detergents in crystallography is extremely challenging. This is because the properties of the protein-detergent complex do not favour the formation of well-ordered lattices due to the flexible and dynamic nature of the detergent that surrounds the protein. Furthermore, despite the use of an ultrafiltration membrane with a cut off higher than the DDM micelle size, it might be possible that a large number of micelles were still present in the final sample, preventing the formation of the crystals. As the expression levels were rather low for

structural studies, further experiments were focused on the biochemical characterisation of full-length *Hs*KMO.

### 3.3.3. Effects of pH and Temperature on *Hs*KMO activity

KMO catalyses the NADPH-dependent hydroxylation of L-kynurenine into 3-hydroxy-kynurenine. The activity of KMO enzyme was initially tested as described in Section 2.2.8 as a function of temperature and pH to find the optimal conditions for maximal enzyme activity. The enzymatic reaction was monitored by following the decrease in absorbance of NADPH at 340 nm with saturating concentrations of L-KYN and NADPH. Figure 3.13A shows the dependence of activity on the temperature and reveals that there is little activity below 10°C and at temperatures higher than 50°C. The temperature optimum for KMO activity lies within the range 33-38°C, which is similar to the temperature used for enzymatic assays with crude or purified mammalian KMOs (temperatures between 30-37°C) under similar conditions. Although these studies do not clarify the temperature choice the enzyme activity could reasonably expected to maximised in this temperature range [208, 210].

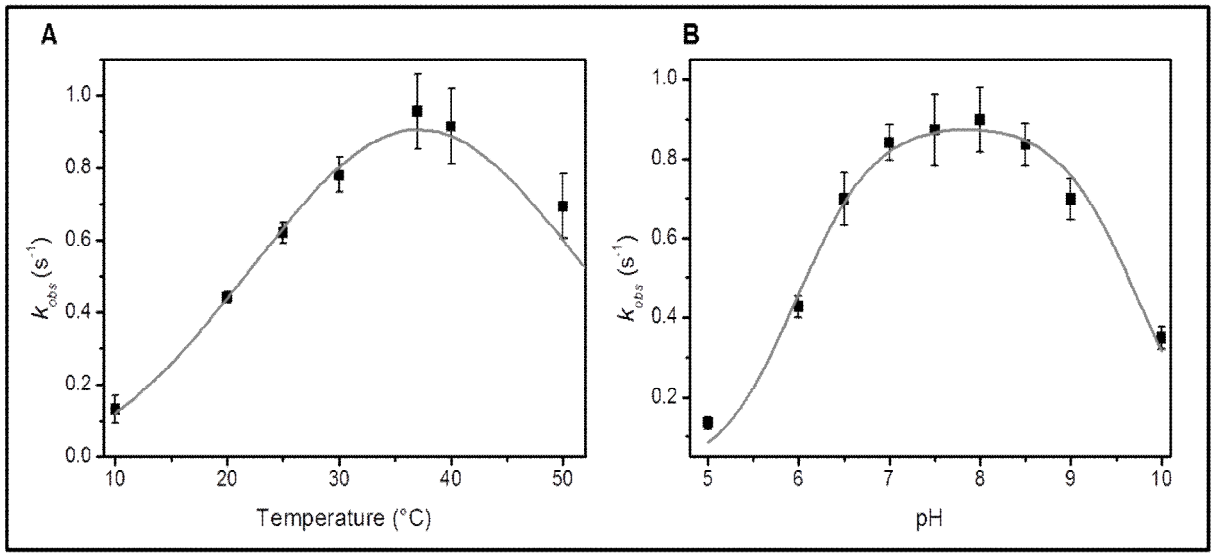


**Figure 3.13. Effects of temperature and pH on *Hs*KMO activity**. The biochemical activity was assayed with 500 mM L-KYN and 1 mM NADPH. The enzymatic reaction was monitored by following the decrease in absorbance of NADPH at 340 nm with temperatures from 10 to 40ºC (Panel A) and pH values

from 6 to 10 (Panel B). The temperature profile was fitted to a Gaussian curve (Equation 2) and the pH profile was fit to the two macroscopic pKa value equation (Equation 3).

The activity of full-length *Hs*KMO was also monitored at different pH values, which showed an optimum at pH 8.0 with significant loss of activity at pH values below 6 and higher than 9 (Figure 3.13 B). The pH profile of *Hs*KMO activity gave rise to two apparent pKa values of 5.9 and 9.7. The pH optimum obtained in this study is comparable with previous reports on recombinant *Hs*KMO and rat liver extracts where a pH optimum of 7.5 was measured for the KMO activity [208, 9]. Similar values are also observed in lower organisms, ranging from pH 7.5-8.5 [212, 207].

### 3.3.4. Kinetic analysis of *Hs*KMO

A complete kinetic analysis of *Hs*KMO was carried out by initial-velocity measurements of the overall reaction, varying either the L-KYN or NADPH concentrations. Control assays were also performed in the absence of the substrate L-KYN and showed that very slow rates of NADPH oxidation were observed that were independent of enzyme concentration. This corresponds to endogenous NADPH oxidation and this background rate was taken into account for the calculation of the KMO activity. For each assay the substrate kinetic parameters were measured in the presence of an excess of the other substrate. Rates were determined by fitting the decrease in absorbance at 340 nm to a straight line over the first 30 seconds. *Hs*KMO activity follows simple Michaelis-Menten kinetics and the $K_m$ values for both substrates were determined by fitting the data of the rate of turnover versus the substrate concentration to the Michealis-Menten equation (Equation 1, Section 2.2.8). Apparent steady-state parameters were measured at an optimal temperature (37ºC) and pH (pH 8.0) so that the values could be directly comparable with published data.

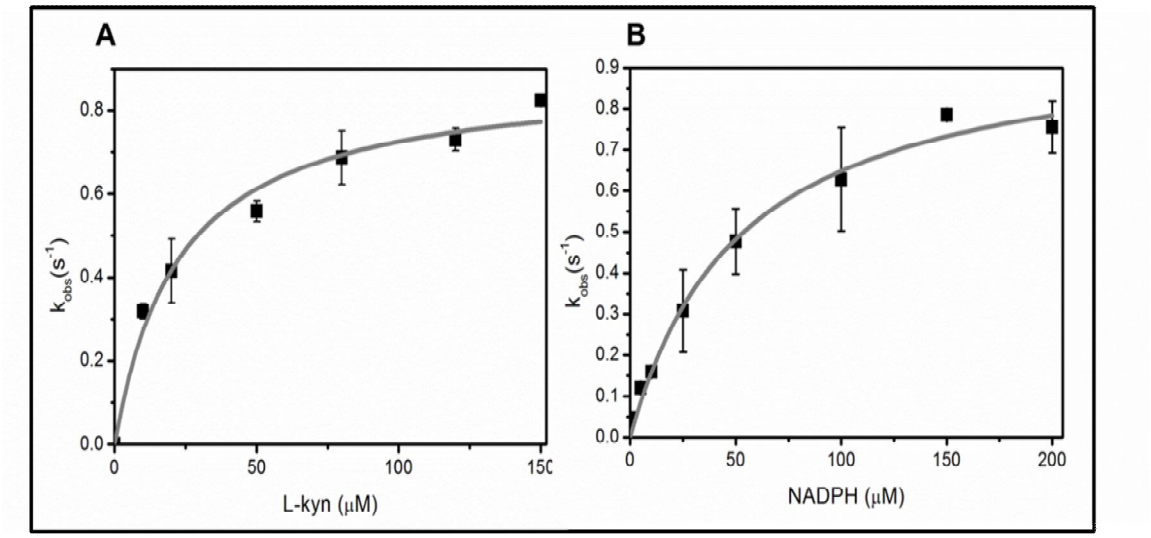


**Figure 3.14: Overall initial-velocity measurements of *Hs*KMO activity at varying concentrations of L-KYN or NADPH.** The enzymatic reaction was monitored by following the decrease in absorbance of NADPH at 340 nm. Saturation curve was calculated by fitting the data to the Michaelis-Menten equation.

**Table 3.5. Apparent steady-state parameters for *Hs*KMO**

| Kinetic Coefficients | Values |
|---|---|
| $K_{M\ NADPH}$ (μM) | 52.6 ± 9 |
| $K_{M\ L\text{-}KYN}$ (μM) | 22.6 ± 4 |
| $k_{cat}$ ($s^{-1}$) | 0.9 ± 0.05 |

Figure 3.14 shows a hyperbolic dependence of the turnover rate on the concentration of both substrates with a $K_m$ of 52.6 ± 9 μM and 22.6 ± 4 μM for NADPH and L-KYN, respectively and a $k_{cat}$ of 0.89 ± 0.05 $s^{-1}$. The $K_m$ value for L-KYN (22.6 ± 4.4 μM) is similar to that observed for the native protein from rat liver mitochondria preparations (16 μM) [9] and human liver enzyme (13.0 ± 3.3 μM) [10]. However, the value is approximately 4-fold different to previously published results on recombinant *Hs*KMO expressed in COS-1 cells (100 μM ± 1) [208]. No published data is available regarding $K_m$ values for NADPH in *Hs*KMO, although the value obtained is a similar range to the $K_m$ value determined for *Rattus norvegicus* ($K_m$= 23 ± 1.8 μM) [9]. Interestingly, similar kinetic parameters are also observed among lower organisms, for instance *Pseudomonas fluorescens and Saccharomyces cerevisiae* (Table 1.3). The $k_{cat}$

value was also found to be similar to previous studies on recombinant *Hs*KMO (2.18 $s^{-1}$) [208], providing evidence that we have expressed and purified functional *Hs*KMO.

### 3.3.5. Inhibition Assays of *Hs*KMO

Inhibition assays were carried out with one of the most potent inhibitors of KMO, UPF 648. This tight binding inhibitor has been used in several *in vivo* and *in vitro* studies to test and validate the hypothesis that KMO inhibition is a viable therapeutic strategy in Huntington's disease [249, 3]. The inhibition of *Hs*KMO activity by the UPF 648 KMO inhibitor was investigated by following the formation of the product 3-HK at varying UPF 648 concentrations and at saturating concentration of the L-KYN substrate (500μM). Figure 3.16A shows typical HPLC elution curves of the product (3-HK) and substrate (L-KYN) at varying concentration of the UPF 648 inhibitor. At increasing concentrations of UPF 648, the formation of 3-HK dramatically decreases with more of the L-KYN substrate remaining unconverted. The initial rate of 3-HK formation was fitted to the Morrison's equation, which is used for tight binding ligands or when the dissociation constant of the inhibitor is similar to the total concentration of enzyme in the sample (Figure 3.16B). It is important to emphasise that these kind of inhibitors bind so tightly to the target enzyme that the concentration of free inhibitor decreases significantly when the enzyme-inhibitor complex is formed and therefore, simple binding equations based on Michaelis-Menten principles are no longer valid. As a general rule, the Morrison's equation should be used whenever the dissociation constant of a certain inhibitor is less than 1000-fold greater than the total enzyme concentration.

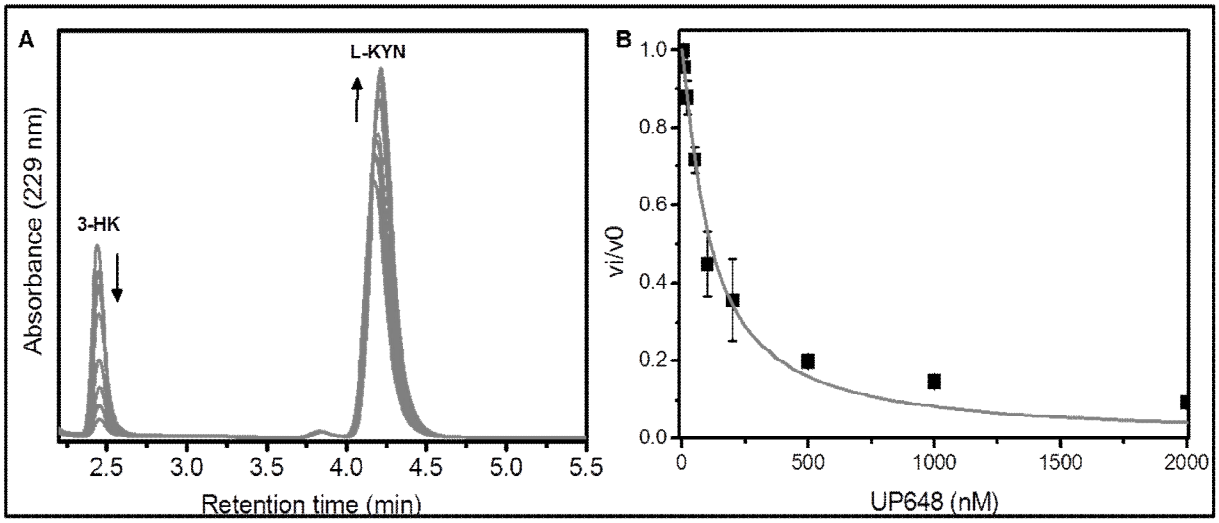


**Figure 3.15. Fractional velocity of 3-HK formation as a function of UP648 concentration with *Hs*KMO.** 100 nM enzyme was incubated at 37ºC with 2 mM NADPH, 500 μM L-kyn and different concentrations (0-2 μM) of the UPF 468 inhibitor. The product formation was analysed by reversed-phase HPLC. A: HPLC elution curves of product (3-HK) and substrate (L-KYN) at varying concentration of the UPF 648 inhibitor. B: The data was fitted to the Morrison equation for tight binding inhibitors.

UPF 648 was found to be highly efficient as a KMO inhibitor, with an apparent $K_i$ of 56.7 ± 8.0 nM. This value is very similar to previous reports, where the $IC_{50}$ determined in an *in vivo* gerbil model with this ligand was 40 nM [172], although the concentration of substrate used in their assays is not clear. It should be noted that for tight binding inhibitors the $IC_{50}$ or $K_i^{app}$ values depend on the substrate concentration and therefore our results cannot be directly comparable to published data unless the specific substrate concentration used in the experiments are known. These data are the first direct measurement of inhibitor constants for UPF 648 with pure *Hs*KMO and provide additional support that the recombinant *Hs*KMO purified in this study behaves in the same way as the native protein. We can speculate that UPF 648 acts as a tight binding competitive inhibitor as the structure is very similar to the physiological L-KYN substrate with an additional cyclopropyl ring in the side chain. The potential mode of inhibition will be discussed further in Chapter 5.

As previously mentioned, another KMO inhibitor, Ro 61-8048, has also been extensively used as a tool to study the effects of KP manipulation in several diseases [173, 1, 167]. This compound is highly insoluble in aqueous buffers and it was only

possible to solubilise in DMSO. As the inhibition assays were carried out for long incubation periods, *Hs*KMO precipitated even with nM concentrations of Ro 61-8048 and therefore, it was not possible to calculate the apparent $K_i$ of this compound.

## 3.4. CONCLUDING REMARKS

In this chapter we tested two different expression systems to express and purify *Hs*KMO: *Pichia pastoris* and insect cells/baculovirus system. A C-terminal transmembrane deletion mutant was expressed in *P. pastoris* and purified although no structural information was acquired despite numerous efforts to optimise conditions for crystallogenesis. In terms of catalytic activity, there was no evidence of NADPH oxidation during activity assays, which might be related to the truncation in the C-terminal region. The lack of ΔKMO383 activity is in accordance with published data showing that the C-terminal region of *Hs*KMO is required for enzyme activity [246]. Although the role of the C-terminus of *Hs*KMO in catalysis is not clear, we can speculate that it is involved in NADPH binding as there was no NADPH oxidation during catalytic assays. Since this truncated KMO did not allow a full biochemical characterisation of the *Hs*KMO enzyme the expression of full-length *Hs*KMO was pursued in another host strain.

Full-length *Hs*KMO was expressed in insect cells using the baculovirus system and purified to homogeneity. A complete biochemical characterisation of the enzyme was carried out and the kinetic parameters and inhibitor coefficients were shown to be very similar to KMO purified from mitochondria preparations, which provides strong evidence that we have expressed and purified fully active protein. Consequently, we now have a robust system to use as a future screening methodology for testing the efficacy of possible KMO inhibitors. An activity profile of various C-terminal deletions mutants may provide valuable information regarding the role of this region in *Hs*KMO activity.

In terms of structural studies none of the systems provided protein that led to crystals. Extensive crystallisation conditions were performed with ΔKMO383 although the protein aggregated in the majority of the conditions. Due to the uncertainty of using the truncated *Hs*KMO as a good model for the study of full-length *Hs*KMO, this strategy was not pursued further. As regards full-length KMO, there were also several issues

during the course of this project that prevented further crystallisation trials of *Hs*KMO. One of the major reasons was the very low yield of protein expression, which was sufficient for a biochemical characterisation but not for detailed crystallogenesis trials. As the expressed KMO from insect cells contained a GST-tag, which is rather large for crystallography purposes, attempts were made to cleave it with thrombin. However, this process was ineffective and together with the low expression yield made it very difficult to obtain reasonable amounts of *Hs*KMO suitable for crystallography.

In conclusion, although it was not possible to structurally characterise *Hs*KMO, the new strategies developed in this project to express, purify and kinetically study *Hs*KMO are extremely useful in a future high throughput platform for screening of inhibition compounds that are able to decrease the activity of the KMO enzyme.

# CHAPTER 4

# BIOCHEMICAL AND BIOPHYSICAL CHARACTERISATION OF *SACCHAROMYCES CEREVISIAE* KYNURENINE 3-MONOOXYGENASE

# 4. BIOCHEMICAL AND BIOPHYSICAL CHARACTERISATION OF *SACCHAROMYCES CEREVISIAE* KYNURENINE 3-MONOOXYGENASE

## 4.1. INTRODUCTION

In chapter 3, although further elucidation of the enzyme catalytic mechanism was not possible due to the very low expression levels, I provided a detailed biochemical characterisation of human KMO (*Hs*KMO). Furthermore, the structural studies conducted on human KMO did not provide suitable results in terms of conditions to obtain crystals despite numerous attempts to crystallise both full length and truncated forms of KMO.

Due to the difficulties encountered with the structural and biochemical studies on *Hs*KMO, an alternative strategy was pursued. Several KMO enzymes from different organisms were analysed in order to find a suitable homology model for the study of *Hs*KMO. The choice of KMO homologues were based on the sequence similarity and probability of crystallisation of the respective protein based on software tools for protein crystallisability prediction. KMO homologues from higher eukaryotes were excluded due to the high sequence identity (See Figure 1.9) and therefore the hydrophobic residues that could function as transmembrane regions were still present.

Of particular interest is the KMO from yeast *Saccharomyces cerevisiae* (*Sc*KMO). Although the analysis of the *Sc*KMO primary sequence, based on predicted secondary structures, suggested the presence of a hydrophobic amino acid stretch in the C-terminus of KMO between residues 425-455 (Figure 4.1), the probability of obtaining diffraction quality crystals was significantly higher compared with the predicted transmembrane regions for *Hs*KMO. Additionally, predictive crystallisation software tools suggested that there was an increased likelihood of crystallising the *Sc*KMO compared to *Hs*KMO.

A persuasive argument for the study of *Sc*KMO as a good homology model for *H*sKMO came from a genome-wide screen in yeast that identified the yeast orthologue of KMO (BNA4) as a suppressor of mutant htt toxicity, suggesting that the mechanism of polyQ tract toxicity is preserved - at least in part - in yeast and humans [2]. Moreover, in

addition to the KMO enzyme, all of the other enzymes involved in the kynurenine pathway were shown to be conserved in yeast, supporting the hypothesis of a conserved mechanism of this pathway in lower organisms.

In order to gain a better understanding of the reaction mechanism of KMO, *Sc*KMO has now been heterologously expressed in *E. coli*, purified and characterised using a variety of spectroscopic techniques, including UV/Visible and fluorescence spectroscopy. Elucidation of the reductive and oxidative half reactions was performed using kinetic and stopped flow techniques. Ligand binding and inhibition studies with KMO inhibitors were undertaken and compared to the dissociation constants obtained in Chapter 3 to validate *Sc*KMO as a good homology model for the study *Hs*KMO.

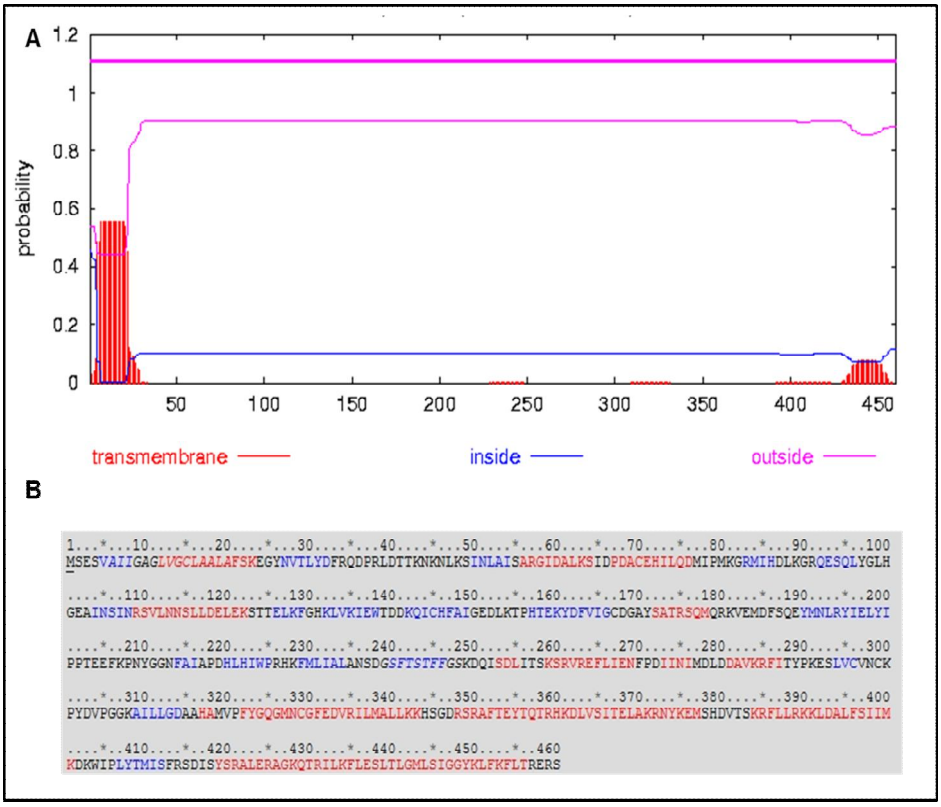


**Figure 4.1. Prediction of membrane helices and secondary structures in *Sc*KMO** – Panel A: The plot shows the location of the predicted hydrophobic regions ( between residues 1-27 and 425-455) (by *THMM*[236]). Panel B: Prediction of secondary structures based on KMO primary sequence The letters coloured in black represent predicted loops, in red helices and blue s trands. The software *XtalPred* did not predict any transmembrane region (by *XtalPred*[237]).

Figure 4.2 shows the sequence alignment of KMO from *H. sapiens* and *S. saccharomyces.* They share 34.1 % identity and 51.4 % similarity. Although these values

are not significantly high, the dinucleotide binding motif characteristics of flavin monooxygenases that require NADP(H) and FAD as coenzymes (Figure 4.2 -first boxed fragment) is conserved as well as putative consensus domains for both FAD and NAD(P)H binding ( Figure 4.2 - second and third boxed fragments).

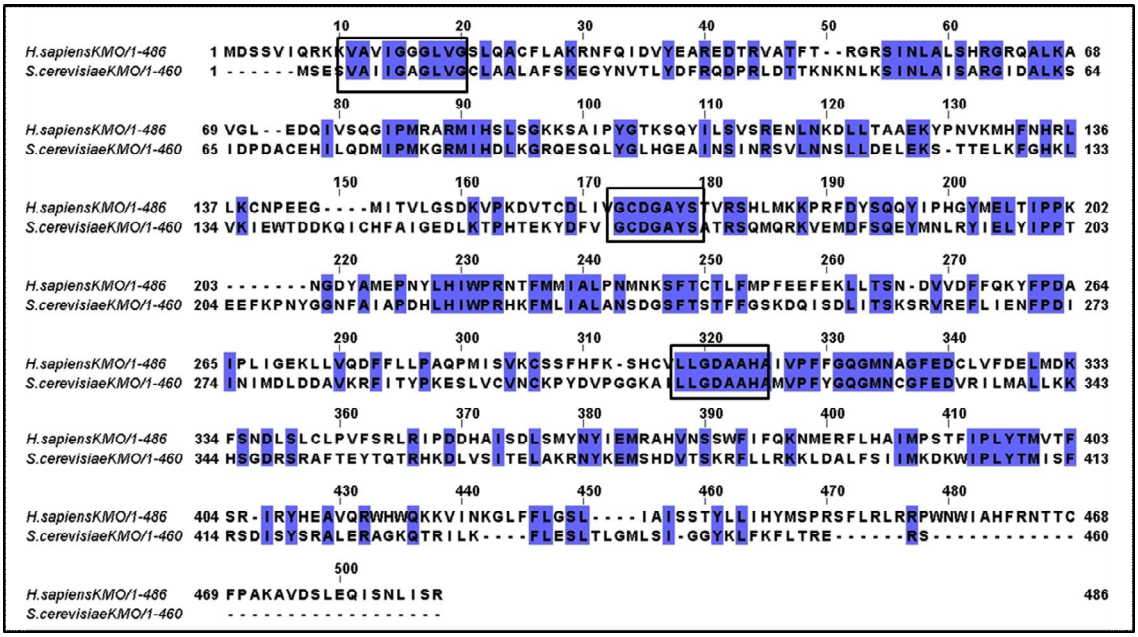


**Figure 4.2. Multiple alignment of the amino acid sequence of KMO from *H. sapiens* and *S. cerevisiae*.** Blue coloured residues denote sites of conserved amino acids. Sequence alignment was generated by ClustalOmega and drawn by Jalview software. Boxed areas are sequences associated with NADP(H) and FAD binding that are conserved in human and yeast KMO.

## 4.2. EXPRESSION AND PURIFICATION OF *Sc*KMO

Synthetic ScKMO gene was codon optimised for overexpression in *E. coli* (Section 2.2.1.3). The choice of this bacterial system lies in the fact that it is the most widely used host system for protein amplification and there is an extensive choice of cloning vectors compared to other host organisms. Furthermore, due to the fact that it is the simplest and easiest system to grow in high yields, it was our first choice in attempting to express *Sc*KMO.

*Sc*KMO was cloned into pET15b and pET24b vectors in order to compare the expression levels of the recombinant protein with N- and C-terminal $His_6$-tags, respectively. The resulting constructs were confirmed post-miniprep by DNA sequencing

using the forward T7 and reverse T7 term primers. The plasmids were then transformed into *E. coli* BL21(DE3) cells.

Expression trials were carried out with both constructs to select optimal growth conditions. Figure 4.3 shows a Western Blot of soluble lysates of the different KMO constructs at varying growth temperatures and IPTG concentrations. Both the pET24b-KMO and pET15b-KMO plamids yielded overexpressed KMO protein in the soluble fraction of BL21(DE3) cells. The maximum expression levels were achieved with 0.1 M IPTG and at 25ºC for both constructs.

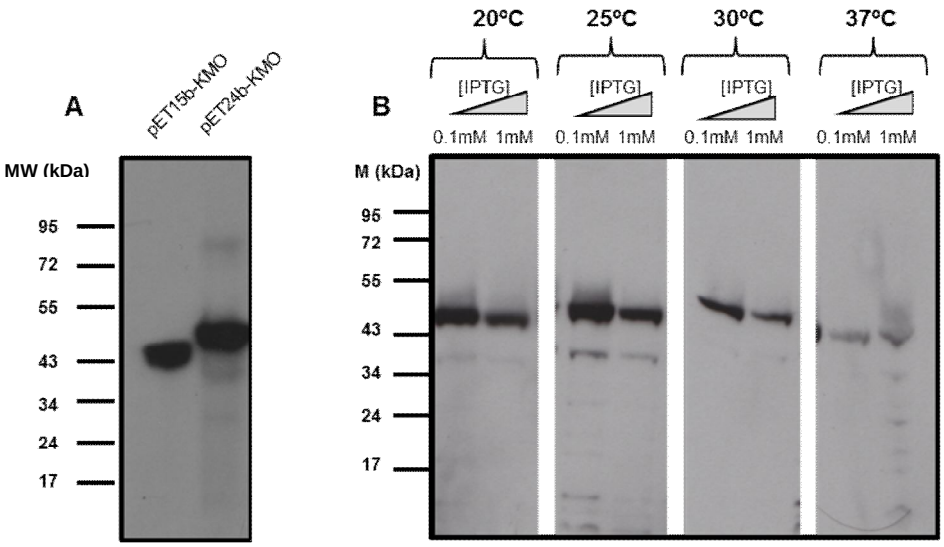


**Figure 4.3: Expression trials of *Sc* KMO variants. Panel A -** Western Blot of soluble lysate of pET15b-KMO and pET24b-KMO variants with anti-His antibody. **Panel B** - Western Blot of soluble lysate of pET15b-KMO with anti-KMO antibody at different temperatures and IPTG concentrations.

As purification strategies have not previously been reported for *Sc*KMO, the first approach was to follow the purification steps used for human truncated KMO expressed in *P. pastoris* (Section 3.1.2.). As both pET vectors contained His-tags, the first purification step involved using $Ni^{2+}$ affinity chromatography as described in the Materials and Methods section. The protein from this step was purified further using a Blue Sepharose Chromatography column. Finally, size exclusion chromatography was used to further polish the final sample or simply to exchange buffer into optimal conditions for crystallography. This procedure could be used to purify N-terminally His-tagged KMO (Figure 4.4) but did not result in pure KMO when the His-tag was attached

to the C-terminus. The results with this protein suggest that the C-terminal His tag might not be solvent exposed as the protein did not bind to the nickel resin. Several attempts to optimise the purification protocol were carried out using anion (DE-52) and cation (Mono S) exchange chromatography techniques, as well as hydrophobic interaction chromatography, but without success. As a result, the pET15b-KMO construct was used to produce N-terminally His-tagged KMO for further biochemical and biophysical studies. Typical expression levels obtained for pET15b-KMO were 4 mg/L of culture, which was sufficient to progress for further characterisation of the enzyme.

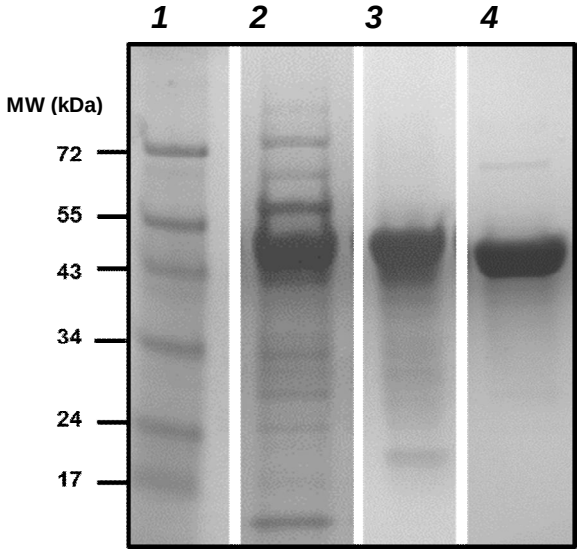


**Figure 4.4. SDS-PAGE analysis of ScKMO purity after each purification step.** Lane 1: Protein Marker, Lane 2: post nickel sepharose column, Lane 3: post Blue Sepharose column, Lane 4: post size exclusion chromatography.

Western Blot (Figure 4.3) and SDS-PAGE gel analyses of purified *Sc*KMO (Figure 4.4) showed a band migrating at ~48 kDa which is lower than the expected molecular weight of 57 kDa, calculated from the amino acid sequence. The difference in the apparent molecular weight might be due to cleavage in the C-terminal region by exoproteolysis during protein expression, as the N-terminus is intact and was recognised by antibodies to the His-tag. Interestingly, from the Western Blot (Figure 4.3) it is possible to visualise a subtle difference in the molecular weight of both KMO variants, where the C-terminally His-tagged KMO presents a higher molecular weight. In this case the C-terminal region is preserved and was recognised by antibodies to the His-tag. We hypothesise that the His-tag in the C-terminus might prevent the exposure of some residues where proteolysis is more likely, although analysis of the primary sequence did

not suggest any characteristic proteolysis site in the KMO C-terminal region. Protein instability could also be caused by loosely structured peripheral regions such as the C-terminal end and therefore allowing a number of degradation processes to occur. The exact molecular weight of pure *Sc*KMO was confirmed by Electrospray Ionisation Mass Spectrometry (EL-MS) (Figure 4.5).

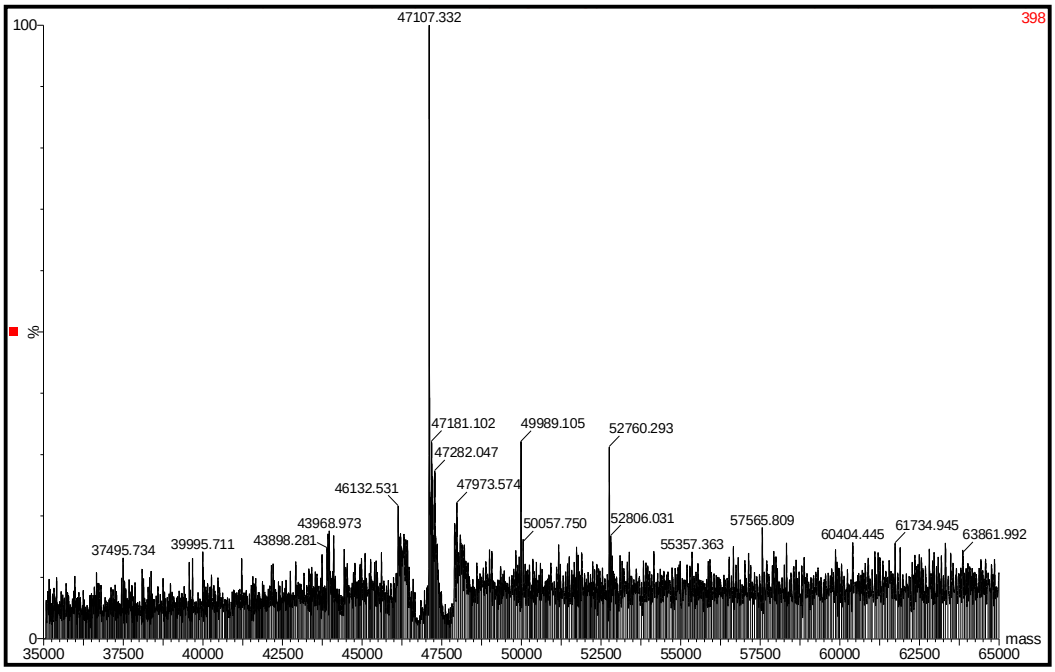


**Figure 4.5. The electrospray ionization liquid chromatography-mass spectrometry of semi purified *Sc*KMO.** Deconvoluted Mass spectrum shows an exact molecular weight of 47.107kDa.

According to the molecular weight obtained from EI-MS, 47.1 kDa, and protein sequence analysis, the protein was cleaved after Phenylalanine 396. Initial crystallographic structure of *Sc*KMO was solved as described in Section 5.3. However, in order to prevent ambiguities in the definition of the C-terminal region and to prevent future problems with further cleavage, an engineered truncated form was generated, ΔKMO394, by site directed mutagenesis to delete the residues 395 to 460.

ΔKMO394 was expressed and purified following the same steps carried out for *Sc*KMO. The protein yield obtained was significantly higher for this truncated form (15 mg/L of culture) when compared to the cleaved *Sc*KMO, which supports the hypothesis that the hydrophobic residues in the C-terminus were preventing the efficient expression of soluble KMO.

## 4.3. pH AND TEMPERATURE DEPENDENCE ON ΔKMO394 ACTIVITY

The activity of the *Sc*KMO enzyme was initially tested at a range of different temperatures and pHs to find the optimal conditions for maximal enzyme activity. Assays were conducted as described in section 2.2.8 and the enzymatic reaction was monitored spectroscopically by following the decrease in absorbance of NADPH at 340 nm at saturating concentrations of L-KYN and NADPH.

Initial measurements revealed that cleaved *Sc*KMO and ΔKMO394 were kinetically identical, as expected, and therefore, all subsequent the kinetic characterisations were carried out exclusively with ΔKMO394.

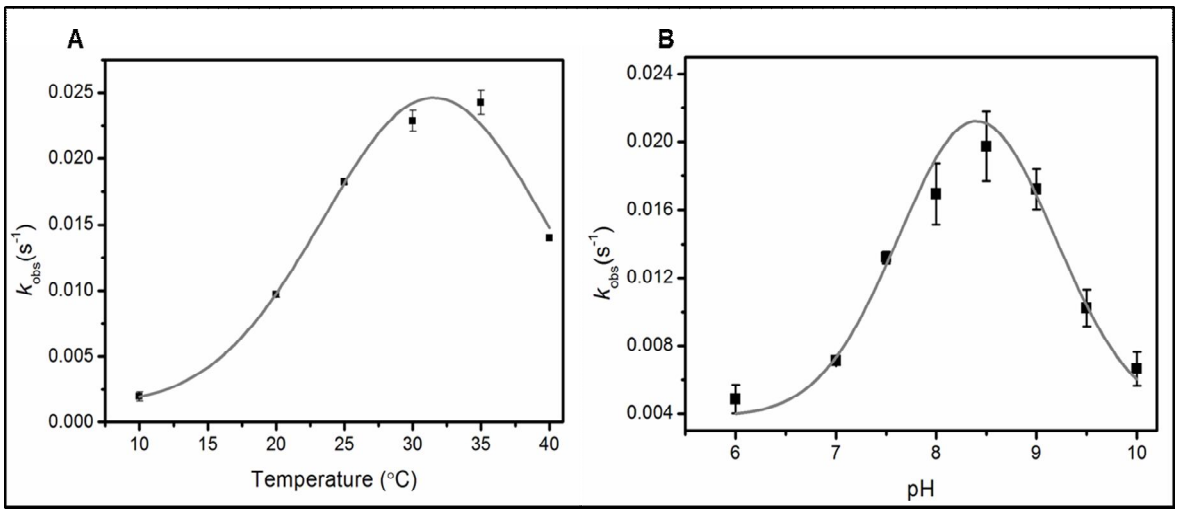


**Figure 4.6. Effects of temperature and pH on ΔKMO394 activity.** The biochemical activity was assayed with 500 μM ΔKMO394, 200 μM L-KYN and 200 μM NADPH. The enzymatic reaction was monitored by following the decrease in absorbance of NADPH at 340 nm with temperatures ranging from 10 to 40ºC (Panel A) and pH ranging from 6 to 10 (Panel B). The temperature profile was fit to a hyperbola and the pH profile was fit to two pKa's equation.

The temperature has a major effect on the activity of ΔKMO394, with the highest activity achieved at temperatures between 30-35°C and a rapid decrease on either side of this interval (Figure 4.6A). The activity was also found to be stable when assays were performed with enzyme that had been pre-incubated at the same temperature over a period of at least 20 minutes. However, the enzyme started to precipitate upon prolonged incubation at temperatures higher than 35°C and consequently, further steady state and

inhibition assays were carried out at 30°C. The optimal temperature range for the activity of yeast KMO is in the same range as described in section 3.2.3 for recombinant human KMO ($T_{opt}$= 33-38°C) and is similar to reported results carried out in crude or partially purified mammalian KMOs under similar conditions [208, 210]. No published data is available regarding the optimal temperature for yeast KMO.

An activity pH-profile was also obtained for the *Sc*KMO enzyme (Figure 4.6B). ΔKMO394 was most active between pH 7.5 and pH 9 with an optimum pH at 8.5. Analysis of the pH profile using the two p$K_a$'s equation (Equation 2) gave a first p$K_a$ of 7.2 and a second p$K_a$ of 9.5. On either side of these values the enzyme activity decreases significantly.

The pH optimum obtained for ΔKMO394 is comparable with previous reports on mitochondrial preparations of *Sc*KMO where maximal KMO activity was observed at a pH of 8.0[250]. The value obtained is also in the same range for recombinant *Hs*KMO described in section 3.2.3 where the optimum pH was 8.0.

## 4.4. KINETIC ASSAYS OF ΔKMO394

As mentioned in the previous section, KMO activity can be monitored by following the decrease in absorbance of NADPH at 340 nm. A complete kinetic analysis of ΔKMO394 was carried out by using initial-velocity measurements of the overall reaction at varying L-KYN or NADPH concentrations as described in Section 3.2.4. Apparent steady-state parameters were measured at an optimal temperature (30ºC) and pH (pH 8.5) for ΔKMO394 so that the values could be directly comparable to published data.

The initial kinetic analysis of ΔKMO394 was carried out with NADPH concentrations ranging from 0-200 μM based on the $K_m$ values reported in the literature [250]. However, using this range of concentrations the enzyme activity did not saturate. The extinction coefficient of NADPH (6.22 mM $cm^{-1}$) limited the use of concentrations higher than 200 μM in a standard cuvette due to the high absorbance and therefore an accurate $K_m$ for NADPH was not determined in this way. Consequently, the kinetic analysis was performed by following the formation of the product 3-HK by HPLC, as

described in section 2.2.9. 3-HK was quantified by comparison with a 3-hydroxykynurenine calibration curve.

Figure 4.7 shows the initial-velocity measurements of ΔKMO394 activity at varying concentrations of L-KYN and NADPH. The $K_m$ values for both substrates were determined by fitting the rate of turnover to the Michaelis Menten equation (Equation 1).

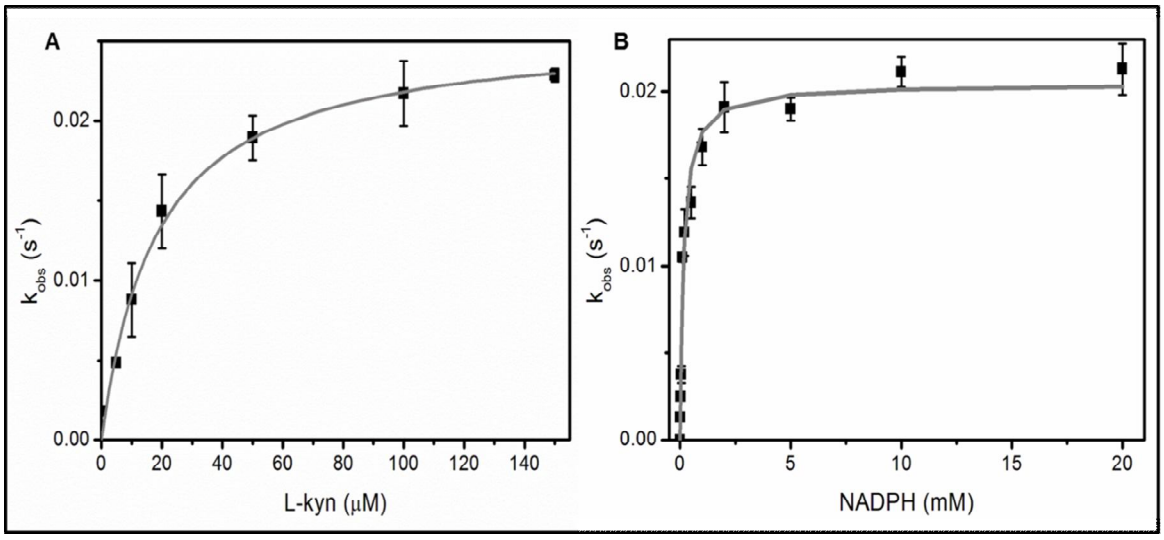


**Figure 4.7. Overall initial-velocity measurements of ΔKMO394 activity at varying concentration of L-KYN (Panel A) and NADPH (Panel B).** $K_m$ values were calculated by fitting the data to the Michaelis-Menten equation.

**Table 4.1. Apparent steady-state parameters for ΔKMO394**

| Kinetic Coefficients | Values |
|---|---|
| $K_{m\ NADPH}$ (μM) | 155.7 ± 26 |
| $K_{m\ L\text{-}KYN}$ (μM) | 17.9 ± 2.5 |
| $k_{cat}$ ($s^{-1}$) | 0.02 ± 0.003 |

The kinetic analysis of recombinant ΔKMO394 shows a hyperbolic dependence on the concentration of L-KYN with an experimental $K_m$ value (17.98 ± 2.5 μM) that is similar to those observed for native protein in *Saccharomyces cerevisiae* mitochondria preparations ($K_m$ = 40 μM) [250]. In contrast, $K_m$ for NADPH ($K_m$ = 155.7 ± 26 μM) is approximately 10-fold higher than $K_m$ values previously reported in the literature for

native *Saccharomyces cerevisiae* ($K_m$ = 16 μM) [250], as well as for higher organisms such as *Rattus norvegicus* ($K_m$ = 23 μM) [9].

Although there is no published data regarding the rate of turnover for *Sc*KMO, the $k_{cat}$ of approximately 0.02 $s^{-1}$ is significantly slower than the rate obtained in the previous chapter for recombinant *Hs*KMO ($k_{cat}$ = 0.89 $s^{-1}$). The turnover number is also significantly lower than those obtained for KMO from other organisms [207, 251]. Although we were not able to purify full length *Sc*KMO with a C-terminal His-tag, the expression levels were sufficient to carry out enzyme activity assays using the soluble lysate fraction. The concentration of the enzyme was estimated by Western Blot and compared with pure ΔKMO394 of known concentration. The activity of both enzymes was compared by following the formation of the product 3 hydroxykynurenine by $C_{18}$ reversed-phase HPLC. The full length *Sc*KMO was estimated to give a $k_{cat}$ = 0.13± 0.02 $s^{-1}$ which is approximately 6 times higher than ΔKMO394.

It is possible that the lower turnover number in the truncated protein could be engineered result of the C-terminal deletion of the protein. As previously explained in Chapter 3, there is evidence that the C-terminal region might be involved in the catalytic activity of the enzyme, although its role is not completely clear. From the results obtained for human truncated KMO (Chapter 3), we hypothesise that it might be related to NADPH binding. This hypothesis has now been further explored by studying individually the reductive half reaction of the catalytic cycle (see below).

## 4.5. KINETICS OF THE REDUCTIVE HALF REACTION

The rate of reduction of the flavin cofactor by NADPH was measured spectrophotometrically using stopped-flow methods. Studies of reaction processes by stopped-flow methods enable analysis of reaction rates on the millisecond timescale and can be used to directly determine the rate constants for the reductive half-reaction of KMO. ΔKMO394 was mixed anaerobically with high concentrations of NADPH (10 mM) and in the presence and absence of 500 μM L-KYN or inhibitor (UPF 648). The rate of flavin reduction was monitored at 450 nm and the transients obtained were fitted to a single exponential (Figure 4.8). The reduction rates obtained are similar to the $k_{cat}$ value ($0.02s^{-1}$) calculated using steady-state experiments, suggesting that reduction by NADPH

is the rate-determining step of the reaction. The limiting rate constant obtained for the free enzyme is similar to the rate of reduction in the presence of the L-KYN substrate but is approximately two-fold lower in the presence of the UPF 648 inhibitor. These results are not in accordance with reports from several class A flavoprotein monooxygenases, in which flavin reduction by NADPH is strongly stimulated by formation of the enzyme-substrate complex [188]. Results from *Pseudomonas fluorescens* KMO had shown that reduction of complex KMO-L-KYN is 2500 faster compared to the free enzyme [206].

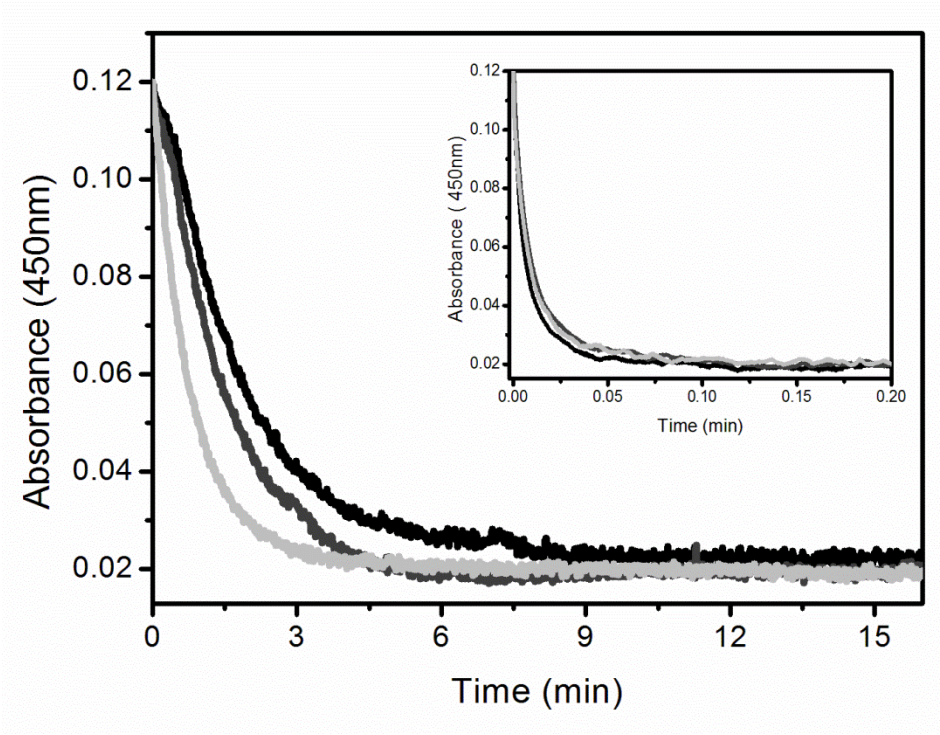


**Figure 4.8: Reductive half reaction of ΔKMO394 in the presence and absence of ligands**. Anaerobic mixtures of 20 $\mu$M KMO (Black trace) and saturating concentrations of L-KYN (Dark grey trace) and UPF 648 (Light grey trace) were mixed against anaerobic NADPH (10 mM) on a stopped-flow spectrophotometer at 10 °C. The decrease in flavin absorbance was observed at 450 nm. The insect depicts the same reaction but performed with Dithionite instead of NADPH. Traces obtained were fit to a single exponential.

**Table 4.2. Rate constants for ΔKMO394 upon reduction with NADPH and Dithionite**

| | NADPH | Sodium Dithionite |
|---|---|---|
| **ΔKMO394** | $0.009 \pm 9x10^{-4}$ $s^{-}$ | $1.9 \pm 0.04$ $s^{-1}$ |
| **ΔKMO394L-KYN** | $0.012 \pm 1x10^{-4}$ $s^{-1}$ | $1.4 \pm 7x10^{-4}$ $s^{-1}$ |
| **ΔKMO394UPF 648** | $0.02 \pm 3$ $x10^{-4}$ $s^{-1}$ | $1.5 \pm 0.03$ $s^{-1}$ |

The reductive half reaction of ΔKMO394 was also measured by substituting NADPH with sodium dithionite as an electron donor, in order to infer the possible involvement of NADPH in the low activity of the enzyme (Figure 4.8 *Inset* and Table 4.2). Interestingly, the rate constants for flavin reduction of ΔKMO394 with sodium dithionite are much higher compared to reduction with the NADPH cofactor. However, they are now similar to the reduction rates observed for *Pseudomonas fluorescens* KMO-L-KYN complex by NADPH ($k_{obs}$= 4.9 ± 0.3 $s^{-1}$) [206], providing further evidence that binding of NADPH may be limiting the catalytic efficiency of ΔKMO394. It is likely that the NADPH binding site of ΔKMO394 may be less accessible or structurally modified by the C-terminal deletion in this protein. This hypothesis will be discussed further throughout Chapter 5.

As the reductive half reaction with NADPH occurs on the minutes timescale, the dependence of the observed rate constant for reduction of ΔKMO394 on the concentration of NADPH was carried out anaerobically using a standard spectrophotometer rather than a stopped-flow instrument. This was achieved by mixing ΔKMO394 with different concentrations of NADPH in the presence of an excess of L-KYN substrate and by fitting the flavin absorbance changes at 450 nm to a single exponential equation to obtain an apparent rate constant.

Representative absorbance changes for the reduction of ΔKMO394 are shown in Figure 4.9 at different concentrations of NADPH. The dependence of the rate of reduction on NADPH concentration yielded an apparent $K_m$ for NADPH of 1.08 ± 0.3 mM (Figure 4.10). This value is approximately 6-fold higher than the $K_m$ value obtained from the

steady state measurements (see above) and at this stage it is unclear why such a discrepancy should exist.

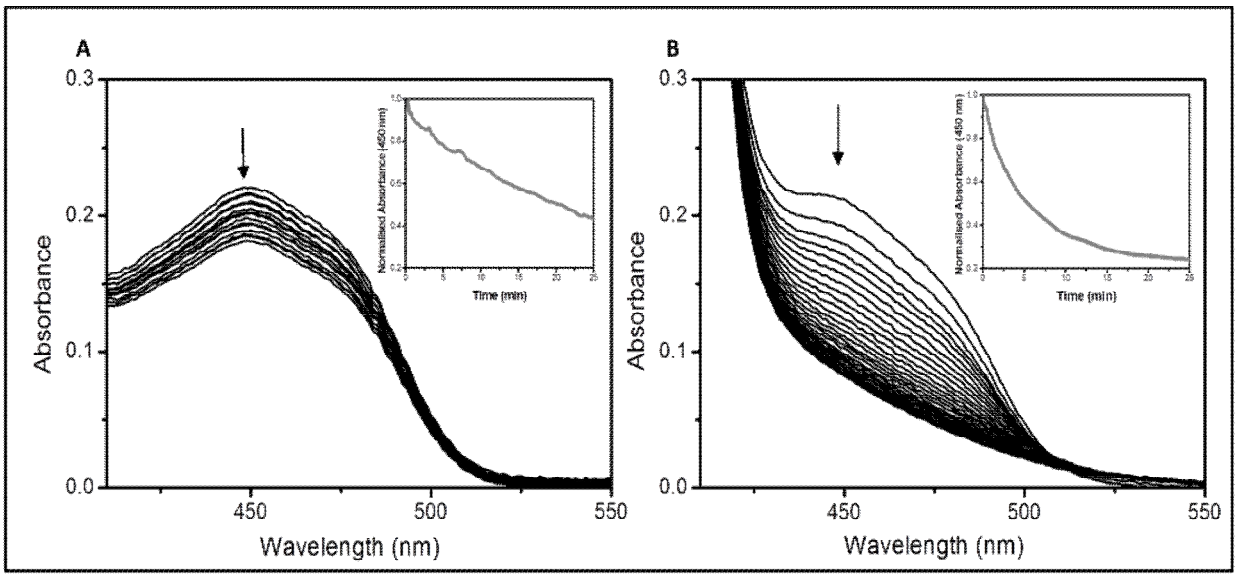


**Figure 4.9. Absorbance changes due to the reduction of ΔKMO394 with different concentrations of NADPH.** Anaerobic mixtures of 20 $\mu$M ΔKMO394 were titrated with 70 μM (Panel A) and 20 mM NADPH (Panel B) and the reaction was monitored for 10 minutes in cycle mode to compare the reduction rate. The insets of both panels show the absorbance changes at 450 nm over 25 minutes.

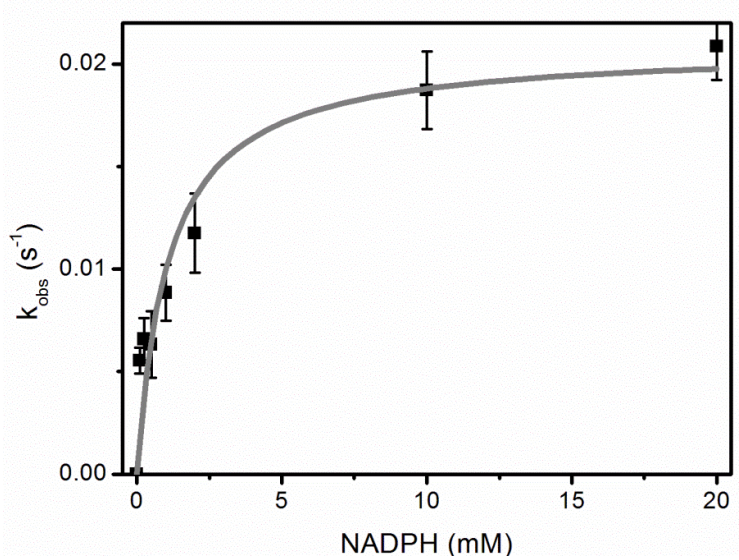


**Figure 4.10. Dependence of the observed reduction rate constant of ΔKMO394-L-KYN on the concentration of NADPH**. Anaerobic mixtures of 20 $\mu$M ΔKMO394 in the presence of an excess of L-KYN were titrated with different concentrations of NADPH (0-20mM) and the flavin absorbance changes at 450 nm were measured and fitted to a single exponential equation to obtain an apparent rate constant. The dependence of the apparent rate constants on the concentration of NADPH was fitted to a one site binding equation.

## 4.6. KINETIC ANALYSIS OF THE OXIDATIVE HALF REACTION

In order to study the mechanism of the oxidative half reaction of ΔKMO394, the anaerobically reduced KMO-L-KYN complex was mixed with oxygenated buffer using a stopped-flow spectrometer (Figure 4.11).

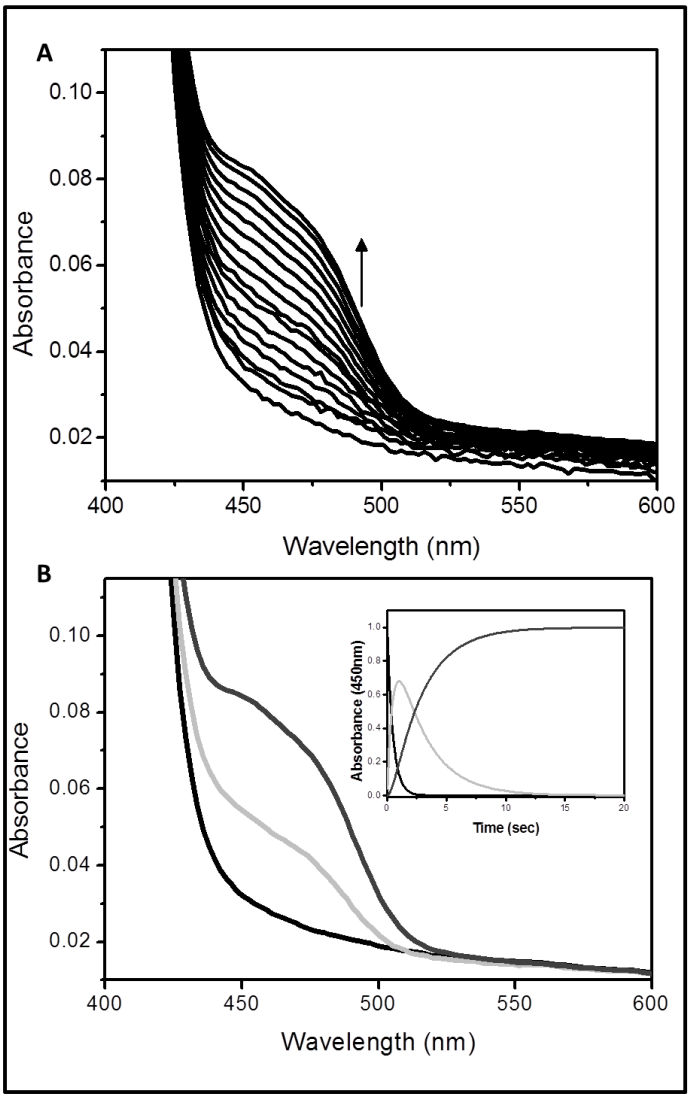


**Figure 4.11. Oxidation of ΔKMO394 in the stopped-flow instrument.** A) Raw data Spectral changes recorded after mixing equal volumes of the fully reduced L-KYN-KMO complex and oxygenated buffer The spectrum corresponds to the fully reduced enzyme, and the oxidized enzyme ($\lambda_{max}$ of 450 nm), respectively. The arrow indicated the formation of the oxidized enzyme. B) Pure deconvoluted intermediate spectra observed in the reoxidation of the KMO-Lkyn complex resulted from global analysis, indicating a two-step process of oxidation. Inset: Relative concentration of species over time

The raw data shows that in the presence of molecular oxygen the KMO-L-KYN complex fully oxidises with the formation of a peak at 450 nm characteristic of FAD molecule (Figure 4.11A). The data were analysed using global analysis where the spectral changes were fitted to a sequential model of A → B → C (Figure 4.11B). In the deconvoluted spectrum of species B the intermediate that accumulates after mixing with dioxygen is similar to the spectrum of the oxidised enzyme and may arise after hydroxylation of L-KYN. It is possible that this species is the C4a-hydroperoxyflavin intermediate, which is the hydroxylating species that is typically formed in this class of flavoproteins. However, it was difficult to confirm the identity of the species as this intermediate would typically be expected to absorb in the 370 – 380 nm region and is complicated by the overlapping spectra of the L-KYN substrate, 3-HK product and the NADPH cofactor in this same wavelength region. In subsequent stopped-flow experiments on the oxidative half reaction the reaction was followed by measuring the increase in absorbance at 450 nm. Biphasic absorbance transients were observed for KMO in the presence and absence of L-KYN upon mixing with oxygen (Figure 4.12). The observed rate constant for the first phase revealed a hyperbolic dependence on the concentration of molecular oxygen with rate constants of $k_1$ = 2.1 $s^{-1}$ in the absence of L-KYN and $k_1$ = 1.8 $s^{-1}$ in the presence of L-KYN. It was possible to calculate an apparent $K_m$ for oxygen of 341.8 ± 54 μM, However, at low oxygen concentrations it should be noted that the rate of the first phase is similar to that of the second phase (Figure 4.12 *Inset*), which makes an accurate determination of the first rate constant more difficult. In previous studies the rate of the first phase has shown a linear dependence on oxygen concentration and it has been suggested that it is likely to represent the binding of molecular oxygen to the enzyme followed by the formation of the C(4a)-hydroperoxide species. However, the apparent hyperbolic dependence on oxygen concentration in the current study suggests that the reaction may be more complicated and it is likely that additional experiments will be required to confirm the identity of this intermediate. Additional studies were also carried out in the presence of the UPF 648 inhibitor in order to compare the oxidative rate constants relative to the physiological substrate L-KYN (Table 4.3). Interestingly, the fact that the inhibitor complex gets fully oxidised supports the hypothesis that the oxidative half reaction is not dependent on the binding of the substrate with an activated ring but can undertake the subsequent steps with a different ligand. The observed spectral changes are similar to those observed in the presence of the

native substrate L-KYN, although the first rate constant for the KMO-UPF 648 complex is slightly decreased ($k_1$=1.3 $s^{-1}$), suggesting that the oxygen binding site might be occupied or structurally disturbed in the presence of the KMO inhibitor.

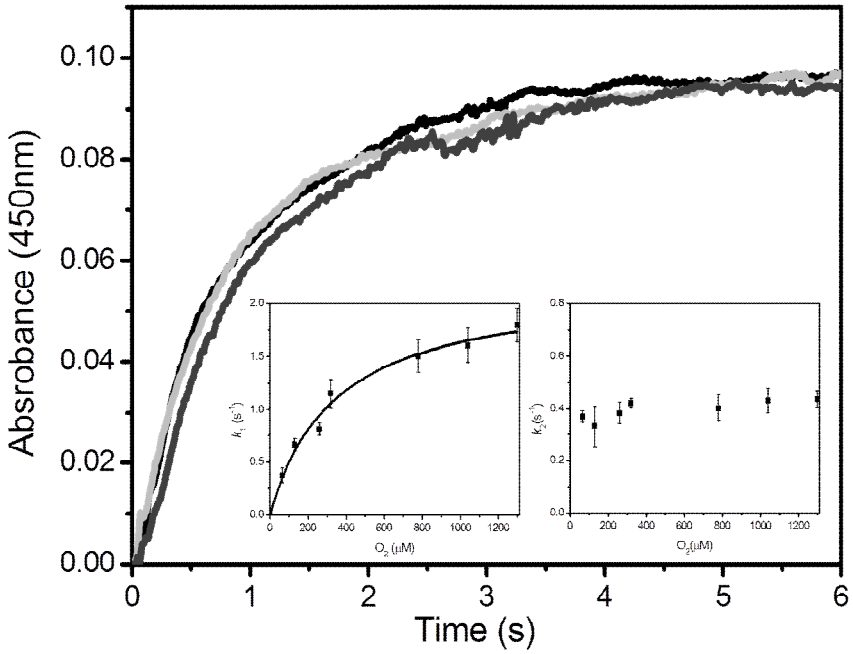


**Figure 4.12. Oxidative half reaction of ΔKMO394 in the presence of oxygen.** Absorbance traces for KMO in the presence (in black) and absence of L-KYN (in light grey) and in the presence of UPF 648 (dark grey) showing the oxidation of the flavin cofactor with saturating $O_2$. *Inset*: dependence of the observed rate constants, $k_1$ and $k_2$ on the concentration of dioxygen for KMO-L-KYN.

The rate of the second phase showed little or no dependence on the concentration of oxygen with rate constants of $k_2$ = 0.3 $s^{-1}$ in the absence of L-KYN and $k_2$ = 0.4 $s^{-1}$ in the presence of L-KYN. Similar results were also reported for the oxidative half reaction of *Pseudomonas fluorescens* KMO[198]. Consequently, this phase has been attributed to the hydroxylation step where the distal oxygen reacts in an electrophilic attack with the L-KYN substrate to form the hydroxylated product, water and the flavin C(4a)-hydroxide which is then hydrated to the oxidised enzyme. There is no evidence of the hydroxyflavin species as a second intermediate possibly because this species is formed instantly after the hydroxylation of the aromatic substrate. According to their results, the second intermediate C4(a)-hydroxyflavin was not observed and therefore they suggested that the dehydration of hydroxyflavin does not depend on the release of the product and takes

place instantly after the hydroxylation of the aromatic substrate. The rate of the second phase is also reduced in the presence of the UPF 648 inhibitor, suggesting that a bound ligand may also affect this process.

**Table 4.3. Rate constants for the oxidative half reaction for ΔKMO394**

| | $k_1$ ($s^{-1}$) | $k_2$ ($s^{-1}$) |
|---|---|---|
| **ΔKMO394** | 2.1 ± 0.3 | 0.5 ± 0.04 |
| **ΔKMO394L-KYN** | 1.8 ± 0.4 | 0.4 0 ± 0.03 |
| **ΔKMO394UPF 648** | 1.3 ± 0.2 | 0.2 ± 0.04 |

## 4.7. INHIBITION ASSAYS OF ΔKMO394

The inhibition of ΔKMO394 activity by the KMO inhibitor UPF 648 was investigated by following the formation of the product 3-HK by reversed phase HPLC at saturating L-KYN conditions (500μM) and at varying UPF 648 concentrations. As previous results on the recombinant *Hs*KMO have already showed the efficacy of UPF 648 (Section 3.3.5) the main purpose of these measurements was to compare the inhibition constants of both enzymes in order to verify that the yeast enzyme is a good model for studying inhibitor binding in *Hs*KMO. UPF 648 is a tight binding inhibitor and therefore the data from the inhibition studies was fitted to the Morrison equation. Additional explanations on tight binding inhibitors and the use of the Morrison's equation are described in Section 3.3.5.

As with the *Hs*KMO, UPF 648 also shows tight binding inhibition for yeast ΔKMO394 with an apparent $K_i$ of 73.96 ± 14.3 nM (Figure 4.13). This value is in the same range to previous studies carried out in gerbil models with an $IC_{50}$ = 40 nM [172], providing further evidence that UPF 648 is a very attractive ligand to use in future co-crystallization studies. Comparisons with *Hs*KMO will be discussed further in Section 4.9.

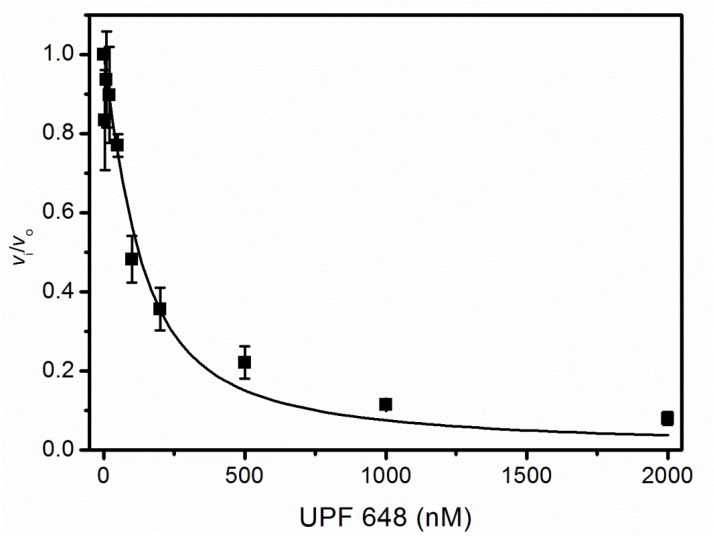


**Figure 4.13. Fractional velocity of 3-HK formation as a function of UP648 concentration with *S. cerevisiae* KMO**. 100 nM enzyme was incubated with 2 mM NADPH, 500 μM L-kyn and different concentrations (0-2 μM) of the inhibitor UPF 468. The product formation was analysed by reversed-phase HPLC. The data were fitted to the Morrison equation for tight binding inhibitors and yielded an apparent $K_i$ = 73.96 ± 14.3 nM.

## 4.8. LIGAND BINDING ASSAYS OF ΔKMO394

Binding assays, based on changes in the fluorescence emission spectra of FAD, were conducted to determine the binding affinity ($K_d$) of substrates or KMO inhibitors to ΔKMO394. As explained in Section 3.2.4., certain substrates and analogues are able to quench or enhance the fluorescence of the FAD depending on any conformation changes in the active site. The fluorescence of the FAD cofactor, which was recorded after excitation at 450 nm, has been measured at different ligand concentration after titration of the ligand the enzyme solution. Fluorescence spectra of ΔKMO394 in the absence and presence of different ligands are shown in Figure 4.14. The binding isotherm of the interactions between each compound and ΔKMO394 is also shown in the respective inset panels.

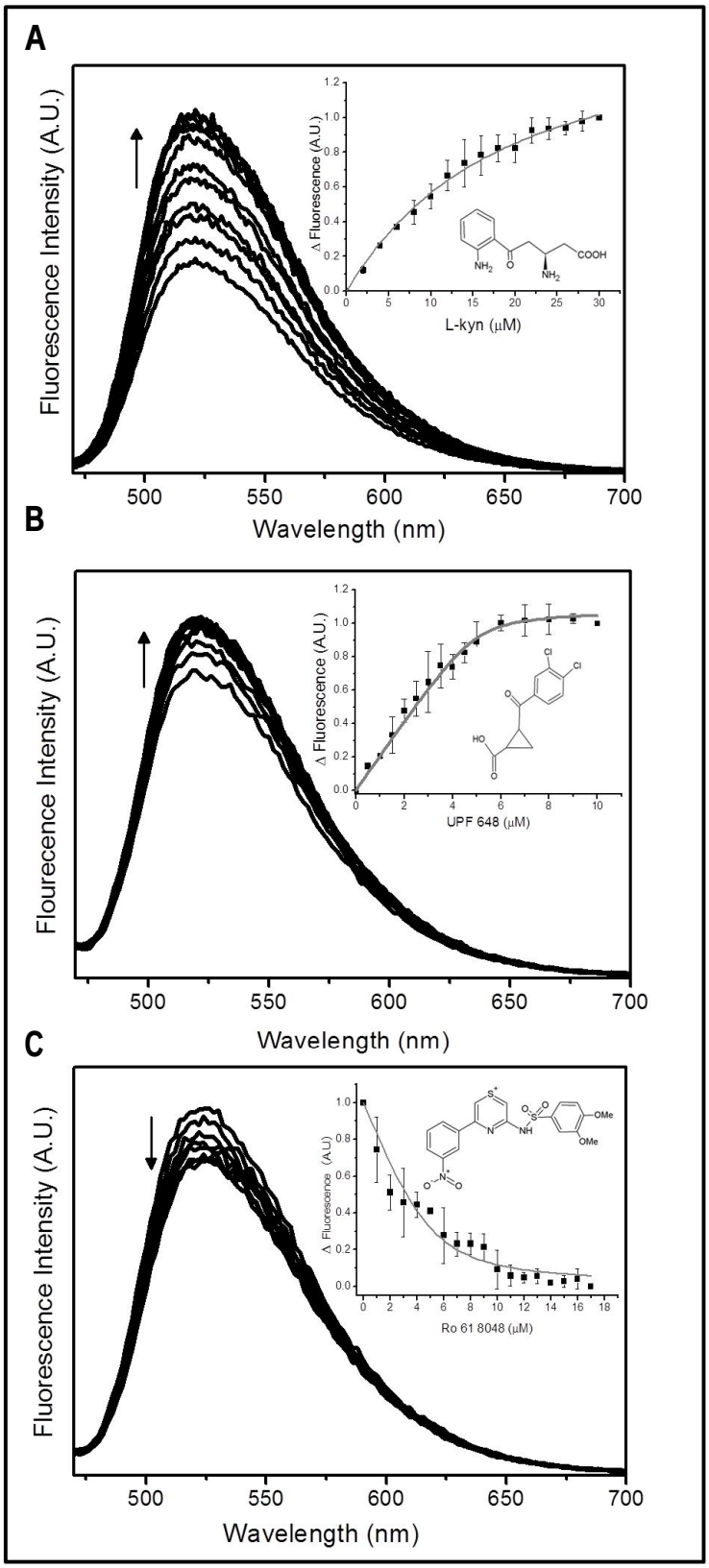


**Figure 4.14. Measurements of the binding constants for L-KYN, UPF 648 and Ro 61-8048 by ligand perturbation of flavin fluorescence emission**. Titration of ligands into 5 μM ΔKMO was carried out under aerobic conditions at 25 ºC. The perturbation in fluorescence emission was followed at 520 nm using an excitation wavelength of 450 nm. (A) Titration of L-KYN (0-30μM from *top* to *bottom*) to ΔKMO394 led to an increase in the FAD fluorescence. *Inset*: Fluorescence changes at 520 nm as a function of L-KYN concentration. Fitting of the data to the Morrison equation yields an observed $K_d$ of 14.53 ± 1.6 μM. (B) Titration of UPF 648 (0-10 μM from *bottom* to *top*) to ΔKMO394 led to an increase in the FAD fluorescence *Inset*: Fluorescence changes at 520 nm as function of UPF 648 concentration. Fitting of the data to the Morrison equation yields an observed $K_d$ of 137.7 ± 8.3 nM. (C) Titration of Ro 61-8048 (0-17 μM from *top* to *bottom*) to ΔKMO394 led to a decrease in the FAD fluorescence *Inset*: Fluorescence changes at 520 nm as a function of the Ro 61-8048 concentration. Fitting of data to the Morrison equation yields an observed $K_d$ of 750.3 ± 132.4 nM.

**Table 4.4. Dissociation constants for the binding of selected KMO drugs and substrate to ΔKMO394**

| Substrate/Inhibitor | $K_d$ |
|---|---|
| **L-KYN** | 14.5 ± 1.6 μM |
| **UPF 648** | 137.7 ± 8.3 nM |
| **Ro 61-8048** | 750.3 ± 132.4 nM |

Binding of the L-KYN substrate led to an increase in the fluorescence of the FAD cofactor at 520 nm in a dose-dependent manner giving a dissociation constant of 14.5 ± 2 μM (Figure 4.14A). The dissociation constant obtained for the physiological substrate is within a factor of 4 of the $K_d$ calculated for the truncated form of *Hs*KMO (See section 3.2.4) and in both cases an enhancement of the FAD fluorescence was observed upon titration with L-KYN, suggesting that the binding mode of the substrate is conserved in yeast and human KMO. As previously mentioned in Section 3.2.4, the enhancement in the fluorescence suggests that conformation changes in ΔKMO394 upon ligand binding expose the flavin isoalloxazine ring to the solvent, which leads to the increase in the fluorescence signal.

An enhancement in the flavin fluorescence was also observed in the titration of ΔKMO394 with the UPF 648 inhibitor (Figure 4.14B). The observed $K_d$ was 138 ± 8 nM, which indicates a tight binding of the ligand to the ΔKMO394, as expected from the apparent $K_i$ of 74 ± 14.3 nM previously obtained during inhibition assays (Section 4.7). In addition, the fluorescence changes upon ligand binding are similar to those of the natural substrate, suggesting a similar mode of binding, which may well be expected as the UPF 648 inhibitor is a substrate analogue.

The KMO inhibitor Ro 61 80-48 was also tested to explore the conformation changes induced in the active site upon ligand binding (Figure 4.14C). Interestingly, while the previous ligands enhanced the FAD fluorescence, Ro 61-8048 quenched the fluorescence with an observed $K_d$= 750.3 ± 132 nM. This suggests that binding of this ligand may cause a conformational rearrangement of the surrounding protein that ensures that the FAD is less solvent exposed. The same behaviour was also observed for truncated *Hs*KMO, suggesting a similar mode of binding to both enzymes (Section 3.2.4). In combination, these results suggest that ΔKMO394 might undergo different

conformational changes and binding modes compared to the physiological substrate, possibly binding in a second binding pocket re-side of FAD. However, importantly both human and yeast KMO enzymes show a comparable mechanism in the binding mode of Ro 61-8048. The dissociation constant is 20 times higher compared with the $IC_{50}$ value of 37 nM that was previously reported for this inhibitor in KMO from rat kidney mitochondria preparations [173] but is within a factor of 3 when compared to recombinant truncated *Hs*KMO (Section 3.2.4).

## 4.9. CONCLUDING REMARKS

Initial experiments to elucidate the catalytic mechanism of *Hs*KMO (Chapter 3) using spectroscopic, kinetics and crystallographic methods were not possible due to the poor stability and low expression yield of this protein. Given the difficulties in expression of high quantities of *Hs*KMO suitable for further biochemical and biophysical assays we turned our attention to *Sc*KMO, which is closely related to *H*sKMO (38 % identity and 51 % similarity). This chapter has presented a quantitative biochemical characterisation of *Sc*KMO. Expression of full-length *Sc*KMO in *E. coli* yielded a protein fragment with a lower molecular weight than anticipated and electrospray ionisation mass spectrometry indicated proteolytic cleavage at residue 394. Consequently, a truncated ΔKMO394 (deleted in residues 395 to 460) version of the enzyme was engineered by site-directed mutagenesis to define the exact cleavage point and to prevent further cleavage. The biochemical characterisation of ΔKMO394 was carried out by using a combination of UV/Visible absorbance spectroscopy, fluorescence spectroscopy, HPLC-based assays and stopped-flow analyses and revealed important kinetic and ligand binding properties of this enzyme. The purified ΔKMO394 enzyme was active as a flavin-dependent monooxygenase and therefore, facilitates structural characterisation of KMO, which will be discussed in more detail in Chapter 5.

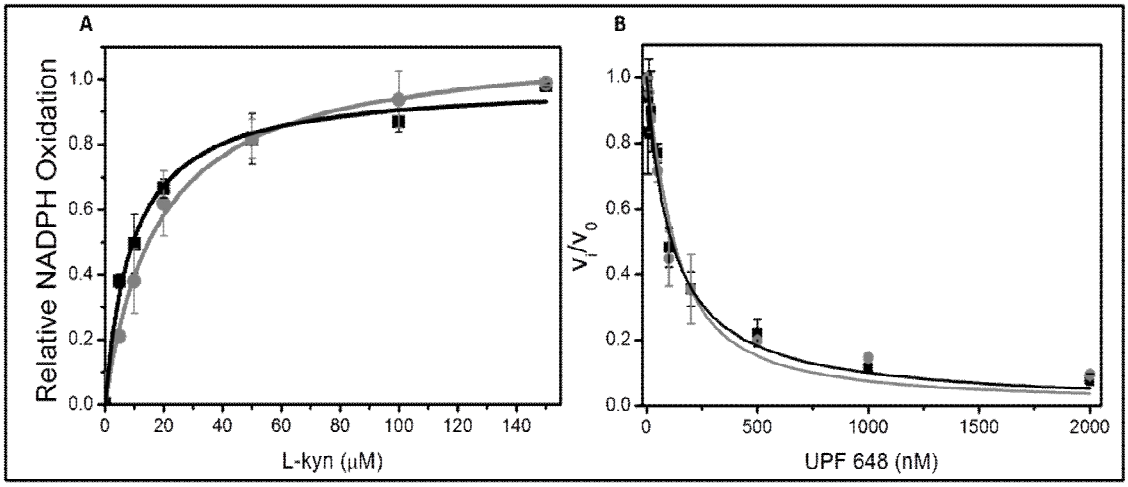


**Figure 4.15. Kinetic comparison between *Hs*KMO and *Sc*KMO.** (A) Initial velocity measurements of *Hs*KMO (grey trace) and *Sc*KMO (black trace) activity varying the concentration of the substrate L-kynurenine. The data was fitted with Michaelis Menten equation yields a $K_m$= 24.35± 4.1 and $K_m$= 18.24± 2.58 for *Sc*KMO. (B) Fractional velocity of 3-HK formation as a function of UP648 concentration with *Hs*KMO (grey trace) and *Sc*KMO (black trace). 100nM enzyme was incubated with 2mM NADPH, 500μM L-kyn and different concentrations (0-2μM) of the inhibitor UPF 468. The product formation was analysed by reversed-phase HPLC. The data was fitted with Morrison equation for tight binding inhibitors yields an apparent $K_i$ = 56.74 ± 8.02 nM for HsKMO and $K_i$ = 73.96 ± 14.3 for *Sc*KMO

**Table 4.5- Apparent kinetic constants for *Hs*KMO and *Sc*KMO**

| Enzyme | $K_m$ L-KYN (μM) | $K_{i\ app}$UPF648 (nM) |
|---|---|---|
| ***HsKMO*** | 24.4 ± 4.1 | 56.7 ± 8.0 |
| ***Sc*KMO** | 18.2 ± 2.6 | 73.9 ± 14.3 |

ΔKMO394 generated 3-HK in multiple turnover measurements and was inhibited by UPF 648 ($K_i$ 74 nM) with a similar potency to that with *Hs*KMO (Figure 4.15 and Table 4.5). Figure 4.14 and Table 4.5 illustrate *Hs*KMO and *Sc*KMO present similar kinetic and inhibitor constants, which confirm that the mechanism of the KMO enzyme is remarkably well conserved between yeast and humans. As UPF 648 is a substrate analogue of L-KYN and both ligands bind with the same selectivity in human and yeast KMO, it is tempting to speculate that the active site of KMO is preserved among both enzymes, providing support that *Sc*KMO is a good homology model for the study of *Hs*KMO.

However, a comparison of the rate of turnover between ΔKMO394 and full length yeast and human KMO revealed that the activity of ΔKMO394 is significantly slower (6 and 44 fold lower respectively). The simplest and most likely explanation for this difference is that the truncation of the C-terminal region of the protein plays an important role in the activity of the protein. As previously explained in Chapter 3, studies conducted on full length pig KMO and C-terminal deletion mutants revealed that a segment of 20 amino acid residues close to the C-terminus is necessary for the enzymatic activity although its exact role remains elusive [246].

Moreover, the results from the reductive half reaction studies suggest that the truncation of the protein may influence the NADPH binding properties of the enzyme. The reduction of flavin by NADPH is the rate-limiting step in the activity of ΔKMO394 and we have shown that the rate of flavin reduction with sodium dithionite is considerably higher. In addition, the dissociation constant obtained for NADPH (1.08 ± 0.3 mM) is significantly higher than previously published data where $K_d$ values are typically in the μM range [250, 9].

An alternative explanations for the lower turnover might be related to the the expression of a eukaryotic protein in a prokaryotic system. It is known that native KMO from *Saccharomyces cerevisiae* is localised in the membranes of mitochondria and promitochondria [212, 250]. Consequently, the overexpression of full length soluble KMO in *E. coli*, without the C-terminal membrane anchoring region, may lead to a decrease in the catalytic activity of the enzyme. In addition, it is known that KMO protein that is expressed in *E. coli* will not contain any of the native post-translational modifications or glycosylation. Although there are relatively few studies reporting such changes it is possible that the catalytic activity of an enzyme could be modulated by post-translational modifications [252]. As protein phosphorylation is the most frequent type of post-translational modification in *Saccharomyces cerevisiae* [252] phosphorylation modification prediction software has been used to estimate any probable phosphorylation sites in the *Sc*KMO protein sequence (Figure 4.16). The attachment of a phosphoryl group is hypothesised to affect the energy landscape of the modified protein, but in the majority of cases the tertiary structure of the enzyme is not affected [253]. The main advantage of avoiding post-translational modifications by using *E. coli* as a host expression system is that such modifications have been linked to intrinsically disordered

protein regions and therefore the possibility of crystallising *Sc*KMO would be significantly lower.

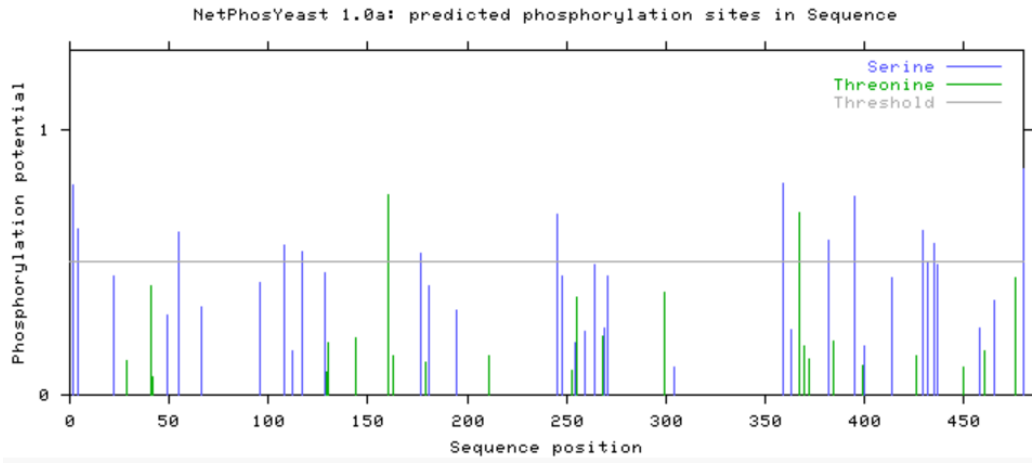


**Figure 4.16. Prediction of phosphorylation sites in *Sc*KMO using the online tool NetPhosYeast 1.0 Server** [254].

Stopped-flow measurements were also used to study the mechanism of the oxidative half reaction. The rates constants that were determined for this step are in the same range to KMO from *P. fluorescens* [198] and are comparable to other flavoprotein monooxygenases [255]. The biphasic traces and analysis of deconvoluted spectra suggests the formation of only one intermediate during the oxidation step, which is hypothesised to be the C(4a)-hydroperoxide species. The second intermediate that is typically characteristic of the oxidation step in flavoportein monooxygenases was not observed. Many other studies have shown similar results, suggesting that the dehydration of the hydroxyflavin does not depend on the release of the product and takes place instantly after the hydroxylation of the aromatic substrate. Further details on the mechanism of KMO and a comparison with other flavoproteins monooxygenases will be discussed in the next chapter, which describes the structural characterisation of *Sc*KMO and ΔKMO394 and complements the results from this chapter.

# CHAPTER 5

# STRUCTURAL CHARACTERISATION OF SACCHAROMYCES CEREVISIAE KYNURENINE 3-MONOOXYGENASE

# 5. STRUCTURAL CHARACTERISATION OF SACCHAROMYCES CEREVISIAE KYNURENINE 3-MONOOXYGENASE

## 5.1. INTRODUCTION

Inhibition of KMO is an attractive therapeutic strategy for several acute and chronic neurological diseases, particularly HD. Despite major interest in therapeutically targeting KMO only a few potent inhibitors are currently available [178, 8]. In order to rationally design novel KMO inhibitory compounds through structure-based drug design it is vital to obtain structural information for this protein, both native and bound to existing drugs. This will permit docking screens using virtual libraries of compounds, which may ultimately identify novel inhibitor scaffolds that possess the selectivity and affinity necessary to open novel opportunities for therapeutic intervention in HD and other brain disorders.

However, since *Hs*KMO is membrane associated, it has proven to be extremely difficult to obtain sufficient quantities of this enzyme for structural studies and therefore there is no structural knowledge of this enzyme. It is widely known that the crystallisation of membrane-associated proteins is a very challenging process that often ends in the failure to obtain diffraction quality crystals. This fact is consistent with the rarity of such structures solved by X-ray crystallography. To date, the investigation of the binding modes of possible KMO inhibitors has been carried out using structure and ligand-based computer-aided design tools based on structurally and functionally related enzymes [180, 181].

Chapter 3 reports attempts to crystallise *Hs*KMO and despite extensive efforts this study failed to yield crystals. In Chapter 4 we provide strong evidence that *Sc*KMO is functionally similar to *Hs*KMO and therefore it can be used as a model to develop new therapeutic inhibitors of the highly related (38 % identity and 51% similarity) *Hs*KMO.

The current chapter reports on the biophysical and structural studies of *S*cKMO, both the initial proteolytic soluble form of *Sc*KMO and ΔKMO394 (deleted in residues 394 to 460). The elucidation of the *Sc*KMO structure in complex with inhibitor UPF 648

will also be reported as well as the modelling of the physiologic substrate L-KYN. The residues involved in ligand binding will be verified by site directed mutagenesis and validated by inhibitor binding and kinetic assays.

## 5.2. BIOPHYSICAL CHARACTERISATION OF *Sc*KMO

*Sc*KMO was successfully isolated, expressed and purified, as described in Chapter 4. A sufficient quantity of soluble protein was obtained to carry out further biophysical and structural studies. Prior to structural analysis, *Sc*KMO was subjected to Thermofluor and MALLS analysis to determine their suitability for crystallography.

### 5.2.1. Thermofluor Assay

The Thermofluor assay is used to determine optimal buffer and additive conditions to further maximize the protein stability and increase the chances of protein crystallisation. Optimal buffers are necessary to allow proteins to be concentrated to the high levels often used in crystallography (5-30 mg/mL).

The JBS Solubility Kit buffer screen (Section 2.2.12 Material and Methods) consisting of 24 buffer solutions at different pH values, ranging from 4.5 to 9.0, with concentrations of 50 mM was used to screen *Sc*KMO. Among the 24 buffers tested, there were some buffers that appeared to be more favourable for *Sc*KMO stabilisation, particularly ammonium acetate pH 7.0, HEPES pH 7.5, and potassium/sodium phosphate pH 7.0 with $T_m$ of 54.5ºC, 50.2ºC and 47.8ºC respectively (Table 5.1). The ammonium acetate pH 7.0 and HEPES pH 7.5 buffers were subsequently used for further assays including the addition of additives capable of improving protein stability (Table 5.2).

**Table 5.1. Melting temperatures of buffer screen of ScKMO**

| Buffer | pH | *T*m (°C) |
|---|---|---|
| Citric acid | 4.0 | 34.2 |
| Sodium/potassium phosphate | 5.0 | 43.2 |
| Sodium citrate | 5.0 | 42.8 |
| Sodium/potassium phosphate | 6.0 | 45.7 |
| Bis-Tris | 6.0 | 46.4 |
| Bis-Tris propane | 6.5 | 45.3 |
| Ammonium acetate | 7.0 | 54.5 |
| Sodium/potassium phosphate | 7.0 | 47.8 |
| HEPES | 7.5 | 50.2 |
| Imidazole | 8.0 | 42.8 |
| Tris | 8.5 | 39.3 |
| Control | 7.5 | 47.1 |

Buffers shown are from the JBS Solubility Kit part A. Buffers which did not produce a $T_m$ are not shown. Final concentrations for all buffers were 50 mM diluted from 100 mM stocks. . Sample control is in 20 mM phosphate buffer pH 7.5.

**Table 5.2. Melting temperatures of additive screen of ScKMO**

| Addtive | Buffer | *T*m (°C) | Buffer | *T*m (°C) |
|---|---|---|---|---|
| NaCl 200 mM | 1 [1] | 56.2 | 2[2] | 47.4 |
| NaCl 400 mM | 1 | 54.1 | 2 | 46.2 |
| Glycerol 20% | 1 | 55.3 | 2 | 44.3 |
| CHAPS 8mM | 1 | 53.3 | 2 | 40.2 |
| Dodecyl Maltoside 0.4% | 1 | 53.8 | 2 | 45.9 |
| BME 40mM | 1 | 55.7 | 2 | 47.3 |
| DTT 4mM | 1 | 54.2 | 2 | 44.6 |
| DTT 20mM | 1 | 53.9 | 2 | 43.1 |
| Sample control | 1 | 54.8 | 2 | 47.6 |

Additives shown are from the JBS Solubility Kit part B. Additives which did not produce a $T_m$ are not shown.

[1] Buffer 1 correspond to Ammonium Acetate pH 7.0

[2] Buffer 2 corresponds to HEPES pH 7.0

Enhanced thermal stability of *Sc*KMO was observed following the addition of 200 mM Sodium Chloride, 40 mM BME and 4mM DTT in ammonium acetate pH 7.0 buffer (Table 5.2). These results are consistent with previous reports of KMO protein from *Pseudomonas fluorescens* in which the enzyme is more stable with moderate concentrations of NaCl and increases its activity in the presence of reducing agents [207]. Although the addition of 20% Glycerol improved the thermal stability of *Sc*KMO by 0.5ºC, this component was not included in the final buffer. High concentrations of this additive tend to be avoided in crystallography as it inhibits nucleation. Non-enhanced thermal stability was observed with the addition of additives when in MOPS pH 7.0.

Following Thermofluor analysis *Sc*KMO crystallisation samples were initially made up in Ammonium Acetate pH 7.0 with the addition of 150 mM NaCl and 7 mM BME.

### 5.2.2. MultiAngle Laser Light Scattering(MALLS)

Prior to crystallogenesis, MALLS was conducted on *Sc*KMO to provide information about the polydispersity and aggregation state of the sample.

Traces from the light scattering and refractive index for *Sc*KMO were monitored and are shown in Figure 5.1. The traces show a single peak eluted after approximately 15 mL with average molecular weight of 47.8 kDa. The standard deviation (S.D.) of the $R_H$ is 20.6% across the three axes, indicating that *Sc*KMO is a globular monomeric protein in solution, consistent with the plot from the $M_r$ values, in which the molecular weight values remains constant over the duration of the elution peak (Figure 5.1 *Inset*). The single light scattering peak is concurrent with the refractive index peak.

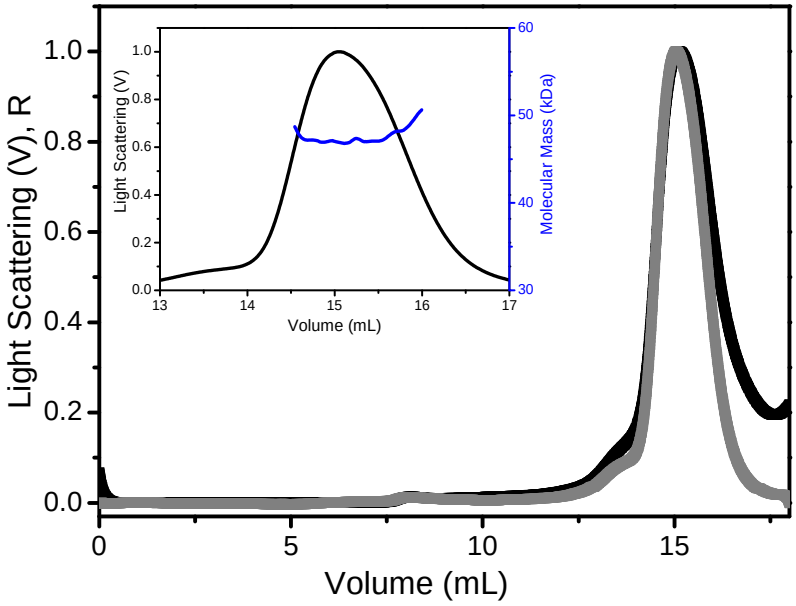


**Figure 5.1. MALLS analysis of *Sc*KMO.** Trace from a MALLS run of a sample of *Sc*KMO. Light scattering is indicated as a voltage and refractive index is a relative scale. A single peak elutes at approximately 15 mL indicating only one species of *Sc*KMO. *Inset* - Plot of the molecular masses against the elution volume.

Based on the primary sequence analysis, and according to the results obtained from EL-MS (Section 4.2), the molecular weight of the *Sc*KMO is approximately 47kDa, taking into account that the protein was cleaved by exoproteolysis at residue 396. This is consistent with the $M_r$ determined by MALLS and provides further evidence that *Sc*KMO exists as a monomer in solution and has been isolated in a form highly suitable for crystallographic studies. The lack of information in the literature regarding the oligomerisation state of KMO from *Saccharomyces cerevisiae* and other species of yeast did not allow a direct comparison with our results. As previously described in Section 3.2.6, the only study predicting the molecular weight and aggregation state of KMO was conducted in *Rattus norvegicus* KMO [210], suggesting a molecular weight of 200 kDa based on the elution pattern on size exclusion chromatography and results from SDS-PAGE. They have also concluded that native *R. novergicus* exists as dimer in solution [210], which differs from the results obtained in *Sc*KMO.

## 5.3. STRUCTURAL CHARACTERISATION OF *Sc*KMO

### 5.3.1. Crystallisation trials of ScKMO

Crystallogenesis trials of highly purified *Sc*KMO were performed using the sitting drop vapour diffusion technique as described in Section 2.2.14.1. Initial screening involved the use of five commercially available crystallisation screens from Molecular Dimensions (Newmarket, UK) (JCSG +, PACT, Clear Strategy I + II, Morpheus). A broad range of protein concentrations (7-16 mg/mL) were also tested to improve the chance of obtaining crystals. Co-crystallisation experiments were performed with L-KYN, UPF 648, Ro 80-6048 and NADPH in order to facilitate the formation of crystals. Proteins may be stabilised when they are complexed with a substrate through enhanced thermal stability and reduced flexibility [256, 257]. Furthermore, the complex structure with ligands would be also extremely useful to understand the mechanism of catalysis and the key residues involved in ligand binding. Ligand concentrations were calculated to be approximately 10 times the $K_d$ plus protein concentration.

Very few of the initially screened conditions gave rise to protein crystals either with or without ligands. *Sc*KMO crystals were obtained from JCSG + E12 (0.1M Imidazole 7.8, 11% w/v PEG 8K) and Clear Strategy II B7 (0.1M Sodium Acetate 5.5, 35% propanol). In both conditions the protein was screened at a concentration of ~14 mg/mL, with crystals forming over a period of ~72 h at 277K.

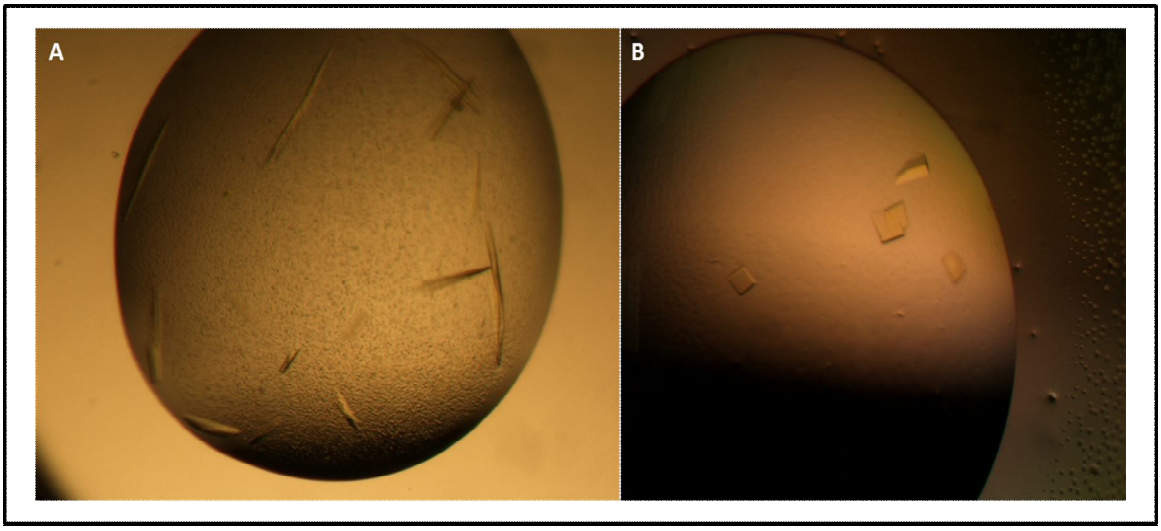


**Figure 5.2. Crystallogenesis of *Sc*KMO and ΔKMO394.** Crystals obtained from crystallisation trials of *Sc*KMO and ΔKMO394. (A) *Sc*KMO crystals obtained from B7 (0.1M Sodium Acetate 5.5, 35% propanol) CSS2 crystallisation screen, (B) *Sc*KMO crystals obtained from E12 (0.1M Imidazole 7.8, 11% w/v PEG 8K) JCSG crystallisation screen.

Two distinct crystal morphologies were observed (Figure 5.2). Condition B7 from Clear Strategy II gave rise to needles, whilst E12 from JCSG + produced crystals with a more plate like appearance. The presence of ligands during crystallogenesis did not produce any further variation in the observed morphology.

Both crystals display a yellow colour, indicating that the FAD cofactor was bound to the protein. Initial hit conditions were refined; through the use of grid screening variations were made in the pH, percentage of propanol and weight of PEG. Numerous *Sc*KMO crystals were obtained, particularly with the propanol conditions, the majority of them producing large isolated crystals. The colour and morphologies of crystals remained unchanged. Given the possibility that the crystals obtained by co-crystallisation with ligands would not retain those compounds, protein crystals were additionally soaked with saturated solutions of ligands solubilised in the mother liquor. Crystals with appropriate size were flash frozen in liquid $N_2$ and analysed at the Diamond Synchrotron (Didcot, Oxfordshire).

### 5.3.2. Data Collection and Phase problem

The data collection from the X-ray diffraction was analysed by Dr Colin Levy (University of Manchester). A complete data set was collected to 2.6 (Figure 5.3) Å resolution from a single crystal and belonged to space group $P2_1$. X-ray diffraction data were integrated and scaled using the program XDS as described in Section 2.2.14.2.

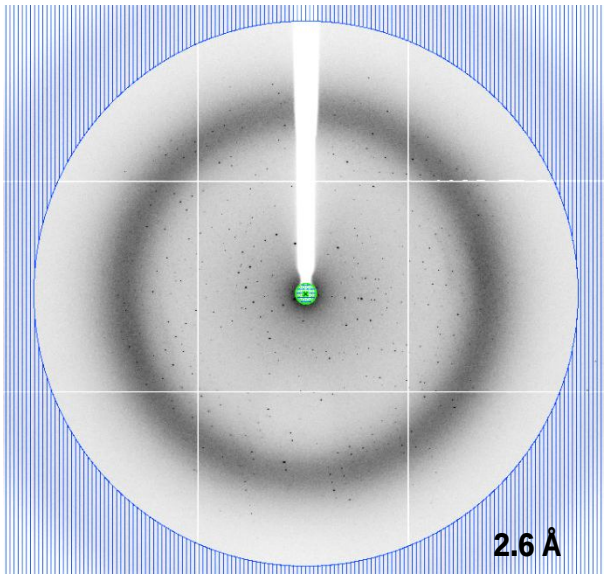


**Figure 5.3. Representative X-ray diffraction pattern for *Sc*KMO.** The X-ray diffraction pattern shows a resolution of 2.6 Å. Diffraction data from *Sc*KMO crystals were collected from single cryofrozen samples at the Diamond Light Source, Harwell, UK, with a wavelength of 0.9795 Å

Initial attempts to solve the structure of *Sc*KMO were made by molecular replacement (MR) using the PHBH structure (1Q5E) as a search model. However, these enzymes share only approximately 18% identity and no solution was found. Further studies carried out by Dr. Colin Levy using combined algorithms for protein structure modelling with those developed for crystallographic structure determination (Rosetta MR) [258] were also conducted but again these attempts proved fruitless. The results were not unexpected since MR is usually used efficiently for homologues with a sequence identity of 30% or higher [258].

Heavy atom soaks were carried out in an attempt to provide a multiple isomorphous replacement (MIR) [259, 260]. A variety of heavy atom reagents were screened but the majority of crystals were damaged after the soaking. Those crystals that were able to withstand the soaking procedure failed to yield any suitable derivatives.

The Single-wavelength Anomalous Dispersion (SAD) technique utilising the anomalous signal from Selenomethionine (SeMet) was also employed for phase determination. SeMet has been widely used as a phasing tool due to the relative ease with which this intrinsic anomalous scatter can be introduced into the target of choice. This technique avoids the problems associated with non isomorphism that often plague more traditional MIR [261]. Furthermore, in the majority of cases, the crystallisation of SeMet proteins tends to occur in similar conditions when compared to the wild type protein. There are several methods for prokaryotic expression of SeMet-labelled proteins which include the use of a methionine auxotroph strain of *E. coli*, the inhibition of methionine biosynthesis shortly before induction, growing the culture directly in LeMaster media supplemented with SeMet and the use of auto-inducing media with a non-auxotrophic strain [261]. The first attempts to produce *Sc*KMO-SeMet using the defined LeMaster medium resulted in a very low yield. Subsequently, a methionine inhibition method was applied. This technique supplements the minimal media with high concentrations of isoleucine, leucine, phenylalanine, lysine and threonine, efficiently shutting down methionine biosynthesis [261]. This repression is instigated immediately prior to induction and the introduction of SeMet into the media (Details of the method are described in Section 2.2.14.2).

The expression levels obtained using this method were comparable to that of the wild type *Sc*KMO providing evidence that the SeMet was not toxic to the cells. Purification of selenomethionine incorporated *Sc*KMO (*Sc*KMOSeMet) was conducted as described for conventional *Sc*KMO (Section 2.2.4.3) with the exception that all the buffers were degassed to avoid oxidation of SeMet. Crystals with similar shape to those for native *Sc*KMO were obtained in propanol conditions (0.1 M sodium acetate, pH 5.5, and 35 % isopropanol).

Initial phases were obtained from a single SAD data set collected at the selenium edge. Selenium sites were located using Phenix AutoSol [226] yielding an electron density map that could be auto traced using Phenix AutoBuild [227].

### 5.3.3. Structure Determination and Refinement

As mentioned in the previous section, single-wavelength anomalous dispersion (SAD) data set at the selenium edge was used for initial phase determination. The resulting model was completed through iterative rounds of rebuilding in COOT [228] and refinement in Phenix [229]. Structure validation with MOLPROBITY [231] was integrated as part of the iterative rebuild and refinement procedure. Subsequent structures were solved by molecular replacement in PHASER [230] using this initial SeMet derived structure as the template. Data collection and refinement statistics for *Sc*KMO, *Sc*KMO-SeMet are presented in Table 5.3.

**Table 5.3. X-ray data collection and refinement statistics for *Sc*KMOSeMet and*Sc*KMO**

| | ***Sc*KMOSeMet** | ***Sc*KMO** |
|---|---|---|
| **Data collection** | | |
| Space group | $P2_1$ | $P2_1$ |
| Cell dimensions | | |
| *a*, *b*, *c* (Å) | 59.1, 99.4, 85.3 | 58.9, 98.7, 85.9 |
| $\alpha$, $\beta$, $\gamma$ (°) | 90, 105.6, 90 | 90, 105.1, 90 |
| Resolution (Å) | 2.6(2.71-2.6) | 2.4(2.5-2.4) |
| $R_{meas}$ | 9.3(75.5) | 9.1(68.4) |
| $I/\sigma I$ | 12.0(2.1) | 15.0(2.5) |
| Completeness (%) | 99.3(98.4) | 98.3(95.3) |
| Redundancy | 3.9(3.9) | 2.6(2.6) |
| **Refinement** | | |
| Resolution (Å) | 2.6 | 2.4 |
| No. reflections | 29686 | 36692 |
| $R_{work/}$ $R_{free}$ | 19.8 / 25.6 | 19.9 / 24.4 |
| No. atoms | | |
| Protein | 6035 | 5892 |
| Ligand/ion | 106 | 106 |
| Water | 107 | 243 |
| B-factors | | |
| Protein | 26.6 | 33.6 |
| Ligand/ion | | |
| Water | 17.5 | 29.4 |
| R.m.s deviations | | |
| Bond lengths (Å) | 0.009 | 0.002 |
| Bond angles (°) | 1.3 | 0.6 |

The final model of *Sc*KMO contains residues 1-97 and 101-390 and the bound FAD cofactor (Figure 5.4). The missing residues have no clear electron density. The crystal form contains a putative KMO dimer in the asymmetric unit (Figure 5.5A). PISA analysis (Protein Interfaces, Surfaces and Assemblies) [262] of the crystallographic dimer indicates that this is likely an artifact of crystallization and is not reflected in the solution state. This interpretation is further supported by the results obtained from the Electrospray Ionisation Mass Spectrometry and MALLS revealing a molecular weight consistent with a monomer in solution.

The overall fold of *Sc*KMO is similar to the flavin-dependent hydroxylase family [255] and the highest structural similarity, based on a search of the Protein Data Bank with the program DALI [263] is obtained with 2-methyl-3-hydroxypyridine-5-carboxylic acid oxygenase [264], an enzyme from the vitamin $B_6$ catabolic pathway (rmsd of 2.3 Å over 310 Cα, overall sequence identity 16%, Q score 0.43, Z score 15.0).

*Sc*KMO forms a complex of three discernible domains (Figure 5.4B). There is the FAD-binding domain that exhibits the typical dinucleotide-binding fold, including 5 β-sheets and 4 α-helices, and this domain is responsible for the interactions between the protein and FAD in an extended conformation (blue domain).

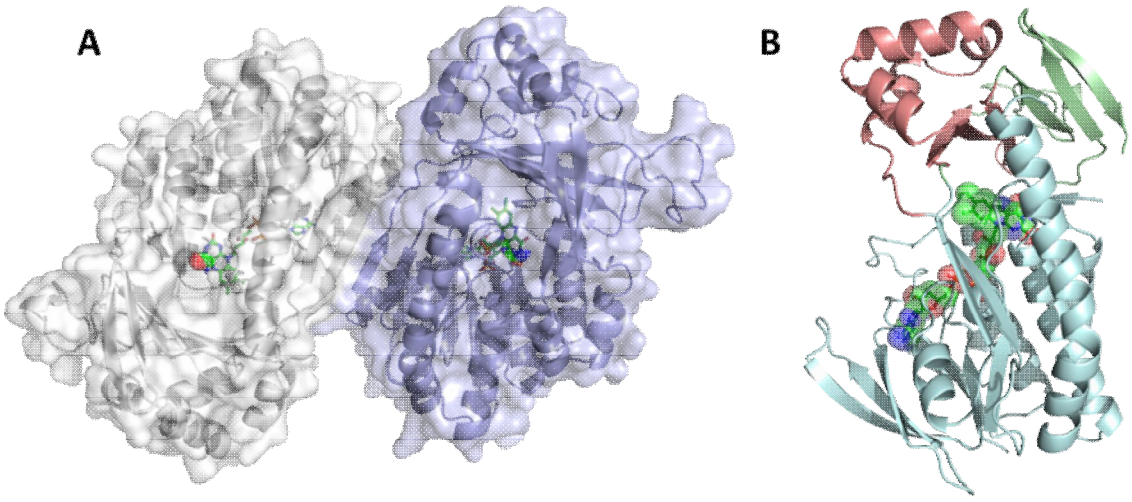


**Figure 5.4. Structural features of ScKMO.** (A) A depiction of the *Sc*KMO dimer displayed in ribbon format with transparent surface. FAD is represented as sticks and coloured by all atom type. (B) *Sc*KMO monomer represented in ribbon format coloured according to the different domains; In salmon is the head domain, in light green the lateral domain and in light blue the FAD binding domain.

The large FAD binding domain (residues 1-76, 97-192 and 293-390) contains the three main FAD sequence motifs. The first sequence (residues 9-14) contains the Rossmann fold motif GxGxxG [193], commonly found in FAD- and NAD(P)H-dependent monooxygenases and is generally found at the N-terminal part of the protein sequence. The second sequence (residues 313-314) contains the GD sequence in hydroxylases and forms part of a helix and the following loop. The third conserved motif is a part of a loop (residues 168-169) and contains the DG short amino acid sequence motif commonly shared for this group of enzymes.

The functions of the other two domains (salmon and green domains) were not clear based on the apo structure of *Sc*KMO, although subsequent structures will show that they are involved in ligand binding (Section 5.7).

The *re*-face of the FAD is connected to the solvent by a narrow water-filled cavity that runs perpendicular to the active site cleft (Figure 5.5A). The isoalloxazine ring moiety is located at one end of the large cleft that runs through the protein interior, with a large part of FAD being exposed to the solvent region. The residues involved in FAD binding are shown in Figure 5.5B.

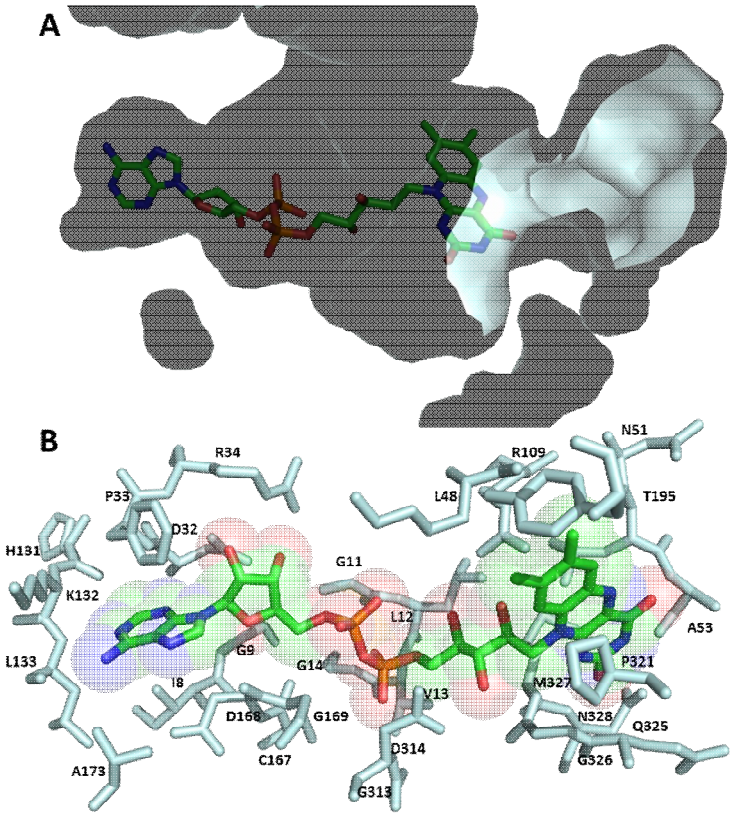


**Figure 5.5. *Sc*KMO FAD-binding site** (A) Surface cavity of FAD-binding site. (B) Residues around the FAD-binding site are shown as stick models and labelled.

The C-terminal α-helix becomes increasingly disordered from residue 380 onwards with residues 390 and above not visible in the electron density map. Subsequent structural characterisation of *Sc*KMO was conducted on the engineered truncated form ΔKMO394 to prevent ambiguities in the definition of the C-terminal region and to prevent future problems with further cleavage. Additionally, the protein yield obtained was significantly higher for this truncated form (15 mg/L of culture) when compared to the cleaved *Sc*KMO (4mg/L of culture) which facilitates further structural work.

## 5.4. STRUCTURAL CHARACTERISATION OF ΔKMO394

### 5.4.1. Crystallisation and structural determination of ΔKMO394

Highly purified ΔKMO394 was subjected to crystal trials across the same range of conditions tested for *Sc*KMO. ΔKMO394 diffraction quality crystals were grown in condition E12 (0.1M Imidazole 7.8, 11% w/v PEG 8K) from JCSG + crystallisation screen, in trays containing 14mg/mL of ΔKMO394, with crystals forming over a period of ~24 h at 277K.

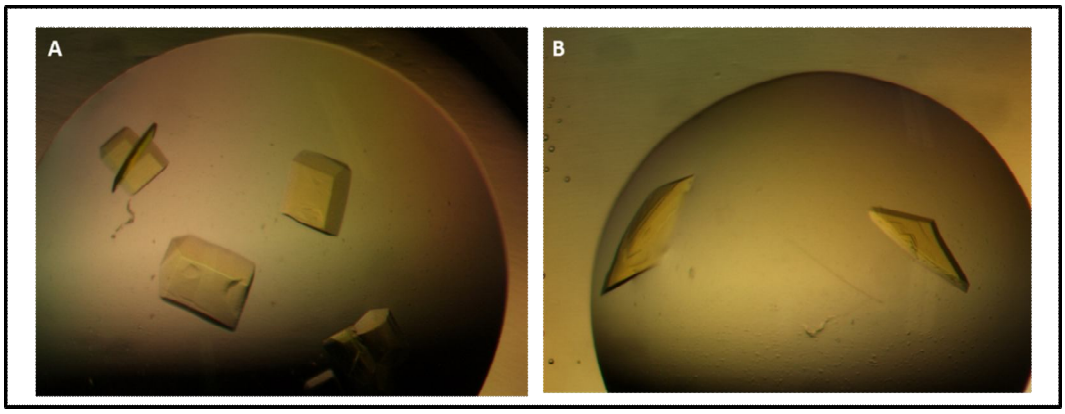


**Figure 5.6. Crystallogenesis of ΔKMO394.** ΔKMO394 crystals obtained from B7 (0.1M Sodium Acetate 5.5, 35% propanol) CSS2 crystallisation screen.

ΔKMO394 crystals are significantly larger compared to ScKMO crystals and present a variety of shapes (Figure 5.6A / B ). They also display a yellow colour

indicative of FAD bound to the protein. ΔKMO394 crystals were reproduced in a variety of PEG conditions with the colour of the crystals remaining yellow and the morphology identical. ΔKMO394 structures were solved by molecular replacement in PHASER [230] using this initial *Sc*KMOSeMet derived structure as the template (Table 5.4).

The final model of ΔKMO394, obtained at a resolution of 1.8 Å, was isostructural with *Sc*KMO. ΔKMO394 did give rise to a more readily reproducible crystal form and therefore this engineered truncated form was used for all further crystallisation trials in order to obtain structure complexes with ligands.

**Table 5.4. X-ray data collection and refinement statistics for ΔKMO394, ΔKMO394UPF and ΔKMO394His$^-$**

| | **ΔKMO394** | **ΔKMO394UPF** | **ΔKMO394His-** |
|---|---|---|---|
| **Data collection** | | | |
| Space group | $P2_1$ | $P2_1$ | $P2_1$ |
| Cell dimensions | | | |
| *a*, *b*, *c* (Å) | 58.4, 98.7, 85.4 | 73.0, 89.8, 82.8 | 59.1, 98.8, 86.3 |
| $\alpha, \beta, \gamma$ (°) | 105.3 | 90, 110.6, 90 | 90, 105.8, 90 |
| Resolution (Å) | 1.8(1.9-1.8) | 2.1(2.2-2.1) | 2.0(2.1-2.0) |
| $R_{meas}$ | 7.1(141.2) | 6.1(80.8) | 7.6(60.6) |
| $I/\sigma I$ | 16.5(2.4) | 14.7(2.6) | 10.4(2.7) |
| Completeness (%) | 99.6(99.7) | 99.2(99.0) | 98.6(99.3) |
| Redundancy | 3.4(3.5) | 3.3(3.4) | 3.4(3.5) |
| **Refinement** | | | |
| Resolution (Å) | 1.8 | 2.1 | 2.0 |
| No. reflections | 83287 | 55578 | 60714 |
| $R_{work/}$ $R_{free}$ | 18.7 / 22.2 | 19.6 / 23.5 | 20.1 / 24.1 |
| No. atoms | | | |
| Protein | 6046 | 5776 | 6106 |
| Ligand/ion | 106 | 122 | 106 |
| Water | 584 | 358 | 414 |
| B-factors | | | |
| Protein | 21.8 | 13.8 | 42.8 |
| Ligand/ion | | 13.6 | |
| Water | 28.8 | 14.7 | 44.6 |
| R.m.s deviations | | | |
| Bond lengths (Å) | 0.007 | 0.003 | 0.008 |
| Bond angles (°) | 1.1 | 0.8 | 1.2 |

An overlay of the individual ΔKMO394 ligand free monomers reveals significant variation in two different positions (Figure 5.7A). The first disordered region is the C-terminal α-helix, with most monomers showing disorder beyond residue 380. The high flexibility of C-terminal α-helix does not seem to be involved in the catalysis of KMO and is hypothesised to be related to the truncation of the region of the peptide chain after residue 394, resulting in a flexible region being able to move away from the remainder of the protein. This flexibility could possibly disrupt some interactions within the protein and therefore could explain in part the slow turnover rate obtained for ΔKMO394. The linker region immediately following the second strand of the antiparallel β-sheet is also disordered with large variations occurring in the position of residues 96-97 and 101-104. The relative position of the FAD-binding domain and the six-stranded antiparallel β–sheet domain is also subject to minor variation, reminiscent of domain motion coupled to substrate binding documented for other members of this family [255].

The inherent flexibility in the relative position of both domains flanking the KMO active site in the absence of substrate is reflected in the distinct conformations observed for amino acids lining the active site (Figure 5.7B)

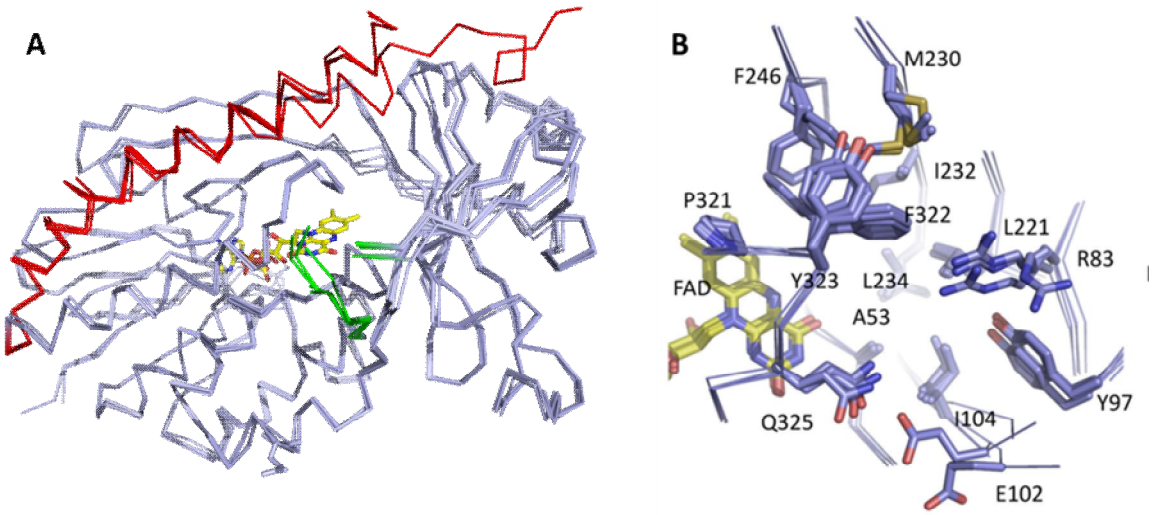


**Figure 5.7. Detailed view of the ΔKMO394 structural changes**. (A) Overlay of the 5 ligand-free KMO monomers displayed in ribbon format. The C-terminal region (residue 348 onwards) is coloured red, the flexible linker region (residue 96-104) is depicted in green.(B). Overlay of the free ΔKMO394 structures obtained from various crystal forms.

### 5.4.2. Structure of UPF 648 bound to ΔKMO394

We were able to co-crystallise ΔKMO394 with UPF 648 inhibitor, a tight-binding substrate-like inhibitor, in the same condition E12 (0.1M Imidazole 7.8, 11% w/v PEG 8K) from JCSG + crystallisation screen used for crystallisation of the apo-enzyme (Table 5.4). The electron density of the inhibitor was clearly observed in a pocket adjacent to the FAD *re*-face (Figure 5.8). The UPF 648 carboxylate group is bound by conserved residues Arg-83 and Tyr-97 while the aromatic dichlorobenzene moiety is flanked by several hydrophobic residues, including Leu-221, Met-230, Ile-232, Leu-234, Phe-246, Pro-321, and Phe-322 (Figure 5.8B). The binding of UPF 648 induced several structural changes in the enzyme, most notably the reorientation of the 321-325 loop flanking the *re*-side of the FAD (indicated by the arrow in Figure 5.8A). In addition, a minor reorientation in the position of the six-stranded antiparallel β-sheet domain with respect to the flavin binding domain is also evident (Figure 5.8B). Both of these changes result in increased disorder of the C-terminal alpha-helix, which is only visible up to Arg-359. The reorientation of the 321-325 loop is a direct consequence of adaptation of the active site to the presence of the vicinal chloride substituents of UPF 648, neither of which have a counterpart in the kynurenine substrate. To provide sufficient space for both chlorides, Phe-322 moves away from the active site, effectively occupying the position previously occupied by Tyr-323. In turn, the P321-Q325 loop reorients to compensate for the altered Phe-322 position.

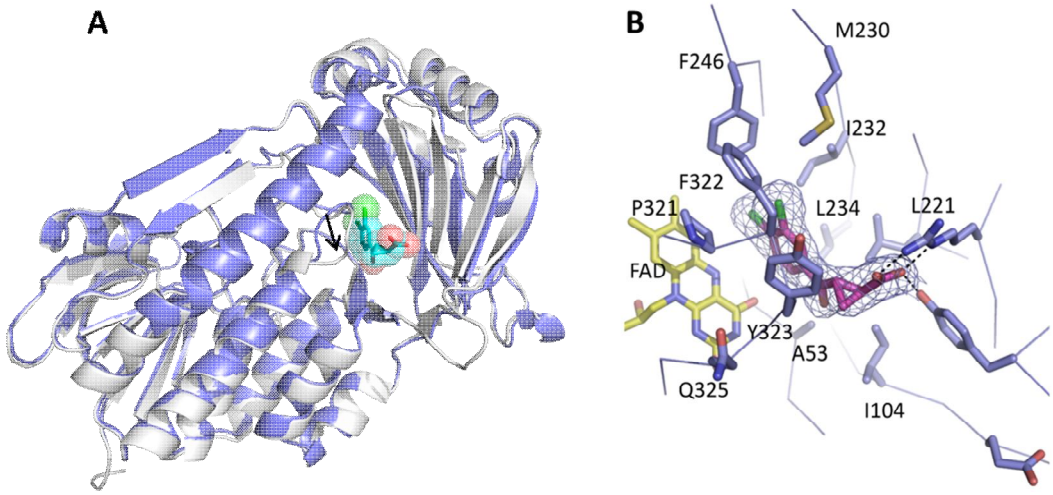


**Figure 5.8. A depiction of changes induced by binding of the KMO inhibitor UPF 648.** An overlay of ΔKMO394 and ΔKMO394UPF is presented, the unbound monomer coloured in grey. The UPF-

bound monomer is coloured in blue. The UPF ligand and the FAD are shown as atom coloured spheres. The arrow indicate the changes induced by binding of UPF 648. There is also a rearrangement of six-stranded antiparallel β-sheet domain.

### 5.4.3. Model of L-KYN bound to ΔKMO394

Attempts to obtain a complex with the physiological substrate kynurenine proved unsuccessful. Both co-crystallisation and soaking strategies were employed but failed to yield a suitable complex. One of the reasons that could explain the failure of achieving a complex with kynurenine or with any other ligand through soaking might lie in the presence of the N-terminal his-tag within the active site. Although this region was weakly defined in the electron density because of flexibility, within the confines of the crystal lattice it is clear that a proportion of his-tags encroach into the active site pocket. Whilst this might not be a problem for solution studies, it is likely to have a deleterious impact upon soaking studies. Hence, the N-terminal His-tag was efficiently cleaved (ΔKMO394-HIS$^-$) by overnight incubation with Thrombin as described in Section 2.2.4.3. ΔKMO394-HIS$^-$ was subsequently crystallised in the same conditions as ΔKMO394 (Table 5.4). However, despite extensive soaking experiments with different concentrations of kynurenine and several additional KMO inhibitors, no complex was produced.

The similarity between UPF 648 and the kynurenine substrate allows modelling of the latter in the KMO active site using the position of UPF 648 as a starting point (see Section 2.2.14.3). This suggests that the substrate is bound in a similar manner, but without any effect on the P321-Q325 loop. The aromatic substrate moiety is located in the conserved hydrophobic pocket (made by residues Leu-221, Met-230, Ile-232, Leu-234, Phe-246, Pro-321, and Phe-322) on the *re*-face of the flavin (Figure 5.9). In this case, additional polar contacts between the conserved Gln-235 and the kynurenine ketone group, and between the substrate aniline nitrogen and the FAD O4, are observed. While the amino acid carboxylate is bound by the Arg-83 and Tyr-97 motif, the amino group is devoid of direct interactions with the protein in this model. It is possible that an additional salt bridge is made between the kynurenine amine and the side chain of Glu-102, which is located on a highly flexible region of the KMO structure. However, the latter amino acid is often conservatively replaced by a Gln in other KMOs, indicating such an interaction is less critical to enzyme activity (Figure 5.9).

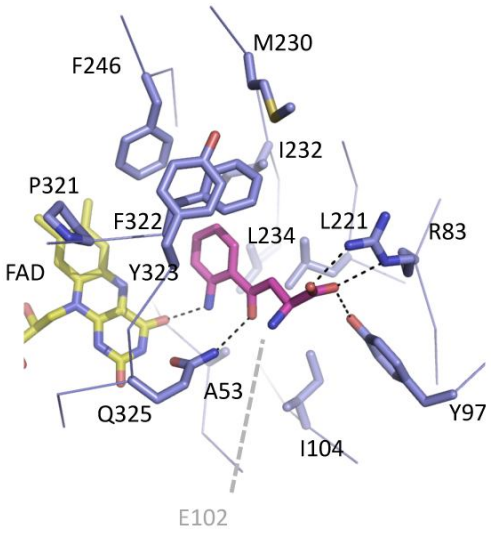


**Figure 5.9. Detailed view of the ΔKMO394 active site.** Model for the KMO:kynurenine complex.

Multiple sequence alignment was performed with several KMOs, ranging from bacterial to human enzymes, to confirm that the key residues in the active of *Sc*KMO were conserved among different KMOs (Figure 5.10). Interestingly, all residues implied by the KMO:kynurenine model to be involved in kynurenine binding are preserved across KMOs, which shows a conserved mechanism in the KMO catalysis.

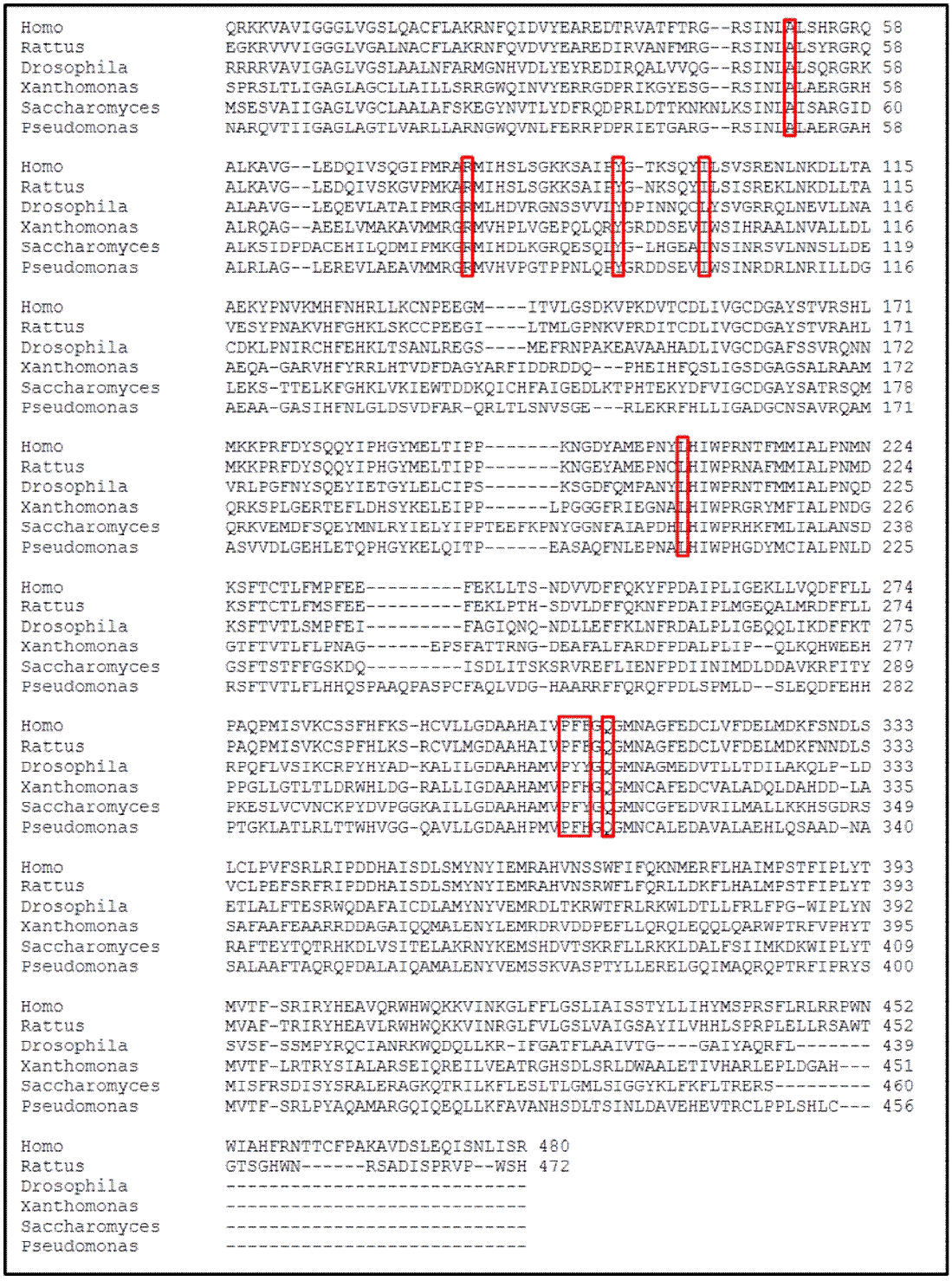


**Figure 5.10. Multiple alignment of amino acid sequences of KMO from diverse organisms.** *Homo sapiens* KMO (Accession number NP_003670), *Rattus norvegicus* KMO (Accession number NP_067604), *Drosophila melanogaster* KMO (Accession number A1Z746), *Xanthomonas oryzae* KMO (Accession number B2SIT6), *Saccharomyces cereviseae* KMO (Accession number P38169), *Pseudomonas fluorescens* (Accession number Q84HF5). Residues involved in ligand binding are conserved and highlighted in red.

### 5.4.4. Active site mutants of ΔKMO394

Based on the KMO:kynurenine model, the carboxylate moiety of the substrate forms a salt bridge with the side chains of Arg-83 and Tyr-97 and these interactions are critical to enzyme activity. Therefore the perturbation of these interactions is hypothesised to affect dramatically the binding of the substrate. The validation of this model was conducted by targeting the active site residue Arg-83. Two distinctive mutations were performed by site direct mutagenesis (see Section 2.2.1.3), by replacing the Arginine residue 83 to an Alanine and a Methionine. The choice of these mutations lies in the fact that the Alanine substitution could preserve the chemical bonds with the substrate but the smaller bulk would possibly interfere with the ligand binding, and Methionine, with an overall size similar to Arginine, it is not able to form chemical interactions with carboxy moiety of the substrate.

Both mutants were expressed and purified as described for wild type (Section 2.2.4.3) and the enzyme activity was compared to the wild type by following formation of the product 3-hydroxykynurenine by $C_{18}$ reversed-phase HPLC with excess of NADPH (2mM) and kynurenine (500 μM).

The enzyme activity was significantly compromised following mutations with 25% and 3% of wild-type activity for Ala-83 and Met-83 KMOs respectively (Figure 5.11), consistent with the model for kynurenine binding.

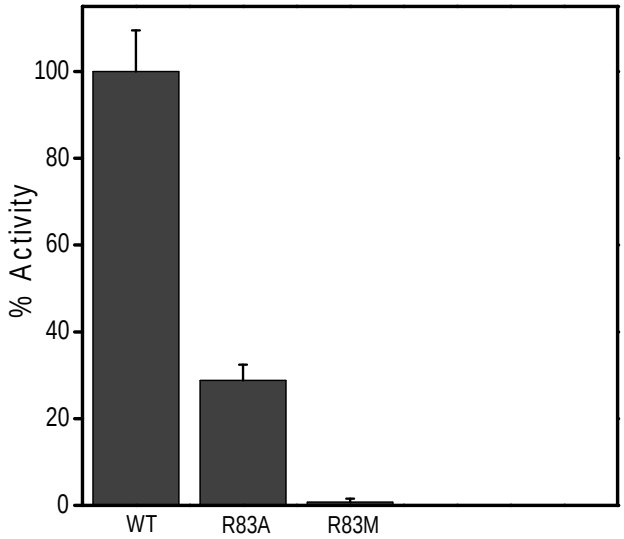


**Figure 5.11. Enzymatic activity comparison between wild type KMO and R83 mutants.** Enzyme activity is significantly reduced following mutation (< 25% and < 3% of wild-type activity for Ala-83 and Met-83 KMOs).

Additional kinetic assays to calculate the inhibition efficiency of UPF648 ($K_i^{app}$) for KMO mutants could not be carried out since the enzymatic activity was significantly compromised following mutations. Alternatively, fluorescence emission measurements were performed to determine dissociation constants ($K_d$) of the KMO inhibitor by ligand perturbation of flavin fluorescence (Figure 5.12).

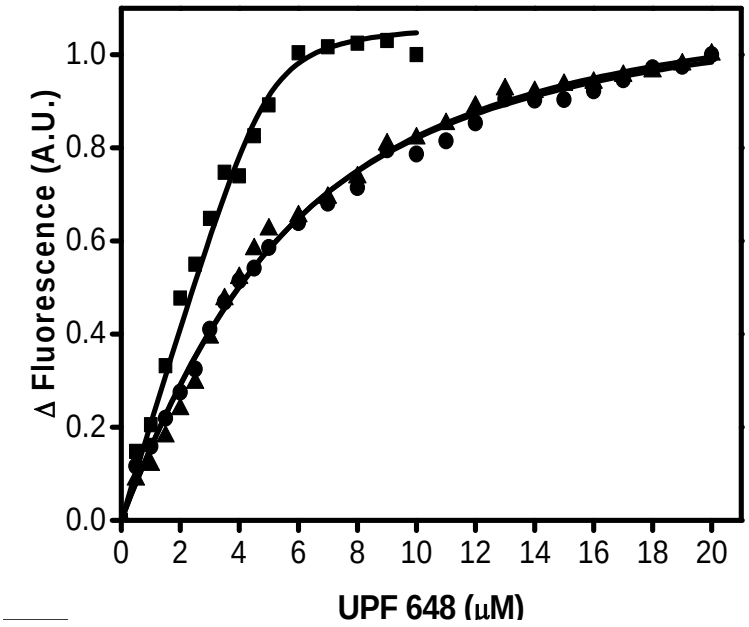


**Figure 5.12. Measurement of binding constant for KMO inhibitor UPF 648 by ligand perturbation of flavin fluorescence emission.** Titration of UPF 648 to 5 μM wild type KMO (closed squares), R83M (closed triangles) and R83A (closed circles) mutants resulted in perturbation of 520 nm fluorescence emission. Fluorescence changes at 520 nm as function of UPF 648 concentration were fitted to Morrison equation yields an observed $K_d$= 137.8 ± 8 nM for wild type KMO, $K_d$= 3.1± 0.2 μM for R83M and $K_d$= 3.2 ± 0.2 μM for R83A.

The affinity of R83A and R83M for binding of KMO inhibitor UPF 648 is extremely similar with $K_d$= 3.1± 0.2 μM and $K_d$= 3.2±0.2 μM respectively (Table 5.5) and these values are approximately 23 fold lower than that of native KMO consistent with the structure which implicates Arg-83 in inhibitor binding.

**Table 5.5: Dissociation constants ($K_d$) for binding of native and active-site mutants to UPF 648**

| | Native | R83A mutant | R83M mutant |
|---|---|---|---|
| $K_d$ UPF648 (μM) | 0.14 ± 0.008 | 3.1 ± 0.2 | 3.2 ± 0.2 |

### 5.4.5. Prediction of NADPH binding mode

Although many attempts were performed at either co-crystallising or soaking with NADPH, we were unable to obtain a structure in complex with the cofactor. The binding mode of NADPH in many NAPH-dependent flavoproteins such as Class B flavoprotein monooxygenases is relatively easy to predict due to the presence of two dinucleotide binding domains for binding FAD and NADPH, respectively [187]. However, the binding mode of NADPH in flavin monooxygenases belonging to Class A is not fully understood yet, because they do not present a well-defined domain for NADPH binding. In the absence of a NADPH-KMO crystal complex, the NADPH-binding site can be inferred from the comparison with the structures of the NADPH complexes of flavoenzymes with similar folding topology. With this aim, we have exploited the structure of human p-hydroxybenzoate hydroxylase (PHBH).

As pointed out in Section 1.4.2.1, p-Hydroxybenzoate hydroxylase (PHBH) is the most extensively studied flavoprotein monooxygenase and it is representative of Class A monooxygenases. This enzyme has been studied in detail since its first crystal structure was published in 1979 [189], nevertheless the binding mode of NADPH remains elusive. In 2002, Wang *et al* performed some studies in the mutant R220Q of PHBH enzyme, because this mutant had lower affinity for the substrate and previous efforts to crystallise the apo-enzyme were not successfully [190]. They have obtained the structure of this mutant in complex with NADPH and shown that the coenzyme binds at the surface of the protein in a channel that crosses the binding site of FAD [190] (Figure 5.14). Although the adenosyl moiety was well-defined by the electron density, the nicotinamide moiety was less defined, possibly indicating a high mobility. According to their model, in one side of the channel the Tyr-38, Arg-42 and Arg-44 are implicated in the binding of the adenosyl moiety of NADPH and this pocket is also lined by the pyrophosphate and

adenosyl moieties of FAD, and on the other side of the channel His-162 and Arg-269 were the key residues involved in binding the pyrophosphate moiety (Figure 5.13).

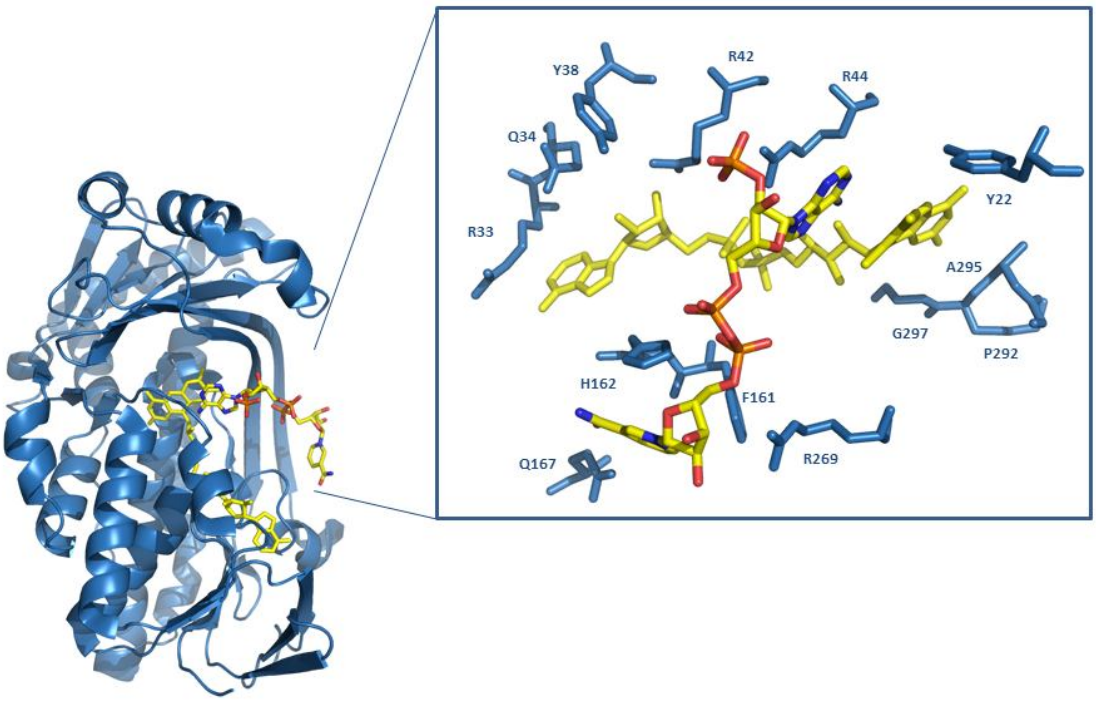


**Figure 5.13. Crystal structure of p-hydroxybenzoate and proposed interdomain binding of NADPH**. **This** enzyme does not present a recognizable domain to bind NADPH as the majority of flavin monooxygenases. Interestingly NADPH binds in an extended conformation at the surface of the protein in a channel that crosses the binding site of FAD (Adapted from [190]).The inset is the Stereo view of the NADPH binding site with the key residues involved in NADPH binding

Even though *Sc*KMO and PHBH from *Pseudomonas aeruginosa* do not present a significant high primary sequence identity (16%) and similarity (28%), the structural alignment revealed that both enzymes share the same topology and overall fold (Figure 5.14).

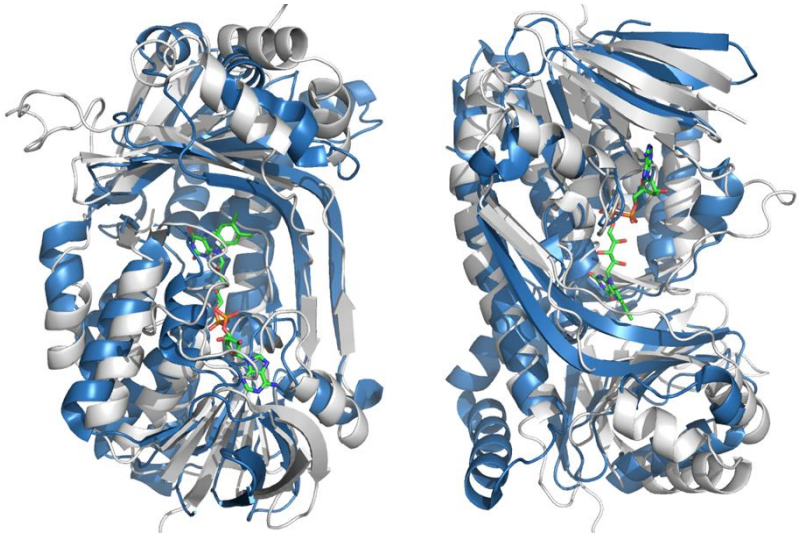

**Figure 5.14. Structural alignment of KMO and PHBH structures.** ΔKMO394 protein is shown in grey and PHBH in blue. The two different orientations highlight the conserved topology of both proteins.

Both have a large domain that has the characteristics of a Rossman fold, responsible for the interaction of FAD with the active site of the protein and a head domain responsible for the binding of the aromatic substrate in the active site. The active site of both enzymes forms a channel inside the structures running through the interior and large part of the FAD molecule is exposed to the solvent. As it happens for KMO, PHBH does not have a clear recognisable domain for binding of NADPH.

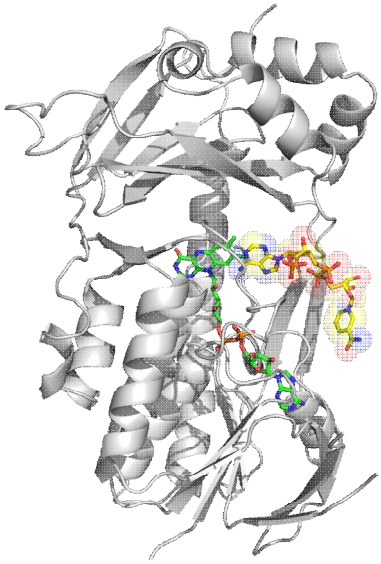

**Figure 5.15. Prediction of NADPH binding mode in *Sc*KMO based on the PHBH homology model.** NADPH is predicted to bind in an extended conformation on the surface of the NADPH-binding domain.

Based on the similarity with these two enzymes, it is postulated that NADPH may bind in a manner similar to that observed for PHBH (Figure 5.15), however further studies would need to be performed to provide structural evidence to this effect.

It is important to emphasize that the NADPH binding mode of Class A flavoprotein monooxygenases remains to be elucidated. Several attempts were carried out with many Class A flavoprotein mononooxygenases without success and therefore it is not yet known if the NADPH binding mode of PHBH is representative of this class of enzymes. The complex structure of NADPH-PHBH was obtained by soaking crystals in the absence of the substrate pOHB with a very high concentration of NADPH (50mM) [190]. Furthermore, the isoalloxazine ring of FAD and the dihydronicotinamide moiety of NADPH were not in a position to react and consequently it remains uncertain that the NADPH binding mode obtained in this report represents the real reactive complex. Although this model has been supported by earlier studies using mutagenesis and chemical modification in the same key residues [265, 266] there are also proposed NADPH binding modes significantly different from the one based on the Arg 220 PHBH mutant NADPH structure. Eppink *et al.* (1998) had shown by mutagenesis that the adenosine 2'-phosphate moiety of NADPH interacts with the residues of Arg33, Tyr38 and Arg42, part of Helix H2 in PHBH, which is a highly conserved region among NADPH-specific PHBH enzymes but differs from the only PHBH enzyme that has higher affinity towards NADH, PHBH from **Pseudomonas** sp. CBS3 [267].

Therefore, we cannot rule out the possibility that the NADPH binding mode in *Sc*KMO is not consistent with this model.

### 5.4.6. Proposed Mechanism for KMO catalysis

The proposed mechanism for KMO hydroxylation of kynurenine is based on the *Sc*KMO:kynurenine model. The aromatic substrate moiety is located in the conserved hydrophobic pocket on the *re*-face of the flavin with polar contacts between Gln-325 and the kynurenine ketone group and between the substrate aniline nitrogen and the FAD O4 (Figure 5.9).

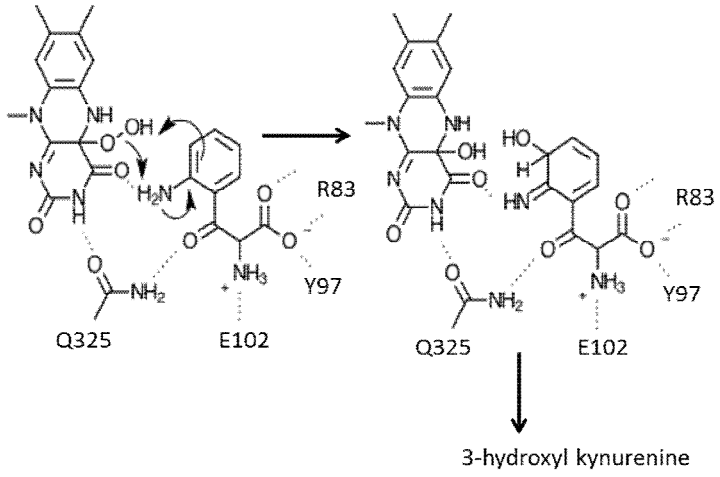


**Figure 5.16. The proposed mechanism for kynurenine hydroxylation by KMO based on the *Sc*KMO:kynurenine model**. The 3 arrows present a concerted mechanism in which the aromatic group attacks the flavin peroxide breaking the O-O bond and pick up a proton from the substrate $NH_2$ group. The electrons are released at the $NH_2$ group by removal of a proton to the flavin peroxide flow into the aromatic group. Following hydroxylation, the intermediate rearranges to form the 3-hydroxyl kynurenine product.

The orientation of the substrate in the KMO:kynurenine model places the C3 atom directly adjacent to the flavin C4a, in a position poised for nucleophilic attack on the flavin C4a peroxide adduct and hydroxylate of the substrate. The substrate hydroxylation must produce the C4a-hydroxyflavin and the elimination of one water molecule will enable the reoxidation of the isoalloxazine. Following hydroxylation, the intermediate rearranges to form the 3-hydroxyl kynurenine product (Figure 5.16).

Interestingly, a structural water molecule is located directly above the FAD C4a, mimicking the position of the C4a-peroxide adduct formed upon reaction with oxygen. The dimethylbenzene moiety of the isoalloxazine ring is protected from solvent by Lys 48 and the conserved residue Tyr 195 (Figure 5.17), suggesting that a “waving flavin” motion as part of the flavin reduction process, as demonstrated in other FAD-dependent mono-oxygenases [268], is unlikely to occur in the absence of large protein rearrangements.

This flavin motion, mostly described for PHBH enzyme [268], involves the movement of the FAD from an in-position for hydroxylation of p-hydroxybenzoate (pOHB) substrate, to an out-position for reduction of the flavin by NADPH. However, unlike KMO, PHBH does not have any restrains nearby the isoalloxazine ring and therefore is can move to a solvent-accessible position. Since the structural data obtained

for *Sc*KMO in the current project showed clearly an *in conformation* in which the flavin is proximal to the substrate to achieve hydroxylation, it is difficult to hypothesise further conformations in the active site unless new crystallographic data is available.

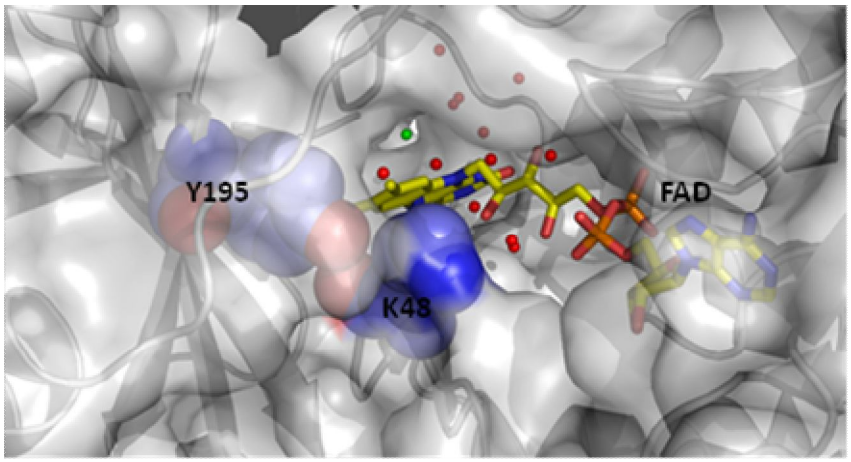


**Figure 5.17. Solvent access channel to the FAD isoalloxazine moiety**. The *re*-face of the FAD is connected to the solvent by a narrow water filled cavity that runs perpendicular to the active site cleft. The structural water molecule located directly above the FAD C4a, mimicking the position of the C4a-peroxide adduct formed upon reaction with oxygen, is shown in green. Other water molecules in the channel are depicted as red spheres. The dimethylbenzene moiety of the isoalloxazine ring is protected from solvent by Lys 48 and the conserved residue Tyr 195, both depicted in atom coloured spheres. The solvent accessible KMO surface is shown as a transparent grey surface.

### 5.4.7. Homology model of *Hs*KMO

Throughout Chapter 4 we have shown that *Sc*KMO is highly related to *Hs*KMO (38 % identity and 51 % similarity) and we provide further evidence that the mechanism of action of KMO is remarkably well conserved between yeast and humans with similar kinetic and inhibition constants.

From the structural point of view, although there is no information regarding the crystal structure of *Hs*KMO, the multiple sequence alignment with other KMOs together with the crystal structure of *Sc*KMO provide further information regarding conserved residues and confirm that the key residues implied by the KMO:kynurenine model to be involved in kynurenine and FAD binding are preserved in *Hs*KMO, suggesting a conserved mechanism of KMO catalysis.

A homology model of *Hs*KMO was built with the I-TASSER server [269], using the structure of *Sc*KMO as a template (Figure 5.18A). The core structures of both enzymes are remarkably conserved with decreasing similarity towards the C-terminus of *Hs*KMO which is predicted to be the transmembrane region. As this part of the homology model was built without template, since *Sc*KMO does not share the C-terminal region with *Hs*KMO, it is probable that the predicted region is not reliable

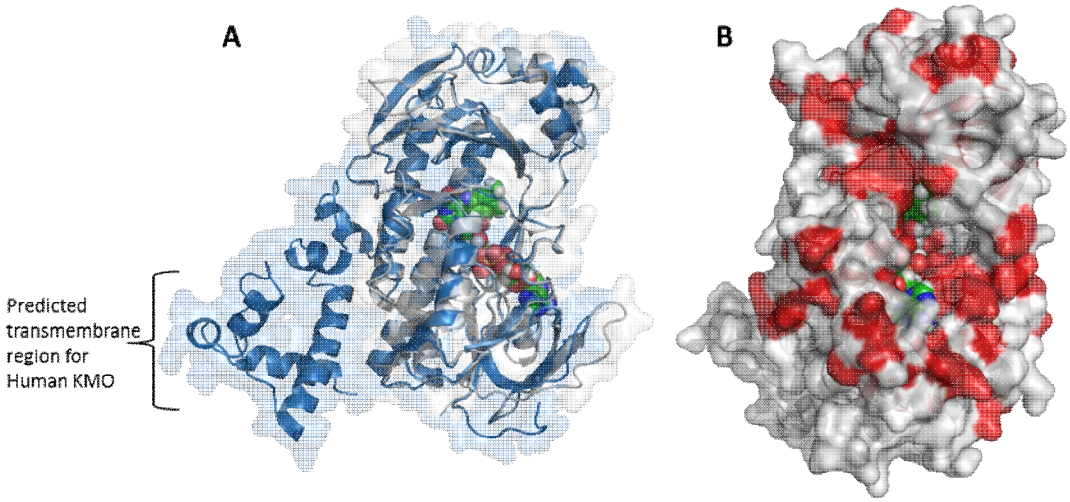


**Figure 5.18. *Hs*KMO homology model** (A) Structural alignment of *Homo sapiens* and *Saccharomyces cerevisiae* KMO. *Hs*KMO homology model was generated by I-TASSER using ΔKMO394 as template. The *Hs*KMO protein (blue) and ΔKMO394 (white) are shown in cartoon with transparent surface. (B) Conserved residues are shown in red. KMO surface is shown as a transparent grey surface. Ribbon with surface transparent (and conserved residues in red)

The conserved residues are shown in Figure 5.18B and it is evident that the region in the vicinity of the active site is highly conserved, demonstrating again that the active site of KMO is preserved among both enzymes.

## 5.5. DISCUSSION

This chapter reports on the structural studies of *Sc*KMO and complements the biochemical results from Chapter 4.We solved the crystal structures of the initial proteolytic soluble form (2.6 Å) and ΔKMO394 (1.8 Å) version of the enzyme and both structures are identical as expected. The KMO overall fold is similar to other class A flavin monooxygenases [190] with one large domain that includes the Rossman fold with 5 β-sheets and 4 α-helices responsible for the interactions between the protein and FAD. A structural alignment of the various KMO constructs reveals greatest variation in the C-terminal α-helix. Flexibility in this region of the structure might interfere with the activity of the protein, not because the C-terminal α-helix plays any crucial role in the catalytic activity, but perhaps the high flexibility observed induces structural perturbations that have a negative impact on the core structure of the enzyme. Such changes may obstruct or alter important ligand or cofactor binding pockets. This hypothesis remains elusive and further experiments need to be conducted to validate the present concept.

The crystal structure of ΔKMO394 in complex with the KMO inhibitor UPF 648 revealed structural changes in the enzyme, particularly in a pocket facing the *re*-side of the FAD. Due to the similarity of UPF 648 and L-KYN, the latter was modelled in the KMO active site and all residues involved in L-KYN binding were found to be conserved across KMOs, ranging from bacterial to human enzymes providing evidence that the KMO catalytic mechanism is preserved. We further validated this model by targeting the active site residue Arg-83 (to Ala-83 and Met-83) and performed inhibitor binding and kinetic assays, confirming that mutations led to a significant decrease in enzyme activity and ligand binding affinity.

During this project numerous attempts were made to obtain additional structure complexes with a variety of ligands, however these attempts failed to yield the desired complexes. The determination of cofactor- and product-bound structures of KMO would be of great assistance in elucidating the catalytic mechanism of KMO. Ligand binding assays were performed prior to co-crystallisation and long incubation periods with ligands were also conducted to confirm ligand binding, but none of them resulted in a complex structure. To aid these efforts, crystallisation of the ligand-free protein with subsequent soaking with ligands was also carried out unsuccessfully. One of the hypotheses suggested to explain why we never achieved any complex through soaking might lie in

the presence of the N-terminal his-tag within the active site. As explained in Section 5.8, while this might not be problem for solution studies, it could have possibly affected our attempts for soaking anything. Although we have tried the His-tag cleaved version of ΔKMO394, due to time constraints of this PhD project, further studies with this KMO variant were curtailed. Hence, if we are to continue with this project, extensive crystallisation screens should be proceeded with ΔKMO394HIS- in order to solve structure complexes with ligands of interest.

Since we were unable to obtain a structure complex with NADPH, the binding site of this cofactor remains indefinable. KMO, as many class A flavoprotein monooxygenases, does not have a clear recognizable domain for binding of NADPH and there is a lack of published structures in complex with this factor, which complicates the prediction of NADPH binding mode. The hypotheses suggested for NADPH binding in KMO is based in on the structure of PHBH in complex with NADPH and based on the similarity with these two enzymes, NADPH is predicted to bind in an extended conformation at the surface of the protein.

It has been proposed throughout Chapter 3 and 4 that the KMO C-terminal deletion might have interfered with the catalytic activity of the enzyme both in human and yeast KMO. One of the hypotheses suggested to explain the low turnover number based on kinetic assays was that the NADPH binding pocket could have been structurally affected by the C-terminal deletion, affecting the cofactor affinity. With the structural information of *Sc*KMO together with the assumption that KMO shares the same NADPH binding mode as PHBH enzyme, the residues forming the binding pocket are not in the vicinity of the C-terminal region and therefore is unlikely that structural changes might have occurred in the NADPH binding domain.

Regarding the proposed mechanism of KMO, the structural information obtained in this Chapter complemented with the studies conducted spectroscopically on the reductive and oxidative half reaction (Chapter 4) indicate that the catalytic mechanism is similar to other flavin monooxygenases, with an electrophilic attack to the aromatic ring carried out by the reactive species C(4a) hydroperoxyflavin and the distal oxygen is inserted at the ortho position of the activated ring forming the hydroxilated product, C4a-hydroxyflavin and one water molecule with the reoxidation of the isoalloxazine. Following hydroxylation, the intermediate rearranges to form the 3-hydroxyl kynurenine product. Interestingly, the “waving flavin” motion as part of the flavin reduction process,

as demonstrated in other FAD-dependent monooxygenases, is improbable as the dimethylbenzene moiety of the isoalloxazine ring is protected from solvent. To infer the possible movement of the flavin during the catalytic process more crystallographic studies need to be conducted with *Sc*KMO, preferentially with a variety of ligands, to assess the possible positions of the flavin prosthetic group within the enzyme. The crystallographic studies should also be complemented with spectroscopic studies to study the dynamic events involved in catalysis.

A homology model of *Hs*KMO was built using the structure of *Sc*KMO as template, and the active site topology of both enzymes bears significant resemblance, particularly the regions of ligand and FAD binding, showing a conserved mechanism in the KMO catalysis and validating *Sc*KMO as a good candidate for the development of novel inhibitors for *Hs*KMO.

In conclusion, we were able to perform for the first time, the structural characterisation of *Sc*KMO. We determined the crystal structure of *S*cKMO complexed with UPF 648 and established that this enzyme-inhibitor structure can be used for the future design of novel KMO inhibitors with the affinity and specificity necessary and for optimization of brain penetrance that could ultimately have major therapeutic value.

# CHAPTER 6

# CONCLUSIONS AND OUTLOOK

# 6. CONCLUSIONS AND OUTLOOK

## 6.1 SUMMARY AND FUTURE WORK

Metabolites of the kynurenine pathway (KP), which arise from the degradation of tryptophan, have been studied in detail for over a century and garnered the interest of the neuroscience community in the late 1970s and early 1980s with work uncovering the neuromodulatory potential of this pathway [135, 136, 98]. Much research in the following decades found that perturbations in the levels of KP metabolites likely contribute to the pathogenesis of several neurodegenerative diseases. More recently, it has become apparent that targeting KP enzymes, in particular kynurenine 3-monoxygenase (KMO), may hold substantial therapeutic potential for these disorders. The most compelling evidence supporting a role for KP metabolites in neurodegenerative disease comes from studies in Huntington's disease (HD), using cell and animal models [159, 158, 4].

To date several KMO inhibitors have been developed and characterised, however, none of them appears to appreciably cross the BBB [172, 174, 270, 173, 178]. Although pharmacological inhibition of KMO in the blood has proven to be sufficient to ameliorate disease phenotypes in mouse models of AD and HD [3], the development of KMO inhibitors able to cross the BBB is essential to ensure efficient delivery directly to the brain, to reduce the levels of neurotoxic metabolites, and to increase the levels of neuroprotective KYNA [174, 179].

The approaches used for drug design have changed over time, from experimental techniques to the development of more sophisticated computational software with the aim of reducing the number of possible ligands, enhancing the accuracy of analysis and reducing the cost and time spend in the drug discovery process [271]. Structure-based drug design has been gaining more credit within the pharmaceutical industry exactly because the amount of time, cost and work spent is comparatively low particularly in 'hit identification' and 'hit-to-lead' phases [272].

A number of studies characterised the activity of KMO from different organisms in terms of substrate, coenzyme and cofactor specificity, as well as strategies for expression and purification of KMO from higher organisms including recombinant *Hs*KMO [208, 207, 235]. However, as this enzyme is membrane associated, it has proven

to be extremely difficult to obtain sufficient quantities of *Hs*KMO for structural studies and therefore, until now there was no structural knowledge of this enzyme [208, 273]. Such information – both with native KMO and ligand-bound enzyme - would aid in the rational design of novel KMO inhibitory compounds. In order to partially address this issue, the investigation of the binding modes of possible KMO inhibitors has been carried out using structure and ligand-based computer-aided design tools based on structurally and functionally related enzymes [180, 181]. Nonetheless, obtaining the crystal structure of KMO is necessary to truly inform rational design of novel inhibitors with the affinity and specificity necessary for clinical trials and which may also be optimised for brain penetrance.

The work conducted in this thesis has presented a complete biochemical and structural characterisation of the KMO enzyme, elucidating the mechanisms of ligand binding and providing insights into the structure of the active site of KMO that are essential for the future development of novel inhibitor scaffolds. During this project, we described efficient strategies to express and purify recombinant *Hs*KMO. We have initially explored truncated forms of *Hs*KMO by deleting the transmembrane regions in order to prevent insolubility. The spectral features of ΔKMO383 (without transmembrane helices) were characteristic of a flavoprotein with maximum absorbance peaks at 375 and 450 nm, and the enzyme was shown to bind the physiological substrate L-KYN and KMO inhibitor Ro 61-8046. However, this truncation variant was not able to catalyse the hydroxylation of the substrate. In addition, crystallisation screens did not retrieve positive hits despite intensive efforts. We thus turned our attention to the expression of full-length *Hs*KMO using the insect cell baculovirus system, which yielded small quantities (~0.5 mg/L of culture) of detergent solubilised active *Hs*KMO. The recombinant form exhibited similar kinetic constants to native KMO isolated from pig liver mitochondrial preparations [216]. The inhibitor UPF 648 was found to bind recombinant *Hs*KMO tightly with an apparent $K_i$ of 56.7 nM. These data are the first direct measurements of a binding/inhibitor constant for KMO inhibitor with pure recombinant *Hs*KMO and this strategy can also be used as a valuable tool for high throughput drug screening methodologies.

However, the very low yield, together with the challenges associated with working with membrane proteins, meant that progression with structural studies ceased. It

was decided that a great deal of time would be required in order to simply produce enough quantities of full length KMO in a suitable form for further crystallographic studies. Furthermore, the fact that initial crystallisation screens did not retrieve any positive hits prevented additional efforts to crystallise *Hs*KMO.

An alternative approach was adopted and focused on *Sc*KMO, which is closely related to *Hs*KMO (38 % identity and 51 % similarity). Expression and purification of *Sc*KMO revealed that this enzyme was active as a flavin-dependent monooxygenase, generated authentic 3HK in HPLC-based assays and was inhibited by UPF 648 ($K_i$ 74 nM) with potency similar to that observed with *Hs*KMO, thus supporting the hypothesis that *Sc*KMO would be a good homology model for the study of *Hs*KMO. Attempts to express full length *Sc*KMO resulted in proteolytic clipping of the enzyme. This was corroborated by electrospray mass spectrometry and Multi Angle Laser Light Scattering analysis, which identified a protein with a molecular weight of 47 kDa, consistent with a truncation of KMO at residue 396. The proteolysis might have been caused by several factors, such as the instability of the full-length protein or the flexibility of the C-terminal region, which might have exposed susceptible residues to proteolysis during expression. Regardless of the truncated version of *Sc*KMO, the engineered truncated form of *Sc*KMO (Δ394KMO) has been shown to interact with L-KYN, NADPH and KMO inhibitors, although the rate observed is likely to be much lower than the true catalytic rate.

In this thesis I described the first crystal structure of KMO from *Saccharomyces cerevisiae* in complex with the tight-binding inhibitor UPF 648. The overall structure of KMO is reminiscent of the flavin-dependent hydroxylase family [255], sharing the classic Rossman fold with five β-sheets and four α-helices in the large domain responsible for interactions with FAD. The potentially most important accomplishment to come from the studies of *Sc*KMO was the identification of key residues involved in substrate binding, confirmed by functional assays and active site mutagenesis, and the confirmation that those residues are conserved among KMOs from different organisms. Structural comparison of *Sc*KMO and *Hs*KMO has shown that the active site is essentially identical, validating the yeast KMO:UPF 648 structure as a template for structure-based drug design and the future development of novel inhibitors. To further support these studies, the same residues can also be mutated in *Hs*KMO by sequence and structural comparison with *Sc*KMO and validated with functional assays.

As the structure of full-length KMO remains elusive, both from *S. cerevisiae* and *H. sapiens*, the role of the C-terminal α-helix in the enzymatic activity remains unclear. Hypotheses were made throughout the project, supported by evidence from previous studies, showing that the C-terminus of KMO is important for its catalytic activity [246]. As the binding affinity of the truncated *Sc*KMO enzyme for the physiological substrate and analogues are similar with results from the literature, the most likely explanation for the role of the C-terminal region is its involvement in NADPH binding. The structure of *Sc*KMO and the structural alignment with PHBH gave some insight into the possible mechanism of NADPH binding, although the binding mode of this cofactor in external flavoproteins remains elusive. NADPH is predicted to bind in an extended conformation on the surface of the NADPH-binding domain. If this mechanism represents the true mechanism for NADPH binding in KMO enzymes, the truncation in the C-terminus should not interfere with the catalytic activity since the predicted binding pocket is structurally distant from the C-terminal α-helix. The flexibility of the C-terminal region, shown by comparison of free enzyme monomers corroborate the hypothesis that proteolytically **c**leaved distal C-terminal residues might have been caused by excess of α-helix movement and thereby exposing such residues to exoproteolysis. Such flexibility could also be responsible for breaking interactions of the α-helix with remaining core structure, explaining the lower catalytic rate when compared to full-length *Hs*KMO.

In the future, the elucidation of the role of the C-terminal region in the catalytic activity of KMO might be achieved through a number of different approaches. A possible strategy could be the development of a variety of C-terminal KMO deletion mutants and their comparison in terms of enzymatic activity with the full-length KMO by monitoring the formation of the product 3-HK using the HPLC-based assays described in this thesis. This would allow the identification of the exact region of the C-terminus responsible for the loss of the KMO activity. This approach could be carried out for both human and yeast KMO. In the first case, the recombinant expression could be conducted using the baculovirus system as described for expression of detergent solubilised full length *Hs*KMO (Chapter 3). In the latter case, the recombinant expression of C-terminal deletion mutants of *Sc*KMO could follow the same approach used for expression of the proteolytic version of N-terminal His-tagged *Sc*KMO and ΔKMO394 in *E. coli*, with the requirement that mutation(s) in the *proteolysis site* must be carried out to prevent cleavage after Asp 396. An alternative approach would be to explore C-terminally His-tagged *Sc*KMO. We

established that it is possible to express full length C-terminally His-tagged *Sc*KMO using the pET-24b vector, although the yield obtained did not allow us to further explore alternative purification strategies. It appears that the His-tag at the C-terminal of KMO somehow prevented proteolysis at susceptible cleavage sites and therefore, it might be a viable approach to explore alternative vectors such as pET45b or pET51b (*Novagen*). In case these approaches fail, one could also develop the C-terminal deletion mutants fused to a larger tag than the $His_6$-tag, to stabilise and protect the recombinant fused protein from proteolysis, as appears to occur during expression trials. These tags may include GST- or thioredoxin.

In addition to standard activity assays, further studies can also be carried out using stopped-flow assays with emphasis on the reductive half-reaction. By mixing anaerobically saturating concentrations of NADPH (with and without the presence of L-KYN) with KMO variants and monitoring the FAD reduction at 450 nm, it is possible to calculate the limiting rate constants and compare these values across the different mutants. In case this parameter varies according to the size of the C-terminal truncated, it will confirm the hypothesis that the C-terminus is in fact affecting the NADPH binding pocket. The dependence of the rate of reduction on NADPH concentration can also be performed and the comparison of the apparent $K_m$ for NADPH can determine if the C-terminal deletion is responsible for weakening NADPH affinity.

Further structural analysis of the respective mutants might also be critical for the elucidation of C-terminal flexibility and its relation to enzyme catalytic activity. The extensive co-crystallisation and soaking methodologies with different concentrations of NADPH should also be pursued with the intention of understanding the molecular mechanism of NADPH binding. To obtain the structure of the complex of NADPH-KMO, perhaps crystallisation in anaerobic conditions could possibly stabilise the protein and facilitate the crystallisation process, since the enzyme would be permanently in the reduced state and would not be oxidised by the presence of molecular oxygen. The reduction of FAD can be monitored spectroscopically at 450 nm prior to crystallisation to assure the efficient binding of NADPH.

Biophysical characterisation by circular dichroism (CD) analysis can be a valuable tool to compare C-terminal deletion mutants, in order to confirm the secondary structural integrity of mutants and assessing the structural relationships between wild type and mutant proteins. The overall structural features can also be deduced by CD and conformational changes caused by ligand binding may also be inferred. This technique

can be of particular interest when analysing the UV and visible regions since relatively small structural differences can be detected. In addition, analysis of the flavin environment can also be studied.

Previous FAD-dependent monooxygenase structural studies [268] have suggested that a "waving flavin" motion is part of the flavin reduction process in order to make contact with the nicotinamide ring at the protein surface. Although the structure of *Sc*KMO suggests that this movement is unlikely to take place in the absence of large protein rearrangements, CD analysis as well as FTIR and NMR can be alternative approaches to explore the conformational dynamics upon NADPH binding in KMO enzyme. These studies can be also complemented with structural data and conformational dynamics, which can be indicative of the catalytic mechanism of KMO enzyme. Ideally, a whole set of crystal structures of *Sc*KMO, ranging from native, NADPH bound, substrate and product bound must be solved to provide key insights into the catalytic mechanism of this enzyme. Alternatively, CD spectroscopy together with kinetic data could also give valuable information into the binding and recognition modes of ligands and cofactors providing a structural basis for the catalytic mechanism of KMO.

## 6.2 CONCLUSIONS

Despite great interest in the therapeutic potential of KMO inhibitors, to date none have been tested in clinical trials. The work presented in this thesis elucidates for the first time the crystal structure of ligand-bound KMO. This is a major breakthrough that will permit docking screens using virtual libraries of compounds, which may ultimately identify novel inhibitor scaffolds. Fragment-based screening or modelling could also potentially be employed to design and refine competitive inhibitor molecules that possess the selectivity and affinity necessary to open novel opportunities for therapeutic intervention in a variety of brain disorders, and other conditions. Critically, such approaches may also inform development of brain-penetrant KMO inhibitors. Biophysical analysis of positive hits can be performed using the techniques carried out in this project, such as fluorescence spectroscopy and HPLC-based assays to calculate dissociation constants and compare inhibitor efficiency and affinity. HPLC assays are particularly efficient to carry out high throughput screening experiments.

Overall, the main objectives of this research, which were the elucidation of the crystal structure of KMO for future development of KMO inhibitors and the understanding of the catalytic mechanism of KMO, have been met. Results from this thesis are important to understand the nature of ligand binding in KMO and have exploited a multifaceted approach using biochemical, biophysical and structural data to obtain a comprehensive understanding of the mechanism and function of this enzyme.
The prospect of elucidating the catalytic mechanism of KMO, using spectroscopic, kinetic and crystallographic methods, are much greater for the soluble ScKMO enzyme by comparison to using detergent-solubilised *Hs*KMO, given the difficulties in expression and isolation of high quantities of *Hs*KMO. This work has also raised a number of questions about the catalytic mechanism of KMO, and future studies will surely uncover a deeper understanding that will contribute to additional knowledge of class A flavoprotein monooxygenases. Crystallographic methods combined with stopped-flow assays would appear to be the most prosperous way forward. In terms of drug discovery, both enzymes studied in this thesis, *Sc*KMO and *Hs*KMO, can efficiently be incorporated in high throughput drug screening experiments.

The understanding of the mode of KMO inhibition will help the future development of inhibitors able to cross the BBB and will no doubt increase enormously their therapeutic effectiveness. Future analysis of the efficacy of new KMO inhibitors can be complemented in various HD models that ultimately would aid in the development of new effective therapies for HD and other neurodegenerative diseases that despite affecting millions have no cure or treatments.

*"In the excitement of the abnormal gene identification in 1993, many of us in HD families imagined that a cure – or at least an effective treatment – was close at hand. That dream has not yet been realized. But if the history of Huntington's can provide clues for the future, it suggests that change does not always happen gradually. Change can also happen swiftly. And that, I believe, is a great source of hope….For families and individuals struggling daily with HD, effective therapies cannot come soon enough. But while major discoveries in the lab have not yet been matched by similar advances in treatment, the volume of research has increased tremendously in the past decade. Disease-altering interventions are now moving closer to the clinic"*[274]

Although aware that the future development of KMO inhibitors and its validation in clinical trials will take several years or decades, I am honoured that this thesis can possibly contribute to the future development of a therapeutic intervention against HD and other neurodegenerative diseases that are on the fast rise in developed countries where the ageing population is growing without stop.

*"Please don't give up, keep fighting with us"*

This sentence was said by a patient with HD in my first Hereditary Disease Foundation Conference in 2010 that I will never forget and will always follow me in my future projects.

---

# 7. REFERENCES


1. Giorgini F, Moller T, Kwan W, et al (2008) Histone deacetylase inhibition modulates kynurenine pathway activation in yeast, microglia, and mice expressing a mutant huntingtin fragment. J Biol Chem 283(12):7390–7400

2. Giorgini F, Guidetti P, Nguyen Q, Bennett SC, Muchowski PJ (2005) A genomic screen in yeast implicates kynurenine 3-monooxygenase as a therapeutic target for Huntington disease. Nat Genet 37(5):526–531

3. Zwilling D, Huang SY, Sathyasaikumar K V, et al (2011) Kynurenine 3-monooxygenase inhibition in blood ameliorates neurodegeneration. Cell 145(6):863–874

4. Campesan S, Green EW, Breda C, Sathyasaikumar K V, Muchowski PJ, Schwarcz R, Kyriacou CP, Giorgini F (2011) The kynurenine pathway modulates neurodegeneration in a Drosophila model of Huntington's disease. Curr Biol 21(11):961–966

5. Green EW, Campesan S, Breda C, Sathyasaikumar K V, Muchowski PJ, Schwarcz R, Kyriacou CP, Giorgini F (2012) Drosophila eye color mutants as therapeutic tools for Huntington disease. Fly (Austin) 6(2):117–120

6. Chen Y, Guillemin GJ (2009) Kynurenine pathway metabolites in humans: disease and healthy States. Int J Tryptophan Res 2(02):1–19

7. Schwarcz R, Bruno JP, Muchowski PJ, Wu HQ (2012) Kynurenines in the mammalian brain: when physiology meets pathology. Nat Rev Neurosci 13(7):465–477

8. Reinhart PH, Kelly JW (2011) Treating the periphery to ameliorate neurodegenerative diseases. Cell 145(6):813–814

9. Saito Y, Hayaishi O, Rothberg S (1957) Studies on oxygenases.Enzymatic formation of 3-hydroxy-L-Kynurenine from L-Kynurenine. J Biol Chem 2(229):921–934

10. Alberati-Giani D, Cesura AM, Broger C, Warren WD, Röver S, Malherbe P (1997) Cloning and functional expression of human kynurenine 3-monooxygenase. FEBS Lett 410(2-3):407–412

11. Huntington G (1872) On Chorea. Med Surg Rep 26:317–321

12. Gusella JF, Wexler NS, Conneally PM, et al (1983) A polymorphic DNA marker genetically linked to Huntington's disease. Nature 306(5940):234–238

13. Huntington T, Macdonald ME, Ambrose CM, et al (1993) A Novel Gene Containing a Trinucleotide That Is Expanded and Unstable on Huntington ' s Disease Chromosomes. Cell 72(6):971–983

14. Bano D, Zanetti F, Mende Y, Nicotera P (2011) Neurodegenerative processes in Huntington's disease. Cell Death Dis 2(11):e228

15. Mangiarini L, Sathasivam K, Seller M, et al (1996) Exon 1 of the HD gene with an expanded CAG repeat is sufficient to cause a progressive neurological phenotype in transgenic mice. Cell 87(3):493–506

16. DiFiglia M, Sapp E, Chase KO, Davies SW, Bates GP, Vonsattel JP, Aronin N (1997) Aggregation of huntingtin in neuronal intranuclear inclusions and dystrophic neurites in brain. Science 277(5334):1990–1993

17. Davies SW, Turmaine M, Cozens BA, DiFiglia M, Sharp AH, Ross CA, Scherzinger E, Wanker EE, Mangiarini L, Bates GP (1997) Formation of neuronal intranuclear inclusions underlies the neurological dysfunction in mice transgenic for the HD mutation. Cell 90(3):537–548

18. Paradisi I, Hernández A, Arias S (2008) Huntington disease mutation in Venezuela: age of onset, haplotype analyses and geographic aggregation. J Hum Genet 53(2):127–35

19. Roze E, Bonnet C, Betuing S, Caboche J (2010) Huntington ' s Disease. In: Ahmad SI (ed) Diseases of DNA Repair. Landes Bioscience and Springer Science, pp 45–63

20. Walker FO (2007) Huntington ' s disease. Lancet 369:218–228

21. Sturrock A, Leavitt BR (2010) The clinical and genetic features of Huntington disease. J Geriatr Psychiatry Neurol 23(4):243–59

22. Anderson KE (2011) Huntington's disease, 1st ed. Handbook of clinical neurology / edited by PJ Vinken and GW Bruyn 100:15–24

23. Kremer B, Weber B, Michael R (1992) New Insights into the clinical features, pathogenesis and molecular genetics of Huntington's disease. Brain Pathol 335(2):321–335

24. Paulsen JS, Ready RE, Hamilton JM, Mega MS, Cummings JL (2001) Neuropsychiatric aspects of Huntington ' s disease. J Neurol Neurosurg Psychiatry 5(71):310–314

25. Farrer L (1986) Suicide and attempted suicide in Huntington disease: implications for preclinical testing of persons at risk. Am J Med Genet 24(2):305–11

26. Paulsen JS, Ph D, Hoth KF, Nehl C, Stierman L (2012) Critical Periods of Suicide Risk in Huntington ' s Disease. Am J Psychiatry (162):725–731

27. Macedo-Ribeiro S, Almeida LP De, Carvalho AL, Rego AC (2007) Polyglutamine expansion diseases - The case of Machado-Joseph disease. In: Malva JO, Rego AC, Cunha RA, Oliveira CR (eds) Interaction Between Neurons and Glia in Aging and Disease, 1st ed. Coimbra, pp 391–426

28. Borrell-Pagès M, Zala D, Humbert S, Saudou F (2006) Huntington's disease: from huntingtin function and dysfunction to therapeutic strategies. Cell Mol Life Sci 63(22):2642–60

29. DiFiglia M, Sapp E, Chase K, et al (1995) Huntingtin is a cytoplasmic protein associated with vesicles in human and rat brain neurons. Neuron 14(5):1075–1081

30. Saudou F, Finkbeiner S, Devys D, Greenberg ME (1998) Huntingtin acts in the nucleus to induce apoptosis but death does not correlate with the formation of intranuclear inclusions. Cell 95(1):55–66

31. Truant R, Atwal R, Burtnik A (2006) Hypothesis: Huntingtin may function in membrane association and vesicular trafficking. Biochem Cell Biol 84(6):912–917

32. Reiner A, Albin RL, Anderson KD, D'Amato CJ, Penney JB, Young a B (1988) Differential loss of striatal projection neurons in Huntington disease. Proc Natl Acad Sci U S A 85(15):5733–7

33. Cattaneo E, Zuccato C, Tartari M (2005) Normal huntingtin function: an alternative approach to Huntington's disease. Nat Rev Neurosci 6(12):919–30

34. Rubinsztein DC, Leggo J, Coles R, et al (1996) Phenotypic characterization of individuals with 30-40 CAG repeats in the Huntington disease (HD) gene reveals HD cases with 36 repeats and apparently normal elderly individuals with 36-39 repeats. Am J Hum Genet 59(1):16–22

35. Albin RL, Tagle DA (1995) Genetics and molecular Huntington ' s disease biology of. Trends Neurosci 18:11–14

36. Diamond MI, Robinson MR, Yamamoto KR (2000) Regulation of expanded polyglutamine protein aggregation and nuclear localization by the glucocorticoid receptor. Proc Natl Acad Sci U S A 97(2):657–661

37. Ho LW, Carmichael J, Swartz J, Wyttenbach A, Rankin J, Rubinsztein DC (2001) The molecular biology of Huntington ' s disease. Psychol Med 31(1):3–14

38. Davies SW, Turmaine M, Cozens B, DiFiglia M, Sharp A, Ross C, Scherzinger E, Wanker EE, Mangiarini L, Bates GP (1997) Formation of neuronal intranuclear inclusions underlies the neurological dysfunction in mice transgenic for the HD mutation. Cell 90(3):537–48

39. Arrasate M, Mitra S, Schweitzer ES, Segal MR, Finkbeiner S (2004) Inclusion body formation reduces levels of mutant huntingtin and the risk of neuronal death. Nature 431(7010):805–10

40. Miller J, Shaby BA, Mitra S, Masliah E, Finkbeiner S (2011) Quantitative relationships between huntingtin levels, polyglutamine length, inclusion body formation, and neuronal death provide novel insight into Huntington's disease molecular pathogenesis. J Neurosci 30(31):10541–10550

41. Kuemmerle S, Gutekunst CA, Klein AM, Li XJ, Li SH, Beal MF, Hersch SM, Ferrante RJ (1999) Huntington aggregates may not predict neuronal death in Huntington's disease. Ann Neurol 46(6):842–849

42. Gutekunst C, Li S, Yi H, Mulroy JS, Kuemmerle S, Jones R, Rye D, Ferrante RJ, Hersch SM, Li X (1999) Nuclear and Neuropil Aggregates in Huntington ' s Disease : Relationship to Neuropathology. J Neurosci 19(7):2522–2534

43. Arrasate M, Finkbeiner S (2012) Protein aggregates in Huntington's disease. Exp Neurol 238(1):1–11

44. Klement I a, Skinner PJ, Kaytor MD, Yi H, Hersch SM, Clark HB, Zoghbi HY, Orr HT (1998) Ataxin-1 nuclear localization and aggregation: role in polyglutamine-induced disease in SCA1 transgenic mice. Cell 95(1):41–53

45. Myers RH (2004) Huntington ' s Disease Genetics. NeuroRx 1:255–262

46. (1996) Unified Huntington's disease rating scale: Reliability and consistency. Mov Disord 11(2):136–142

47. Politis M, Piccini P (2012) Positron emission tomography imaging in neurological disorders. J Neurol 259(9):1769–1780

48. Van den Bogaard S, Dumas E, van der Grond J, van Buchem M RR (2012) MRI biomarkers in Huntington's disease. Front Biosci (Elite Ed) 4:1910–25

49. De Tommaso M, Serpino C, Sciruicchio V (2011) Management of Huntington's disease: role of tetrabenazine. Therapeutics and clinical risk management 7:123–9

50. Huntington Study Group (2006) Tetrabenazine as antichorea therapy in Huntington disease: a randomized controlled trial. Neurology 66(3):366–72

51. Frank S (2010) Tetrabenazine: the first approved drug for the treatment of chorea in US patients with Huntington disease. Neuropsychiatr Dis Treat 6:657–65

52. De Tommaso M, Difruscolo O, Sciruicchio V, Specchio N, Livrea P (2007) Two Years' Follow-up of Rivastigmine Treatment in Huntington Disease. Clin Neuropharm 30:

53. Milnerwood AJ, Gladding CM, Pouladi M a, et al (2010) Early increase in extrasynaptic NMDA receptor signaling and expression contributes to phenotype onset in Huntington's disease mice. Neuron 65(2):178–90

54. Investigators of the Huntington Study Group and European Huntington's Disease Network (2012) Randomized, Double-Blind, Placebo-Controlled Study of

Dimebon in Individuals with Mild-to-Moderate Huntington disease. Neutherapeutics 1(9):239

55. Imarisio S, Carmichael J, Korolchuk V, et al (2008) Huntington's disease: from pathology and genetics to potential therapies. Biochem J 412(2):191–209

56. Kim DH, Rossi JJ (2007) Strategies for silencing human disease using RNA interference. Nat Rev Genet 8(3):173–84

57. Stiles DK, Zhang Z, Ge P, et al (2012) Widespread suppression of huntingtin with convection-enhanced delivery of siRNA. Experimental Neurology 233(1):463–71

58. DiFiglia M, Sena-Esteves M, Chase K, et al (2007) Therapeutic silencing of mutant huntingtin with siRNA attenuates striatal and cortical neuropathology and behavioral deficits. Proc Natl Acad Sci U S A 104(43):17204–9

59. Shi N, Pardridge WM (2000) Noninvasive gene targeting to the brain. Proc Natl Acad Sci U S A 97(13):7567–72

60. Boado RJ (2007) Blood-brain barrier transport of non-viral gene and RNAi therapeutics. Pharmacol Res 24(9):1772–87

61. Davidson BL, McCray PB (2011) Current prospects for RNA interference-based therapies. Nat Rev Genet 12(5):329–40

62. Gabathuler R (2010) Approaches to transport therapeutic drugs across the blood-brain barrier to treat brain diseases. Neurobiol Dis 37(1):48–57

63. Zeitlin S, Liu JP, Chapman DL, Papaioannou VE, Efstratiadis A (1995) Increased apoptosis and early embryonic lethality in mice nullizygous for the Huntington's disease gene homologue. Nat Genet 11(2):155–163

64. Hu J, Matsui M, Corey DR (2009) Allele-selective inhibition of mutant huntingtin by peptide nucleic acid-peptide conjugates, locked nucleic acid, and small interfering RNA. Ann N Y Acad Sci 1175:24–31

65. Van Bilsen PHJ, Jaspers L, Lombardi MS, Odekerken JCE, Burright EN, Kaemmerer WF (2008) Identification and allele-specific silencing of the mutant huntingtin allele in Huntington's disease patient-derived fibroblasts. Hum Cell 19(7):710–9

66. Olshina MA, Angley LM, Ramdzan YM, Tang J, Bailey MF, Hill AF, Hatters DM (2010) Tracking mutant huntingtin aggregation kinetics in cells reveals three major populations that include an invariant oligomer pool. J Biol Chem 285(28):21807–21816

67. Nagai Y, Inui T, Popiel HA, Fujikake N, Hasegawa K, Urade Y, Goto Y, Naiki H, Toda T (2007) A toxic monomeric conformer of the polyglutamine protein. Nat Struct Biol 14(4):332–40

68. Lesort M, Chun W, Johnson GVW, Ferrante RJ (1999) Tissue Transglutaminase Is Increased in Huntington ' s Disease Brain. J Neurochem 73(5):2018–2027

69. Chun W, Lesort M, Tucholski J, Ross C a, Johnson G V (2001) Tissue transglutaminase does not contribute to the formation of mutant huntingtin aggregates. J Cell Biol 153(1):25–34

70. Bailey CDC, Johnson GVW (2005) Tissue transglutaminase contributes to disease progression in the R6/2 Huntington's disease mouse model via aggregate-independent mechanisms. J Neurochem 92(1):83–92

71. Lesort M, Chun W, Tucholski J, Johnson GVW (2002) Does tissue transglutaminase play a role in Huntington ' s disease ? Neurochem Int 40:37–52

72. Karpuj M V, Becher MW, Steinman L (2002) Evidence for a role for transglutaminase in Huntington ' s disease and the potential therapeutic implications. Neurochem Int 40(1):31–36

73. Cooper a J, Sheu KF, Burke JR, Onodera O, Strittmatter WJ, Roses a D, Blass JP (1997) Polyglutamine domains are substrates of tissue transglutaminase: does transglutaminase play a role in expanded CAG/poly-Q neurodegenerative diseases? J Neurochem 69(1):431–4

74. Green H (1993) Human Genetic Diseases Due to Codon Reiteration: Relationship to an Evolutionary Mechanism. Cell 74:955–9556

75. Van Raamsdonk JM, Pearson J, Bailey CDC, Rogers D a, Johnson GVW, Hayden MR, Leavitt BR (2005) Cystamine treatment is neuroprotective in the YAC128 mouse model of Huntington disease. J Neurochem 95(1):210–20

76. Apostol BL, Kazantsev A, Raffioni S, et al (2003) A cell-based assay for aggregation inhibitors as therapeutics of polyglutamine-repeat disease and validation in Drosophila. Proc Natl Acad Sci U S A 100(10):5950–5

77. Dubinsky R, Gray C (2006) CYTE-I-HD: phase I dose finding and tolerability study of cysteamine (Cystagon) in Huntington's disease. Mov Disord 21(4):530–3

78. Gibrat C, Cicchetti F (2011) Potential of cystamine and cysteamine in the treatment of neurodegenerative diseases. Prog Neuropsychopharmacol Biol Psychiatry 35(2):380–9

79. RP103 (DR Cysteamine) for Huntington's Disease. http://www.raptorpharma.com/RP103_huntingtons.html.

80. Sarkar S, Perlstein EO, Imarisio S, et al (2009) Small molecules enhance autophagy and reduce toxicity in Huntington ' s disease models. Nat Chem Biol 3(6):331–338

81. Venkatraman P, Wetzel R, Tanaka M, Nukina N, Goldberg AL (2004) Sequences and Release Them during Degradation of Polyglutamine-Containing Proteins. Mol Cell 14:95–104

82. Bhutani N, Venkatraman P, Goldberg a L (2007) Puromycin-sensitive aminopeptidase is the major peptidase responsible for digesting polyglutamine sequences released by proteasomes during protein degradation. EMBO J 26(5):1385–96

83. Gil-Mohapel JM (2012) Screening of therapeutic strategies for Huntington's disease in YAC128 transgenic mice. CNS Neurosci Ther 18(1):77–86

84. Ross CA, Tabrizi SJ (2011) Huntington's disease: from molecular pathogenesis to clinical treatment. Lancet neurology 10(1):83–98

85. Ravikumar B, Vacher C, Berger Z, et al (2004) Inhibition of mTOR induces autophagy and reduces toxicity of polyglutamine expansions in fly and mouse models of Huntington disease. Nat Genet 36(6):585–595

86. Harris H, Rubinsztein DC (2011) Control of autophagy as a therapy for neurodegenerative disease. Nat Rev Neurol 8(2):108–17

87. Ravikumar B, Duden R, Rubinsztein DC (2002) Aggregate-prone proteins with polyglutamine and polyalanine expansions are degraded by autophagy. Hum Genet 11(9):1107–1117

88. Williams A, Sarkar S, Cuddon P, et al (2009) Novel targets for Huntington ' s disease in an mTOR-independent autophagy pathway. Nat Chem Biol 4(5):295–305

89. Manji HK, Lenox RH (1998) Lithium: a molecular transducer of mood-stabilization in the treatment of bipolar disorder. Neuropsychobiology 19(3):161–6

90. Sarkar S, Krishna G, Imarisio S, Saiki S, Kane CJO, Rubinsztein DC (2008) A rational mechanism for combination treatment of Huntington ' s disease using lithium and rapamycin. Hum Mol Genet 17(2):170–178

91. Luthi-carter R, Strand AD, Hanson SA, et al (2002) Polyglutamine and transcription : gene expression changes shared by DRPLA and Huntington ' s disease mouse models reveal context-independent effects. Hum Mol Genet 11(17):1927–1937

92. Sadri-Vakili G, Cha J-HJ (2006) Mechanisms of disease: Histone modifications in Huntington's disease. Nat Clin Pract Neurol 2(6):330–8

93. Mielcarek M, Benn CL, Franklin S a, Smith DL, Woodman B, Marks P a, Bates GP (2011) SAHA decreases HDAC 2 and 4 levels in vivo and improves molecular phenotypes in the R6/2 mouse model of Huntington's disease. PloS one 6(11):e27746

94. Hockly E, Richon VM, Woodman B, et al (2002) Suberoylanilide hydroxamic acid , a histone deacetylase inhibitor , ameliorates motor deficits in a mouse model of Huntington ' s disease. Proc Natl Acad Sci U S A 100(4):2021–2046

95. Veterans B, Medical A, Neurology D, et al (2003) Histone Deacetylase Inhibition by Sodium Butyrate Chemotherapy Ameliorates the Neurodegenerative Phenotype in Huntington ' s Disease Mice. J Neurosci 23(28):9418–9427

96. Thomas EA, Coppola G, Desplats PA, et al (2008) The HDAC inhibitor 4b ameliorates the disease phenotype and transcriptional abnormalities in Huntington ' s disease transgenic mice. Proc Natl Acad Sci U S A 105(40):15564–15569

97. Cowan CM, Raymond LA (2006) Selective Neuronal Degeneration in Huntington's Disease. Curr Top Dev Biol 75(06):25–71

98. Schwarcz R, Whetsell Jr. WO, Mangano RM (1983) Quinolinic acid: an endogenous metabolite that produces axon-sparing lesions in rat brain. Science 219(4582):316–318

99. Stone TW (2000) Development and therapeutic potential of kynurenic acid and kynurenine derivatives for neuroprotection. Trends Pharmacol Sci 21(4):149–54

100. Young AB, Greenamyre JT, Hollingsworth Z, Albin R, Amato CD, Shoulson IRA, Penney JB (1987) NMDA Receptor Losses in Putamen firom Patients with Huntington ' s Disease. Science 5867(1977):1986–1988

101. Chen N, Luo T, Raymond L a (1999) Subtype-dependence of NMDA receptor channel open probability. J Neurosci 19(16):6844–54

102. Zeron MM, Chen N, Moshaver A, Lee AT, Wellington CL, Hayden MR, Raymond LA (2001) Mutant huntingtin enhances excitotoxic cell death. Mol Cell Neurosci 17(1):41–53

103. Zeron MM, Fernandes HB, Krebs C, Shehadeh J, Wellington CL, Leavitt BR, Baimbridge KG, Hayden MR, Raymond LA (2004) Potentiation of NMDA receptor-mediated excitotoxicity linked with intrinsic apoptotic pathway in YAC transgenic mouse model of Huntington's disease. Mol Cell Neurosci 25(3):469–79

104. Li L, Fan M, Icton CD, Chen N, Leavitt BR, Hayden MR, Murphy TH, Raymond LA (2003) Role of NR2B-type NMDA receptors in selective neurodegeneration in Huntington disease. Neurobiol Aging 24(8):1113–1121

105. Atlason PT, Garside ML, Meddows E, Whiting P, McIlhinney R a J (2007) N-Methyl-D-aspartate (NMDA) receptor subunit NR1 forms the substrate for oligomeric assembly of the NMDA receptor. J Biol Chem 282(35):25299–307

106. O'Suilleabhain P, Dewey RB (2003) A randomized trial of amantadine in Huntington disease. Arch Neurol 60(7):996–8

107. Group HS (2003) Dosage effects of riluzole in Huntington's disease: A multicenter placebo-controlled study. Neurology 61(11):1551–1556

108. Kremer B, Clark CM, Almqvist EW, et al (1999) Influence of lamotrigine on progression of early Huntington disease: A randomized clinical trial. Neurology 53(5):1000–1000

109. Huntington T, Group S (2001) A randomized, placebo-controlled trial of coenzyme Q10 and remacemide in Huntington's disease. Neurology 57(3):397–404

110. Beister A, Kraus P, Kuhn W, Dose M, Weindl A, Gerlach M (2004) The N-methyl-D-aspartate antagonist memantine retards progression of Huntington's disease. J Neural Transm Suppl 68:117–122

111. Clinical Trials.gov. http://www.clinicaltrials.gov/ct2/show/NCT00652457?term=Huntington's+Disease&rank=21.

112. Okamoto S, Pouladi MA, Talantova M, et al (2009) Balance between synaptic versus extrasynaptic NMDA receptor activity influences inclusions and neurotoxicity of mutant huntingtin. Nat Med 15(12):1407–13

113. Zádori D, Klivényi P, Szalárdy L, Fülöp F, Toldi J, Vécsei L (1997) Mitochondrial disturbances, excitotoxicity, neuroinflammation and kynurenines: Novel therapeutic strategies for neurodegenerative disorders. J Neurol Sci. doi: 10.1016/j.jns.2012.06.004

114. Lin MT, Beal MF (2006) Mitochondrial dysfunction and oxidative stress in neurodegenerative diseases. Nature 443(7113):787–95

115. Panov A V, Gutekunst C-A, Leavitt BR, Hayden MR, Burke JR, Strittmatter WJ, Greenamyre JT (2002) Early mitochondrial calcium defects in Huntington's disease are a direct effect of polyglutamines. Nat Neurosci 5(8):731–6

116. Choo YS, Johnson GVW, MacDonald M, Detloff PJ, Lesort M (2004) Mutant huntingtin directly increases susceptibility of mitochondria to the calcium-induced permeability transition and cytochrome c release. Hum Mol Genet 13(14):1407–20

117. Gutekunst C, Li S, Yi H, Ferrante RJ, Li X, Hersch SM (1998) The Cellular and Subcellular Localization of Huntingtin-Associated Protein 1 ( HAP1 ): Comparison with Huntingtin in Rat and Human. J Neurosci 18(19):7674–7686

118. Orr AL, Li S, Wang C-E, Li H, Wang J, Rong J, Xu X, Mastroberardino PG, Greenamyre JT, Li X-J (2008) N-terminal mutant huntingtin associates with mitochondria and impairs mitochondrial trafficking. J Neurosci 28(11):2783–92

119. Gu M, Gash MT, Mann VM, Javoy-Agid F, Cooper JM, Schapira AH (1996) Mitochondrial defect in Huntington's disease caudate nucleus. Ann Neurol 39(3):385–389

120. Gu M, Gash M, Mann V, Javoy-Agid F, Cooper J, Schapira A (1996) Mitochondrial defect in Huntington's disease caudate nucleus. Ann Neurol 39(3):385–389

121. Thevandavakkam MA, Schwarcz R, Muchowski PJ, Giorgini F (2010) Targeting kynurenine 3-monooxygenase (KMO): implications for therapy in Huntington's disease. CNS Neurol Disord Drug Targets 9(6):791–800

122. Han Q, Cai T, Tagle D, Li J (2010) Structure, expression, and function of kynurenine aminotransferases in human and rodent brains. Cell Mol Life Sci 67(3):353–68

123. Ying W (2008) NAD+/NADH and NADP+/NADPH in cellular functions and cell death: regulation and biological consequences. Antioxid Redox Signal 10(2):179–206

124. Grohmann U (2003) Tolerance, DCs and tryptophan: much ado about IDO. Trends Immunol 24(5):242–248

125. Frumento G, Rotondo R, Tonetti M, Damonte G, Benatti U, Ferrara GB (2002) Tryptophan-derived Catabolites Are Responsible for Inhibition of T and Natural Killer Cell Proliferation Induced by Indoleamine 2,3-Dioxygenase. J Exp Med 196(4):459–468

126. Katz JB, Muller AJ, Prendergast GC (2008) T-cell tolerance and tumoral immune escape. Immunol Rev 222:206–221

127. Pilotte L, Larrieu P, Stroobant V, et al (2012) Reversal of tumoral immune resistance by inhibition of tryptophan 2,3-dioxygenase. Proc Natl Acad Sci U S A 109(7):2497–502

128. Munn DH (2006) Indoleamine 2,3-dioxygenase, tumor-induced tolerance and counter-regulation. Curr Opin Immunol 18(2):220–225

129. Uyttenhove C, Pilotte L, Théate I, Stroobant V, Colau D, Parmentier N, Boon T, Van den Eynde B (2003) Evidence for a tumoral immune resistance mechanism based on tryptophan degradation by indoleamine 2,3-dioxygenase. Nat Med 9(10):1269–74

130. Nguyen NT, Kimura A, Nakahama T, Chinen I, Masuda K, Nohara K, Fujii-Kuriyama Y, Kishimoto T (2010) Aryl hydrocarbon receptor negatively regulates dendritic cell immunogenicity via a kynurenine-dependent mechanism. Proc Natl Acad Sci U S A 107(46):19961–19966

131. Mezrich JD, Fechner JH, Zhang X, Johnson BP, Burlingham WJ, Bradfield CA (2010) An interaction between kynurenine and the aryl hydrocarbon receptor can generate regulatory T cells. J Immunol 185(6):3190–3198

132. Röhrig UF, Awad L, Grosdidier A, et al (2010) Rational design of indoleamine 2,3-dioxygenase inhibitors. J Med Chem 53(3):1172–89

133. Yue EW, Douty B, Wayland B, et al (2009) Discovery of potent competitive inhibitors of indoleamine 2,3-dioxygenase with in vivo pharmacodynamic activity and efficacy in a mouse melanoma model. J Med Chem 52(23):7364–7367

134. Opitz CA, Litzenburger UM, Sahm F, et al (2011) An endogenous tumour-promoting ligand of the human aryl hydrocarbon receptor. Nature 478(7368):197–203

135. Lapin IP (1978) Stimulant and convulsive effects of kynurenines injected into brain ventricles in mice. J Neural Transm 42(1):37–43

136. Stone TW, Perkins MN (1981) Quinolinic acid: a potent endogenous excitant at amino acid receptors in CNS. Eur J Pharmacol 72(4):411–412

137. Behan WM, McDonald M, Darlington LG, Stone TW (1999) Oxidative stress as a mechanism for quinolinic acid-induced hippocampal damage: protection by melatonin and deprenyl. Br J Pharm 128(8):1754–60

138. Rios C, Santamaria A (1991) Quinolinic acid is a potent lipid peroxidant in rat brain homogenates. Neurochem Res 16(10):1139–43

139. Whetsell WO, Schwarcz R (1989) Prolonged exposure to submicromolar concentrations of quinolinic acid causes excitotoxic damage in organotypic cultures of rat corticostriatal system. Neurosci Lett 97:271–275

140. Stone TW, Mackay GM, Forrest CM, Clark CJ, Darlington LG (2003) Tryptophan metabolites and brain disorders. Clin Chem Lab Med 41(7):852–9

141. Perkins MN, Stone TW (1982) An iontophoretic investigation of the actions of convulsant kynurenines and their interaction with the endogenous excitant quinolinic acid. Brain Research 247(1):184–187

142. Wang J, Simonavicius N, Wu X, Swaminath G, Reagan J, Tian H, Ling L (2006) Kynurenic acid as a ligand for orphan G protein-coupled receptor GPR35. J Biol Chem 281(31):22021–22028

143. Sapko MT, Guidetti P, Yu P, Tagle DA, Pellicciari R, Schwarcz R (2006) Endogenous kynurenate controls the vulnerability of striatal neurons to quinolinate : Implications for Huntington ' s disease. Exp Neurol 197:31–40

144. Fukui S, Schwarcz R, Rapoport SI, Takada Y, Smith QR (1991) Blood-brain barrier transport of kynurenines: implications for brain synthesis and metabolism. J Neurochem 56(6):2007–2017

145. Fulop F, Szatmari I, Vamos E, Zadori D, Toldi J, Vecsei L (2009) Syntheses, transformations and pharmaceutical applications of kynurenic acid derivatives. Curr Med Chem 16 16:4828–4842

146. Gellért L, Fuzik J, Göblös A, et al (2011) Neuroprotection with a new kynurenic acid analog in the four-vessel occlusion model of ischemia. Eur J Pharmacol 667(1-3):182–7

147. Vamos E, Pardutz A, Klivenyi P, Toldi J, Vecsei L (2009) The role of kynurenines in disorders of the central nervous system: possibilities for neuroprotection. J Neurol Sci 283(1-2):21–7

148. Okuda S, Nishiyama N, Saito H, Katsuki H (1996) Hydrogen peroxide-mediated neuronal cell death induced by an endogenous neurotoxin, 3-hydroxykynurenine. Proc Natl Acad Sci U S A 93(22):12553–12558

149. Okuda S, Nishiyama N, Saito H, Katsuki H (1998) 3-Hydroxykynurenine, an endogenous oxidative stress generator, causes neuronal cell death with apoptotic features and region selectivity. J Neurochem 70(1):299–307

150. Guillemin GJ, Kerr SJ, Smythe GA, Smith DG, Kapoor V, Armati PJ, Croitoru J, Brew BJ (2001) Kynurenine pathway metabolism in human astrocytes: a paradox for neuronal protection. J Neurochem 78(4):842–853

151. Guillemin GJ, Croitoru-Lamoury J, Dormont D, Armati PJ, Brew BJ (2003) Quinolinic acid upregulates chemokine production and chemokine receptor expression in astrocytes. Glia 41(4):371–81

152. Pearson SJ, Reynolds GP (1992) Increased brain concentrations of a neurotoxin , 3-hydroxykynurenine , in Huntington ' s disease. Neurosci Lett 144:199–201

153. Ogawa T, Matson W, Beal M, Myers R, Bird E, Milbury P, Saso S (1992) Kynurenine pathway abnormalities in Parkinson's disease. Neurology 42(9):1702–6

154. Sardar A, Reynolds P (1995) Frontal cortex indoleamine-2,3-dioxygenase activity is increased in HIV-l-associated dementia. Neurosci Lett 187:9–12

155. Guidetti P, Schwarcz R (1999) 3-Hydroxykynurenine potentiates quinolinate but not NMDA toxicity in the rat striatum. Eur J Neurosci 11(11):3857–63

156. Schwarcz R, Pellicciari R (2002) Manipulation of Brain Kynurenines : Glial Targets , Neuronal Effects , and Clinical Opportunities. J Pharmacol Exp Ther 303(1):1–10

157. Schwarcz R, Bruno JP, Muchowski PJ, Wu H-Q (2012) Kynurenines in the mammalian brain: when physiology meets pathology. Nat Rev Neurosci 13(465):1–13

158. Guidetti P, Luthi-Carter RE, Augood SJ, Schwarcz R (2004) Neostriatal and cortical quinolinate levels are increased in early grade Huntington's disease. Neurobiol Dis 17(3):455–461

159. Guidetti P, Bates GP, Graham RK, Hayden MR, Leavitt BR, MacDonald ME, Slow EJ, Wheeler VC, Woodman B, Schwarcz R (2006) Elevated brain 3-hydroxykynurenine and quinolinate levels in Huntington disease mice. Neurobiol Dis 23(1):190–197

160. Giorgini F (2012) Targeting the Kynurenine Pathway in Huntington ' s Disease. ACNR 12(1):7–8

161. Jauch D, Urbaiiska EM, Guidetti P, Bird ED, Vonsattel JG, Whetsell W, Schwartz R (1995) Dysfunction of brain kynurenic acid metabolism in Huntington ' s disease : focus on kynurenine aminotransferases. J Neurol Sci 130:39–47

162. Stone TW, Darlington LG (2002) Endogenous kynurenines as targets for drug discovery and development. Nat Rev Drug Discov 1(8):609–20

163. Giorgini F, Möller T, Kwan W, et al (2008) Histone deacetylase inhibition modulates kynurenine pathway activation in yeast, microglia, and mice expressing a mutant huntingtin fragment. J Biol Chem 283(12):7390–400

164. Tai F, Pavese N, Gerhard A, Tabrizi SJ, Barker RA, Brooks DJ, Piccini P (2007) Microglial activation in presymptomatic Huntington ' s disease gene carriers. Brain 130:1759–1766

165. Sathyasaikumar K V, Stachowski EK, Amori L, Guidetti P, Muchowski PJ, Schwarcz R (2010) Dysfunctional kynurenine pathway metabolism in the R6/2 mouse model of Huntington's disease. J Neurochem 113(6):1416–25

166. Giorgini F, Guidetti P, Nguyen Q, Bennett SC, Muchowski PJ (2006) A genomic screen in yeast implicates kynurenine 3-monooxygenase as a therapeutic target for Huntington's disease. Nat Genet 37(5):526–531

167. Campesan S, Green EW, Breda C, Sathyasaikumar K V, Muchowski PJ, Schwarcz R, Kyriacou CP, Giorgini F (2011) The kynurenine pathway modulates neurodegeneration in a Drosophila model of Huntington's disease. Curr Biol 21(11):961–6

168. Moroni F, Russi P, Gallo-mezo MA, Moneti G, Pellicciari R (1991) Modulation of Quinolinic and Kynurenic Acid Content in the Rat Brain: Effects of Endotoxins and Nicotinylalanine. J Neurochem 57(5):1630–1635

169. Decker RH, Brown RR, Price JM (1963) Studies on the Biological Activity of Nicotinylalanine, an Analogue of Kynurenine. J Biol Chem 238(3):1049–1051

170. Pellicciari R, Natalini B, Costantino G, Mahmoud MR, Mattoli L, Sadeghpour BM, Moroni F, Chiarugi A, Carpenedo R (1994) Modulation of the kynurenine pathway in search for new neuroprotective agents. Synthesis and preliminary evaluation of (m-nitrobenzoyl)alanine, a potent inhibitor of kynurenine-3-hydroxylase. J Med Chem 37(5):647–655

171. Giordani A, Corti L, Cini M, Marconi M, Pillan A, Ferrario R, Schwarcz R, Guidetti P, Speciale C, Varasi M (1996) Benzoylalanine analogues as inhibitors of rat brain kynureninase and kynurenine 3-hydroxylase. Adv Exp Med Biol 77:499–505

172. Pellicciari R, Amori L, Costantino G, Giordani A, Macchiarulo A, Mattoli L, Pevarello P, Speciale C, Varasi M (2003) Modulation of the kynurenine pathway of tryptophan metabolism in search for neuroprotective agents. Focus on kynurenine-3- hydroxylase. Adv Exp Med Biol 527:621–628.

173. Röver S, Cesura a M, Huguenin P, Kettler R, Szente A (1997) Synthesis and biochemical evaluation of N-(4-phenylthiazol-2-yl)benzenesulfonamides as high-affinity inhibitors of kynurenine 3-hydroxylase. J Med Chem 40(26):4378–85

174. Ceresoli-Borroni G, Guidetti P, Amori L, Pellicciari R, Schwarcz R (2007) Perinatal Kynurenine 3-Hydroxylase Inhibition in Rodents : Pathophysiological Implications. J Neurosci Res 85(4):845–854

175. Amori L, Guidetti P, Pellicciari R, Kajii Y, Schwarcz R (2009) On the relationship between the two branches of the kynurenine pathway in the rat brain in vivo. J Neurochem 109(2):316–25

176. Carpenedo R, Meli E, Peruginelli F, Pellegrini-Giampietro DE, Moroni F (2002) Kynurenine 3-mono-oxygenase inhibitors attenuate post-ischemic neuronal death in organotypic hippocampal slice cultures. J Neurochem 82(6):1465–71

177. Grégoire L, Rassoulpour A, Guidetti P, Samadi P, Bédard PJ, Izzo E, Schwarcz R, Di Paolo T (2008) Prolonged kynurenine 3-hydroxylase inhibition reduces development of levodopa-induced dyskinesias in parkinsonian monkeys. Behav Brain Res 186(2):161–7

178. Zwilling D, Huang S-Y, Sathyasaikumar K V, et al (2011) Kynurenine 3-monooxygenase inhibition in blood ameliorates neurodegeneration. Cell 145(6):863–74

179. Amori L, Wu HQ, Marinozzi M, Pellicciari R, Guidetti P, Schwarcz R (2009) Specific inhibition of kynurenate synthesis enhances extracellular dopamine levels in the rodent striatum. Neuroscience 159(1):196–203

180. Constantino G, Mattoli L, Moroni F, Natalini B, Pellicciari R (1996) kynurenine 3-hydroxylase and its selective inhibitors. In: Filippini GA (ed) Recent advances in tryptophan research. New York, pp 493–497

181. Courtney S, Scheel A (2010) Modulation of the Kynurenine Pathway for the Potential Treatment of Neurodegenerative Diseases. In: Dominguez C (ed) Neurodegenerative Diseases. pp 149–176

182. Warburg O, W. C (1933) The yellow enzyme and its functions. Biochem Z 266:377–411

183. Massey V (2000) The chemical and biological versatility of riboflavin. Biochem Soc Trans 28(4):283–96

184. Edwards ANAM (2006) General Properties of Flavins. Flavins Photochemistry and Photobiology, 1st ed. Royal Society of Chemistry, pp 1–11

185. Massey V, Hemmerich P (1980) Active-site probes of flavoproteins. Biochem Soc Trans 8(3):246–57

186. Massey V, Ghisla S (1989) The Mechanism of Action of Flavoprotein - Catalyzed Reactions. Eur Arch Psychiatry Clin Neurosci 181(1):1–17

187. Van Berkel WJH, Kamerbeek NM, Fraaije MW (2006) Flavoprotein monooxygenases, a diverse class of oxidative biocatalysts. J Biotech 124(4):670–89

188. Van Berkel WJ, Benen J a, Eppink MH, Fraaije MW (1999) Flavoprotein kinetics. In: Chapman S, Reid G (eds) Methods in molecular biology Flavoproteins Protocol. Humana press, pp 61–85

189. Wierenga RK, De Jong RJ, Kalk KH, Hol WG, Drenth J (1979) Crystal structure of p-hydroxybenzoate hydroxylase. J Mol Biol 131(1):55–73

190. Wang J, Ortiz-Maldonado M, Entsch B, Massey V, Ballou D, Gatti DL (2002) Protein and ligand dynamics in 4-hydroxybenzoate hydroxylase. Proc Natl Acad Sci U S A 99(2):608–13

191. Schulz GE, Schirmer RH (1974) Topological comparison of adenyl kinase with other proteins. Nature 250:142–144

192. Wierenga RK, Terpstra P, Hol WG (1986) Prediction of the occurrence of the ADP-binding beta alpha beta-fold in proteins, using an amino acid sequence fingerprint. J Mol Biol 187(1):101–7

193. Rao ST, Rossmann MG (1973) Comparison of super-secondary structures in proteins. J Mol Biol 76(2):241–56

194. Eggink G, Engel H, Vriend G, Terpstra P, Witholt B (1990) Rubredoxin reductase of Pseudomonas oleovorans. Structural relationship to other flavoprotein oxidoreductases based on one NAD and two FAD fingerprints. J Mol Biol 212(1):135–42

195. Schreuder HA, Laan JM Van Der, Ho WGJ, Drenth J (1988) Crystal Structure of p-Hydroxybenzoate Hydroxylase Complexed with its Reaction Product. J Mol Biol 199:637–648

196. Eppink MHM, Schreuder HA, Van Berkel WJH (1997) Identification of a novel conserved sequence motif in flavoprotein hydroxylases with a putative dual function in FAD/NAD(P)H binding. Protein Sci 6:2454–2458

197. Okamoto H, Hayaishi O (1967) Flavin adenine dinucleotide requirement for kynurenine hydroxilase of rat liver mitochondria. Biochem Biophys Res Commun 29(3):394–399

198. Crozier-Reabe KR, Phillips RS, Moran GR (2008) Kynurenine 3-monooxygenase from Pseudomonas fluorescens: substrate-like inhibitors both stimulate flavin reduction and stabilize the flavin-peroxo intermediate yet result in the production of hydrogen peroxide. Biochemistry 47(47):12420–33

199. De Castro FT, Price JM, Brown R. (1956) Reduced triphosphopyridinenucleotide requirement for the enzymatic formation of 3-hydroxykynurenine from L-kynurenine. J Am Chem Soc 78:2904–2905

200. Okamoto H, Yamamoto S, Nozaki M, Hayaishi O (1967) On the submitochondrial localization of L-kynurenine-3-hydroxylase. Biochem Biophys Res Commun 26(3):309–314

201. Erickson JB, Flanagan EM, Russo S, Reinhard Jr. JF (1992) A radiometric assay for kynurenine 3-hydroxylase based on the release of 3H2O during hydroxylation of L-[3,5-3H]kynurenine. Anal Biochem 205(2):257–262

202. De Castro FT, Brown RR, Price JM (1957) The intermediary metabolism of tryptophan by cat and rat tissue preparations. J Biol Chem 28:777–784

203. Heyes MP, Saito K, Markey SP (1992) Human macrophages convert L-tryptophan into the neurotoxin quinolinic acid. Biochem J 283:633–635

204. Uemura T, Hirai K (1998) L-kynurenine 3-monooxygenase from mitochondrial outer membrane of pig liver: purification, some properties, and monoclonal antibodies directed to the enzyme. J Biochem 123(2):253–262

205. Guillemin GJ, Kerr SJ, Smythe G, Smith DG, Kapoor V, Armati PJ, Croitoru J, Brew BJ (2001) Kynurenine pathway metabolism in human astrocytes: a paradox for neuronal protection. J Neurochem 78(4):842–53

206. Crozier-Reabe KR, Phillips RS, Moran GR (2008) Kynurenine 3-monooxygenase from Pseudomonas fluorescens: substrate-like inhibitors both stimulate flavin reduction and stabilize the flavin-peroxo intermediate yet result in the production of hydrogen peroxide. Biochemistry 47(47):12420–33

207. Crozier KR, Moran GR (2007) Heterologous expression and purification of kynurenine-3-monooxygenase from Pseudomonas fluorescens strain 17400. Protein Exp Purif 51(2):324–33

208. Breton J, Avanzi N, Magagnin S, Covini N, Magistrelli G, Cozzi L, Isacchi A (2000) Functional characterization and mechanism of action of recombinant human kynurenine 3-hydroxylase. Eur J Biochem 267(4):1092–9

209. Panozzo C, Nawara M, Suski C, Kucharczyka R, Skoneczny M, Becam AM, Rytka J, Herbert CJ (2002) Aerobic and anaerobic NAD+ metabolism in Saccharomyces cerevisiae. FEBS Lett 517(1-3):97–102

210. Nisimoto Y, Takeuchi F, Shibata Y (1975) Isolation of L-dynurenine 3-hydroxylase from the mitochondrial outer membrane of rat liver. J Biochem 78(3):573–81

211. Nishimoto Y, Takeuchi F, Shibata Y (1979) Purification of L-kynurenine 3-hydroxylase by affinity chromatography. J Chromatogr 169:357–64

212. McLean-Bowen C a, Parks LW (1981) Corresponding changes in kynurenine hydroxylase activity, membrane fluidity, and sterol composition in Saccharomyces cerevisiae mitochondria. J Bacteriol 145(3):1325–33

213. Shin M, Sano K, Umezawa C (1982) Inhibition of L-kynurenine 3-hydroxylase from Saccharomyces carlsbergensis by alpha-keto acid derivatives of branched chain amino acids. J Nutr Sci Vitaminol (Tokyo) 28(3):191–201

214. Pinamonti S, Chiarelli-Alvesi G (1974) Studies on the kynurenine-3-hydroxylase of Schistocerca Gregaria. Insect Biochem 4:9–16

215. Macheroux P (1999) UV-visible spectroscopy as a Tool to Study Flavoproteins. In: Chapman S, Reid G (eds) Methods in molecular biology Flavoproteins Protocol. pp 1–7

216. Uemura T, Hirai K (1998) L-kynurenine 3-monooxygenase from mitochondrial outer membrane of pig liver: purification, some properties, and monoclonal antibodies directed to the enzyme. J Biochem 123(2):253–62

217. Gatti DL, Palfey BA, Lah MS, Entsch B, Massey V, Ballou DP, Ludwig ML (1994) The mobile flavin of 4-OH benzoate hydroxylase. Science 266(5182):110–4

218. Hiromoto T, Fujiwara S, Hosokawa K, Yamaguchi H (2006) Crystal structure of 3-hydroxybenzoate hydroxylase from Comamonas testosteroni has a large tunnel for substrate and oxygen access to the active site. J Mol Biol 364(5):878–96

219. Enroth C, Neujahr H, Schneider G LY (1998) The crystal structure of phenol hydroxylase in complex with FAD and phenol provides evidence for a concerted conformational change in the enzyme and its cofactor during catalysis. Structure 6(5):605–17

220. Gatti DL, Palfey B a, Lah MS, Entsch B, Massey V, Ballou DP, Ludwig ML (1994) The mobile flavin of 4-OH benzoate hydroxylase. Science (New York, NY) 266(5182):110–4

221. Shoun H, Arima K, Beppu T (1983) Inhibition of p-hydroxybenzoate hydroxylase by anions: possible existence of two anion-binding sites in the site for reduced nicotinamide adenine dinucleotide phosphate. J Biochem 93(1):169–76

222. Romanos M a, Scorer C a, Clare JJ (1992) Foreign gene expression in yeast: a review. Yeast 8(6):423–88

223. Privé GG (2007) Detergents for the stabilization and crystallization of membrane proteins. Methods 41(4):388–97

224. Arnold T, Linke D (2007) Phase separation in the isolation and purification of membrane proteins. BioTechniques 43(4):427–440

225. Kabsch W (2010) XDS. Acta crystallogr D Biol crystallogr 66(Pt 2):125–32

226. McCoy AJ, Storoni LC, Read RJ (2004) Simple algorithm for a maximum-likelihood SAD function. Acta crystallogr D Biol crystallogr 60(Pt 7):1220–8

227. Terwilliger TC, Grosse-Kunstleve RW, Afonine P V, Moriarty NW, Zwart PH, Hung LW, Read RJ, Adams PD (2008) Iterative model building, structure refinement and density modification with the PHENIX AutoBuild wizard. Acta crystallogr D Biol crystallogr 64(Pt 1):61–9

228. Emsley P, Cowtan K (2004) Coot: model-building tools for molecular graphics. Acta crystallogr D Biol crystallogr 60(Pt 12 Pt 1):2126–32

229. Adams PD, Afonine P V, Bunkóczi G, et al (2010) PHENIX: a comprehensive Python-based system for macromolecular structure solution. Acta crystallogr D Biol crystallogr 66(Pt 2):213–21

230. McCoy AJ, Grosse-Kunstleve RW, Adams PD, Winn MD, Storoni LC, Read RJ (2007) Phaser crystallographic software. J Appl Crystallogr 40(Pt 4):658–674

231. Chen VB, Arendall WB, Headd JJ, Keedy D a, Immormino RM, Kapral GJ, Murray LW, Richardson JS, Richardson DC (2010) MolProbity: all-atom structure validation for macromolecular crystallography. Acta crystallogr D Biol crystallogr 66(Pt 1):12–21

232. Phillips JC, Al. E (2005) Scalable molecular dynamics with NAMD. J Comput Chem (76):1781–1802

233. Wendy DC, et al. (1995) A second Generation Force Field for the Simulation of Proteins, Nucleic Acids, and Organic Molecules. J Am Chem Soc (117):5179–5197

234. Jakalian A, Jack DB, Bayly CI (2002) Fast, efficient generation of high-quality atomic charges. AM1-BCC model: II. Parameterization and validation. J Comput Chem (23):1623–1641

235. Nisimoto Y, Takeuchi F, Shibata Y (1977) Molecular properties of L-kynurenine 3-hydroxylase from rat liver mitochondria. J Biochem 81(5):1413–1425

236. Krogh a, Larsson B, Von Heijne G, Sonnhammer EL (2001) Predicting transmembrane protein topology with a hidden Markov model: application to complete genomes. J Mol Biol 305(3):567–80

237. Slabinski L, Jaroszewski L, Rychlewski L, Wilson I a, Lesley S a, Godzik A (2007) XtalPred: a web server for prediction of protein crystallizability. Bioinformatics (Oxford, England) 23(24):3403–5

238. Webb BN, Ballinger JW, Kim E, Belchik SM, Lam K-S, Youn B, Nissen MS, Xun L, Kang C (2010) Characterization of chlorophenol 4-monooxygenase (TftD) and NADH:FAD oxidoreductase (TftC) of Burkholderia cepacia AC1100. J Biol Chem 285(3):2014–27

239. European Bioinformatics Institute, Cambridge U (2007) Kasuza Database. http://www.kazusa.or.jp/codon/.

240. Li P, Anumanthan A, Gao X-G, Ilangovan K, Suzara V V., Düzgüneş N, Renugopalakrishnan V (2007) Expression of Recombinant Proteins in Pichia Pastoris. Appl Biochem Biotechnol 142(2):105–124

241. Romanos M (1995) Advances in the use of Pichia pastoris for high-level gene expression. Curr Opin Biotechnol 6(5):527–533

242. Rover S, Cesura AM, Huguenin P, Kettler R, Szente A (1997) Synthesis and biochemical evaluation of N-(4-phenylthiazol-2-yl)benzenesulfonamides as high-affinity inhibitors of kynurenine 3-hydroxylase. J Med Chem 40(26):4378–4385

243. Niesen FH, Berglund H, Vedadi M (2007) The use of differential scanning fluorimetry to detect ligand interactions that promote protein stability. Nat Protoc 2(9):2212–21

244. Dias A, Bouvier D, Crépin T, McCarthy A a, Hart DJ, Baudin F, Cusack S, Ruigrok RWH (2009) The cap-snatching endonuclease of influenza virus polymerase resides in the PA subunit. Nature 458(7240):914–8

245. Bergfors TM (2009) Protein Crystallization: Second Edition. International Univ Line

246. Hirai K, Kuroyanagi H, Tatebayashi Y, Hayashi Y, Hirabayashi-Takahashi K, Saito K, Haga S, Uemura T, Izumi S (2010) Dual role of the carboxyl-terminal region of pig liver L-kynurenine 3-monooxygenase: mitochondrial-targeting signal and enzymatic activity. J Biochem 148(6):639–50

247. Huber T, Steiner D, Röthlisberger D, Plückthun A (2007) In vitro selection and characterization of DARPins and Fab fragments for the co-crystallization of membrane proteins: The Na(+)-citrate symporter CitS as an example. J Struct Biol 159(2):206–21

248. Gasymov O, Abduragimov AR, Merschak P, Redl B, Glasgow BJ (2008) Oligomeric State of Lipocalin-1 (LCN1) by Multiangle Laser Light Scattering and Fluorescence Anisotropy Decay. Biochim Biophys Acta 1774(10):1307–1315

249. Sapko MT, Guidetti P, Yu P, Tagle DA, Pellicciari R, Schwarcz R (2006) Endogenous kynurenate controls the vulnerability of striatal neurons to quinolinate: Implications for Huntington's disease. Exp Neurol 197(1):31–40

250. Schott HH, Staudinger H, Ullrich V (1971) The Regulatory Function of L-Kynurenine 3-Hydroxylase (EC 1.14.1.2) for the biosynthesis of pyridine nucleotides in anaerobically and aerobically grown Saccharomyces cerevisiae. Hoppe Seylers Z Physiol Chem 350(12):1654–1658

251. Han Q, Calvo E, Marinotti O, Fang J, Rizzi M, James a a, Li J (2003) Analysis of the wild-type and mutant genes encoding the enzyme kynurenine monooxygenase of the yellow fever mosquito, Aedes aegypti. Insect Mol Biol 12(5):483–90

252. Oliveira AP, Sauer U (2012) The importance of post-translational modifications in regulating Saccharomyces cerevisiae metabolism. FEMS Yeast Res 12(2):104–17

253. Xin F, Radivojac P (2012) Post-translational modifications induce significant yet not extreme changes to protein structure. Bioinformatics (Oxford, England) 28(22):2905–13

254. Ingrell CR, Miller ML, Jensen ON, Blom N (2007) NetPhosYeast: prediction of protein phosphorylation sites in yeast. Bioinformatics (Oxford, England) 23(7):895–7

255. Palfey B, McDonald C (2010) Control of catalysis in flavin-dependent monooxygenases. Arch Biochem Biophys 493(1):26–36

256. Hassell AM, An G, Bledsoe RK, et al (2007) Crystallization of protein-ligand complexes. Acta crystallogr D Biol crystallogr 63(Pt 1):72–9

257. Celej MS, Montich GG, Fidelio GD (2003) Protein stability induced by ligand binding correlates with changes in protein flexibility. Protein Sci 1496–1506

258. DiMaio F, Terwilliger TC, Read RJ, et al (2011) Improved molecular replacement by density- and energy-guided protein structure optimization. Nature 473(7348):540–543

259. Garman E, James W (2003) Heavy-atom derivatization. Acta Crystallographica Section D (D59):1903–1913

260. Taylor G (2003) The phase problem. Acta crystallogr D Biol crystallogr 59(11):1881–1890

261. Walden H (2010) Selenium incorporation using recombinant techniques. Acta crystallogr D Biol crystallogr 66(Pt 4):352–7

262. Krissinel E, Henrick K (2007) Inference of macromolecular assemblies from crystalline state. J Mol Biol 372:774–797

263. Holm L, Kääriäinen S (2010) Dali server: conservation mapping in 3D. Nucleic Acids Res 38:545–549

264. McCulloch M, Mukherjee T, Begley TP, Ealick SE (2010) Structure of the PLP Degradative Enzyme 2-Methyl-3- hydroxypyridine-5-carboxylic acid Oxygenase from Mesorhizobium loti MAFF303099 and its Mechanistic Implications. Biochemistry 48(19):4139–4149

265. Eppink MH, Bunthol C, Schreuder HA, Van Berkel WJ (1999) Phe161 and Arg166 variants of p-hydroxybenzoate hydroxylase. Implications for NADPH recognition and structural stability. FEBS Lett 443(3):251–5

266. Eppink MH, Schreuder H a, Van Berkel WJ (1998) Interdomain binding of NADPH in p-hydroxybenzoate hydroxylase as suggested by kinetic, crystallographic and modeling studies of histidine 162 and arginine 269 variants. J Biol Chem 273(33):21031–9

267. Seibold B, Matthes M, Eppink MHM, Lingens F, Berkel WJHVAN, Muller R (1996) Purification , characterization , gene cloning , sequence analysis and assignment of structural features determining the coenzyme specificity. Eur J Biochem 239:469–478

268. Ortiz-Maldonado M, Ballou DP, Massey V (2001) A rate-limiting conformational change of the flavin in p-hydroxybenzoate hydroxylase is necessary for ligand exchange and catalysis: studies with 8-mercapto- and 8-hydroxy-flavins. Biochemistry 40(4):1091–101

269. Zhang Y (2008) I-TASSER server for protein 3D structure prediction. BMC Bioinformatics 9:40

270. Amori L, Guidetti P, Pellicciari R, Kajii Y, Schwarcz R (2009) On the relationship between the two branches of the kynurenine pathway in the rat brain in vivo. J Neurochem 109(2):316–325

271. Kalyaanamoorthy S, Chen Y-PP (2011) Structure-based drug design to augment hit discovery. Drug Discov Today 16(17-18):831–9

272. Chen Y, Chen F (2008) Using bioinformatics techniques for gene identification in drug discovery and development. Curr Drug Metab 9(6):567–7

273. Alberati-Giani D, Cesura AM, Broger C, Warren WD, Rover S, Malherbe P (1997) Cloning and functional expression of human kynurenine 3-monooxygenase. FEBS Lett 410(2-3):407–412

274. Wexler A (2012) Huntington ’ s Disease – A Brief Historical Perspective. J Huntington’s Disease 1:3–4

# 8. SUPPLEMENTARY SECTION

## 8.1. SUPPLEMENTARY FIGURES

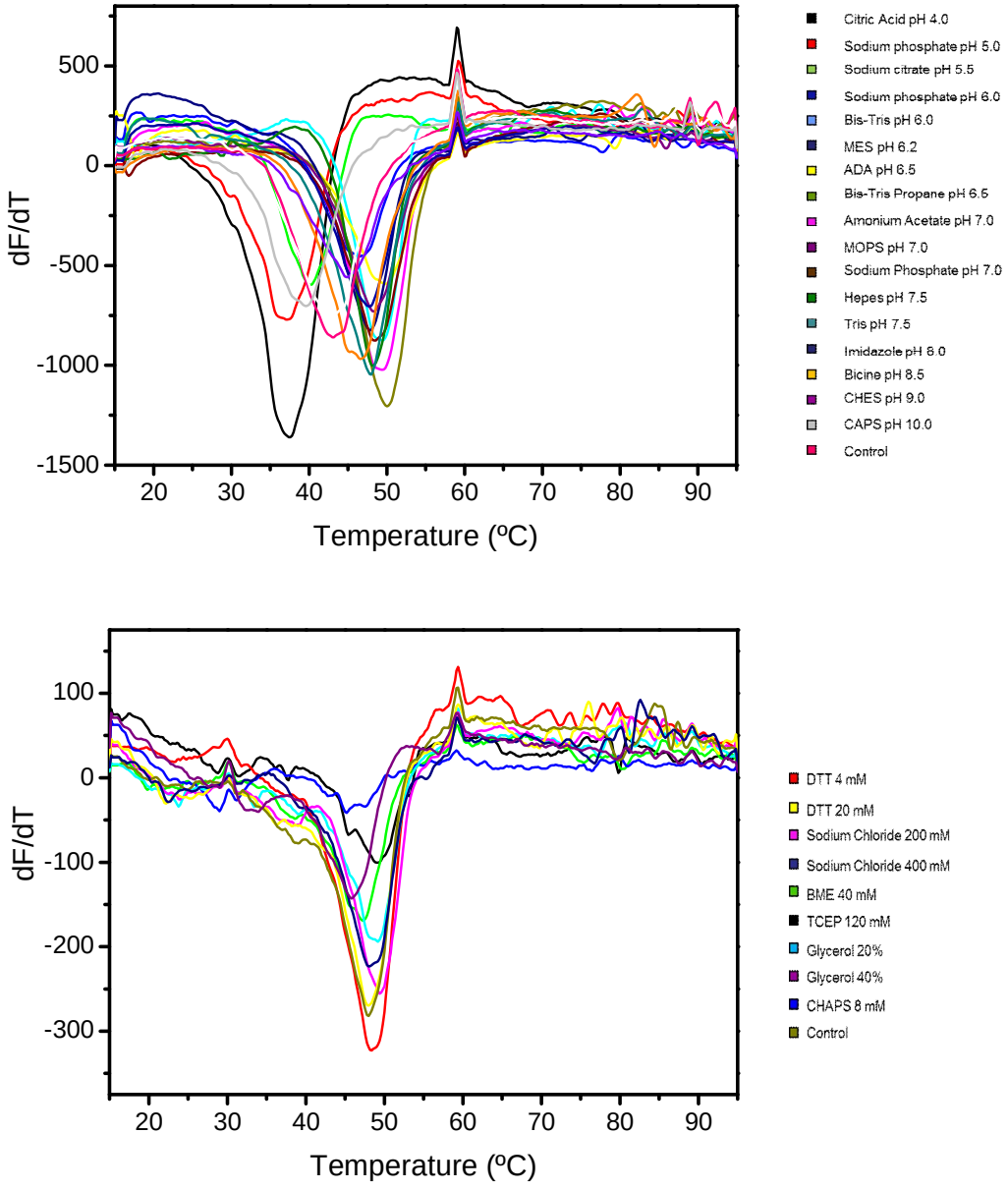


**Supplementary Figure 1. Thermofluor assay of ΔKMO383 buffer and additive screen**. Negative first derivatives of the melting curves produced by ΔKMO383 are shown in a range of different buffers (A) and additives (B) from the JBS Solubility Kit. The minimum value represents the midpoint of the unfolding transition, providing a quick and robust method for determining the *T*m of samples in individual wells. Only the buffers from which a Tm could be derived are shown. dF/dT represents fluorescence change at different temperatures. Sample control is in 20 mM phosphate buffer pH 7.5 (B) Representative curves of

the additive screen using Bis-Tris Propane pH 6.5 as the standard buffer. Sample control is in Bis-Tris Propane pH 6.5 without additives.

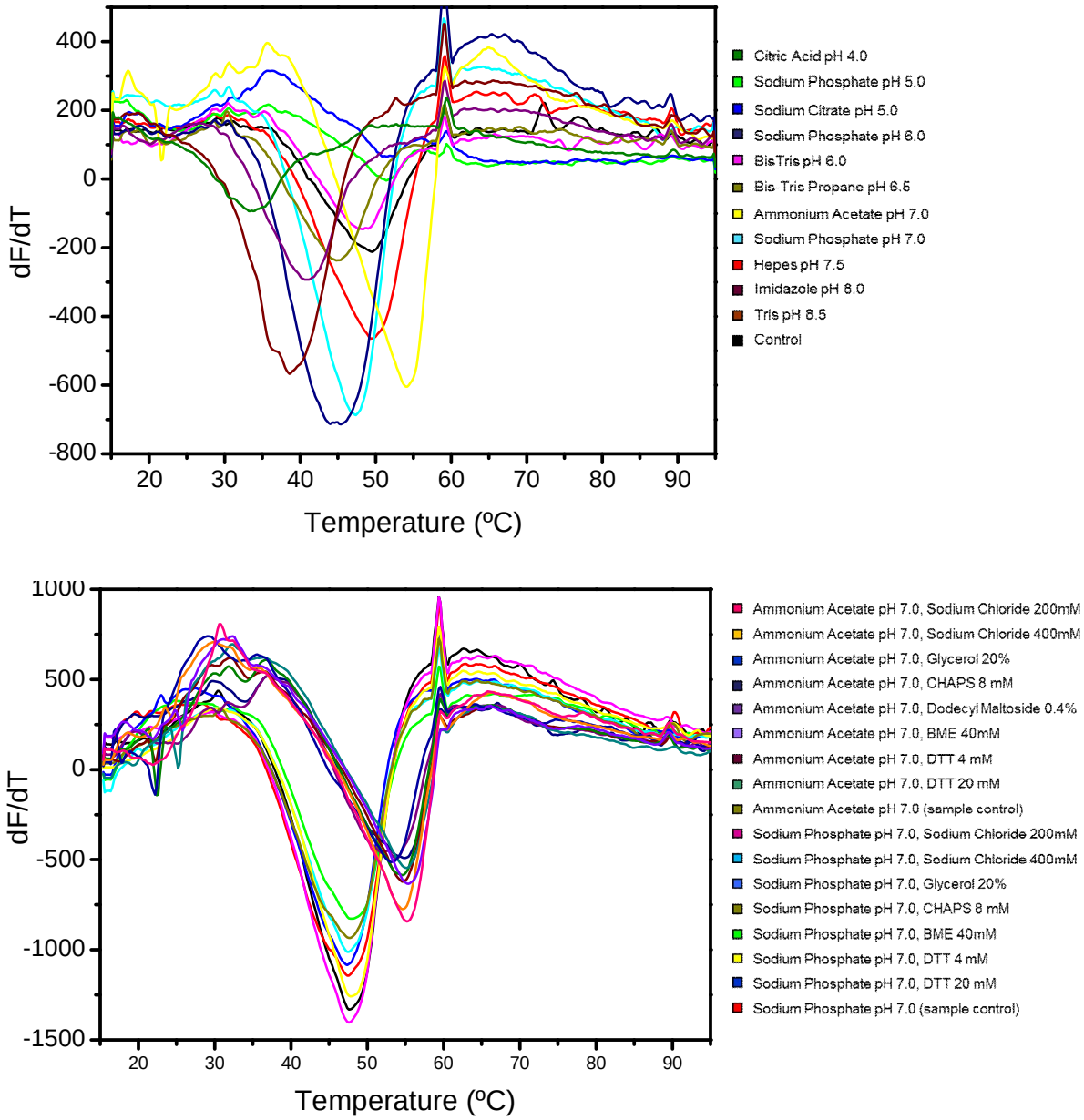


**Supplementary Figure 2. Thermofluor assay of *Sc*KMO buffer and additive screen.** (A) Negative first derivatives of the melting curves produced by *Sc*KMO are shown in a range of different buffers from the JBS Solubility Kit. The resulted curve usually shows a sharp transition between folded and unfolded states and the melting temperature ($T_m$) is precisely the midpoint of temperature of this unfolded transition. Only the buffers from which a $T_m$ could be derived are shown. dF/dT represents fluorescence change at different temperatures. Sample control is in 20 mM phosphate buffer pH 7.5. (B) Negative first derivatives are shown of the Representative melt curves produced by *Sc*KMO supplemented with additives from the JBS Solubility Kit screen using Ammonium Acetate pH 7.0 and Sodium phosphate pH 7.0 as the standard buffers.

## 8.2. PUBLISHED PAPER:

Amaral, M., Levy, C., Heyes D.J., Lafite P., Outeiro, T., Giorgini, F., Scrutton, N., *Structural basis of inhibition in the neurodegeneration target kynurenine 3-monooxygenase*, Nature, doi:10.1038/nature12039